
THE UNIVERSITY *of* EDINBURGH

# Post formation processing of cardiac ultrasound data for enhancing image quality and diagnostic value

**Antonios Perperidis**


A thesis submitted for the degree of Doctor of Philosophy

**The University of Edinburgh**

March 2011

*To my family and my fiancée Claire*

# Declaration of Originality

I hereby declare that the research recorded in this thesis, as well as the thesis itself, was originated and conducted entirely by myself, except where explicitly stated otherwise. All work was performed in the Unit of Medical Physics and Medical Engineering at the University of Edinburgh and has not been submitted for any other degree or professional qualification.

Name:…**Antonios Perperidis**…… Date: … **20/10/2011**……

# Abstract

Cardiovascular diseases (CVDs) constitute a leading cause of death, including premature death, in the developed world. The early diagnosis and treatment of CVDs is therefore of great importance. Modern imaging modalities enable the quantification and analysis of the cardiovascular system and provide researchers and clinicians with valuable tools for the diagnosis and treatment of CVDs. In particular, echocardiography offers a number of advantages, compared to other imaging modalities, making it a prevalent tool for assessing cardiac morphology and function. However, cardiac ultrasound images can suffer from a range of artifacts reducing their image quality and diagnostic value. As a result, there is great interest in the development of processing techniques that address such limitations.

This thesis introduces and quantitatively evaluates four methods that enhance clinical cardiac ultrasound data by utilising information which until now has been predominantly disregarded. All methods introduced in this thesis utilise multiple partially uncorrelated instances of a cardiac cycle in order to acquire the information required to suppress or enhance certain image features. No filtering out of information is performed at any stage throughout the processing. This constitutes the main differentiation to previous data enhancement approaches which tend to filter out information based on some static or adaptive selection criteria.

The first two image enhancement methods utilise spatial averaging of partially uncorrelated data acquired through a single acoustic window. More precisely, *Temporal Compounding* enhances cardiac ultrasound data by averaging partially uncorrelated instances of the imaged structure acquired over a number of consecutive cardiac cycles. An extension to the notion of spatial compounding of cardiac ultrasound data is *3D-to-2D Compounding*, which presents a novel image enhancement method by acquiring and compounding spatially adjacent (along the elevation plane), partially uncorrelated, 2D slices of the heart extracted as a thin angular sub-sector of a volumetric pyramid scan. Data enhancement introduced by both approaches includes the substantial suppression of tissue speckle and cavity noise. Furthermore, by averaging decorrelated instances of the same cardiac structure, both compounding methods can enhance tissue structures, which are masked out by high levels of noise and shadowing, increasing their corresponding tissue/cavity detectability.

The third novel data enhancement approach, referred as *Dynamic Histogram Based Intensity Mapping (DHBIM)*, investigates the temporal variations within image histograms of consecutive frames in order to (i) identify any unutilised/underutilised intensity levels and (ii) derive the tissue/cavity intensity threshold within the processed frame sequence. Piecewise intensity mapping is then used to enhance cardiac ultrasound data. *DHBIM* introduces cavity noise suppression, enhancement of tissue speckle information as well as considerable increase in tissue/cavity contrast and detectability.

A data acquisition and analysis protocol for integrating the dynamic intensity mapping along with spatial compounding methods is also investigated. The linear integration of *DHBIM* and *Temporal Compounding* forms the fourth and final implemented method, which is also quantitatively assessed. By taking advantage of the benefits and compensating for the limitations of each individual method, the integrated method suppresses cavity noise and tissue speckle while enhancing tissue/cavity contrast as well as the delineation of cardiac tissue boundaries even when heavily corrupted by cardiac ultrasound artifacts.

Finally, a novel protocol for the quantitative assessment of the effect of each data enhancement method on image quality and diagnostic value is employed. This enables the quantitative evaluation of each method as well as the comparison between individual methods using clinical data from 32 patients. Image quality is assessed using a range of quantitative measures such as signal-to-noise ratio, tissue/cavity contrast and detectability index. Diagnostic value is assessed through variations in the repeatability level of routine clinical measurements performed on patient cardiac ultrasound scans by two experienced echocardiographers. Commonly used clinical measures such as the wall thickness of the Interventricular Septum (IVS) and the Left Ventricle Posterior Wall (LVPW) as well as the cavity diameter of the Left Ventricle (LVID) and Left Atrium (LAD) are employed for assessing diagnostic value.

# Acknowledgements

This thesis would not be possible without the help and support from many people. I would therefore like to thank my supervisors Tom Anderson, Norman McDicken and Tom MacGillivray for their guidance and constructive feedback throughout the four years of my studies. I would like express my gratitude to Audrey White and David Cusack for providing me with an abundance of valuable resources along with their personal time and professional opinion. I would also like to thank Professor D'hooge and Dr Sboros for agreeing to be the examiners for this thesis.

On a personal note, I would like to thank the people of the Medical Physics Unit, past and present, that have made these last four years a very enjoyable journey. Special thanks to Mairead, everyone that has done time in the lab-benches (Ben, Padraig and David) and the broom-cupboard (Dave, Michael and many more), for making sure that I will not complete my thesis before my 4$^{th}$ year deadline. Irene deserves a special mention for making my work life so much easier. Also, many thanks to my family and friends that I have neglected over the last few busy months.

Finally, I would to express my gratitude and love to my parents Maika and Stelios and my brother Dimitris for helping me become the person I am. Last but not least, I would like to thank my lovely fiancée Claire for the constant support and inspiration she has provided me these last few years. The help from all of you has been invaluable and I would therefore like to dedicate this work to you.

# Contents

# Abbreviations

| | |
|---|---|
| **ABTF** | Adaptive Brightness Transfer Function |
| **AV** | Atrioventricular Valve |
| **BPDHE** | Brightness Preserving Dynamic Histogram Equalisation |
| **BSE** | British Society of Echocardiography |
| **CCC** | Combined Correlation Coefficient |
| **CDI** | Colour Doppler Imaging |
| **CHD** | Coronary Heart Disease |
| **CNR** | Contrast to Noise Ratio |
| **CP** | Control Point |
| **CR** | Coefficient of Repeatability |
| **CT** | Computed Tomography |
| **CVD** | Cardiovascular Disease |
| **DHBIM** | Dynamic Histogram Based Intensity Mapping |
| **DHE** | Dynamic Histogram Equalisation |
| **ECG** | Electrocardiogram |
| **ED** | End Diastole/Diastolic |
| **ES** | End Systole/Systolic |
| **fps** | frames per second |
| **FSI** | Fast Surface Interpolation |
| **HTN** | Hypertensive Heart Disease |
| **IVS(d)** | Interventricular Septal Thickness (diastolic) |
| **LADs** | Left Atrium Dimension (systolic) |
| **LV** | Left Ventricle |
| **LVIDd** | Left Ventricular Internal Dimension (diastolic) |
| **LVIDs** | Left Ventricular Internal Dimension (systolic) |
| **LVPWd** | Left Ventricular Posterior Wall (diastolic) |
| **M** | Mean |
| **MAD** | Mean Absolute Deviation |
| **MDCT** | Multi-Detector row Computed Tomography |
| **MRI** | Magnetic Resonance Imaging |
| **MSE** | Mean Square Error |
| **NMI** | Normalised Mutual Information |
| **NXC** | Normalised Cross Correlation |
| **PET** | Positron Emission Tomography |
| **$R^2$** | Linear regression |
| **RMS(E)** | Root Mean Square (Error) |
| **ROI** | Region Of Interest |
| **RT3DE** | Real-Time 3D Echocardiography |
| **RV** | Right Ventricle |
| **SAR** | Synthetic Aperture Radar |
| **SD** | Standard Deviation |
| **SDNR** | Signal Difference to Noise Ratio |
| **SNR** | Signal to Noise Ratio |
| **SPECT** | Single Photon Emission Computed Tomography |
| **SSD** | Sum of Squared Differences |
| **STE** | Speckle Tracking Echocardiography |
| **TDI** | Tissue Doppler Imaging |
| **TEE** | Transesophageal Echocardiography |
| **TGC** | Time Gain Compensation |
| **THI** | Tissue Harmonic Imaging |
| **TMM** | Tissue Mimicking Material |
| **TTE** | Transthoracic Echocardiography |

# List of figures

# List of tables

# Chapter 1

# Introduction

*Cardiovascular diseases* (*CVDs*) constitute a leading cause of death, including premature death, in the developed world. The early diagnosis and treatment of CVDs is therefore of great importance. Modern imaging modalities enable the quantification and analysis of the cardiovascular system and provide researchers and clinicians with valuable tools for the diagnosis and treatment of CVDs. In particular, echocardiography offers a number of advantages, compared to other imaging modalities, making it a prevalent tool for assessing cardiac morphology and function. However, cardiac ultrasound data can suffer from a range of artifacts reducing their image quality and diagnostic value. As a result, there is great interest in the development of processing techniques that address such limitations. This chapter provides a synopsis on the fundamental principles of the cardiac anatomy and function. A brief review on current imaging modalities along with a more thorough analysis of modern ultrasound imaging of the cardiovascular system is also provided. Finally, the motivation behind this work is identified and elucidated by taking into consideration the benefits and limitations of cardiac ultrasound imaging.

## 1.1. Cardiovascular system

The cardiovascular system is a transport system linking the external environment to the tissues of the human body (Bray et al., 1999). It distributes substances essential for metabolism, such as $O_2$ from the lungs and nutrients from the gastrointestinal tract, while removing by-products of metabolism such as $CO_2$ from tissue, transferring them to the lungs, kidneys and liver (Bray et al., 1999). The cardiovascular system also participates in homeostatic mechanisms such as the regulation of body temperature, maintenance of fluids and producing and circulating hormones (Bray et al., 1999; Berne et al., 2004). The heart is the principal organ orchestrating the effective operation of the cardiovascular system and is therefore one of the most vital organs in the human body. Failure of the continuous and uniform heart operation can have an immense impact in the operation of the body and even

cause death. Detailed information on the morphology and function of the cardiovascular system can be found in a number of textbooks (Guyton, 1991; Seeley et al., 1996; Guyton & Hall, 1997; Bray et al., 1999; Berne et al., 2004). A brief description of the cardiac morphology and function is provided in the subsequent sections.

### 1.1.1. Cardiac morphology and function

Blood circulation can be divided into two stages, (i) the *pulmonary circulation* in which the blood is transferred from the heart through the lungs in order to get oxygenated and (ii) the *systemic circulation* in which the oxygenated blood is pumped from the heart to all other tissues of the human body (Seeley et al., 1996). High pressure vessels known as *arteries* distribute blood from the heart, while low pressure vessels known as *veins* collect returning blood to the heart (Bray et al., 1999). The heart consists of two separate pumps lying side by side; the right heart (pump), which is responsible for the pulmonary circulation (low pressure), and the left heart (pump), which is responsible for the systemic circulation (high pressure) (Bray et al., 1999). In turn, each pump consists of two chambers, an *atrium* and a *ventricle* (Guyton, 1991). The atrium primarily acts as a weak primer pump, or an entryway, for the ventricle. The ventricle supplies the main force that propels the blood through the circulatory system (Guyton, 1991). The pumping action of the heart is generated from the muscle wall surrounding its chambers, also known as the *myocardium*, which consists of the *endocardium* (inner layer), the *epicardium* (outer surface) and is enclosed by the *pericardium*. The atrial myocardium is a thin structure and as a result generates low pressure, while ventricular myocardium is thick, generating higher pumping pressure (Bray et al., 1999). Furthermore, the two ventricles are separated by the *interventricular septum* (*IVS*) muscle (Seeley et al., 1996). The aperture between each atrium and the corresponding ventricle is guarded by an *atrioventricular valve* (*AV*), which is attached to the corresponding ventricular muscles through tendinous cords (*chordae tendineae*) (Bray et al., 1999). The valve in the right half of the heart has three cusps (known as the *tricuspid valve*) while the corresponding left valve has two cusps (known as the *bicuspid* or *mitral valve*). The exits from the right ventricle into the *pulmonary artery* and from the left ventricle into the *aorta* are guarded by the pulmonary and aortic *semilunar valves* respectively (Bray et al., 1999). These four valves ensure that the cardiac flow is unidirectional (Berne et al., 2004). A diagram of the cardiac physiology is provided in Figure 1.1.

Venous (deoxygenated) blood continuously flows from the systemic circulation through the superior and inferior *venae cavae* into the right atrium. When the pressure in the atrium becomes higher than the corresponding ventricular pressure, the tricuspid valve opens and

blood flows into the right ventricle while the ventricle relaxes following its previous contraction (Guyton, 1991; Seeley et al., 1996; Guyton & Hall, 1997; Bray et al., 1999). When the ventricle is at about 80% capacity, the right atrium contracts forcing enough blood though the tricuspid valve to complete the ventricular filling. After a very short pause, the right ventricle begins to contract, forcing the tricuspid valve shut, ensuring the unidirectional blood flow. The ventricular pressure increases continuously until the pulmonary semilunar valve is forced open, pumping blood into the pulmonary trunk and from there into the lungs, where the carbon dioxide is released and oxygen is absorbed (Guyton, 1991; Seeley et al., 1996; Guyton & Hall, 1997; Bray et al., 1999). In a very similar pattern, oxygenated blood continuously flows from the lungs, into the left atrium through the four pulmonary veins. It then flows through the mitral valve into the left ventricle, which in turn distributes it through the aorta to all parts of the body, except the part of the lungs responsible for the blood oxygenation. It is important to understand that both atria contract at the same time followed by both ventricles contracting at the same time (Guyton, 1991; Seeley et al., 1996; Guyton & Hall, 1997; Bray et al., 1999).

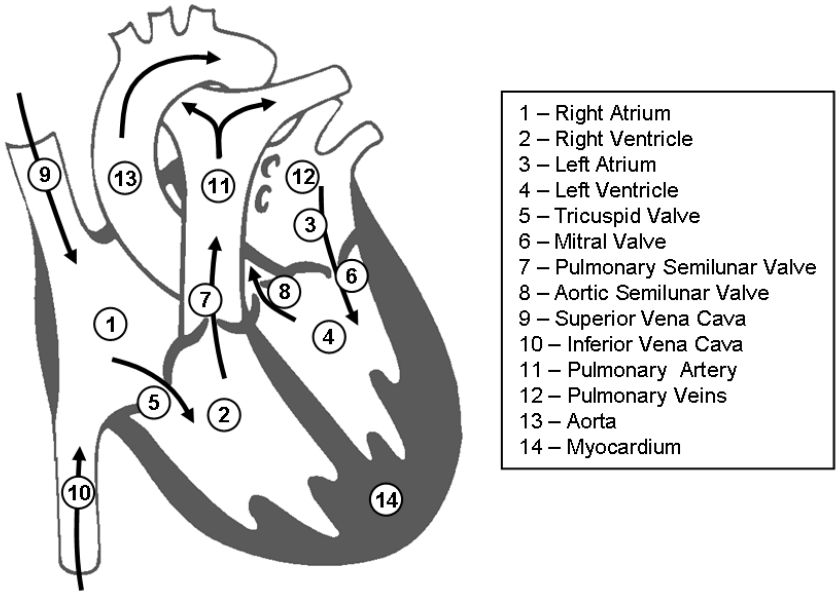


**Figure 1.1.** Cardiac physiology. The tissue and cavity structures of the human heart [adapted from (Bray et al., 1999)].

### 1.1.2. Cardiac cycle

The cardiac muscle has the ability to contract rhythmically without nervous input (myogenic rhythm) (Bray et al., 1999). The rhythmic action, known as cardiac cycle, is the result of a potential generated by a pacemaker at the top end of the right atrium and transmitted through

the heart along specialised conducting pathways. Due to the arrangement of the conducting pathways, there is a delay of more than 0.1 seconds between the transmission of the cardiac impulse from the atria into the ventricles (Guyton, 1991). This delay enables the atria to mildly contract prior to the corresponding, high-pressure ventricular contraction. Action potentials conducted rhythmically through the heart generate electric currents that can be detected at the surface of the human body through strategically placed electrodes (Seeley et al., 1996). The detected signal is known as an *electrocardiogram* (*ECG*) (Bray et al., 1999). The pattern of the ECG depends on the placement of the electrodes during acquisition. Nevertheless, specific features are present in all ECGs (Figure 1.2.a). More precisely, a normal ECG consists of a *P wave*, a *QRS complex* and a *T wave* (Seeley et al., 1996). The P wave and QRS complex are by-products of atrial and ventricular depolarisation respectively. On the other hand, the T wave is generated from repolarisation. More information on the electrical properties of the heart can be found in (Guyton, 1991; Seeley et al., 1996; Guyton & Hall, 1997; Bray et al., 1999; Berne et al., 2004).

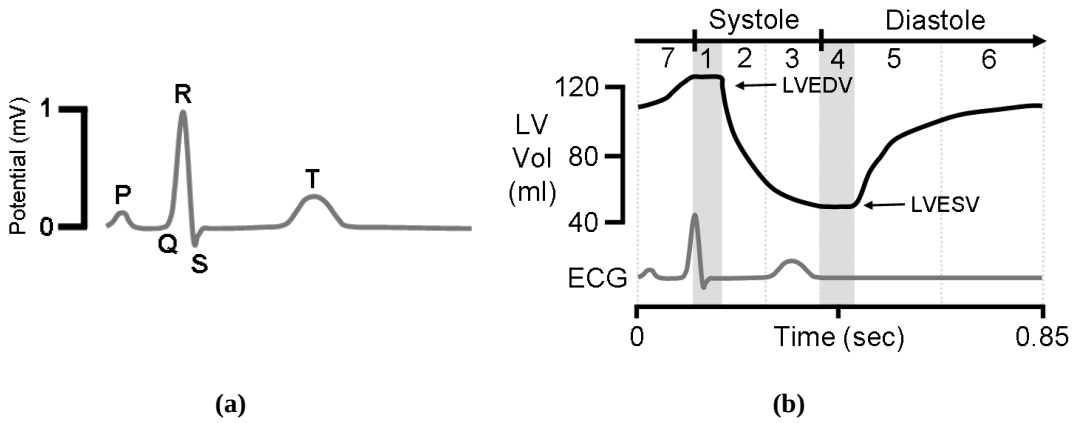


**Figure 1.2.** (a) Standard ECG signal for a resting heart, (b) an example of the ECG and volume of the heart during the different phases of a cardiac cycle [Adapted from (Berne et al., 2004)].

Under normal conditions, the rhythmic contractions of a healthy adult human heart occur 60 to 80 times per minute. A commonly accepted heart rate (for healthy adults) of 70 beats per minute corresponds to a cardiac cycle of 0.85sec. Each cardiac cycle comprises of two periods. The first period is known as *cardiac systole* and corresponds to the contraction of the ventricles, ejecting blood into the pulmonary and systemic circulation systems (Bray et al., 1999). The second period is known as *cardiac diastole* and corresponds to the relaxation of the ventricles, filling with blood ejected from their corresponding atria (Bray et al., 1999). The duration of the corresponding cardiac systole is expected to be 1/3 of the cardiac cycle duration (i.e. approximately 0.3sec for a 0.85sec cardiac cycle). The duration of the corresponding cardiac diastole is expected to be approximately 2/3 of the cardiac cycle

duration (i.e. 0.55sec). For a healthy human heart, the duration of a cardiac cycle and consequently of the diastole and systole periods remains relatively consistent. However, temporal variations within consecutive cardiac cycles are a common occurrence. These variations tend to have a greater effect in cardiac diastole, since the duration of the cardiac systole is partly controlled by the limited rate that blood can be ejected through the semilunar valves into the circulatory system. A cardiac cycle can be further subdivided into seven independent phases, which enable its better understanding and analysis (Guyton, 1991; Seeley et al., 1996; Guyton & Hall, 1997; Bray et al., 1999; Berne et al., 2004):

- *Isovolumetric contraction* marks the beginning of the cardiac systole and coincides with the peak of the QRS complex in the corresponding ECG (Figure 1.2). During the isovolumetric contraction the volume of the ventricle remains constant while building up pressure required for ejecting blood into the circulatory system. The volume of the ventricle is referred as *end-diastolic* (*ED*) volume.

- *Rapid ejection* takes place when the increased ventricular pressure forces the corresponding semilunar valves open, ejecting blood into the circulatory system. Approximately 70% of blood ejection occurs during this phase (Guyton, 1991).

- *Reduced ejection* pumps the remaining 30% of the ejected blood volume to the circulatory system. The cardiac systole is completed by the end of the reduced ejection phase, coinciding with the T wave in the corresponding ECG (Figure 1.2).

- *Isovolumetric relaxation* marks the beginning of the cardiac diastole. During the isovolumetric relaxation the ventricular volume remains constant while pressure is rapidly released. The ventricular volume is referred to as *end-systolic* (*ES*) volume.

- *Rapid ventricular filling* occurs when the increased atrial pressure forces the corresponding atrioventricular valves open, ejecting blood into the ventricles. Approximately 70% of blood ejection occurs during this phase (Guyton, 1991).

- During *reduced ventricular filling* (*diastasis* (Berne et al., 2004)) blood continues to flow to the corresponding ventricle while its pressure begins to gradually increase.

- Finally, during *atrial contraction* the remaining blood required to complete the ventricular filling is rapidly forced through the atrioventricular valves by contraction of the corresponding atrium. Atrial contraction coincides with the P wave of the ECG (Figure 1.2) and its completion marks the end of the cardiac diastole.

### 1.1.3. Cardiovascular diseases

Reflecting the importance of the cardiovascular system, cardiovascular diseases (CVDs) constitute a leading cause of death, including premature death, in both the developed world as well as developing countries (Fuster et al., 2008). More precisely, every year CVDs account for more than 17 million deaths worldwide and over 4 million deaths in Europe alone (BHF, 2008; WHO, 2008). This translates to approximately 30% of all deaths and 50% of all non-communicable disease related deaths (WHO, 2009). The number of CVD related deaths is expected to grow over the next 20 years (WHO, 2008). The charts in Figure 1.3 illustrate the distribution of deaths caused by various CVDs in Europe, America and Worldwide. *Coronary Heart Disease* (*CHD*) accounts for approximately 50% of all CVD related deaths, while *Cerebrovascular Disease* (*Stroke*) accounts for 20 to 30% and *Hypertensive Heart Disease* (*HTN*) accounts for around 5%. Robert Bonow, president of the American Heart Association, has called CVDs a global epidemic (Bonow et al., 2002). Taking into consideration the extent of the problem; it becomes apparent that effective tools for imaging the cardiovascular system and primarily the heart are essential.

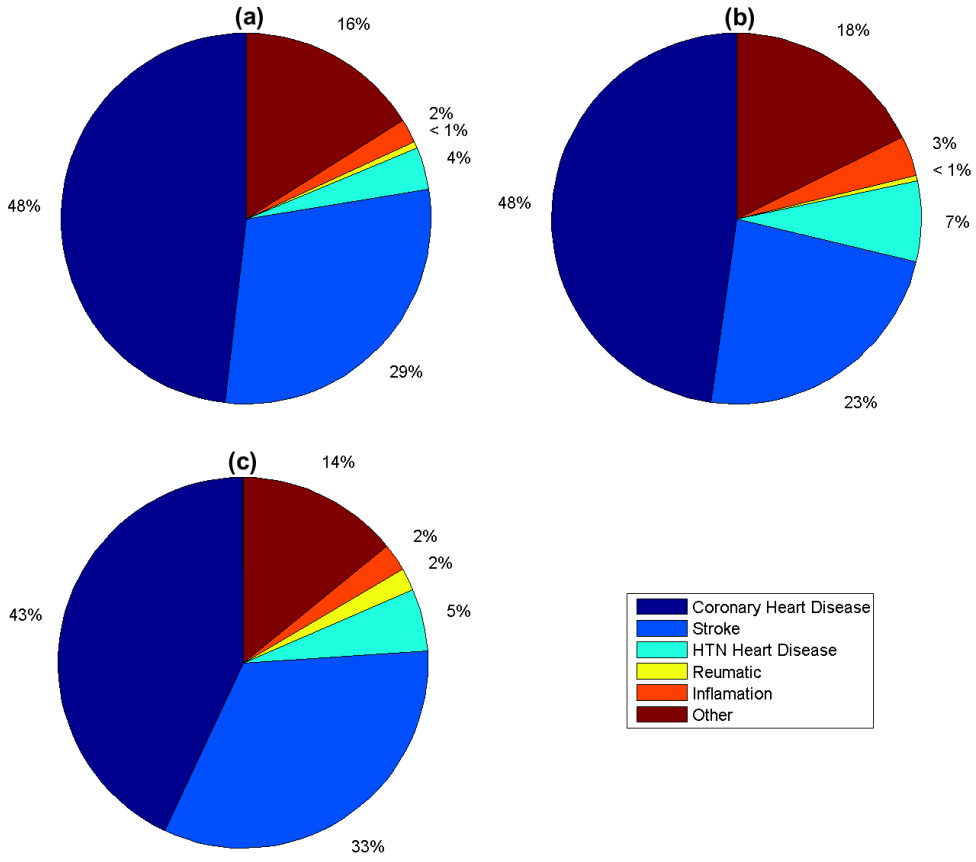


**Figure 1.3.** Distribution of deaths caused by various CVDs in (a) Europe, (b) America and (c) Worldwide (Fuster et al., 2008).

## 1.2. Imaging of the heart

Over the last few decades, a number of modalities have been developed for the effective imaging of the morphology and function of the cardiovascular system. Commonly used imaging modalities include *Computed Tomography* (*CT*), *Single Photon Emission Computed Tomography* (*SPECT*), *Positron Emission Tomography* (*PET*), *Magnetic Resonance Imaging* (*MRI*), and *Ultrasound Imaging* (*Echocardiography*). (Sutton & Rutherford, 2004; Suetens, 2006) provide reviews on the basic principles of each imaging modality. Currently no modality is known to provide all the necessary tools for the assessment of the cardiac morphology and function. Each modality offers a number of benefits for specific imaging applications while suffering from limitations on other applications. (O'Dell & McCulloch, 2000) have introduced a number of criteria for the objective comparison between modalities.

### 1.2.1. Computed tomography

*Computed Tomography* (*CT*) produces cross sectional images representing the corresponding X-Ray attenuation properties of the heart. More precisely, a set of narrow X-Ray beams with a fan-based geometry irradiate through a slice of the heart. The amount of transmitted radiation through the imaged structure is detected by a number of photo-multiplier tubes. This process is repeated for a range of angles by rapidly rotating the transmission and detection tubes around the body. Having acquired attenuation values over a range of possible angles, a 2D image is reconstructed utilising a back projection algorithm. *Multi-Detector row Computed Tomography* (*MDCT*) enables the simultaneous acquisition of up to 320 slices generating a 3D volume of the imaged cardiac structure. While CT provides a very powerful cardiac imaging tool (Sutton & Rutherford, 2004; Schoenhagen et al., 2005; Suetens, 2006), it suffers from a number of limitations. The acquired anatomic data are of high spatial resolution and tissue/bone contrast. However, the contrast between different tissue types is limited and the use of appropriate contrast agents may be required for the effective imaging of the heart. Furthermore, respiration motion during a prolonged acquisition session can introduce motion artifacts such as blurring or streaking on the acquired dataset. Finally, a major disadvantage of CT imaging is the X-Ray radiation transmitted through the patient during a scan session. While newer acquisition protocols and security measures are constantly developed limiting the radiation dose, it is still considered relatively high and CT scans should be avoided unless necessary. More information on the principles of Computed Tomography can be found in (Sutton & Rutherford, 2004; Suetens, 2006).

### 1.2.2. Nuclear imaging

Nuclear imaging utilises radioactive isotopes for the acquisition of physiological information (rather than anatomic) from the imaged structure. More precisely, a tracer molecule carrying an unstable isotope is administered to the patient, usually by intravenous injection. The radio-isotope is combined with specific chemical substances that are known to have binding properties with the tissue structures of interest. The attached radio-isotope gets involved in the metabolic process of the imaged structure generating gamma-rays, which enable the measurement of the isotope concentration as a function of position and time. *Single Photon Emission Computed Tomography* (*SPECT*) and *Positron Emission Tomography* (*PET*) are two commonly used modalities for imaging the cardiovascular system. *SPECT* detects single photons while *PET* detects photon pairs originating after positron emission. Photons are detected and collected through gamma cameras. The collected data is then processed to reconstruct a tomographic slice of the imaged structure. 3D cardiac volumes can be reconstructed as a sequence of such slices. Both modalities have a range of applications in cardiac imaging. However, unlike other cardiac imaging techniques, both SPECT and PET focus on the physiological properties instead of the anatomy of the heart. More information on the principles and application of cardiac SPECT can be found in (Sutton & Rutherford, 2004; Fuster et al., 2008). Details on the principles and clinical applications of PET imaging are available in (Ollinger, 1997; Sutton & Rutherford, 2004; Muehllehner & Karp, 2006; Nandalur et al., 2008). Like all imaging techniques, both SPECT and PET offer a number of benefits while suffering from a number of limitations. The major limitation for both modalities is the exposure to ionising radiation. The total amount of radiation is not insignificant and the radioactive isotope may remain in the body for hours (and even days) after the end of the clinical examination (Suetens, 2006). Similar to CT, nuclear imaging should be avoided unless necessary.

### 1.2.3. Magnetic resonance imaging

*Magnetic Resonance Imaging* (*MRI*) images the magnetic properties of the cardiovascular system. The human body is comprised of water molecules to a large extent. Each water molecule consists of two hydrogen nuclei making them the most prevalent atomic nuclei in the human body. Applying a strong magnetic field, the magnetic moments of the hydrogen nuclei enter a low energy state aligning themselves parallel to the direction of the field. Then, by introducing a radio frequency electromagnetic wave (at the appropriate resonant frequency) the hydrogen nuclei are excited to a higher energy state, altering their alignment

to the original magnetic field. When the electromagnetic field is turned off, the nuclei return to their original alignment (parallel to the magnetic field). The energy difference between the two states is released in the form of a radio frequency wave (photon). These waves are detected by an aerial or body coil and recorded in order to reconstruct an image of the scanned structure. The received frequency depends on the strength of the local magnetic field. Induced variations in the magnetic field strength enable the mapping of intensity as a function of spatial location. Different tissues return to the lower energy states at different rates resulting in different local signal intensities. This information is utilised to visualise different tissue in the reconstructed image. The physical principles behind MRI are considered to be more complex than corresponding principles behind other topographic imaging modalities. More information on the principles of MRI can be found in (Sutton & Rutherford, 2004; Suetens, 2006). A more elemental description on the physics and applications of cardiac MRI is also available in (Heatlie & Pointon, 2003).

MRI is a prevalent modality for the imaging of the heart. The quality and resolution of cardiac MRI data is high and continuously improves with the introduction of new acquisition techniques. MRI can provide high contrast between cardiac tissue and cavities (blood) without the need for contrast agents. Most importantly, MRI utilises no ionising radiation, making it a more attractive imaging option when compared to other tomographic modalities. However, MRI scans are relatively expensive, time consuming and require a certain amount of patient cooperation. Similar to CT, MRI also suffers from motion artifacts. Other limitations include (i) relatively low temporal resolution, and (ii) partial volume effects, which occur on imaged areas corresponding to more than one type of tissue, blurring cardiac tissue edges.

## 1.3. Cardiac ultrasound

*Echocardiography* is a diagnostic procedure that utilises ultrasound to visualise the heart in a non-invasive manner (Feigenbaum, 1994). Echocardiography along with Magnetic Resonance Imaging (MRI) constitute the most widely used methods for the assessment of the cardiac morphology and function (Sutton & Rutherford, 2004). Over the last two decades a range of novel ultrasound modalities have been introduced and refined allowing the extraction of a range of information from cardiac scans (Feigenbaum, 1994). B-mode imaging is the most commonly used ultrasound modality during cardiac examinations. B-mode provides cross sectional imaging of the heart tissue as a sequence of gray scale 2D frames. Each cross sectional frame is composed of a number of radial lines acquired by an

electronically-steered, phased-array transducer. Each radial line propagates at a set angle and is a consequence of the constructive interference of acoustic signals generated from a set of piezoelectric elements using controlled activation delays. The acoustic signals along each radial line interact with tissue and cavity cardiac structures forming a tomographic image of the heart. The frame rate of data acquisition depends on the width and depth of the field of view. Currently, frame rates higher than 100 frames per second (fps) are typical for cardiac B-mode scans.

Cardiac ultrasound data can be acquired from (i) above the thorax of the patient, also known as *Transthoracic Echocardiography* (*TTE*), or (ii) from inside the esophagus of the patient (by utilising specialised acquisition probes), also known as *Transesophageal Echocardiography* (*TEE*) (Feigenbaum, 1994). TEE can generate high quality data. However, the extended acquisition time and personnel requirements along with patient discomfort currently limit its clinical use, making transthoracic echocardiography a common practice in clinical examinations. Depending on the position and the orientation of the transthoracic probe, different cardiac structures can be visualised. The American Society of Echocardiography (Henry et al., 1980) recommends the imaging of three orthogonal cardiac planes referred to as the *long-axis*, the *short-axis* and the *four chamber* planes. Furthermore, each plane can be scanned utilising different transducer positioning such as the *parasternal*, *apical*, *subcostal* and *supersternal*. More information and descriptive diagrams on standardised probe positioning and orientation are available in (Henry et al., 1980; Fuster et al., 2008). Throughout this study, the parasternal long-axis acquisition view (Figure 1.4) is utilised for the acquisition of all clinical data.

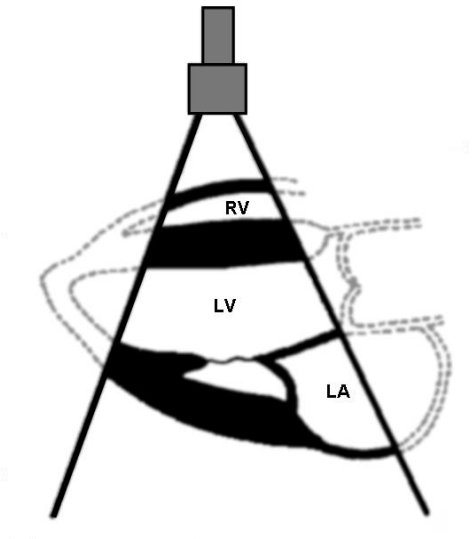


**Figure 1.4.** Long axis parasternal view of the heart [adapted from (Henry et al., 1980)].

### 1.3.1. Doppler imaging

The Doppler Effect – *a change in the frequency of ultrasound signal reflected from moving objects* – has long been utilised for the extraction of blood flow information. (Satomura, 1957) was the first to utilise the Doppler Effect in ultrasound signals for the investigation of one-dimensional blood flow. Early attempts for two dimensional (2D) blood flow imaging provided single frame, static colour flow information (Arenson et al., 1980). (Kasai et al., 1985) developed a novel autocorrelation method for the visualisation of real time blood flow velocity information (displayed in colour) superimposed over B-mode anatomic information (Figure 1.5 - left). This was the first successful attempt on real time colour flow imaging and to date, autocorrelation is still the dominant method utilised by ultrasound scanner manufacturers. Currently, *Colour* (flow) *Doppler Imaging* (*CDI*) provides a powerful diagnostic tool, with a range of clinical applications in echocardiography (Monaghan & Mills, 1989; Foley & Erickson, 1991; Feigenbaum, 1994; Allan et al., 2006; Fuster et al., 2008). Among its numerous benefits, colour flow imaging makes it easier to (i) relate flow to the associated heart structure, (ii) ascertain direction of the flow, and (iii) detect valvular regurgitation (McDicken, 1991; Roelandt et al., 1993).

*Tissue Doppler Imaging* (*TDI*) is a modification of CDI that employs the Doppler principle to measure the velocity of myocardial segments and other cardiac structures (Figure 1.5 - right). TDI was first introduced in the early nineties (McDicken et al., 1992; Miyatake et al., 1995) based on the fact that (i) cardiac tissue motion demonstrates substantially lower velocity than the corresponding blood flow velocity and (ii) Doppler signals generated by cardiac tissue demonstrate substantially larger intensity than the corresponding signals generated by moving red blood cells. Consequently, the measurement of cardiac tissue velocity is feasible by filtering out high frequency, low amplitude Doppler signals. TDI has enabled the derivation of tissue velocity gradient (Fleming et al., 1994) and strain information (Marwick et al., 2007) from cardiac ultrasound data. However, the nature of CDI and TDI acquisition imposes a number of limitations in both technologies. For example, 2D Doppler imaging reduces the axial and potentially the temporal resolution of acquired data (if the scan line density is kept constant). Moreover, high velocities may result in data aliasing. Finally, velocity values derived using Doppler signals correspond to the component of the actual velocities along the acquisition axis. In order to make an accurate velocity measurement using Doppler imaging, prior knowledge on the line of motion is required. While straightforward in laminar blood flow measurements, prior motion knowledge is challenging for cardiac tissue (Thomas, 2004). Nevertheless, besides the limitations, TDI is a

promising technology with great potential in a wide range of clinical applications in echocardiography (Ofili & Nanda, 1998; Nikitin & Witte, 2004; Marwick et al., 2007).

Power Doppler was introduced by (Rubin et al., 1994) in order to overcome some of the shortcomings of the colour Doppler imaging, such as angle dependence and aliasing. Power Doppler displays the integrated power of the Doppler signal instead of its mean Doppler frequency shift (Figure 1.6) (Rubin et al., 1994). Similar to colour Doppler, Power Doppler can be used to visualise both blood flow and myocardium tissue movement. Power Doppler has been reported to (i) be more sensitive and have higher spatial resolution than conventional colour Doppler, (ii) be relatively angle independent, (iii) be unaffected by aliasing, (iv) provide uniform colour distribution without dropouts (Hamper et al., 1997), and (v) enhance visualisation of heart boundaries when compared to B-mode imaging (Hoskins & McDicken, 1997). However, it does not provide velocity (neither magnitude nor direction) information and suffers from flash artifacts (Figure 1.6) (Rubin et al., 1994). Still, Power Doppler is considered a useful adjunct to colour Doppler imaging (Hamper et al., 1997).

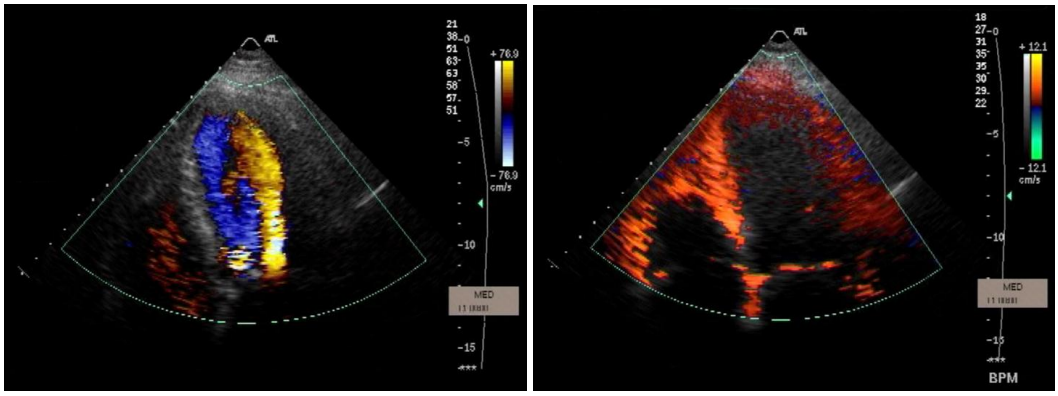


**Figure 1.5.** (Left) CDI: blood flows into the left ventricle causing its diastole. (Right) TDI: moving tissue is highlighted with corresponding velocity.

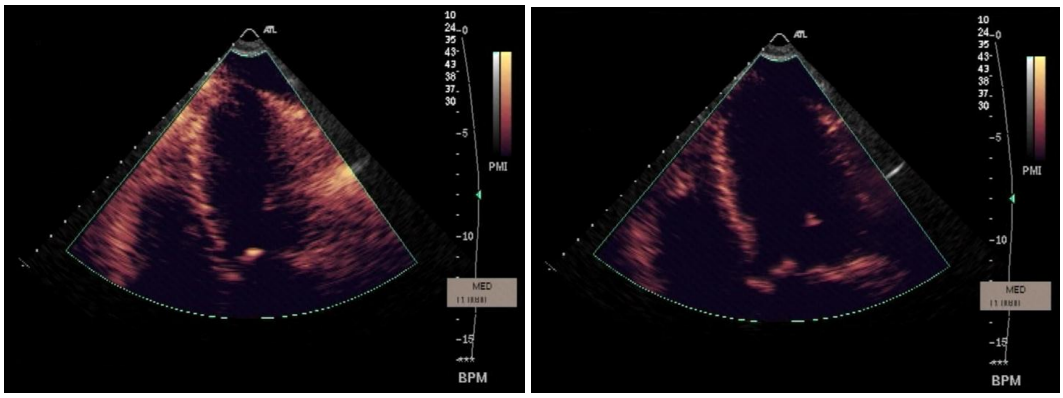


**Figure 1.6.** Tissue Power Doppler images demonstrating the variation within the overall image brightness (flashing artifact) between different stages of the cardiac cycle.

### 1.3.2. Real time 3D cardiac ultrasound

Transthoracic 3D echocardiography can be considered an extension of the two dimensional B-mode imaging. The first attempt of 3D imaging of the human heart was in 1974 by (Dekker et al., 1974). Early approaches reconstructed static 3D cardiac data from a series of 2D B-mode images using positional information derived through mechanical arms (Dekker et al., 1974), acoustic (Moritz & Shreve, 1976) and electromagnetic (Raab et al., 1979; Martin et al., 1993) spatial locating systems. Later attempts utilised parallel slice (Fulton et al., 1994), rotational (Ludomirsky et al., 1994) and fan shaped (Delabays et al., 1995) acquisition mechanisms. Despite these early attempts, the first *real-time 3D echocardiographic* scanner (*RT3DE*) was introduced in the early 1990s. (von Ramm & Smith, 1990) developed the matrix transducer technology in which piezoelectric crystals were arranged in a 2D grid (von Ramm & Smith, 1990; Sheikh et al., 1991; von Ramm et al., 1991). On early matrix transducers not all elements could acquire data simultaneously. Nevertheless, they could acquire a 60°x60° pyramid shaped volume within a single cardiac cycle (Figure 1.7). In 2002, Philips Corporation developed a clinical RT3DE system (Figure 1.8) enabling the real time acquisition and visualisation of the beating heart during a clinical examination (Wang et al., 2003). Current matrix transducer technology enables the acquisition of real-time, non-gated, 4D (3D and time) cardiac ultrasound data through a single acoustic window. The real time 3D dataset can be acquired as a pyramid shaped volume or as a *thick slice*, comprising four adjacent (along the elevation plane) slices (Yang et al., 2008). Similarly to B-mode echocardiography, a range of cardiac structures can be visualised depending on the position and orientation of the probe. Nowadays, all major ultrasound technology manufactures have incorporated RT3DE technology in their cardiac ultrasound systems with acquisition speeds higher than 40 frames per second (fps). Unfortunately, the visual complexity and sometimes incompleteness of RT3DE data (i.e. heart too big to fit in 3D volume) currently limit its clinical usability. Nevertheless, RT3DE has been attracting considerable research interest. The clinical use of the technology is also expected to increase with the development of novel, effective data analysis and processing tools. (Salustri & Roelandt, 1995; Spicer & Marwick, 2000; Xie et al., 2005; Hung et al., 2007; Yang et al., 2008) provide five very informative reviews on the technology, the clinical and research applications of RT3DE.

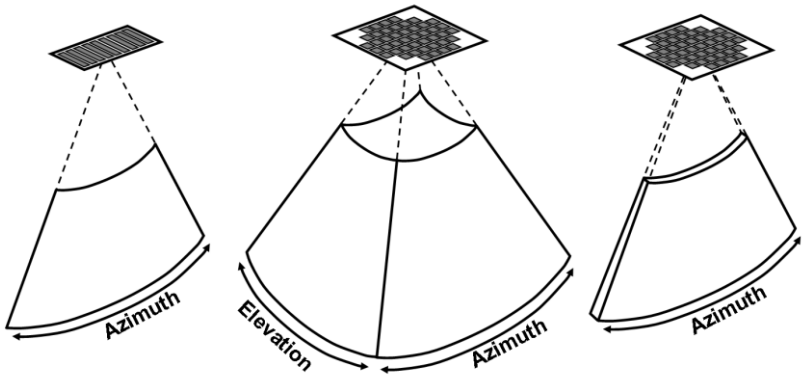


**Figure 1.7.** (Left) 2D acquisition using a phased array probe. (Centre) 3D acquisition using a matrix probe. (Right) Thick Slice acquisition (on Philips IE33) using a matrix probe.

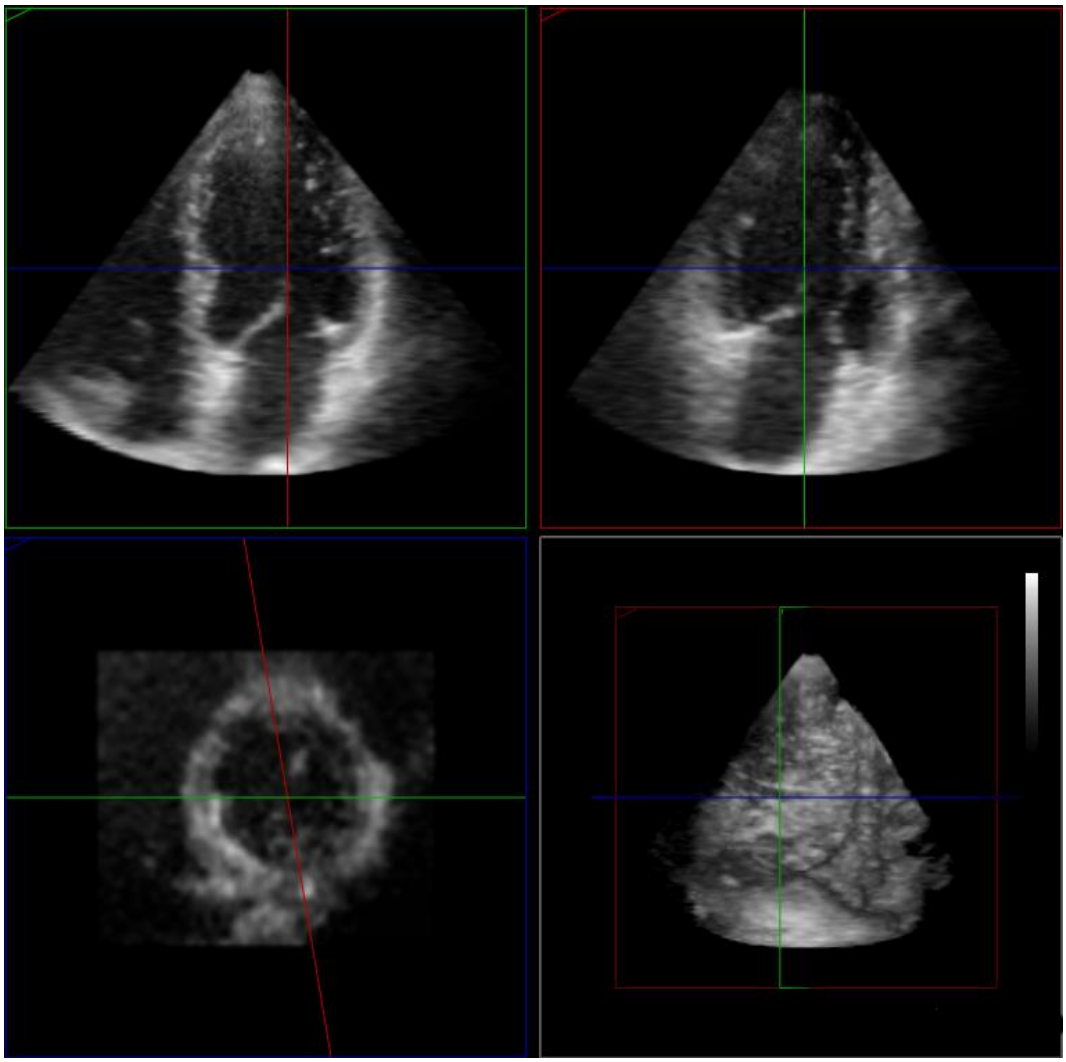

**Figure 1.8.** RT3DE data acquired using a state of the art scanner. 4-chamber, 2-chamber and short-axis views are provided along with a view of the 3D pyramid. 3D data are visually complex making their interpretation and analysis without the assistance of cross sectional data challenging.

### 1.3.3. Current benefits and limitations of cardiac ultrasound

Echocardiography provides a portable, versatile, real-time diagnostic tool with no adverse secondary effects, capable of acquiring data of high spatial and temporal resolution at relatively low operational costs (Sutton & Rutherford, 2004). The wide range of imaging techniques available for cardiac ultrasound enables the qualitative and quantitative assessment of cardiac morphology and function in both 2D and 3D. However, cardiac ultrasound data are often incomplete (partial structure/heart coverage) and suffer from a range of artifacts such as speckle, acoustic shadowing and enhancement, static and dynamic noise (Feigenbaum, 1994; Sutton & Rutherford, 2004). Most artifacts are a consequence of the interaction of the transmitted ultrasound signals with anatomic structures of the examined body. Structures such as bone, lungs (air) and fat have a direct limiting effect on the quality of the acquired data.

Acoustic shadowing occurs when high-attenuation structures, such as bones and lungs (air), lie in the path of the ultrasound beam and obscure the imaging of subsequent cardiac sections. The opposite phenomenon is known as acoustic enhancement and is encountered on tissue structures located posterior low-attenuating media such as blood filled cardiac cavities (Feigenbaum, 1994; Sutton & Rutherford, 2004). Furthermore, various levels of static and dynamic noise occur in cardiac ultrasound data due to a wide range of acoustical phenomena such as reverberation and grating lobes (Feigenbaum, 1994; Sutton & Rutherford, 2004). Noise appears on both tissue and cavity structures imaged using cardiac ultrasound. Near field noise is a commonly observed type of noise in echocardiograms. Near field noise is mostly static and is considered to be the result of high-amplitude vibrations and voltages within the transducer (Feigenbaum, 1994; Sutton & Rutherford, 2004). Another theory suggests that near field noise is a result of reverberation between near field structures such as ribs and intercostal muscles (Hozumi et al., 1998).

Speckle is a type of acoustic noise responsible for the granular appearance of ultrasound data. Speckle is a result of the constructive and destructive interference effect caused by the scattering of an ultrasound beam from random, small scale, tissue inhomogeneities. Speckle is a direct consequence of (i) the reflectivity of scattering media, and (ii) the coherent nature of piezoelectric transducer. Several studies provide detailed information on the origin of speckle and its statistical properties (Goodman, 1976; Burckhardt, 1978; Wagner et al., 1983). Speckle contains information that is invaluable to tissue velocity estimation methods such as *Speckle Tracking Echocardiography* (*STE*). STE is a relatively new method for assessing global and regional cardiac function by tracking the movement of speckle patterns

within consecutive frames of B-mode cardiac ultrasound datasets (Marwick et al., 2007). STE provides a promising alternative to (i) tagged cardiac MRI for assessing left ventricular deformation and torsion (Notomi et al., 2005), and (ii) colour Doppler for strain imaging (D'Hooge et al., 2002), addressing problems associated with angle dependence. Detailed descriptions on the principles of STE as well as current and future clinical applications are provided in (Evans & McDicken, 2000; Marwick et al., 2007; Blessberger & Binder, 2010; Geyer et al., 2010). Methods that enhance speckle information can improve the accuracy and robustness of existing speckle tracking techniques. On the other hand, speckle's granular pattern can sometimes be considered as an undesirable property since it may obscure fine anatomic detail as well as mask low contrast regions. Therefore, means for suppressing speckle can possibly improve the image quality and diagnostic value of a cardiac ultrasound dataset.

## 1.4. Motivation

Effective tools for the qualitative and quantitative analysis of cardiac morphology and function play a crucial role in the diagnosis and treatment of CVDs. Echocardiography is a technology extensively used in clinical examinations of the cardiovascular system. However, a range of artefacts limit the image quality and diagnostic value of the acquired cardiac data. Over the last three decades, a number of advances in data acquisition have substantially improved cardiac ultrasound data quality. Nevertheless, a considerable portion of current cardiac ultrasound data demonstrates very low image quality and sometimes negligible diagnostic value. A recent study performed in Western General Hospital (Edinburgh) using both outdated as well as state of the art cardiac ultrasound systems demonstrated that about 33% of the data are of high, 33% of average and 33% of low image quality and diagnostic value. The findings were independent of the acquisition system but heavily dependent on the echogenicity of the patients.

Currently, a number of post-formation image processing techniques such as image registration, image segmentation, data classification and texture analysis have been introduced for cardiac data acquired using modalities such as CT and MRI (Maintz & Viergever, 1998; Pham et al., 2000; Makela et al., 2002). These techniques enable the development of tools and protocols that enhance the accuracy, robustness and repeatability of the diagnostic process. Over the last few years, similar post-processing techniques have been attempted on cardiac ultrasound data (Hammoude, 1998; Ledesma-Carbayo et al., 2001; Walimbe et al., 2003; Noble & Boukerroui, 2006). Recent advances in RT3DE extend

the potential application of such techniques (Zagrodsky et al., 2005; Nillesen et al., 2007). However, while post-formation image processing techniques may work on high quality images, high levels of noise, low contrast, speckle and shadowing limit their effectiveness in a considerable proportion of the available clinical cardiac ultrasound data.

The development of novel and effective post-processing methods that enhance the image quality and diagnostic value of cardiac ultrasound data is therefore crucial. Post-processing techniques do not require any hardware modifications and can be applied in both existing and new data. The need for such techniques provides the motivation behind the work described in this thesis.

## 1.5. Thesis overview

This dissertation is divided into seven chapters. The first two chapters provide all the background information required in order to put in context the novel work described in Chapters 3 to 6. Chapter 2 provides a thorough review on past and current methods for enhancing cardiac ultrasound data. Restrictions and limitations in existing methods are identified and the aims of the novel work described throughout this thesis are introduced.

Chapters 3 and 4 analyse and evaluate two image enhancement methods that utilise spatial averaging of partially decorrelated data acquired through a single acoustic window. More precisely, Chapter 3 extends the notion of ***Temporal Compounding***, a method for enhancing cardiac ultrasound data by averaging partially decorrelated instances of the imaged structure acquired over a number of consecutive cardiac cycles. Reliable spatial and temporal alignment of the corresponding frames in consecutive cardiac cycles is vital for effective ***Temporal Compounding***. Insufficient temporal alignment will induce the averaging of frames corresponding to different stages of the cardiac cycle resulting in severe blurring of the imaged cardiac structure. Chapter 3 introduces a novel, efficient technique for the accurate and robust spatio-temporal alignment of consecutive cardiac cycles with variable temporal characteristic. The work described in Chapter 3 has been published in:

- Perperidis, A., Cusack, D., McDicken, W.N., MacGillivray, T., Anderson, T. (2009) Temporal Compounding of cardiac ultrasound data: Improving image quality and clinical measurement repeatability. Proceedings of the IEEE Engineering in Medicine & Biology Society Conference. Minneapolis, USA.

- Perperidis, A., Cusack, D., McDicken, W.N., MacGillivray, T., Anderson, T. (2009) Temporal Compounding and its effect on clinical measurements of cardiac ultrasound data. Proceedings of the Medical Imaging Understanding and Analysis Conference. London, UK.

Chapter 4 introduces ***3D-to-2D Compounding*** extending the notion of spatial compounding of cardiac ultrasound data acquired through a single acoustic window presented in Chapter 3. ***3D-to-2D Compounding*** presents a novel image enhancement method by acquiring and compounding spatially adjacent (along the elevation plane), partially decorrelated, 2D slices of the heart. The 2D slices are extracted as a thin angular sub-sector of a volumetric pyramid scan. The methods and findings of Chapter 4 have been published in:

- Perperidis, A., White, A., Cusack, D., McDicken, W.N., MacGillivray, T., Anderson, T. (2010) 3D-to-2D Compounding and its effect on cardiac ultrasound data. Proceedings of the Medical Imaging Understanding and Analysis Conference. Warwick, UK.

In Chapter 5 the ***Dynamic Histogram Based Intensity Mapping*** (***DHBIM***) approach for cardiac ultrasound data enhancement is introduced. ***DHBIM*** investigates the temporal variations within image histograms of consecutive frames in order to (i) identify any unutilised/underutilised intensity levels and (ii) derive the tissue/cavity intensity threshold within the processed frame sequence. Piecewise intensity mapping is then used to enhance cardiac ultrasound data. Chapter 6 investigates a data acquisition and analysis protocol for integrating the dynamic intensity mapping with spatial compounding methods. Finally, Chapter 7 provides a review on the contributions, limitations and future plans of all the work introduced and evaluated throughout this thesis.

# Chapter 2

## Cardiac ultrasound data enhancement

Enhancement of the quality and diagnostic value of ultrasound data has been an ongoing research theme for the last three decades. Cardiac ultrasound suffers from all artifacts that appear in medical ultrasound data such as speckle, acoustic shadowing and enhancement, static and dynamic noise (Feigenbaum, 1994; Sutton & Rutherford, 2004). Most artifacts are a consequence of the interaction of the transmitted ultrasound signals with anatomic structures of the examined body. Structures such as bone, lungs (air) and fat have a direct limiting effect on the quality of the acquired data. Transthoracic cardiac ultrasound images a constantly and rapidly moving structure through the patient's rib cage and alongside the lungs. The nature of such a challenging acquisition enhances the manifestation of common medical ultrasound artifacts (Figure 2.1). More precisely, noise levels in cardiac cavities can be high and comprise both static noise in the near field, and dynamic noise such as acoustic clutter. High levels of noise combined with tissue speckle limit the contrast and detectability between tissue and cavity restricting the delineation of cardiac structures. Imaging of relatively small and rapidly moving structures such as the cardiac valves introduces additional challenges. Besides the limited delineation as a result of noise and speckle, the structure may move into and out of the scanning plane due to the cardiac and patient's respiration motion. Furthermore, reverberations and shadowing appear due to the interaction of the transmitted ultrasound with the patient's rib cage and lungs. Such artifacts may appear momentarily or alter their position and orientation throughout a scan due to the patient's respiration motion. Imaging of cardiac structures is not feasible for areas corrupted by reverberations and shadowing. Over the years numerous studies have attempted to address a range of artifacts in medical ultrasound data. This chapter provides a detailed review of such studies. The limitations of past studies and future research possibilities are identified and the aims of this work are formulated.

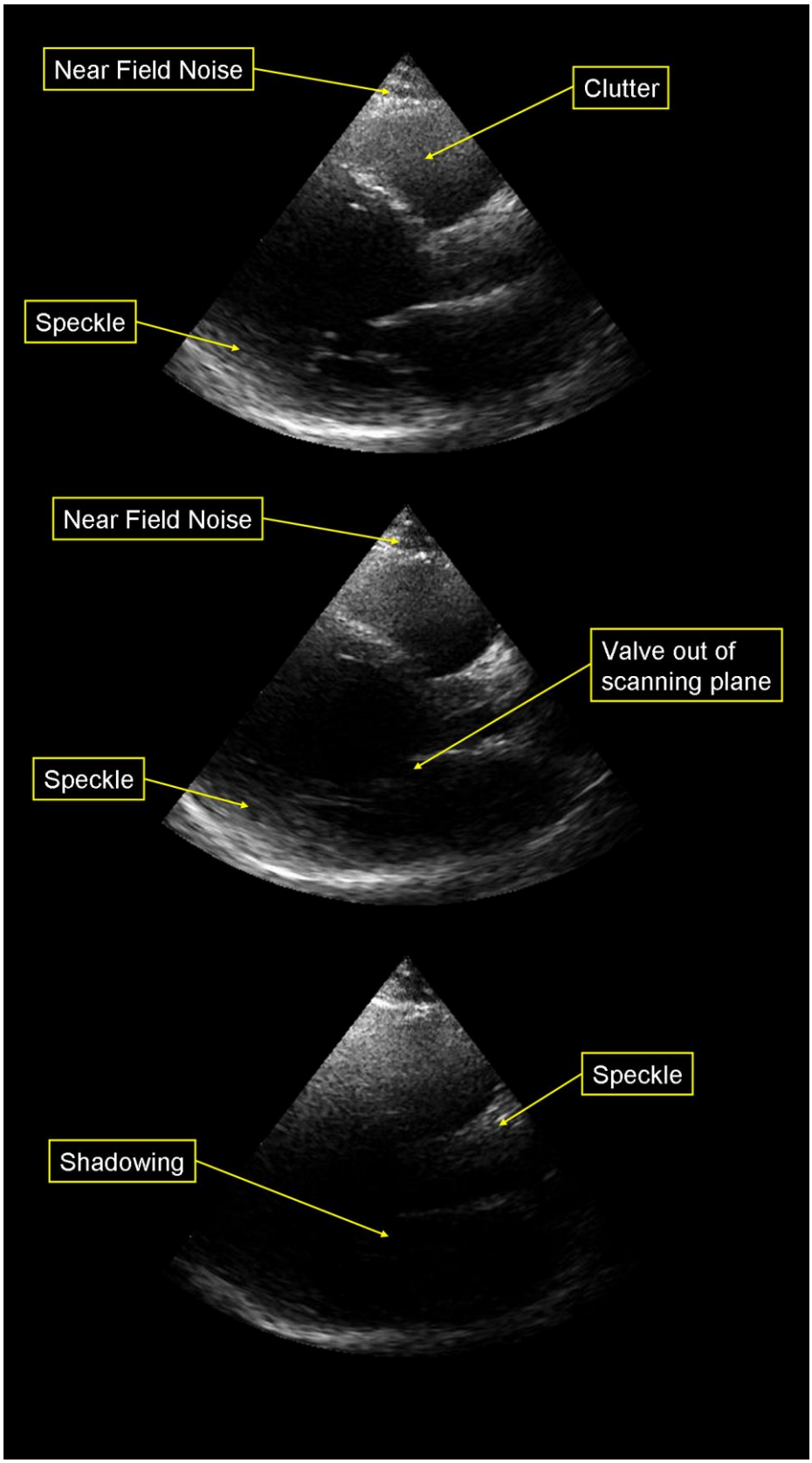


**Figure 2.1.** Examples of corrupted cardiac ultrasound data (over a number of cardiac cycles): near field noise, clutter, shadowing, speckle and structures moving out of the scanning plane.

## 2.1. Speckle and noise suppression techniques

Tissue speckle's granular pattern can sometimes be considered as an undesirable property in medical ultrasound data since it may obscure fine anatomic detail as well as mask low contrast regions. In cardiac ultrasound data, tissue speckle combined with high levels of cavity noise can limit the delineation of cardiac structures. Furthermore, the granular appearance of the data limits the application of post-formation image processing techniques such as image registration and segmentation. However, cardiac tissue speckle caries valuable information utilised in tissue classification as well as in Speckle Tracking Echocardiography in order to derive global and regional cardiac motion characteristics. As a result, there may be cases where suppression of speckle can be beneficial, but there are also cases where enhancement of speckle information is desirable. On the contrary, cavity static and dynamic noise carries no beneficial information and should be kept to minimal levels.

Noise and speckle suppression has been of active research interest for more than twenty years. Ultrasound, and to a greater extent cardiac ultrasound scans, represent a very difficult and demanding application area for noise suppression algorithms because, although they are heavily corrupted by noise, they contain a variety of special features that should be preserved during processing. Such features include interfaces between structures represented with a different grayscale level, for example tissue/cavity boundaries, as well as relatively small structures with dimensions comparable to the average speckle size, for example rapidly moving cardiac valves. Over the years, a number of approaches for suppressing speckle and noise have been introduced. Such approaches can be broadly categorised into post-formation image filtering and incoherent processing techniques. Their effectiveness on enhancing image quality varies greatly.

### 2.1.1. Filtering

Over the years, a range of post-processing filters have been developed for suppressing speckle and noise in medical ultrasound images. From a very early stage, non-adaptive filters, such as mean and median, were identified as inadequate for enhancing medical ultrasound data since they introduced severe blurring on the edges of anatomic structures and consequently loss of valuable diagnostic information (Bamber & Daft, 1986; Loupas et al., 1989). Due to the limitations of commonly used, non-adaptive filters, the development of effective noise and speckle suppression filters for medical ultrasound data evolved into a field of major research interest. To a large extent, most such filters can be broadly

categorised as: (i) adaptive local statistics, (ii) wavelet domain or (iii) anisotropic diffusion filters using a multiplicative approximation model for speckle:

$$I(x, y) = S(x, y) * n(x, y) \quad [2.1]$$

where *I(x, y)* represents the intensity level of the observed image, *S(x, y)* the uncorrupted signal and *n(x, y)* the multiplicative noise component at *(x, y)*. An additive noise component is usually disregarded due to its considerably smaller range when compared to *n(x, y)*.

Adaptive local statistics filters have been used for the suppression of noise and speckle in medical ultrasound images for over 25 years. Such filters utilise statistical information derived from a region-of-interest (ROI) within the processed image, and adapt the parameters of the filter applied to this ROI accordingly. Adaptable parameters include weighting, size and shape of the filter, amongst others. Adaptive local statistics filters were initially applied on Synthetic Aperture Radar (SAR) data that also suffered from high levels of noise and speckle (Lee, 1980; Frost et al., 1982; Kuan et al., 1987; Lopes et al., 1990). (Jin et al., 2004) provided a qualitative and quantitative assessment on the performance of popular SAR filters on medical ultrasound images. Thereafter, a number of adaptive filters have been developed for suppressing noise and speckle in medical ultrasound data (Bamber & Daft, 1986; Loupas et al., 1989; Koo & Park, 1991; Karaman et al., 1995; Chen et al., 2003).

Recently there has been an increased interest in utilising wavelet transforms as a tool for suppressing noise within medical ultrasound images. Wavelet filters attempt to remove noise while preserving the boundaries of anatomic structures. Filters in the wavelet domain consist of three main steps (Kim & Ra, 2005). Initially, the original image is decomposed using a wavelet transform. Then, the wavelet coefficients are modified in order to generate the desired noise suppression. Finally, the enhanced image is reconstructed from the modified wavelet coefficients using an inverse wavelet transform. Wavelets provide an attractive domain for noise suppression in medical ultrasound data due to inherent properties such as: (i) simplicity; multi-scale decomposition simplifies the statistics of complex signals, (ii) multi-resolution; image features are analysed at an appropriate resolution scale, and (iii) edge detection; large wavelet coefficients coincide with image edges (Sudha et al., 2009). Over the years, a range of noise and speckle suppression filters operating in the wavelet domain have been investigated (Donoho, 1995; Achim et al., 2001; Pizurica et al., 2003; Gupta et al., 2005; Kim & Ra, 2005; Rabbani et al., 2008; Sudha et al., 2009). Wavelet based filters can

be broadly classified into homomorphic, filters operating on the image logarithm, and non-homomorphic, filters operating on the original image (Gupta et al., 2005).

Similar to filters in the wavelet domain, anisotropic diffusion filters aim towards the suppression of noise while preserving boundaries between anatomic structures. Diffusion is known as the process that equilibrates concentration differences by distributing particles from areas with high to areas with low concentration (Weickert, 1998). During diffusion, a set of filtered images are iteratively generated until a sufficient level of noise suppression is achieved. The image diffusion and consequently the noise suppression is controlled by a partial differential equation. Within the partial differential equation a diffusion coefficient is utilised in order to identify edges within the image and encourage noise suppression within homogeneous regions instead of across edges. The diffusion coefficient can be a constant scalar value, process known as isotropic diffusion, or a tensor that is a function of the differential structure of the evolving image, process know as anisotropic diffusion (Weickert, 1998). Anisotropic diffusion is required in order to suppress noise while maintaining edges within an image. This process has been referred to as intra-structure smoothing instead of inter-structure smoothing (Loizou et al., 2005). Anisotropic diffusion filters were introduced by (Perona & Malik, 1990). Over the last decade, a wide range of such filters for the suppression of speckle and noise in medical ultrasound data have been developed (Abd-Elmoniem et al., 2000; Yu & Acton, 2002; Sun et al., 2004; Aja-Fernandez & Alberola-Lopez, 2006; Krissian et al., 2007).

The majority of the techniques for noise and speckle suppression in medical ultrasound data have been implemented and evaluated on simulated data (Koo & Park, 1991; Yu & Acton, 2002; Sudha et al., 2009), phantom data (Karaman et al., 1995; Chen et al., 2003; Rabbani et al., 2008) as well as on clinical data of the abdomen (Loupas et al., 1989; Karaman et al., 1995; Achim et al., 2001; Kim & Ra, 2005; Rabbani et al., 2008), breast (Kim & Ra, 2005) and neck (Chen et al., 2003; Rabbani et al., 2008). Such anatomic structures consist of large static tissue containing a number of lesions of different shapes and sizes. (Loizou et al., 2005) provided a very thorough review on the effect of 10 noise and speckle suppression filters on ultrasound data of the carotid artery. A range of adaptive, wavelet and diffusion filters were assessed using 440 clinical images. The assessment consisted of both qualitative analysis by medical experts as well as quantitative analysis using image quality measurements such as signal-to-noise ratio (SNR) and contrast. A similar but smaller scale study was performed on phantom and abdomen data by (Michailovich & Tannenbaum, 2006).

The high levels of noise and low contrast combined with constantly moving tissue structures establish cardiac ultrasound data as a challenging environment for the effective suppression of noise and speckle. Over the years, only a small number of studies have attempted to suppress cardiac noise using post-formation image filters. An early attempt to enhance the quality of cardiac ultrasound data utilised an adaptive filter that identified areas containing speckle based on a-priori knowledge of speckle statistics (Massay et al., 1989). Areas identified as speckled were then heavily smoothed. The approach, while suppressing speckle, degraded the diagnostic value of the data substantially. (Kang et al., 1998) identified the potential of wavelet filters in preserving edges while suppressing noise. (Zong et al., 1998) introduced an algorithm that suppressed noise using multi-scale wavelet analysis (Guo et al., 1994) while enhancing clinically relevant features using adaptive gain non-linear processing (Laine et al., 1994). The algorithm was thoroughly evaluated both qualitatively and quantitatively (using 60 clinical datasets) demonstrating promising data enhancement. (Hao et al., 1999) combined adaptive filtering with wavelet domain techniques for the effective suppression of cardiac ultrasound speckle. More precisely, the Adaptive Weighted Mean Filter (Loupas et al., 1989) was utilised to generate an image containing the signal and an image containing the noise of the original data. Both images were then individually processed using wavelet filters. The final, noise reduced image was obtained by summing the two filtered images. The algorithm was evaluated on limited cardiac datasets from a pig. No results on human cardiac data were presented. A method for noise reduction and feature enhancement of cardiac ultrasound data using anisotropic diffusion was presented by (Abd-Elmoniem et al., 2002). (Yue et al., 2005) combined wavelet transforms along with anisotropic diffusion for the suppression of noise and enhancement of anatomic features within cardiac ultrasound data. More precisely, the original image was decomposed into multi-scale wavelet coefficients, which then individually underwent anisotropic diffusion. The idea was to benefit from the multi-resolution property of wavelets as well the edge preservation property of anisotropic diffusion, introducing a more effective, integrated data enhancement method. The evaluation of the method, while very limited (1 clinical dataset), demonstrated very promising results. Filter based noise suppression techniques for cardiac ultrasound data that do not fall into the three main categories of: (i) adaptive local statistics, (ii) wavelet domain and (iii) anisotropic diffusion filters, have also been developed. (Evans & Nixon, 1996) introduced an adaptive filter utilising spatio-temporal intensity variations over consecutive cardiac frames to derive the corresponding weighting coefficients. Recently, (Tay et al., 2010) developed an iterative approach for identifying and removing local maxima in order to suppress noise and enhance the edges of cardiac structures.

A recent study by (Finn et al., 2011) provided a thorough quantitative evaluation and comparison amongst 15 popular noise and speckle suppression filters on a range of simulated and clinical cardiac ultrasound data. A range of early local statistics adaptive filters (Lee, 1980; Frost et al., 1982; Kuan et al., 1987), wavelet domain filters (Zong et al., 1998; Pizurica et al., 2003; Yue et al., 2005) and anisotropic diffusion filters (Perona & Malik, 1990; Weickert, 1998; Yu & Acton, 2002; Aja-Fernandez & Alberola-Lopez, 2006; Krissian et al., 2007) were evaluated. 100 clinical cardiac ultrasound scans from 40 patients were utilised in order to assess the effect of each filtering algorithm on 5 quantitative image quality metrics: (i) Pratt's Figure of Merit (Pratt, 1977), measuring the displacement of edge pixels between the original and each filtered image, (ii) Structural Similarity (Wang et al., 2004), assessing the preservation of structural information, (iii) Edge region Mean Square Error (MSE), assessing the average absolute difference between the extracted edges in the original and filtered images, (iv) Contrast-to-Noise Ratio (CNR), assessing the effect of each filtering method on the contrast between cavity and tissue cardiac structures and (v) Signal-to-Noise Ratio (SNR), assessing the levels of noise and speckle in the original and filtered images. The quantitative metrics were chosen in order to assess the effect of filters on noise suppression, contrast enhancement and feature and edge preservation. While the utilised metrics covered all the desired assessment areas, it is believed that a range of factors could affect the results, especially on metrics assessing edge preservation for data with high levels of noise. Therefore, more thorough consideration was required on the selection of such assessment metrics. Nevertheless, the study was very comprehensive making some valuable comparisons amongst popular noise suppression filters. From the findings, anisotropic diffusion filters performed better on simulated data. The results were more diverse for clinical cardiac ultrasound data, the quality of which was affected by a wider range of artifacts. The filter developed by (Zong et al., 1998), suppressing noise using multi-scale wavelet while enhancing clinically relevant features using adaptive gain non-linear processing, performed reasonably well. However, the most satisfactory noise suppression and feature preservation was achieved by the Oriented Speckle Reduction Anisotropic Diffusion (OSRAD) filter developed by (Krissian et al., 2007), along with the Nonlinear Multi-scale Wavelet Diffusion (NMWD) filter (Yue et al., 2005), integrating wavelet transforms with anisotropic diffusion. Both filters performed well in the quantitative assessment as well as the visual inspection of the processed images. However, while most of the assessed filters claimed to enhance contrast, both the quantitative results along with the visual assessment of the processed images demonstrated no noteworthy contrast enhancement.

Post-processing image filters for noise and speckle suppression suffer from a number of inherent limitations. Such limitations include the sensitivity to the size and shape of the filter window and sometimes to a required threshold value. In most cases such filter parameters are determined empirically. Inappropriate choice may result in ineffective filtering. Moreover, most filters make assumptions on the nature of the noise adopting a multiplicative model for the noise within ultrasound data. While generally true for speckle, there are more types of noise within cardiac ultrasound data including: (i) static near field noise, (ii) dynamic cavity clutter and (iii) reverberations. The assumption of multiplicative noise can therefore be considered restrictive. Finally, while many filters claim to enhance contrast and anatomic structure edges, what they actually do is contrast and edge preservation by withholding noise suppression along edges. Generally, post-processing filtering techniques may suppress speckle but do not address many artifacts observed in cardiac ultrasound data such as high levels of cavity noise, limited contrast, shadowing and reverberation. The presence of such artifacts may result in loss of clinically valuable information throughout the filtering process. Consequently, there is still a lot of scope in the research and development of alternative methods for enhancing the image quality and diagnostic value of cardiac ultrasound data.

### 2.1.2. Incoherent processing

Incoherent processing involves the averaging of multiple independent or partially decorrelated images of an anatomic structure obtained by varying one or more imaging system parameters during data acquisition. Incoherent processing techniques have been used for the suppression of speckle in medical ultrasound data for about three decades. Spatial and frequency compounding are two commonly used incoherent processing approaches. Frequency compounding involves the averaging of images whose speckle patterns have been modified (decorrelated) by a change in the spectrum of the transmitted or received acoustical pulse (Magnin & von Ramm, 1981; Magnin et al., 1982; Trahey et al., 1986c). Frequency compounding has been reported to reduce speckle contrast and enhance structure boundaries in medical ultrasound images. Spatial compounding on the other hand involves the averaging of independent images whose speckle patterns have been modified (decorrelated) by imaging the target region-of-interest from varying angles. The variation on the imaging angle can be achieved by electronically steering the direction of the transmitted ultrasound signals (Figure 2.2.a) or by repositioning the ultrasound transducer along the scanning plane (Figure 2.2.b). Through electronic signal steering, the acquisition of real time compounded data is feasible. However, electronic steering reduces the temporal resolution of the acquired data.

Repositioning the transducer provides greater flexibility in the level of independence (decorrelation) as well as the number of the independent views of the imaged anatomic structure. However, reliable spatial alignment is required for the effective compounding of data acquired through transducer repositioning. Early studies reported the potential of spatial compounding in speckle and noise suppression of medical ultrasound data (Carpenter et al., 1980; Berson et al., 1981; Shattuck & von Ramm, 1982). Over the years, a number of studies have attempted to combine frequency and spatial compounding (Bencharit et al., 1986; Trahey et al., 1986a) to provide a more effective noise and speckle suppression technique.

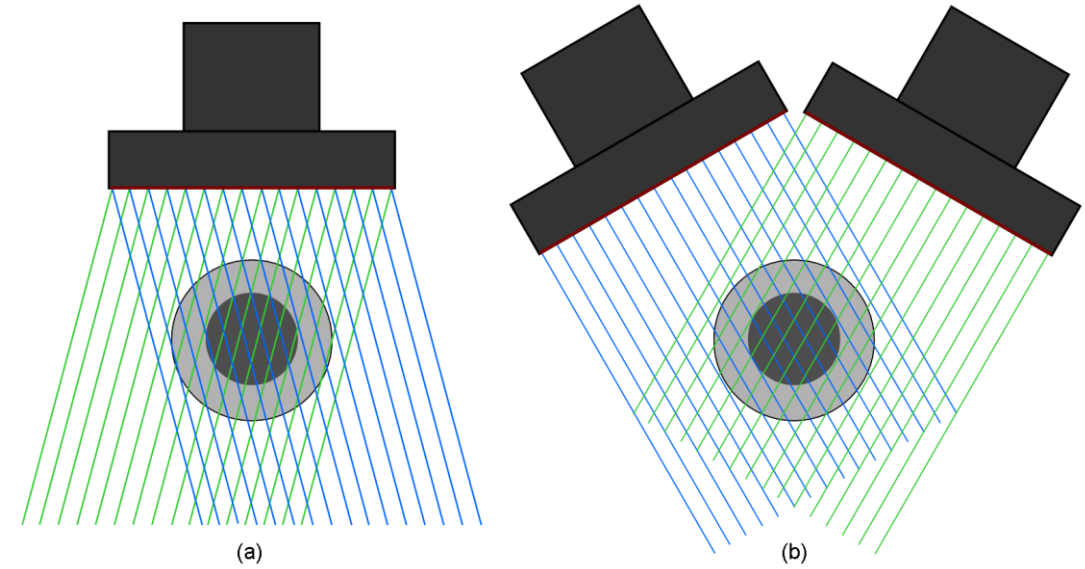


**Figure 2.2.** Variation of the imaging angle required for effective spatial compounding. (a) Electronic steering of transmitted signal. (b) Manual displacement of ultrasound transducer.

The success of both frequency and spatial compounding depends heavily on the statistical independence (correlation) among the speckle patterns of the source data. In order to be able to achieve optimal spatial compounding, a number of studies have attempted to determine the correlation of speckle patterns as a function of aperture translation. (Burckhardt, 1978) demonstrated that if $N$ independent ultrasound images are averaged then the Signal-to-Noise Ratio (SNR) of the compound image will be increased by a factor of $\sqrt{N}$. Moreover, Burckhardt recommended spatial compounding of images acquired with lateral translation of 0.5 aperture lengths. Based on his correlation curve, a translation of 0.5 aperture lengths implies that 2.25 independent images can be obtained per aperture length translation. (Trahey et al., 1986b) conducted experiments measuring the speckle correlation with lateral aperture translation in order to derive an optimal spatial separation of images for speckle reduction. Experiments indicated that independent speckle patterns are obtained with a

translation of approximately 40% of the aperture length, implying that 3.2 independent images can be obtained per aperture length translation. The results of this study were independent of the normalised transducer length, acoustic frequency and target range. (O'Donnell & Silverstein, 1988) performed a similar study which showed that – similarly to (Burckhardt, 1978) – independent speckle patterns can be obtained by lateral translation of 0.5 aperture lengths. However, Burckhardt's correlation function was found to be inaccurate and that a translation of 0.5 aperture lengths implies that 2.8 independent images can be obtained per aperture length translated.

Over the last three decades, there have been numerous studies on spatial compounding for the improvement of medical ultrasound data. There have been reports on the effectiveness of real-time spatial compounding on numerous anatomical structures such as the breast (Entrekin et al., 1999; Huber et al., 2002; Seo et al., 2002), the thyroid gland (Shapiro et al., 2001), the abdomen and pelvis (Oktar et al., 2003; Kim et al., 2004), the rotator cuff (Leotta & Martin, 2000b), the vascular (Kofoed et al., 2001) and the musculoskeletal system (Lin et al., 2002). There have also been a number of studies on novel 2D (Hernandez et al., 1996; Jespersen et al., 1998, 2000; Behar et al., 2003; Bashford & Morse, 2006) as well as 3D (Moskalik et al., 1995; Rohling et al., 1997; Krucker et al., 2000; Leotta & Martin, 2000a; Liu et al., 2004) spatial alignment and compounding methods. Popular spatial alignment approaches made use of articulated arms as well as optical, electromagnetic and acoustic positioning sensors. Some studies have attempted to use noise suppression filters as a pre-processing step to spatial compounding, taking advantage of the benefits introduced by each individual approach (Meuwly et al., 2003; Dantas & Costa, 2007). Over the years a number of alternative compounding strategies to intensity averaging have been suggested. Alternative strategies include minimum, maximum, median, Root Mean Square (RMS), mean after log compression, combination of mean and geometrical mean intensity value (Behar et al., 2003), as well as various forms of weighted averaging to extract optimal results from the compounding of partially decorrelated data (Shankar, 1986; Leotta & Martin, 2000a; Grau & Noble, 2005; Bashford & Morse, 2006). Nevertheless, currently intensity averaging is the most commonly used image compounding strategy.

Spatial compounding of medical ultrasound data has been reported to offer a number of attractive features such as (i) suppressing speckle, clutter and reverberations, (ii) reducing acoustic shadowing and dropout effects, (iii) expanding the field of view, (iv) reducing angle dependencies, and (v) increasing the edge definition of specular targets enabling a better delineation of structure boundaries (Carpenter et al., 1980; Berson et al., 1981; Shattuck &

von Ramm, 1982; Trahey et al., 1986b; Hernandez et al., 1996; Jespersen et al., 2000; Leotta & Martin, 2000a). On the other hand, spatial compounding has been reported to suffer from some shortcomings that need to be addressed (Shattuck & von Ramm, 1982; Trahey et al., 1986b; Jespersen et al., 2000). For example, real time spatial compounding reduces the temporal resolution (frame rate) of the acquired data. The reduced frame rate does not impose a major limitation due to the high temporal resolution available in modern ultrasound scanners, along with the fact that real time spatial compounding is currently applied in predominantly static anatomic structures. Spatial compounding by displacement of the transducer does not reduce the temporal resolution but instead increases the data acquisition time requirements. Furthermore, spatial compounding may introduce inhomogeneities on regions with less coverage. Thorough selection of acquisition sectors can ensure that the anatomic structure of interest is uniformly imaged. Finally, spatial compounding can introduce blurring across the boundaries of the imaged anatomic structures. Blurring across structure boundaries can arise from a wide range of sources including (i) uncertainties in transducer position and tissue velocity, (ii) errors in the assumed mean speed of sound, (iii) spatial variations in the speed of sound, and (iv) tissue movement during the sequential data acquisition. The key to effective spatial compounding is the accurate alignment of the averaged data (Rohling et al., 1997). Accurate spatio-temporal alignment of all individual views of the imaged structure prior to spatial compounding can limit and possibly eliminate blurring across structure boundaries.

Spatial compounding addresses most artifacts limiting the image quality and diagnostic value of cardiac ultrasound data, making it an inherently more suitable noise and speckle suppression approach than post-processing filters. A number of studies have attempted to utilise spatial compounding for the enhancement of cardiac ultrasound data. However, the constant, rapid movement of the heart, the constant respiration motion of the patient's chest and the limited acoustic windows between the rib cage and lungs introduce a number of limitations and challenges on spatial compounding methods. (Soler et al., 2005) performed spatial compounding of two cardiac volumes acquired from different apical acoustic windows. The 3D volumes were spatially aligned without the use of external positioning sensors. The registration approach was performed in two steps; an initial coarse alignment of two semi-automatically segmented LV volumes was followed by a refined rigid registration of the volumetric data. (Grau & Noble, 2005) introduced a method for compounding manually aligned apical and parasternal views of 3D cardiac data. The data compounding was based on image phase, and was implemented using the monogenic signal (Felsberg & Sommer, 2001). Image phase provides contrast invariant information on local structure and

orientation. Considering the low contrast in many cardiac ultrasound data, image phase may provide a robust information resource. (Yao & Penney, 2008) extended the previous attempts by aligning and compounding up to 11 parasternal and apical 3D volumes. A combination of optical position sensors and rigid registration were utilised for the accurate alignment of the volumes. Traditional approaches such as intensity maximum and average, along with phase based compounding, were also investigated. (Rajpoot et al., 2009) developed the first approach utilising a fully automatic, multi-resolution, voxel based rigid registration for the alignment of multiple apical 3D volumes. A novel wavelet based spatial compounding method was also introduced enabling the decomposition and relevant fusion of the aligned volumes in low and high frequency components. (Yao et al., 2010) extended the fully automated data alignment approach suggested by (Rajpoot et al., 2009) utilising weighted averaging for optimised image feature preservation during spatial compounding. (Gao et al., 2009) performed a phantom based feasibility study on the real time compounding of transesophageal cardiac ultrasound volumes. An electromagnetic position sensor was utilised for the spatial alignment of the data. Another recent study investigated the effect of spatial compounding of multiple 3D volumes on fetal cardiac ultrasound data (Gooding et al., 2010). The effect of a range of compounding approaches was examined including, intensity maximum, mean, median as well as wavelet based compounding. The physiology of a fetal heart, small size and high heart rate, along with the absence of standard imaging windows in fetal cardiology introduced additional challenges in effective spatial compounding. Finally, (Szmigielski et al., 2010) performed a thorough qualitative and quantitative assessment on the effect of spatial compounding of 3D cardiac ultrasound data using phantom as well as clinical data from 32 participants. A rigid, fully automatic, voxel based registration was utilised for the spatial alignment of the cardiac volumes.

The aforementioned studies have identified the potential of spatial compounding in improving the image quality and diagnostic value of 3D cardiac ultrasound data. Substantial noise and speckle reduction, field of view increase, acoustic shadowing and reverberation compensation and enhancement of the presence of visually weak cardiac structures are commonly identified benefits of spatial compounding on cardiac volumes. The choice of spatial compounding approach has a direct effect on the processed data. The intensity averaging (mean or median) methods tend to generate a higher level of noise and speckle suppression. Techniques like maximum intensity compounding enhance anatomic feature delineation. More advanced approaches such as phase and wavelet based compounding provide a trade-off between noise suppression and feature delineation. Most compounding techniques have no noteworthy effect on the contrast between cardiac tissue and cavities.

Techniques like maximum intensity, phase based and wavelet compounding have been identified to introduce a modest contrast increase between cardiac tissue and cavity. Nevertheless, more effective contrast enhancement techniques are required.

The accurate spatio-temporal alignment of the 3D volumes is a key process for effective spatial compounding. Insufficient alignment may result in considerable degradation of the diagnostic value of the processed data. Most current approaches utilise fully automated, voxel based rigid spatial registration of the compounded volumes. While non-rigid spatial registration could provide a more accurate alignment, its potential is currently limited due to the high levels of noise and low contrast of the aligned datasets. Moreover, non-linear data transformation may result in undesired deformation of the cardiac physiology and is therefore not advisable. Currently, no study has attempted to address the temporal variability between consecutive cardiac cycles. This constitutes a major limitation in existing studies, which assume regular cardiac cycle within all the compounded volumes. This assumption is very restrictive and may cause severe deformation of cardiac structures affecting the diagnostic value of the processed data. Overall, throughout the years there has been a substantial improvement in data alignment methods. It is expected that future studies will address most current limitations making the compounding of partially decorrelated 3D volumes of the heart a very powerful data enhancement tool. Currently, the visual complexity of 3D cardiac ultrasound data limits their clinical usability. However, spatial compounding can act as a post-processing step in order to improve data quality, enhancing the applicability of common post-processing techniques such as image segmentation and registration. The clinical use of the technology is also expected to increase with the development of novel, effective data analysis and processing tools.

The acquisition of independent cardiac views using 2D ultrasound is more challenging than the corresponding 3D data acquisition. For effective spatial compounding (i) all data need to be acquired over the same or a very similar scan plane and (ii) a substantial overlap between the individual heart views is required. Consequently, acquiring 2D data suitable for effective spatial compounding through different acoustic windows (in a manner similar to 3D volumes) is very ambitious and possibly infeasible with current acquisition and tracking technology. A number of studies have attempted to overcome this limitation, compounding partially decorrelated 2D data of the heart acquired through a single acoustic window. The studies can be broadly categorised as: (i) compounding of temporally adjacent frames, and (ii) compounding frames corresponding to the same cardiac phase acquired over consecutive cardiac cycles.

An early study by (Petrovic et al., 1986) enhanced cardiac ultrasound data by averaging the intensity levels from 3 consecutive frames. Due to the constant motion of the heart, the consecutive frames were partially decorrelated and consequently spatial compounding reduced noise and speckle in the processed images. However, averaging consecutive frames of a constantly and rapidly moving structure, such as the heart, introduced a considerable amount of blurring on the boundaries of cardiac tissue and cavity. Furthermore, averaging 3 frames to generate a single frame reduced the temporal resolution of the processed dataset substantially. A very similar approach was used to enhance intravascular ultrasound images by (Li et al., 1994). (Achmad et al., 2009) attempted to address both limitations of the compounding method introduced by (Petrovic et al., 1986). More precisely, for each frame in the B-mode frame sequence a moving window was defined containing the preceding and the following frames (three frames). Optical flow (Barron et al., 1992) was utilised to derive an intermediate frame between the preceding and the following frame, which was then compounded with the current frame. By performing spatial compounding for each individual frame in the original B-mode frame sequence utilising a moving window, no loss of temporal resolution was introduced. Moreover, by generating a partially decorrelated intermediate frame to compound with each frame in the sequence, no severe tissue/cavity boundary blurring was introduced. However, the noise suppression introduced by averaging two frames was very limited. Similar approaches have been adopted as a pre-processing step to image segmentation by (dos Reis et al., 2008; dos Reis et al., 2009). (Lin et al., 2010) extended further the compounding of temporally adjacent frames by utilising a hierarchical, motion-compensating technique to spatially align (warp) up to 9 frames. Qualitative and quantitative assessment demonstrated considerable noise reduction and enhancement of anatomic structures. However, the technique relied heavily on the accurate non-linear registration of consecutive cardiac ultrasound frames. Currently the applicability of non-linear image registration methods is limited for a large proportion of cardiac ultrasound scans due to high levels of noise and low contrast. Consequently, the applicability of this noise reduction method is limited to cardiac ultrasound data with low levels of noise.

Another set of studies attempted to utilise the repeated rhythmic contractions of the heart in order to acquire multiple 2D images of the same cardiac phase over consecutive cardiac cycles. The process has been referred to as *Temporal Compounding*. Minor random movements during a multi-cycle data acquisition alter the scan plane resulting in the acquisition of partially decorrelated views of the imaged cardiac structure. Compounding such partially decorrelated frames corresponding to the same cardiac phase acquired over consecutive cardiac cycles can therefore enhance the processed images. The key to effective

spatial compounding is to align all data prior to the compounding (Rohling et al., 1997). Therefore, the accurate and robust temporal and spatial alignments of corresponding frames acquired over multiple cardiac cycles are essential processes for effective Temporal Compounding. Insufficient spatio-temporal alignment may result in severe blurring of the imaged cardiac structure. (van Ocken et al., 1981) first identified the potential of fusing information acquired over consecutive cardiac cycles in order to enhance the quality of the ultrasound datasets (Sinclair et al., 1983). (Unser et al., 1989) performed averaging on a normalised time-scale of M-mode ultrasound data acquired over a number of consecutive cardiac cycles. The temporal alignment to a reference cardiac cycle was performed using a dynamic programming time-wrapping algorithm requiring no ECG information. The compounding method enhanced the M-mode cardiac ultrasound scans by suppressing noise with no apparent loss of temporal resolution. (Vitale et al., 1993) presented the first attempt to use compounding of partially decorrelated images acquired over consecutive cardiac cycles on 2D B-mode data. In this early attempt, the temporal alignment of corresponding frames was based on information extracted from the ECG signal. More precisely, the end-diastole (ED) frames from each cardiac cycle were identified at the peaks of the QRS complex of the recorded ECG signal. 22 frames were then extracted using regular temporal displacement between two consecutive ED frames. Corresponding frames from consecutive cardiac cycles were spatially compounded by intensity averaging. The study examined the effect of compounding an increasing number of frames on noise and speckle. The results were promising with data from 10 cardiac cycles providing a good tradeoff between noise suppression and processing resources. Similar approaches have been adopted, combined with compounding of adjacent frames, in recent studies as a pre-processing step for more effective image segmentation of cardiac structures (Amorim et al., 2009; Melo SA Jr et al., 2010). However, these studies suffered from two major limitations. In the first instance, the studies assumed that cardiac cycles are occurring in regular intervals. Unfortunately, this is not the case in most clinical cardiac ultrasound scans. Secondly, no spatial alignment was performed on the temporally aligned frames prior to intensity averaging. Spatial alignment can compensate for larger movements of the heart during the multi-cycle data acquisition. Both limitations can lead to severe blurring of the imaged cardiac structure depreciating substantially the diagnostic value of the processed data. (Olstad, 2002) extended the approach by introducing a rigid spatial alignment to compensate for larger cardiac movements during the multi-cycle data acquisition. (Abiko et al., 1997) presented a novel spatio-temporal alignment approach making no assumption on the temporal characteristics of the cardiac cycle and requiring no ECG information. The spatio-temporal alignment utilised

1D intensity information extracted from the central scan line of each frame. While a crude heuristic method for data alignment, the study demonstrated the potential for an accurate temporal alignment without making (i) any assumptions on the characteristics of the cardiac cycle and (ii) use of ECG information. However, the study utilised very limited information from highly noisy data in order to perform the very important task of spatio-temporal data alignment prior to spatial compounding. Moreover, it assumed no data rotation or translation along the X-Axis (only translation along the Y-Axis) over the multi-cycle scan. This assumption is very restrictive and may result in severe blurring of the imaged cardiac structures in the processed images.

All of these studies have established the benefits of compounding partially decorrelated data from consecutive cardiac cycles. Similar to other spatial compounding techniques, considerable noise suppression can be introduced along with enhancement of visually weak cardiac structures. The potential of the Temporal Compounding approach has also been recognised by a number of studies (Zwirn & Akselrod, 2004, 2005; Amorim et al., 2009; Melo et al., 2010) even for other imaging modalities such as CT (Bhat et al., 2009). However, a major drawback limiting the applicability of current implementations is the absence of a reliable and affective temporal alignment approach. As a result, there is a current research opportunity on the development of such a temporal alignment algorithm.

## 2.2. Other cardiac ultrasound data enhancement techniques

Cardiac ultrasound suffers from a number of artifacts besides noise and speckle. While such artifacts limit the image quality and diagnostic value of the acquired data considerably, there has not been substantial research interest in order to address them. Spatial compounding, by averaging partially decorrelated views of the heart, can address a number of such artifacts including acoustic shadowing, reverberations and structures moving in and out of plane. However, there are artifacts that are not addressed by spatial compounding and require more dedicated approaches.

### 2.2.1. Contrast enhancement

Limited contrast between cardiac tissue and cavity structures constitute a major limitation on cardiac ultrasound data. Limited contrast combined with high levels of noise in cardiac cavities can make the delineation of cardiac structures very challenging for both automatic as well as manual, expert driven approaches. Consequently, low contrast levels limit the diagnostic value as well as the effectiveness of post-processing techniques such as image

segmentation and registration on cardiac ultrasound data. Non-contrast Tissue Harmonic Imaging (THI) has been used in the past in order to suppress the noise in cardiac cavities and enhance the contrast and delineation between cardiac tissue and cavity structures. Harmonics are frequencies that occur at multiples of the fundamental, or transmitted frequency (Shapiro et al., 1998). (Ward et al., 1995, 1997) identified the non-linear propagation properties of tissue contributing to harmonic ultrasound images. (Averkiou et al., 1997) presented some early *in-vivo* harmonic images. Since then a number of studies have qualitatively and quantitatively assessed the effect of THI, using second harmonic frequencies, on cardiac ultrasound data (Becher et al., 1998; Belohlavek et al., 1998; Caidahl et al., 1998; Mulvagh et al., 1998). The effect of THI on specific processes such as stress echocardiography has also been investigated (Skolnick et al., 1999; Franke et al., 2000). The potential benefits of non-contrast THI are well established. THI can improve the quality of cardiac ultrasound data even in technically difficult cases. However, while an established data acquisition technique, there are still a number of challenging cases where effective post-processing techniques are required for the suppression of cavity noise and the contrast enhancement between cardiac tissue and cavities.

Over the years, many studies have introduced post-processing techniques that enhance contrast while suppressing noise in ultrasound data. A number of post-processing filters (Zong et al., 1998; Yue et al., 2005; Tay et al., 2010; Finn et al., 2011), as well as spatial compounding approaches (Yao & Penney, 2008; Rajpoot et al., 2009; Szmigielski et al., 2010), have claimed to enhance the cardiac structure boundaries along with the contrast between cardiac tissue and cavities. However, most of these noise suppression methods actually performed contrast and boundary preservation rather than enhancement. Moreover, even with approaches that have been successful, the contrast enhancement introduced was very modest. While such techniques can be used as a pre-processing step, the development of more focused tools for sizeable contrast enhancement is required. To our knowledge, a very limited number of studies have addressed the low contrast limitation in cardiac ultrasound data.

(Boukerroui et al., 2001) introduced a novel contrast and anatomic feature enhancement approach based on a phase-based feature detection algorithm. The algorithm utilised Feature Asymmetry (Mulet-Parada & Noble, 2000), a 2D extension of Phase Congruency (Kovesi, 1999) providing a robust, brightness and contrast invariant detection of asymmetric image features, such as step edges. The sparse set of extracted features was then interpolated by a Fast sparse Surface Interpolation (FSI) algorithm. Finally, a novel non-linear processing

method was developed reconstructing an approximation to the intensity inhomogeneities within the corrupted data which were subtracted from the original images. The algorithm was applied in a set of B-mode cardiac ultrasound image sequences. The results in contrast and anatomic feature enhancement were promising. However, (Boukerroui et al., 2001) identified that the Feature Asymmetry algorithm was not very effective for data with low Signal-to-Noise Ratio (SNR). This drawback of Feature Asymmetry can impose a major limitation on the applicability of the contrast enhancement approach to the majority of clinical cardiac ultrasound data.

(Zwirn & Akselrod, 2004, 2005) introduced a very interesting technique for the automatic adjustment of the gray-levels used in cardiac ultrasound data aiming to enhance cardiac tissue visualisation and tracking. The technique was referred to as Adaptive Brightness Transfer Function (ABTF) and was based on the assumption that the gray-level histogram of cardiac ultrasound images can be approximated by the sum of three non-overlapping normal distribution functions (Gaussians). Each Gaussian represented a different cardiac structure, with the low intensity Gaussian representing cardiac cavities, and the medium and high intensity Gaussians representing low and high intensity cardiac tissue structures respectively. The intersection between these three Gaussians would then act as thresholds defining the intensity range for each of the three image segments. Each section of the histogram was then processed individually using a number of techniques including, histogram equalisation, specification and scaling. ABTF provided an extension to similar histogram analysis approaches for the enhancement of low contrast images (Abdullah-Al-Wadud et al., 2007; Ibrahim & Kong, 2007). The results from a qualitative and quantitative assessment of the ABTF on suppressing cavity noise and enhancing contrast between cardiac tissue and cavities were very promising. However, like all the histogram-shape based approaches, ABTF made a very strong assumption about the shape of the gray-level histograms of the processed cardiac ultrasound data. While some datasets conform to the assumption there are still a considerable number of datasets for which this assumption does not hold. Furthermore, ABTF assumed constant illumination throughout the scanned structure, which in many cardiac ultrasound scans is not accurate. While both approaches (Boukerroui et al., 2001; Zwirn & Akselrod, 2004, 2005) have demonstrated potential in enhancing the contrast and anatomic features on cardiac ultrasound data, there is plenty of scope for the development of more effective and robust techniques that make fewer assumptions on the nature of the processed data.

### 2.2.2. Static noise suppression

Static noise is an artifact present in most cardiac ultrasound scans, especially in the top end of the field-of-view. Strong static noise corrupts cardiac structures limiting the applicability of commonly used processing techniques such as image registration, segmentation and speckle tracking, as well as the diagnostic value of the data. (Hozumi et al., 1998) provided an early technique for suppressing static noise within cardiac ultrasound images. The main assumption was that static noise was generated by reverberation between near field structures such as ribs and intercostal muscles. Cardiac motion is considerably faster than the motion of such structures, which is predominantly introduced during the patient's respiration. Slow moving structures generate noise that is almost static. (Hozumi et al., 1998) attempted to remove static noise by introducing a high pass filter on data acquired over consecutive frames. More precisely, for each pixel within a reference image, the intensity variations over consecutive frames were extracted as a 1D signal. This signal was decomposed into the tissue generated component and a noise component by utilising a high-pass filter. The high-pass filter was implemented by subtraction between the original noise corrupted signal and a moving average signal representing the static noise. The moving average signal was generated by successively averaging a number of adjacent values of the original signal and shifting the averaging range. While the results in the study appeared promising, a preliminary in-house implementation and evaluation of the technique demonstrated limited effect in noise suppression on clinical cardiac ultrasound data. (Zwirn & Akselrod, 2006) provided a different approach in order to address the static noise within cardiac ultrasound images. Similar to the earlier study, the static noise was assumed to be generated by reverberation between near field slow moving structures such as ribs and intercostal muscles. However, no high-pass filter was employed. Instead, two reference frames were generated. The first reference frame contained the average intensity level over the consecutive frames. For strong static noise, the mean intensity value should be relatively high. The second reference image contained the Mean Square Error (MSE) between each consecutive frame and the average intensity frame. For static noise, the MSE should be relatively low. The corresponding thresholds were derived utilising the three Gaussians histogram decomposition introduced in (Zwirn & Akselrod, 2004, 2005). For the average intensity frame, the threshold was set as the intersection of the two high intensity Gaussians. Any pixel with intensity higher than the threshold could possibly be static noise. For the MSE frame, the threshold was set as the intersection of the two low intensity Gaussians. Any pixel with intensity lower than the threshold could possibly be static noise. Pixels that were identified in both reference images as potential static noise were removed from the original

frame sequence. The results from the study were promising. However, strong relatively akinetic tissue segments, such as the pericardium, could be falsely identified and removed as static noise.

## 2.3. Aims

The main objective of this study is to develop and evaluate techniques that enhance the image quality and diagnostic value of cardiac ultrasound data. Spatial compounding techniques have demonstrated very strong potential in addressing a range of artifacts in cardiac ultrasound data including (i) noise and speckle, (ii) acoustic shadowing, (iii) reverberations, and (iv) structures moving in and out of plane. Spatial compounding of multiple instances of a cardiac cycle acquired over a single acoustic window has been identified as the most promising data enhancement approach for 2D cardiac ultrasound data. Moreover, plenty of scope has been identified on the development of effective and robust techniques to enhance the contrast and detectability between cardiac tissue and cavities by making fewer assumptions on the nature of the processed data. Finally, it is strongly believed that the repetitive cardiac motion can provide an abundance of information to be used for enhancing the quality of cardiac ultrasound data. There is great interest in investigating the potential of such information.

The detailed aims of this thesis are:

- To develop a robust non-linear spatio-temporal alignment approach for partially decorrelated data acquired over consecutive cardiac cycles through a single acoustic window. The data alignment should (i) make no assumptions on the temporal characteristics of the acquired data and (ii) enhance the effectiveness of existing spatial compounding techniques in suppressing undesirable artifacts and improving the appearance of visually weak anatomic structures in cardiac ultrasound data.

- To investigate novel and effective ways to acquire multiple partially decorrelated instances of a cardiac cycle through a single acoustic window using 3D ultrasound acquisition technology. The partially decorrelated data should provide an alternative to multi-cycle acquisition for spatial compounding.

- To investigate the temporal variations within image histograms of consecutive frames in order to (i) suppress noise within cardiac cavities, (ii) increase the dynamic range of tissue speckle information and (iii) enhance the contrast and detectability between cardiac tissue and cavity structures.

- To introduce a fully automated method that integrates spatial compounding with histogram processing in order to suppress cavity noise and tissue speckle while enhancing tissue/cavity contrast as well as the delineation of cardiac cavity boundaries, even when heavily corrupted by a range of cardiac ultrasound artifacts.

- To develop a protocol using a range of quantitative metrics in order to assess the effect of each data enhancement method on the image quality and diagnostic value of cardiac ultrasound data.

# Chapter 3

# Temporal Compounding

This chapter extends the notion of ***Temporal Compounding***, a noise suppression method that utilises spatial averaging of partially decorrelated transthoracic ultrasound data acquired through a single acoustic window. The partially decorrelated data are acquired over a number of consecutive cardiac cycles. Reliable spatial and temporal alignment of the corresponding frames in consecutive cardiac cycles is vital for effective ***Temporal Compounding***. This study introduces a novel, efficient, accurate and robust technique for the temporal alignment of cardiac cycles with variable temporal characteristics. ***Temporal Compounding*** is quantitatively assessed using 32 multi-cycle, clinical cardiac ultrasound datasets. Datasets have been selected so that they provide a representative selection of image qualities and diagnostic values by making sure a wide range of cardiac ultrasound artifacts are present. Furthermore, the effect of **Temporal Compounding** on the noise and contrast within the imaged cardiac structures is quantitatively assessed utilising measures such as tissue Signal-to-Noise Ratio (SNR), cavity SNR as well as tissue/cavity contrast and detectability index. Optimal acquisition parameters such as the number of utilised consecutive cardiac cycles are derived. Finally, this study examines the effect of ***Temporal Compounding*** in five clinical measurements, such as cavity diameter and wall thickness, performed on routine echocardiographic examinations.

## 3.1. Introduction

Speckle/noise suppression on medical ultrasound data has been an ongoing research theme for the last three decades. Ultrasound scans represent a challenging application for noise reduction algorithms because, although they are heavily corrupted by noise, they contain spatial features that should be preserved. Spatial compounding, a widely used technique, suppresses noise by combining independent or partially decorrelated images of an anatomic structure whose speckle patterns have been modified by imaging the target region of interest from varying angles. Chapter 2 provides an extensive review of previous spatial

compounding approaches for the enhancement of medical ultrasound data. However, spatial compounding of cardiac ultrasound data is a challenging task due to the constant, rapid movement of the heart and the limited acoustic windows through the patient rib-cage as well as between the ribs and lungs.

The human heart is constantly under repeated, rhythmic contractions that are responsible for circulating the blood around the body. This almost periodic cardiac motion enables the acquisition of multiple 2D images of the same heart structure at the same cardiac phase from a single acoustic window over multiple cardiac cycles. During a multi-cycle data acquisition there are three primary sources of minor random movements: (i) the almost periodic respiration motion of the patient, (ii) random patient movements, and (iii) operator (echocardiographer) hand tremor. Such random movements during an examination cause small changes to the scan plane with respect to the examined heart structure. While in most cases all three movement sources are kept to a minimum, it would be unrealistic to disregard their existence and effect in a multi-cycle scan. Consequently, small changes to the scan plane along with dynamic noise changes enable the acquisition (over multiple cardiac cycles) of partially decorrelated views corresponding to the same cardiac phase. Compounding such partially decorrelated views can therefore reduce speckle as well as dynamic noise in cardiac ultrasound data.

The process of aligning and compounding data from consecutive cardiac cycles is referred to as ***Temporal Compounding*** and is an extension of the Synchronised Summing Method used to improve SNR of noisy periodic signals in signal processing. The key to effective spatial compounding is to align all data prior to the compounding (Rohling et al., 1997). Therefore, accurate and robust temporal and spatial alignments of corresponding frames acquired over multiple cardiac cycles are vital processes for effective ***Temporal Compounding***. Insufficient spatio-temporal alignment can result in severe blurring of the imaged cardiac structure. A number of studies have attempted to provide elementary implementations of ***Temporal Compounding*** (Vitale et al., 1993; Abiko et al., 1997; Olstad, 2002). Such studies have established the benefits of ***Temporal Compounding*** and have identified, in limited numbers of datasets, its potential on SNR improvement. However, none of the existing studies have attempted to examine the effect of ***Temporal Compounding*** on clinical measures performed during typical cardiac ultrasound examinations.

## 3.2. Aims and contributions

The aim of this chapter is to elucidate and quantitatively evaluate a semi-automated method that spatio-temporally aligns and compounds frames from multi-cycle cardiac B-mode datasets. The compounding method aims at the suppression of tissue speckle as well as dynamic noise within cavities and the enhancement of the detectability between cardiac tissue and cavity structures.

The contributions of this chapter are:

- Advancing ***Temporal Compounding*** by:
    - Developing an accurate and robust method for the semi-automatic identification of End Diastole (ED) and End Systole (ES) frames within a multi-cycle cardiac ultrasound frame sequence using exclusively image intensity information.
    - Utilising an accurate and efficient method for the non-linear temporal alignment of corresponding frames between successive cardiac cycles within a multi-cycle cardiac ultrasound frame sequence.
    - Utilising a robust rigid registration method for the spatial alignment of the temporally aligned frames prior to spatial compounding.
- Assessing the effect of ***Temporal Compounding*** on patient cardiac ultrasound scans using a range of quantitative measures such as tissue SNR, cavity SNR, tissue/cavity contrast and Signal Difference to Noise Ratio (SDNR) also known as detectability index. Optimal acquisition parameters are identified ensuring the clinical feasibility of ***Temporal Compounding***.
- Examining the effect of ***Temporal Compounding*** on routine clinical measurements performed on clinical cardiac ultrasound scans over a range of image qualities and diagnostic values.

## 3.3. Background on data alignment

### 3.3.1. Temporal alignment

The temporal behaviour of a heart may vary during a multi-cycle cardiac ultrasound examination. Variations in the temporal dynamics range from small, for healthy hearts, to large for hearts suffering from arrhythmia or other cardiac diseases. Moreover, temporal

variations can be global, such as differences in the length of cardiac cycles (e.g. one cardiac cycle can be longer that another) or local, such as differences in the dynamic properties of the heart (e.g. one heart may have a longer contraction phase and a shorter relaxation phase). In general, these variations tend to be non-linear with greater effect in the relaxation phase of the cardiac cycle. As a result, identifying consecutive cardiac cycles in a multi-cycle dataset and compounding frames sequentially, (e.g. the second frame of the reference cardiac cycle with the second frames from all the compounded cardiac cycles) is not sufficient since these frames may not correspond to the same stage within their corresponding cardiac cycles (Figure 3.1.a). What is required is to find the temporal relationship between the two image sequences in order to compound frames at corresponding stages within the cardiac cycle (Figure 3.1.b). The accurate and robust temporal data alignment is a key process for effective ***Temporal Compounding***. Insufficient temporal alignment can result in severe blurring of the imaged cardiac structure.

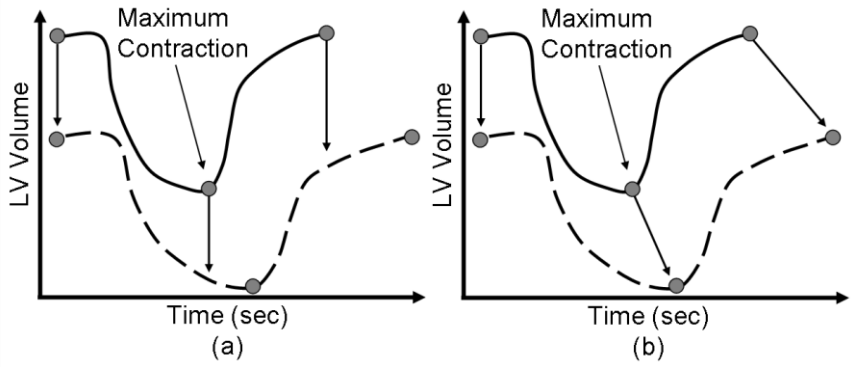


**Figure 3.1.** Example highlighting the necessity of temporal alignment prior to spatial compounding. Dashed and solid lines correspond to the reference and aligned cardiac cycles respectively. (a) No temporal alignment would result in compounding frames corresponding to different cardiac stages, (b) temporal alignment provides a mapping between corresponding temporal positions.

(Abiko et al., 1997) in their early implementation of ***Temporal Compounding*** utilised a crude, heuristic method for the temporal alignment of consecutive cardiac cycles. Utilising Normalised Cross Correlation (*NXC*), their algorithm identified all frames in a multi-cycle dataset corresponding to each frame in a reference cardiac cycle. If the reference frame belonged in the diastole phase, the algorithm performed *exhaustive search* in all the remaining diastole phases in the multi-cycle dataset. Similarly, if the reference frame belonged in the systole phase, the algorithm performed *exhaustive search* in all the remaining systole phases in the dataset. Even though such a method has the potential to generate a very accurate temporal alignment, *exhaustive search* can be very computationally intensive. (Abiko et al., 1997) reduced the computational requirements of their approach by

performing both temporal as well as rigid spatial data alignment using only 1D intensity information extracted from the central scan line of each frame. However, such an approach assumed no data rotation or translation along the X-Axis (only translation along the Y-Axis) over the multi-cycle scan. Moreover, it used very limited information from highly noisy data in order to perform the very important task of the spatio-temporal data alignment prior to spatial compounding.

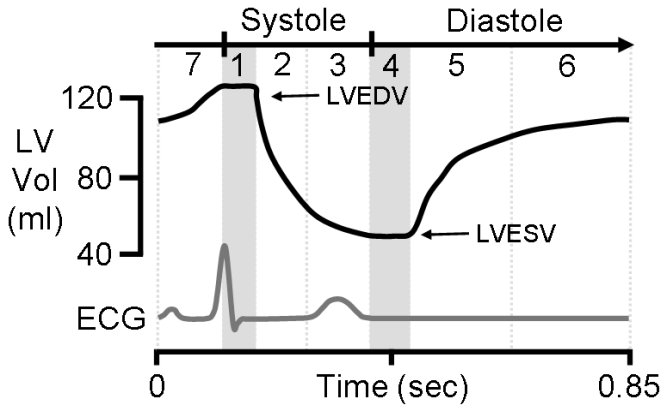


**Figure 3.2.** An example of the ECG and volume of the heart during the different phases of a cardiac cycle [adapted from (Berne et al., 2004)].

The computational requirements of the temporal alignment process can be reduced by providing a mapping between the reference cycle and the aligned cycles using a number of accurately defined frames corresponding to predetermined cardiac phases, such as ED and ES frames. Interpolation can then be utilised to derive the mapping for the remaining frames. A range of methods for the identification of individual phases of the cardiac cycle are currently available. For example the Electrocardiogram (ECG) signal as well as the ventricular pressure can be used (Olstad, 2002). The ECG signal records the electrical activations of the heart which can be related to the phases of the cardiac cycle (Figure 3.2). While ECG enables accurate enough identification of the ED frames (QRS complex), it is much more challenging to extract accurate information related to the other phases of the cardiac cycle (Guyton & Hall, 1997; Bray et al., 1999; Berne et al., 2004). In addition, ECG signals can be very noisy and their interpretation constitutes a field of current research interest (Friesen et al., 1990). Other alternatives, such as the kymogram (Kachelriess et al., 2002; Larson et al., 2004) have been suggested for the detection of the beginning and the end of cardiac contraction. However, kymograms do not provide any information regarding the other phases of the cardiac cycle. Furthermore, kymograms are extracted from raw data of spiral CT of the heart and are therefore not available during cardiac ultrasound examinations. The ventricular pressure could also be used to find temporal correspondence between two

cardiac cycles. However, the pressure information tends not to be recorded and is usually not available in clinical practice. This study attempts to accurately identify independent phases within consecutive cardiac cycles utilising exclusively intensity information from within the B-mode image sequences.

Depending on the number of frames utilised as Control Points (CPs) to define different stages in a cardiac cycle, there is a range of possible temporal alignment mappings. Past implementations of ***Temporal Compounding*** (Vitale et al., 1993; Amorim et al., 2009; Melo et al., 2010) defined cardiac cycles between two consecutive ED frames (ED1 to ED2). It then used linear interpolation to provide a mapping between the frames of the reference and the aligned cardiac cycles. Such a temporal alignment approach can be described by a global affine temporal transformation consisting of a global scaling factor compensating for differences in the cardiac cycle length and a global translation factor aligning the start of the compounded cardiac cycles. However, this method cannot correct any temporal misalignment caused by different contraction and relaxation patterns. Chapter 1 provides information on the 7 cardiac cycle phases (the atrial systole, isovolumetric contraction, rapid ejection, reduced ejection, isovolumetric relaxation, rapid ventricular filling and reduced ventricular filling). Temporal variations, especially for a diseased heart, over consecutive cardiac cycles can have an independent effect on each of those 7 phases. Therefore, using only a global affine temporal transformation to provide a mapping between the temporal characteristics of two cardiac cycles will not suffice in most clinical cases. Figure 3.3 displays example LV volume curves for two consecutive cardiac cycles. The length of each phase varies in each cardiac cycle resulting in different contraction and relaxation patterns. Introducing additional frames that represent different stages in a cardiac cycle can further increase the accuracy of the temporal alignment. (Shekhar et al., 2004) identified all ED and ES frames defining each cardiac cycle with an ED1 – ES – ED2 sequence. Piecewise linear interpolation in each of the contraction and relaxation phases was then performed in order to derive a mapping between the frames of the reference and the aligned cardiac cycles within the multi-cycle dataset. Such an approach, while more accurate, still does not consider local variations in the individual cardiac cycle phases. This study investigates the use of 3, 5 and 7 frames (CPs) representing different stages within a cardiac cycle. The use of 7 independent stages is considered to provide a good representation of both the global, differences in the length, as well as the local temporal variations of the 7 individual cardiac phases (roughly a frame for each cardiac phase). Both piecewise linear and more refined non-linear temporal transformation models are considered.

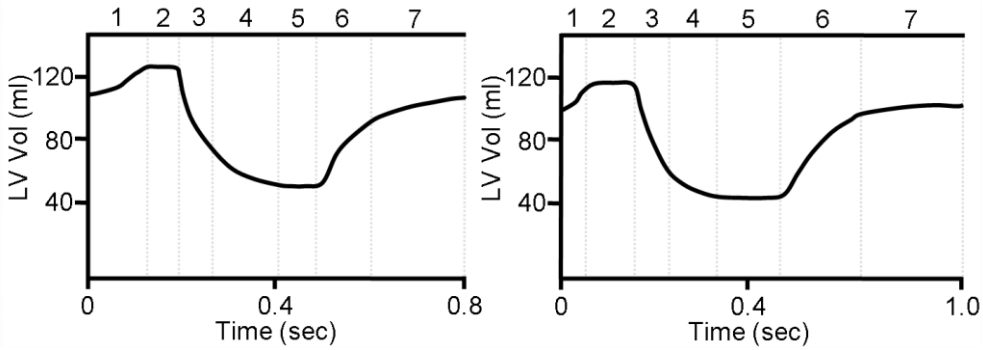


**Figure 3.3.** An example where temporal variations have a different effect in each of the 7 phases of a cardiac cycle. More advanced temporal alignment methods are required in such cases.

### 3.3.2. Spatial alignment

The spatial registration of the temporally aligned frames prior to spatial compounding is required in order to correct for larger displacements of the examined structure with respect to the scanning plane over the multi-cycle data acquisition. Such displacements occur mostly due to probe slippage and changes of the heart orientation during the periodic respiration motion of the patient's chest. If spatial registration is not performed then ***Temporal Compounding*** will introduce additional tissue/cavity boundary blurring on the imaged cardiac structure. Image registration seeks for an optimal mapping, $T$ relating each point of an image $I$ to the corresponding anatomical point in the reference image $I'$. The determination of the optimal transformation $T$ depends on the types of variations between the images and can be broken into the following selection tasks (Brown, 1992): (i) the type of transformation, (ii) the feature space, (iii) the similarity measure, and (iv) the optimisation strategy. A number of review articles can provide useful insights on image registration (Brown, 1992; Zitova & Flusser, 2003), medical image registration (Maintz & Viergever, 1998; Lester & Arridge, 1999; Hill et al., 2001) and cardiac image registration (Makela et al., 2002). Over the last few years there has been an increased research interest on the registration of general medical ultrasound data (Moskalik et al., 1995; Rohling et al., 1997; Rohling et al., 1998; Meyer et al., 1999; Shekhar & Zagrodsky, 2002) as well as cardiac ultrasound data (Zagrodsky et al., 2000; Ledesma-Carbayo et al., 2001; Zagrodsky et al., 2001; Shekhar et al., 2004; Ledesma-Carbayo et al., 2005; Zagrodsky et al., 2005; Aschkenasy et al., 2006; Grau et al., 2007).

The type of spatial transformation used for aligning two images constitutes a fundamental characteristic of any image registration technique. The number of parameters required to describe a transformation are often called *degrees of freedom* and depend on the type of

transformation as well as the dimensionality of images. Rigid body transformations are the simplest form of image transformation in which objects within the transformed images maintain their relative shape and size. Rigid transformations, along with affine transformations are also known as linear since they maintain straight lines and ensure that lines that are parallel prior to the transformation will remain parallel after the transformation. Rigid body transformations are considered sufficient for the correction of small displacements of the examined structure during the multi-cycle data acquisition.

The feature space of the transformation extracts the required information for aligning the images and can be extrinsic, intrinsic and non-image based (Brown, 1992; Maintz & Viergever, 1998). Intrinsic methods rely on patient-generated image information only. On the other hand, extrinsic methods rely on artificial objects attached to the patient while non-image based methods derive the image mapping without utilising image information. Similarity measures provide a way to assess how similar two images are. There is a wide range of similarity measures available and they can be broadly categorised in (i) point based, (ii) surface based, and (iii) intensity based methods (Brown, 1992; Maintz & Viergever, 1998). Intensity similarity approaches provide a great framework for ultrasound registration by removing any explicit segmentation and landmark identification requirements.

There is a wide range of intensity based similarity measures available in literature. Cross Correlation (Rohling et al., 1998), Mean Absolute Deviation (MAD) (Aschkenasy et al., 2006), Sum of Squared Differences (SSD) (Ledesma-Carbayo et al., 2001; Ledesma-Carbayo et al., 2005) and Mutual Information (Meyer et al., 1999; Zagrodsky et al., 2000, 2001; Shekhar & Zagrodsky, 2002; Shekhar et al., 2004; Zagrodsky et al., 2005) have been used in the past for the registration of ultrasound and cardiac ultrasound images. Normalised Cross-Correlation (*NXC*) (Lewis, 1995) and Normalised Mutual Information (*NMI*) (Studholme et al., 1999) are the most accurate, robust and commonly used similarity measures for medical datasets. Preliminary in house testing indicated similar performance for both *NXC* and *NMI* on mono-modal, intra-patient cardiac ultrasound data. However, *NXC* was found to be simpler to implement and more efficient than *NMI*.

Optimisation is an iterative procedure in which each step tries to improve the correspondence of the images. A range of different optimisation approaches, such as the Gradient Descent (Ledesma-Carbayo et al., 2005; Aschkenasy et al., 2006), the Powell (Grau et al., 2006, 2007) and the Iterative Closest Point (ICP) (Zhong et al., 2006), have been used for the registration of cardiac ultrasound data. Information on various optimisation approaches can be found in (Press et al., 1992). Gradient-based optimisation approaches, although fast, are

sensitive to errors in gradient calculation and the presence of local maxima. On the other hand, the simulated annealing approach despite its robustness requires excessive time to converge (Shekhar & Zagrodsky, 2002). Nelder and Mead's simplex approach along with the Marquadt Levenbergh approach have been reported to provide a good tradeoff between robustness and convergence time. The Marquadt Levenbergh algorithm performs better for transformations with high degrees of freedom (Ledesma-Carbayo et al., 2001). However, the Nelder-Mead's simplex approach (Nelder & Mead, 1965), due to its simple implementation, is the most commonly used optimisation algorithm for linear transformations (Meyer et al., 1999; Krucker et al., 2000; Zagrodsky et al., 2001; Shekhar & Zagrodsky, 2002).

## 3.4. Data acquisition and manual analysis

Multi-cycle data from 32 patients (18 male, 14 female, ages ranging from 21 to 88 with an average age of 60) were acquired by an experienced echocardiographer in the Echocardiography department of the Western General Hospital, Edinburgh, during January of 2009. For the data acquisition a GE Vivid 7 Dimension ultrasound scanner was used along with a 3MHz phased array probe. B-mode data of 25 cardiac cycles of the Parasternal Long-Axis view were acquired according to the standards adopted by the British Society of Echocardiography (BSE) (Henry et al., 1980; Feigenbaum, 1994). All patient information was removed from the acquired data in order to ensure the anonymity of the participants. (Abiko et al., 1997) suggested that compounding data from 20 consecutive cardiac cycles provides a good trade-off between noise suppression and increase in the cardiac examination duration. This work utilised data from 25 cardiac cycles in order to quantitatively examine the effect of the number of compounded cardiac cycles on image quality. Images were captured at 25 frames per second (fps). Other acquisition parameters such as acquisition depth, focus depth, sector width, gain and Time Gain Compensation (TGC) were optimally set by the echocardiographer independently during each scan. During a multi-cycle data acquisition there can be movements that modify the scan plane with respect to the examined heart structure. Small changes of the scan plane generate partially decorrelated views of the structure that are beneficial to ***Temporal Compounding***. However, large movements can substantially modify the scanning plane possibly resulting in severe blurring of the examined heart structure during the compounding process. For that reason, the echocardiographers and the patients were requested to avoid large movements during the data acquisition process. Finally, B-mode image sequences of 434 x 636 pixels were exported in DICOM format with no compression applied to them. Prior to any processing each dataset was manually labeled as of high (12), average (12) or low (8) image quality and diagnostic value (Figure 3.4).

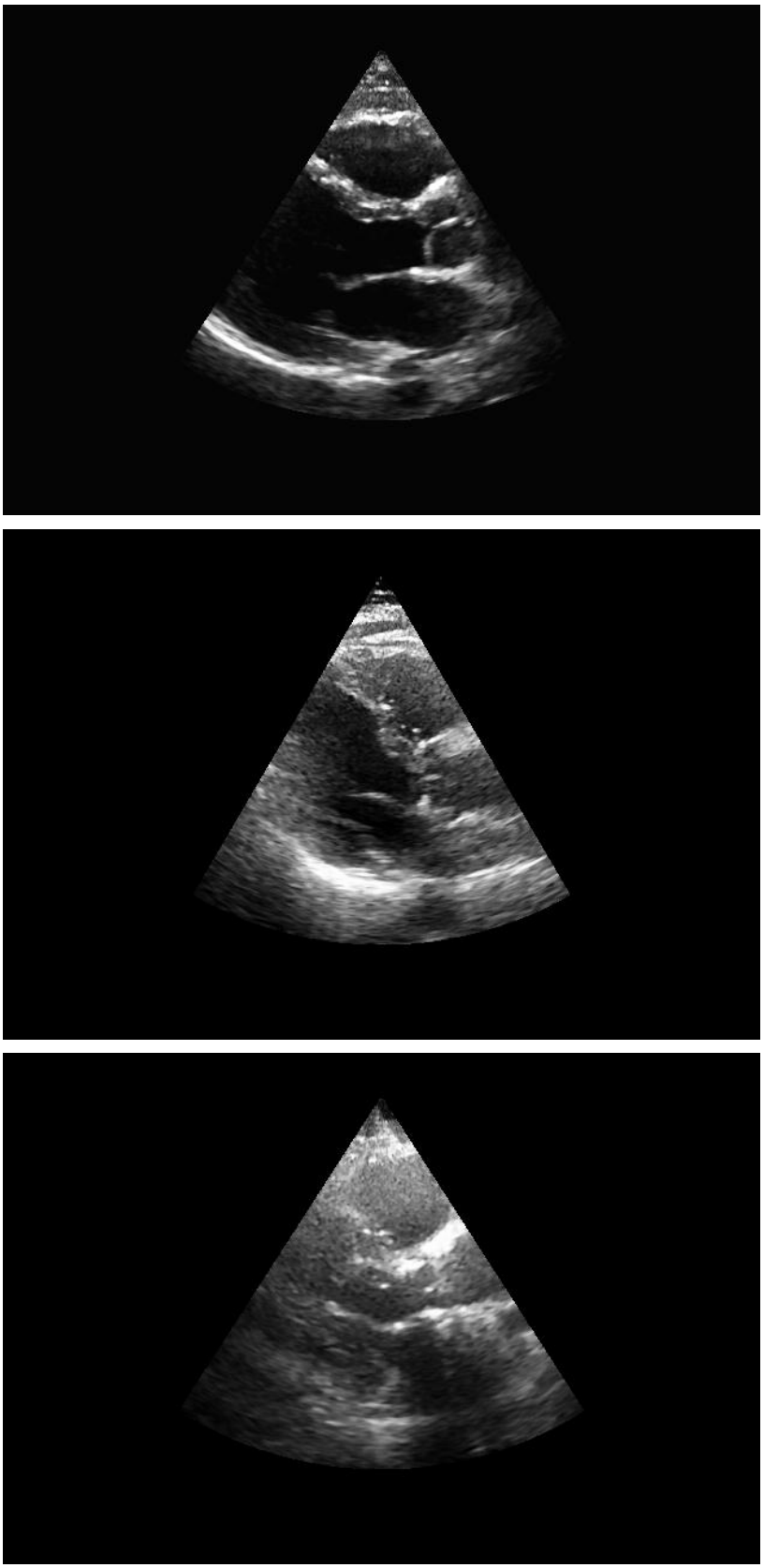

**Figure 3.4.** Examples from the original, unprocessed ED frames of (top) high (patient 12), (middle) average (patient 22) and (bottom) low (patient 6) image quality and diagnostic value.

## 3.5. Data processing

There are 3 steps to ***Temporal Compounding***: (i) the temporal alignment of the multi-cycle data to a reference cardiac cycle, (ii) the spatial alignment of the temporally aligned frames and (iii) the spatial compounding of the spatio-temporally aligned data. Figure 3.5 provides a simple diagram describing the ***Temporal Compounding*** process.

A B-mode cardiac cycle can be described by an ordered sequence of *n* 2D images $S_k(x, y)$ with a fixed field of view $\Omega_{S_k}$ and an acquisition time $t_k$, where $t_k < t_{k+1}$, in the temporal direction. The resulting image sequence can be viewed as 2D+time structure $S(x, y, t)$ defined on the spatio-temporal domain $\Omega_{S_k} \times [t_1, t_n]$. The goal is to derive a transformation $T : (x, y, t) \rightarrow (x', y', t')$, where $(x', y', t') = (x + u, y + v, t + \tau)$, that maps any point in an image sequence $S(x, y, t)$ into its corresponding point in the reference image sequence $S'(x', y', t')$. The mapping *T* used in this study had the form:

$$T(x, y, t) = (x'(x, y), y'(x, y), t'(t)). \qquad [3.1]$$

The proposed mapping form separated the temporal from the spatial alignment of the image sequences. Since the temporal and the spatial domains were different, the mapping was therefore further resolved into decoupled spatial and temporal components respectively:

$$T_{spatial}(x, y) = (x'(x, y), y'(x, y)) \qquad [3.2]$$

and

$$T_{temporal}(t) = t'(t). \qquad [3.3]$$

In this study the temporal transformation component was derived prior to the derivation of the required spatial transformation. A similar spatio-temporal registration approach was proposed by (Caspi & Irani, 2002) for the registration of video sequences . Advantages of the decoupled model include its low computational complexity as well as the ability to easily interchange the type of the temporal and spatial transformations.

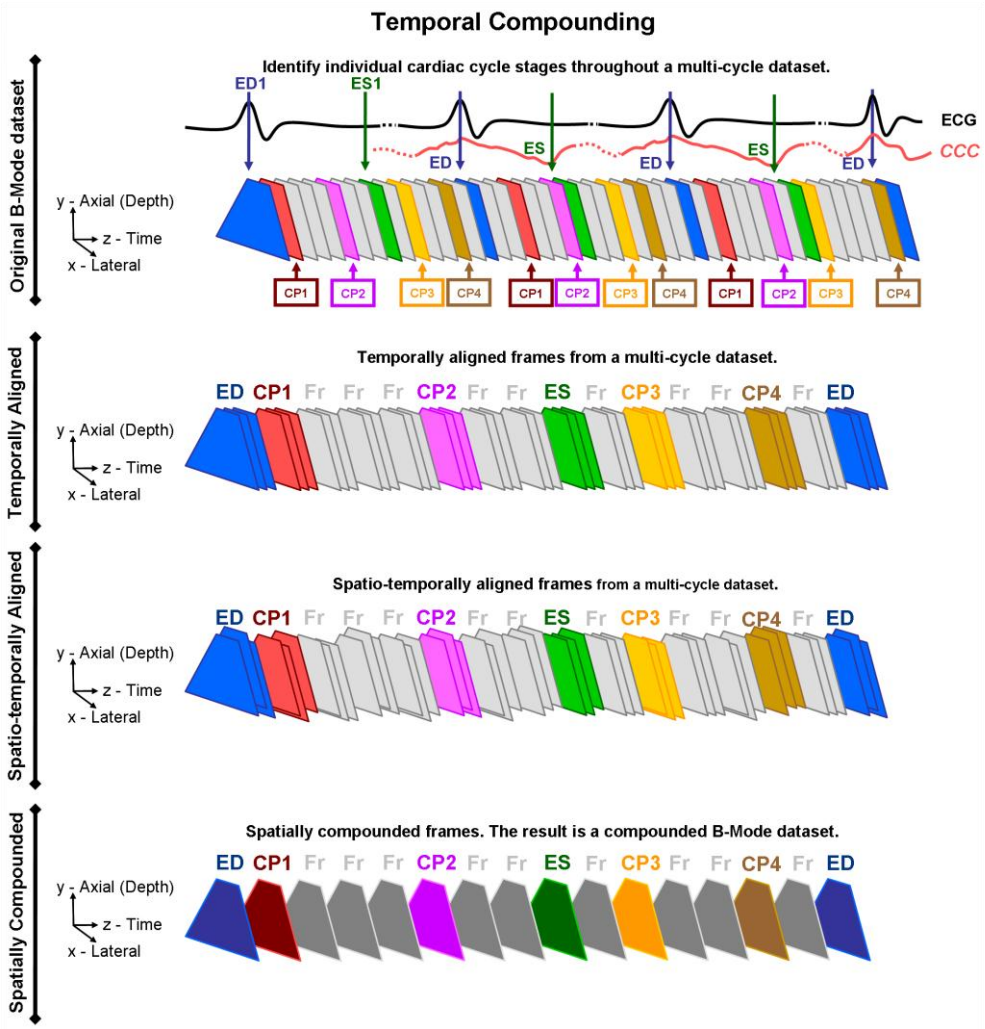


**Figure 3.5.** The *Temporal Compounding* process: (i) the semi-automatic extraction of control points corresponding to individual cardiac cycle stages, (ii) the temporal alignment of the multi-cycle data to a reference cardiac cycle based on the extracted control points, (iii) the spatial alignment of the temporally aligned frames and (iv) the spatial compounding of the spatio-temporally aligned data.

## 3.5.1. Temporal alignment

Temporal alignment was divided into four further steps: (i) the identification of all ED and ES frames within the multi-cycle dataset, (ii) the extraction of a representative reference cardiac cycle for the dataset, (iii) the identification of additional frames as control points for a more accurate temporal alignment and (iv) the temporal mapping between all cardiac cycles to the reference cycle of the dataset.

### 3.5.1.1. Identification of ED and ES frames

This work proposed a semi-automatic approach that identified all ED and ES frames within a multi-cycle dataset utilising exclusively intensity information from the B-mode image

sequence. The method was based on the left ventricular deformation during the cardiac cycle and required the manual identification of one ED (ED1) and one ES (ES1) frame. The similarity between each subsequent frame of a B-mode dataset and the ED1 and ES1 frames was estimated using the normalised cross correlation coefficient (*NXC*) (Lewis, 1995):

$$NXC = \frac{\sum_x \sum_y (S_0(x,y) - \overline{S_0}) \bullet (S_i(x,y) - \overline{S_i})}{\sqrt{\sum_x \sum_y (S_0(x,y) - \overline{S_0})^2} \bullet \sqrt{\sum_x \sum_y (S_i(x,y) - \overline{S_i})^2}} \quad [3.4]$$

where $S_0$ corresponds to ED1 or ES1, $S_i$ is the i-th frame in the sequence and $\overline{S_i}$ its mean intensity.

During systole, due to left ventricular contraction, each consecutive frame appears less similar to ED1 and more similar to ES1. Likewise, during diastole, due to left ventricular relaxation, each consecutive frame seems more similar to ED1 and less similar to ES1. As a result, each end-diastolic frame should demonstrate maximum similarity with ED1 and minimum similarity to ES1. Similarly, each end-systolic frame should demonstrate maximum similarity with ES1 and minimum similarity to ED1. Therefore in theory, a single similarity test between each frame and the manually identified ED should suffice for the identification of all ED and ES frames demonstrating local maxima on end-diastole and local minima on end-systole. However, the high noise levels contained in cardiac ultrasound data necessitated for a more robust approach. Thus, a coefficient combining information on the similarity of each frame with respect to both ED1 and ES1 was defined as:

$$CCC = CED - CES \quad [3.5]$$

where *CED* was the correlation coefficient of a frame with respect to ED1 and *CES* was the correlation coefficient of a frame with respect to ES1. *CCC* stood for Combined Correlation Coefficient and was defined as a simple linear combination of the two individual correlation coefficients. *CCC* is expected to demonstrate stronger local maxima on all ED frames as well as stronger local minima on all ES frames when compared to the individual *NXC* profiles.

#### 3.5.1.2. Extraction of a representative reference cardiac cycle

The identified ED and ES frames were utilised to define each cardiac cycle (as an ED1 – ES – ED2 sequence) within each multi-cycle dataset. They were also utilised in order to extract a reference cardiac cycle, representative for the whole dataset. All remaining cardiac cycles would then be temporally and spatially registered to the reference cardiac cycle prior to the final spatial compounding being applied on their corresponding frames. For the extraction of

a representative reference cardiac cycle, a weighting factor $W_i$ was defined for each cardiac cycle:

$$W_i = | DL_i - \overline{DL} | + | SL_i - \overline{SL} | \quad [3.6]$$

where $DL_i$ and $SL_i$ represented the current cardiac cycle's diastole and systole lengths respectively, while $\overline{DL}$ and $\overline{SL}$ represented the mean diastole and systole lengths respectively over the whole multi-cycle dataset. Systole and diastole lengths were expressed in number of frames. The cardiac cycle with the lowest weighting factor was considered as the most representative within the multi-cycle dataset and was therefore selected as the reference cardiac cycle.

#### 3.5.1.3. Identification of additional control points

Having identified the ED and ES frames defining all cardiac cycles as well as having extracted a reference cardiac cycle within a multi-cycle dataset, additional frames corresponding to different stages of a cardiac cycle were then identified. The additional frames acted as extra control points (CPs) during the temporal interpolation process resulting in a more representative and accurate alignment. Such frames were initially introduced at regular temporal intervals in the contraction (systole) and relaxation (diastole) phases of the reference cardiac cycle. One additional frame was introduced in each phase for the 5 stage cardiac cycle representation (*ED1 – CP – ES – CP2 – ED2*). Similarly, 2 additional frames were introduced in each phase for the 7 stage cardiac cycle representation (*ED1 – CP1 – CP2 – ES – CP3 – CP4 – ED2*). Defining 7 independent stages (CPs) within a cardiac cycle is considered to provide a fair representation of both the global as well as the local temporal variations of the 7 individual cardiac cycle phases. Normalised Cross Correlation (Equation 3.4) was then used in order to identify frames within the remaining cardiac cycles on the multi-cycle dataset corresponding to the additional CPs introduced on the reference cardiac cycle. The systole or diastole phases of each cardiac cycle within the multi-cycle dataset were used as search domains. For every cardiac cycle individually, the *NXC* between each of the additional CPs in the reference cardiac cycle and each frame in the corresponding search domain was derived. Frames corresponding to the additional cardiac stages would induce a global maximum in the *NXC*. Appropriate constraints were utilised in order to avoid the temporal interchange between CPs. In cases where high levels of noise or shadowing obstructed the derivation of a clear local maximum throughout the search, the corresponding cardiac cycle was omitted during the temporal mapping and spatial compounding stages.

### 3.5.1.4. Interpolation process

The final stage of the temporal alignment between two frame sequences (cardiac cycles) aims to generate a transformation function $T_{temporal}:(t)\rightarrow(t')$ establishing a correspondence between time $t$ in the aligned frame sequence and time $t'$ in the reference frame sequence. This process is referred to as temporal interpolation. As mentioned in Section 3.2, cardiac temporal variations can be global such as differences in cardiac cycle lengths, as well as local such as differences in the dynamic properties of the seven individual cardiac cycle phases. Both global and local temporal variations were addressed by decoupling the transformation $T_{temporal}$ into independent global, $T_{temporal}^{global}$, and local, $T_{temporal}^{local}$, components:

$$T_{temporal}(t)=T_{temporal}^{global}(t)+T_{temporal}^{local}(t) \qquad [3.7]$$

The global component of the transformation, $T_{temporal}^{global}$, was represented by an affine transformation of the following form:

$$T_{temporal}^{global}(t)=\alpha t+\beta\,. \qquad [3.8]$$

where $\alpha$ compensated for scaling differences between the two frame sequences (different cardiac cycle lengths) while $\beta$ compensated for translation differences, aligning the start of the two frames sequences. On the other hand, the representation of the local component of the transformation, $T_{temporal}^{local}$, depended on the number of identified frames representing different cardiac cycle stages. The temporal arrangement of such frames indicated the temporal properties of a cardiac cycle and acted as control points (*CP*s) during the temporal interpolation process. Using $[CP_1:CP_n]$ to define the aligned cardiac cycle and $[CP'_1:CP'_n]$ the reference cardiac cycle, $T_{temporal}^{local}$was initially modeled by a piecewise linear transformation:

$$T_{temporal}^{local}(t)=\begin{cases} g_1(t), & \text{if } CP_1<t<CP_2;\\ \ldots & \\ g_i(t), & \text{if } CP_i<t<CP_{i+1};\\ \ldots & \\ g_{n-1}(t), & \text{if } CP_{n-1}<t<CP_n \end{cases} \qquad [3.9]$$

where $n=\{2,3,5,7\}$ and $g_i(t)=\alpha t+\beta$ with:

$$\alpha = \frac{(CP_{i+1} - CP_i)}{(CP'_{i+1} - CP'_i)} \qquad [3.10]$$

and

$$\beta = CP'_i - CP_i . \qquad [3.11]$$

Similarly, for cardiac cycles defined by 5 or 7 individual stages (i.e. $n = \{5, 7\}$) $T_{temporal}^{local}$ was also modeled using a *1D relaxed uniform interpolating cubic B-Spline* curve (Barsky, 1982; Caglar et al., 2006). Given a set of control point pairs $P_1$ to $P_n$, where $P_i = [CP'_i, CP_i]$, a set of control points $S_i$ were derived defining a B-Spline curve interpolating through $P_i$ to $P_n$ (Baker, 2002; Caglar et al., 2006):

$$\begin{pmatrix} 4 & 1 & 0 & 0 & 0 \\ 1 & 4 & 1 & 0 & 0 \\ 0 & 1 & 4 & 1 & 0 \\ & 0 & \ldots & & 1 \\ & & & & 4 \end{pmatrix} \times \begin{pmatrix} S_2 \\ S_3 \\ S_4 \\ \ldots \\ S_{n-1} \end{pmatrix} = \begin{pmatrix} 6P_2 - P_1 \\ 6P_3 \\ 6P_4 \\ \ldots \\ 6P_{n-1} - P_n \end{pmatrix} \qquad [3.12]$$

with $S_1 = P_1$ and $S_n = P_n$ representing the start and end points. $T_{temporal}^{local}$ was then modeled as a series of uniform cubic B-Spline segments (Barsky, 1982):

$$T_{temporal}^{local} = \sum_{l=0}^{3} B_l(u) S_{i+l} \qquad [3.13]$$

where $i = \{1,1,1,2,3,\ldots,n,n,n\}$, $u \in \{0,\ldots,1\}$, $S_i$ represented the *i-th* control point and $B_l$ represented the *l-th* basis function of the B-Spline curve (Figure 3.6):

$$\begin{aligned} B_0(u) &= (1-u)^3/6 \\ B_1(u) &= (3u^3 - 6u^2 + 4)/6 \\ B_2(u) &= (-3u^3 + 3u^2 + 3u + 1)/6 \\ B_3(u) &= u^3/6 . \end{aligned} \qquad [3.14]$$

Multiple instances of the first and last control points were used so the curve interpolated through control points $P_1$ and $P_n$.

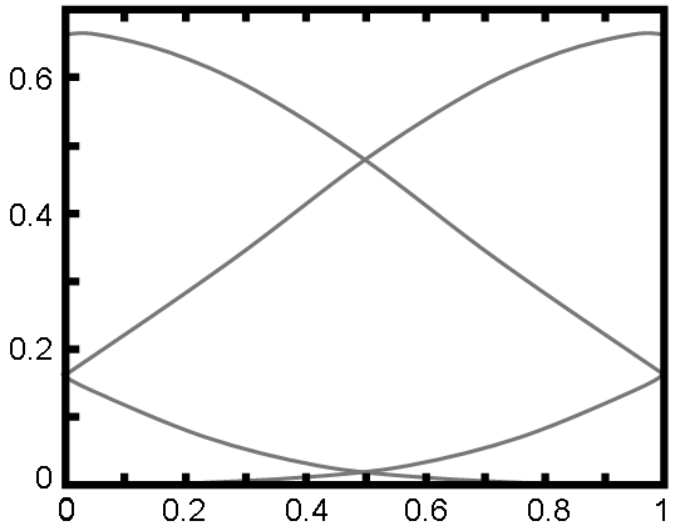


**Figure 3.6.** Graphical representation of B-Splines.

Temporal interpolation $T_{tenporal}(t)$ was applied between the reference cardiac cycle and all the remaining cardiac cycles within a multi-cycle B-mode frame sequence (Figure 3.7). Nearest neighbour interpolation on the transformation curve was used to allocate corresponding frames to each frame within the reference cardiac cycle. Appropriate constraints were utilised in order to ensure a monotonically increasing temporal mapping.

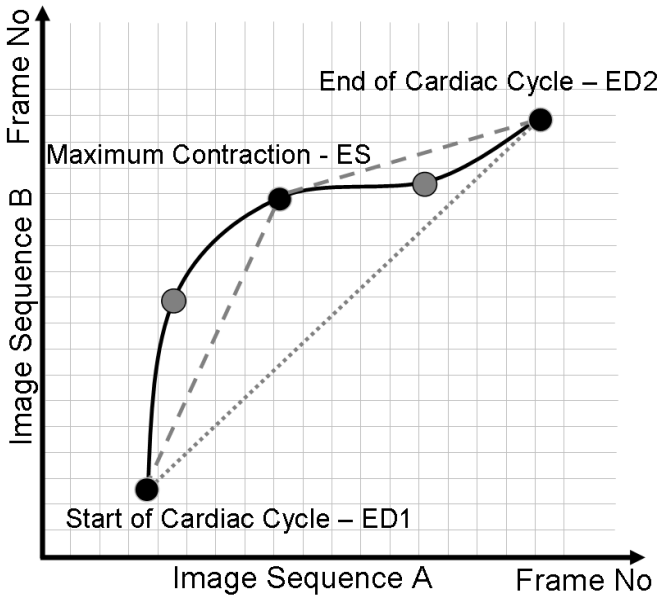


**Figure 3.7.** Temporal mappings between 2 frame sequences using: (i) global linear interpolation (dotted line), (ii) piecewise linear interpolation based on 3 cardiac cycle stages (dashed line) and (iii) B-Spline interpolation based on 5 cardiac cycle stages. Differences between individual interpolation methods are visually apparent.

### 3.5.2. Spatial alignment

The last step prior to the spatial compounding of the data was the automatic spatial registration of the temporally aligned frames. Image registration searched for an optimal mapping, $T$ relating each point of an image $I$ to the corresponding anatomical point in the reference image $I'$. By defining both images as two arrays of a given size denoted by $I$ and $I'$, then the mapping between was expressed as (Brown, 1992):

$$I'(p) = g(I(T(p)) \qquad [3.15]$$

where $p = (x, y)$ was a vector representing the point's location, $I(p)$ and $I'(p)$ denoted the image intensities at position $p$, $g$ was the intensity transformation and $T$ was the coordinate transformation. The spatial domain of the images was denoted as $\Omega_s = \{(x, y) \mid 0 < x < X, 0 < y < Y\}$. A rigid body transformation was utilised for the spatial registration of the temporal aligned frames:

$$T_{spatial}(x, y) = T_{rigid}(x, y). \qquad [3.16]$$

Rigid transformation $T_{rigid}(x, y)$ consisted of rotation and translation components:

$$T_{translation}(x, y) = \begin{pmatrix} x' & y' & 1 \end{pmatrix} = \begin{pmatrix} x & y & 1 \end{pmatrix} \begin{pmatrix} 1 & 0 & 0 \\ 0 & 1 & 0 \\ t_x & t_y & 1 \end{pmatrix} \qquad [3.17]$$

$$T_{rotation}(x, y) = \begin{pmatrix} x' & y' & 1 \end{pmatrix} = \begin{pmatrix} x & y & 1 \end{pmatrix} \begin{pmatrix} \cos(\theta) & \sin(\theta) & 0 \\ -\sin(\theta) & \cos(\theta) & 0 \\ 1 & 1 & 1 \end{pmatrix} \qquad [3.18]$$

where $t_x$ and $t_y$ were the translation parameters along the $x$ an $y$ axes and $\theta$ represented the rotation angle. Both components were combined in a single rigid transformation with three *degrees of freedom*:

$$T_{rigid}(x, y) = \begin{pmatrix} x' & y' & 1 \end{pmatrix} = \begin{pmatrix} x & y & 1 \end{pmatrix} \begin{pmatrix} \cos(\theta) & \sin(\theta) & 0 \\ -\sin(\theta) & \cos(\theta) & 0 \\ t_x & t_y & 1 \end{pmatrix}. \qquad [3.19]$$

Bilinear interpolation was applied during the image transformation process since it has been found to provide the best trade-off between accuracy and computational complexity (Zitova & Flusser, 2003).

An intrinsic registration method utilising intensity similarity information extracted from the patient datasets was employed for the spatial registration of the temporal aligned frames. Furthermore, Nelder-Mead's simplex optimisation method strategy was utilised in order to derive optimal transformation, $T$, which maximised the *NXC* between the registered images:

$$\arg\max_{t_x,t_y,\theta} NXC(I', T(I)). \qquad [3.20]$$

The Nelder-Mead's optimisation method constructed a simplex in the *N*-dimensional parameter space (degrees of freedom) from *N*+1 trial points. In two-space a simplex is a triangle; in three-space it is a pyramid. At the beginning, the algorithm generated an initial simplex. In every step of the iterative process, the point of the simplex with the lowest *NXC* was replaced by a new vertex, inside or near the current simplex, demonstrating higher *NXC*. During optimisation the vertices of the pyramid converged toward the solution (maximisation of *NXC*) while the pyramid shrank in size to a level less than a specified threshold. Listing 3.1 provides a pseudocode implementation of the simplex method as described by (Lagarias et al., 1998). Initial simplex $x_0$ comprised of transformation parameters $[t_x, t_y, \theta] = [1,1,1]$ along with the fourth vertex of the simplex derived by adding 5% from each of the other three components of $x_0$.

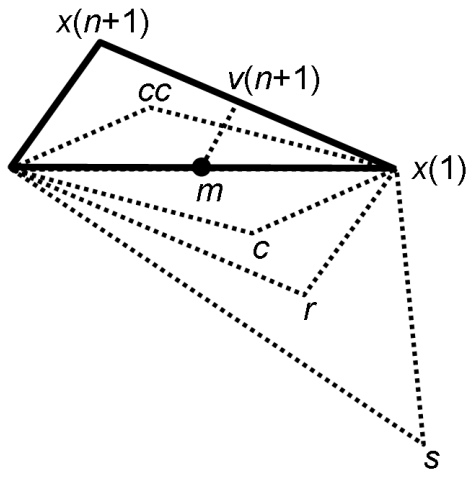


**Figure 3.8.** Points that the Nedler-Mead algorithm may calculate during the procedure along with each possible new simplex [adapted from (Lagarias et al., 1998)].

**Listing 3.1:** Nelder-Mead's Simplex optimisation algorithm.

Let *x(i)* denote the list of points in the current simplex, $i = 1,...,n+1$ while *f(x)* denotes the *NXC* between the two registered images for the transformation represented by simplex *x*.

**Repeat:**

1. Order the points in the simplex from highest function value $f(x(1))$ to lowest $f(x(n+1))$.
2. Generate the reflected point

   $r = 2m - x(n+1)$, where $m = \Sigma x(i)/n$, $i = 1...n$, and calculate $f(r)$.
3. If $f(x(1)) \geq f(r) > f(x(n))$: **Reflect**

   replace $x(n+1)$ of the simplex with $r$ and terminate this iteration.
4. If $f(r) > f(x(1))$,

   calculate the expansion point $s = m + 2(m - x(n+1))$ as well as $f(s)$.

   If $f(s) > f(r)$: **Expand**

   replace $x(n+1)$ of the simplex with $s$ and terminate the iteration.

   Otherwise: **Reflect**

   replace $x(n+1)$ of the simplex with $r$ and terminate the iteration.
5. If $f(r) \leq f(x(n))$,

   perform a contraction between $m$ and the better of $x(n+1)$ and $r$:

   If $f(r) > f(x(n+1))$, calculate

   calculate $c = m + (r - m)/2$ as well as $f(c)$.

   If $f(c) > f(r)$: **Contract outside**

   replace $x(n+1)$ of the simplex with $c$ and terminate the iteration.

   Otherwise

   continue with Step 6 (Shrink).

   If $f(r) \leq f(x(n+1))$,

   calculate $cc = m + (x(n+1) - m)/2$ as well as $f(cc)$.

   If $f(cc) > f(x(n+1))$: **Contract inside**

   replace $x(n+1)$ of the simplex with $cc$ and terminate the iteration.

   Otherwise,

   continue with Step 6 (Shrink).
6. Calculate the n points

   $v(i) = x(1) + (x(i) - x(1))/2$ as well as $f(v(i))$, $i = 2,...,n+1$.

   Simplex at next iteration is $x(1)$, $v(2),...,v(n+1)$. **Shrink**

**Until the diameter of the simplex is less than the specified tolerance.**

### 3.5.3. Spatial compounding

Each frame $I$ within the reference cardiac cycle was finally replaced by a compounded frame $I'$ generated from the spatio-temporally aligned images, one from each cardiac cycle (Figure 3.5). The mean (*M*) as well as the standard deviation (*SD*) in the similarity (*NXC*) between the reference frame and all the corresponding spatio-temporally aligned frames was derived. Frames with *NXC* outside the $M \pm SD$ region were discarded in order to avoid the compounding of dissimilar frames resulting in tissue/cavity boundary blurring. Intensity averaging was utilised as the spatial compounding method since it is a well established and effective method for noise suppression in ultrasound datasets. The intensity of each pixel within a compounded frame was therefore set to the average intensity of the corresponding pixels from all the spatio-temporally aligned data (Figure 3.9):

$$I'(x,y,t) = \frac{1}{N}\sum_{i=1}^{N} I(x,y,t_i) \qquad [3.21]$$

where $N$ was the number of cardiac cycles utilised in ***Temporal Compounding*** and $I(x,y,t_i)$ represented the corresponding spatio-temporally aligned frame on the *i*th cardiac cycle of the multi-cycle dataset.

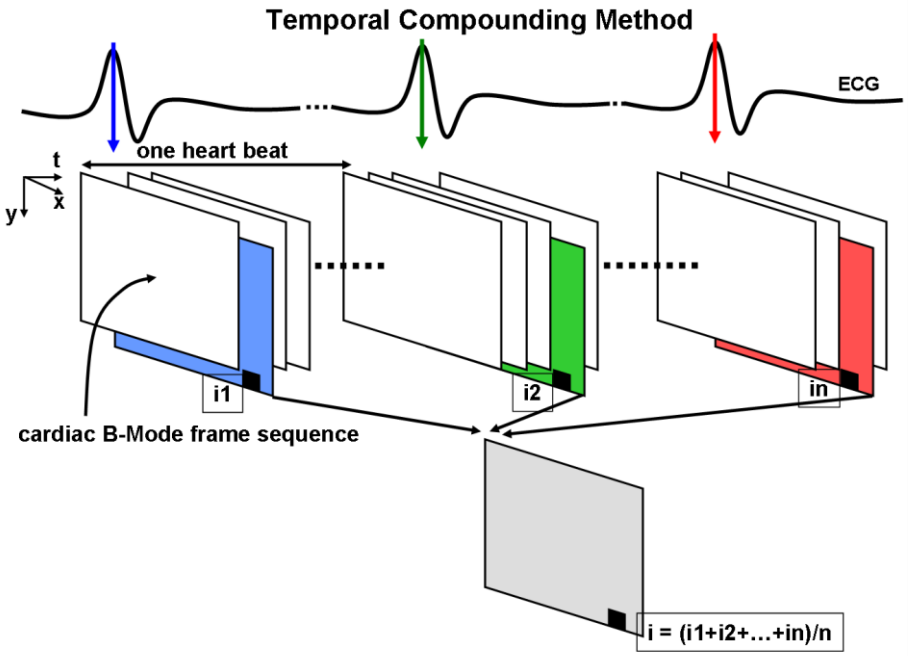


**Figure 3.9.** ***Temporal Compounding*****:** Intensity averaging of temporally aligned frames from consecutive cardiac cycles.

## 3.6. Clinical measurements

Two experienced echocardiographers were asked to perform routine clinical measurements on ED and ES frames from both the original unprocessed as well as the temporally compounded data. A sequence of ED frames was presented and the (i) Interventricular Septal Thickness (IVSd), (ii) Left Ventricular Internal Dimension (LVIDd) and (iii) Left Ventricular Posterior Wall (LVPWd) measurements were performed on each frame. Similarly, a sequence of ES frames was presented and the (i) Left Ventricular Internal Dimension (LVIDs) and (ii) Left Atrium Dimension (LADs) measurements were performed on each frame. Each frame sequence contained one original and one averaged frame for each of the datasets (64 frames in total). The order of the frames was randomised to ensure no bias in the results. The echocardiographers had the ability to abstain from a clinical measurement if they considered there were no sufficient visual cues for the accurate measurement of the structure in the displayed image. All clinical measurements were performed twice, according to the standards adopted by the BSE (Henry et al., 1980; Feigenbaum, 1994; Fuster et al., 2008), to enable the examination of measurement agreement and repeatability (Bland & Altman, 1986).

All measurements were selected as widely used during routine clinical cardiac ultrasound examinations providing valuable information on the state and function of the examined heart. IVSd measures the thickness of the common wall between the Right Ventricle (RV) and the Left Ventricle (LV). IVS is expected to have a similar thickness to the LVPW. However, enlarged IVS and LVPW, in an equal and uniform manner, indicate abnormal septum functionality commonly referred to as septal hypertrophy. Asymmetric Septal Hypertrophy (ASH) can be diagnosed from a disproportional enlarged IVS against the LVPW. Moreover, a thin, atrophic IVS may indicate ischemic heart disease, fibrosis and scarring of the IVS. The LVID measures the distance between the left side of the IVS and the posterior left ventricular endocardium. There is a good correlation between the LVID and the LV volume. Measuring the LVID at ED and ES enables the derivation of end-diastolic and end-systolic LV volumes as well as the heart stroke volume. The LVPW measures the thickness between the endocardial and epicardial echoes of the posterior left ventricular wall. LVPW can be utilised along with the LVID to derive the left ventricular mass. Similarly, the thickness of the LVPW and its relation with the IVS can be an indicator of cardiac hypertrophy and asymmetric cardiac hypertrophy. Finally, the LAD measures the distance between the atrial side of the posterior aortic wall and the anterior surface of the posterior left atrial echo at the level of the aortic valve leaflets. The LAD reaches its maximum value during end-systole

and, in normal subjects, it is comparable to the diameter of the aortic root. Enlargement of the LAD compared to the aortic diameter indicates left atrium dilation. Moreover, the LAD measurement provides important information for patients with mitral valve disease as well as for patients with chronic LV failure. More information and resources on clinical measurements performed in cardiac ultrasounds examinations can be found in (Feigenbaum, 1976).

## 3.7. Data analysis and results

A range of quantitative and qualitative results are presented in order to assess the effect of ***Temporal Compounding*** on cardiac ultrasound data. The main objective is to identify optimal parameters that will ensure the clinical feasibility of ***Temporal Compounding*** by achieving adequate noise suppression while (i) maintaining tissue/cavity boundary blurring to a clinically acceptable level and (ii) keeping data acquisition time and processing requirements to a minimum by limiting the number of compounded cardiac cycles.

### 3.7.1. Temporal alignment

The principal steps during the temporal alignment process are (i) the identification of ED and ES frames and (ii) the temporal interpolation of each individual cardiac cycle in the multi-cycle dataset to a representative reference cardiac cycle. The accuracy and robustness with which these two steps are executed have a direct effect on the effectiveness of the temporal alignment and as a result the ***Temporal Compounding*** process.

#### 3.7.1.1. Identification of ED and ES frames

All 25 ED and ES frames in each multi-cycle dataset were manually identified. Four cues were employed in the identification process: (i) the opening and closing of the Mitral Valve, (ii) the periodic motion of the Left Ventricle (LV) cavity, (iii) the periodic motion of the Right Ventricle (RV) cavity and (iv) the QRS complex on the available ECG signal. Due to high levels of noise and shadowing, no single cue was robust enough to identify the ED and ES on all datasets. In order to assess intra-operator variability, the manual ED and ES detection was repeated 3 times for each dataset. The value with the most common occurrence was selected as the representative reference ED or ES frame for each cardiac cycle. In cases where all three manual identifications were distinct, their mean value was selected as the corresponding reference ED or ES frame. Due to the absence of a gold standard method for deriving accurate ED and ES frames, the reference ED and ES frame sequences were considered as the benchmark for the subsequent algorithm evaluation.

Tables 3.1 and 3.2 illustrate the relationship between the reference ED and ES frames and the corresponding manually as well as automatically identified ED and ES frames. For each of the 32 individual patient datasets, the frame difference between each reference ED frame and the corresponding manually and automatically identified ED frame were calculated. Similarly, the frame difference between each reference ES frame and the corresponding manually and automatically identified ES frame were calculated. The percentage of the identified ED and ES frames that lie within 0, 1, 2 or greater number of frames with respect to the corresponding reference ED and ES frames were also derived. Tables 3.1 and 3.2 also list the maximum, minimum, mean and standard deviation of the derived percentages amongst the 32 patient datasets. Furthermore, for each dataset, the linear regression between the reference and the corresponding manually and automatically identified ED and ES frames was estimated. The Root Mean Square Error (RMSE) values for the derived linear regressions are also listed. The correlation coefficient $R^2$ (for all linear regressions) was estimated to be approximately equal to 1 ($R^2$>=0.9997) and it was therefore omitted from both tables. Finally, the plots in Figure 3.10 display the similarity of each frame within a multi-cycle dataset to a pair of reference ED and ES frames. The three plots illustrate the difference between the use of *NXC* and *CCC* as a similarity measure for the automatic identification of ED and ES frames within a multi-cycle dataset.

**Table 3.1.** Variations (in number of frames) amongst the manual and automatic ED frames identification over the 32 patient datasets.

| | **Manual** | | | | | **Automatic** | | | | |
|---|---|---|---|---|---|---|---|---|---|---|
| **Dataset** | **0** | **≤1** | **≤2** | **≥3** | **RMSE** | **0** | **≤1** | **≤2** | **≥3** | **RMSE** |
| **Mean** | 81.5% | 98.8% | 99.6% | 0.4% | 0.37 | 66.1% | 90.1% | 95.8% | 4.2% | 0.95 |
| **SD** | 14.9% | 3.6% | 1.2% | 1.2% | 0.18 | 20.4% | 12.9% | 8.5% | 8.5% | 0.77 |
| **Min** | 40.0% | 84.0% | 96.0% | 0.0% | 0.00 | 24.0% | 52.0% | 68.0% | 0.0% | 0.20 |
| **Max** | 100% | 100% | 100% | 4.0% | 0.82 | 96.0 | 100% | 100% | 32.0% | 3.44 |

**Table 3.2.** Variations (in number of frames) amongst the manual and automatic ES frames identification over the 32 patient datasets.

| | **Manual** | | | | | **Automatic** | | | | |
|---|---|---|---|---|---|---|---|---|---|---|
| **Dataset** | **0** | **≤1** | **≤2** | **≥3** | **RMSE** | **0** | **≤1** | **≤2** | **≥3** | **RMSE** |
| **Mean** | 53.9% | 93.1% | 99.0% | 1.0% | 0.58 | 42.8% | 85.0% | 97.1% | 2.9% | 0.97 |
| **SD** | 17.7% | 13.9% | 2.3% | 2.3% | 0.17 | 17.3% | 15.2% | 5.9% | 5.9% | 0.52 |
| **Min** | 4.0% | 40.0% | 92.0% | 0.0% | 0.34 | 8.0% | 36.0% | 76.0% | 0.0% | 0.51 |
| **Max** | 88.0% | 100% | 100% | 8.0% | 1.21 | 72.0% | 100% | 100% | 24.0% | 2.87 |

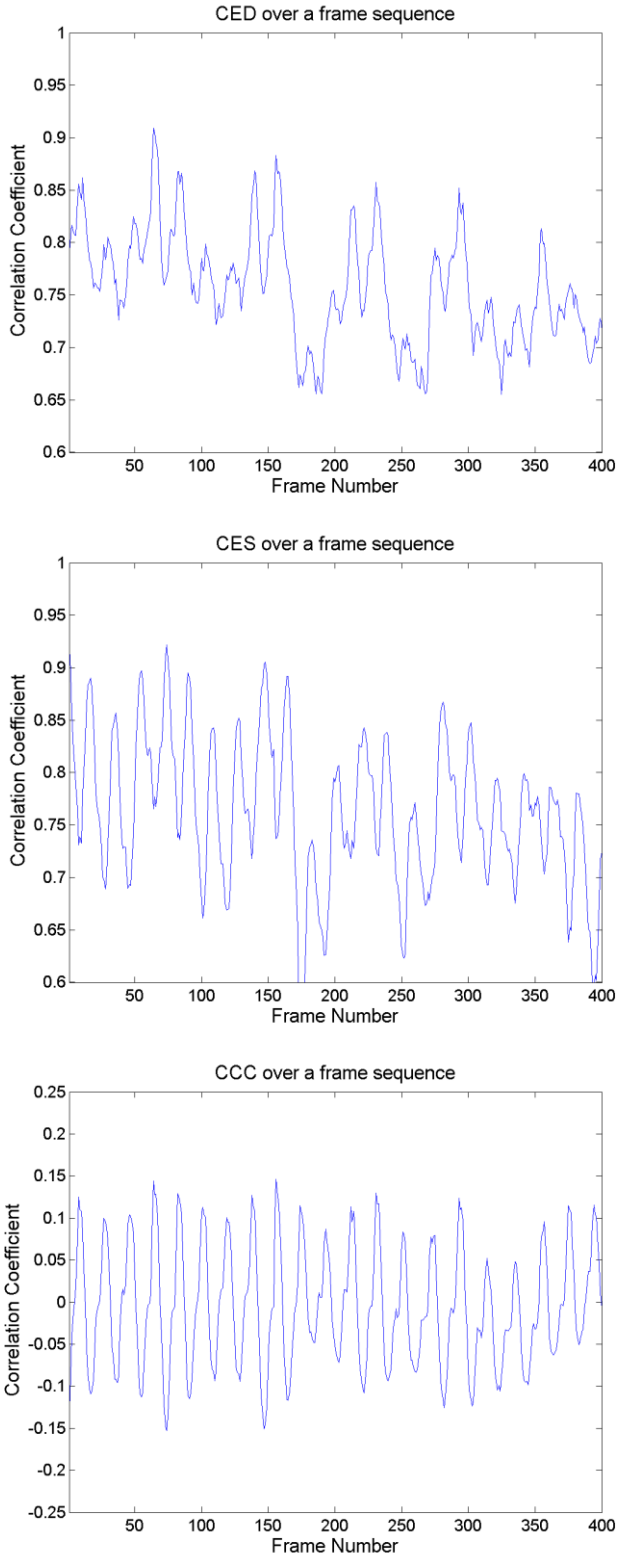


**Figure 3.10.** Example profiles of the Correlation Coefficient between each frame and a manually identified (top) ED frame (*CED)*, (middle) ES frame (*CES)*. (bottom) The Combined Correlation Coefficient (*CCC*) between each frame and both manually identified ED and ES frames. *CCC* provides stronger local maxima and minima indicating ED and ES frames within an image sequence.

#### 3.7.1.2. Temporal interpolation

Figure 3.11 displays curves representing the temporal alignment of four individual cardiac cycles to the reference cardiac cycle for an example patient dataset. Each plot contains curves for each of the 6 proposed temporal interpolation methods (Section 3.5.1.4). As discussed in Section 3.3.1, the use of 7 independent stages as control points for the temporal interpolation is considered to provide a good representation of both the global as well as the local temporal variations of a cardiac cycle (i.e. roughly a frame for each cardiac phase). In addition, the continuous B-Spline interpolation is considered to provide a more realistic representation of the cardiac temporal characteristics than the corresponding linear interpolation. Therefore, due to the absence of a gold standard temporal interpolation method, the 7 point B-Spline interpolation is considered as the benchmark for the subsequent algorithm evaluation.

Table 3.3 illustrates the differences between the 7 point linear interpolation and the corresponding 2, 3 and 5 point interpolations. For each of the 32 individual patient datasets, the frame difference between each temporally aligned frame and the corresponding 7 point temporally aligned frame were calculated. The percentage of the aligned frames that lie within 0, 1, 2 or greater number of frames with respect to the corresponding 7 point temporally aligned frames were also derived. Table 3.3 lists the mean and the standard deviation of the derived percentages amongst the 32 patient datasets. It also indicates the maximum difference in number of frames observed using each of the optional interpolation methods. Similarly, Table 3.4 illustrates the difference between the 5 and 7 control point linear interpolation methods against the corresponding B-Spline interpolations methods. Finally, Figure 3.12 displays four plots illustrating the variations in the temporal alignment between each cardiac cycle and the reference cardiac cycle within four example patient datasets. B-Spline interpolation using 7 control points was utilised to derive each curve. Similar plots can be derived using all other available interpolation options proposed in Section 3.5.1.4.

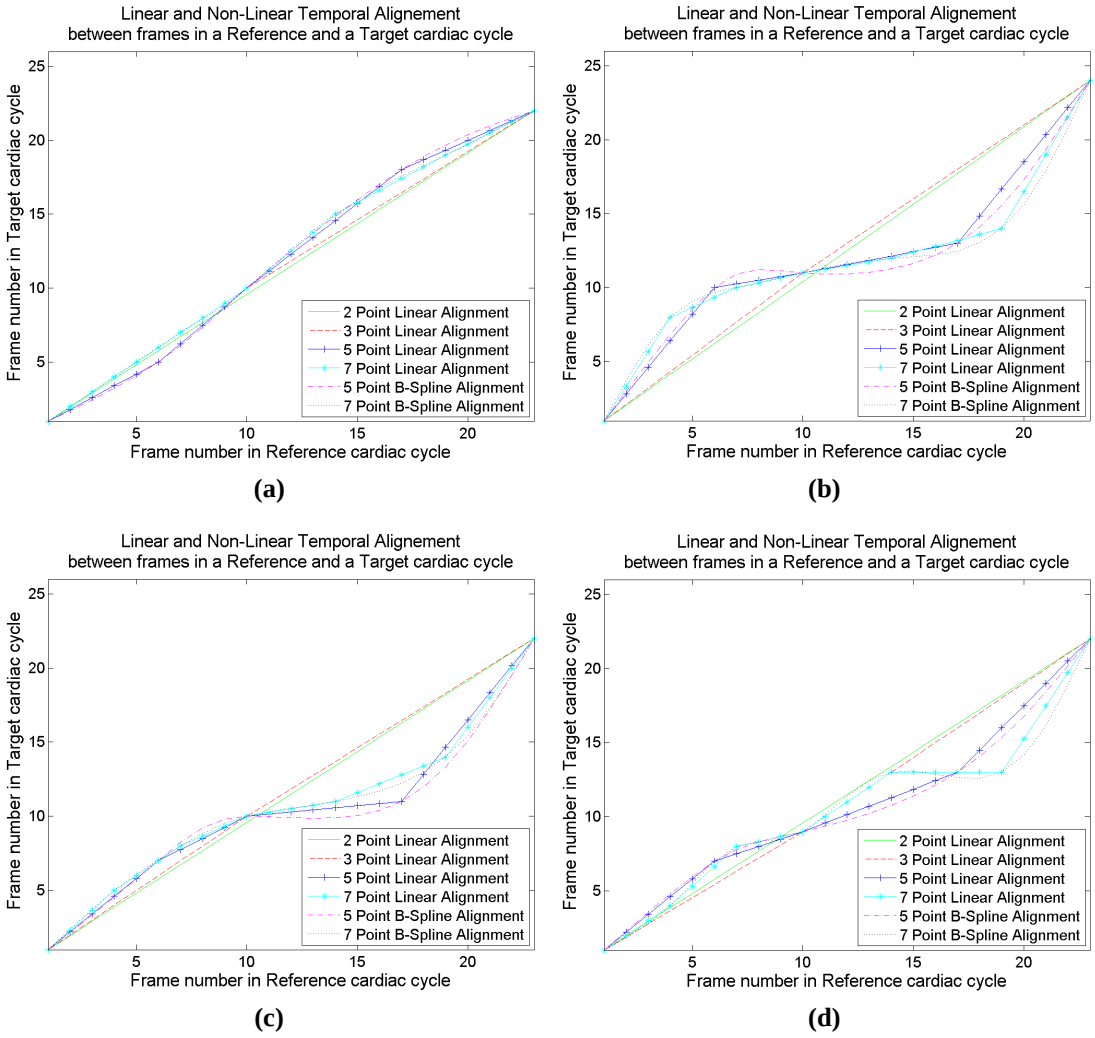


**Figure 3.11.** The temporal alignment of four individual cardiac cycles to the reference cardiac cycle for an example patient dataset (Patient 5). Each plot contains curves for each of the 6 proposed temporal interpolation methods.

**Table 3.3.** Differences (in number of frames) amongst the 7 point linear interpolation and the corresponding 2, 3 and 5 point interpolations over the 32 patient datasets.

| **Frame** | **2 Lin VS 7 Lin** | | **3 Lin VS 7 Lin** | | **5 Lin VS 7 Lin** | |
|---|---|---|---|---|---|---|
| **Difference** | **Mean** | **SD** | **Mean** | **SD** | **Mean** | **SD** |
| **0** | 49.5% | 12.0% | 57.3% | 11.4% | 62.9% | 12.8% |
| **1** | 33.5% | 5.7% | 29.8% | 4.6% | 27.7% | 6.3% |
| **2** | 10.3% | 5.8% | 7.9% | 4.9% | 5.2% | 4.5% |
| **≥3** | 6.8% | 8.8% | 5.0% | 7.3% | 3.1% | 5.2% |
| **Max** | **11** | | **9** | | **9** | |

**Table 3.4.** Differences (in number of frames) amongst the linear interpolation and the corresponding B-Spline interpolations over the 32 patient datasets.

| Frame | 5 Lin VS 5 BS | | 7 Lin VS 7 BS | |
|---|---|---|---|---|
| **Difference** | **Mean** | **SD** | **Mean** | **SD** |
| **0** | 87.8% | 7.6% | 89.4% | 7.5% |
| **1** | 12.0% | 7.2% | 10.5% | 6.9% |
| **2** | 0.2% | 0.5% | 0.1% | 0.2% |
| **≥3** | 0.0% | 0.0% | 0.0% | 0.0% |
| **Max** | **3** | | **2** | |

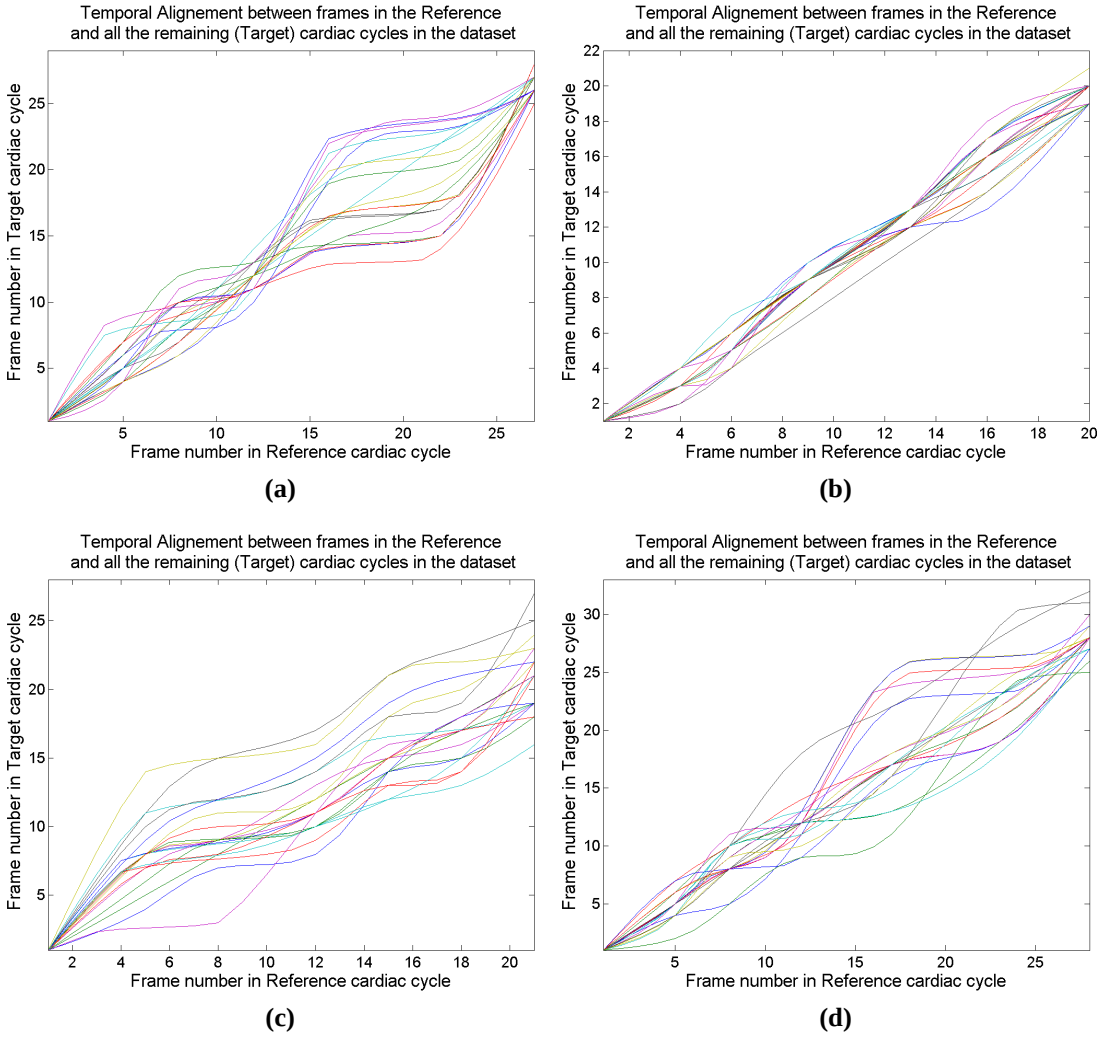


**Figure 3.12.** Variations in the temporal alignment between each cardiac cycle and the reference cardiac cycle in 4 example patient datasets: (a) Patient 6, (b) Patient 10, (c) Patient 23 and (d) Patient 20. 7 control point B-Spline interpolation was used to derive each curve.

### 3.7.2. Temporal compounding

The effect of the number of averaged cardiac cycles utilised during ***Temporal Compounding*** on cardiac tissue and cavity structures is investigated by examining the changes induced on quantitative measurements such as SNR contrast and detectability index (SDNR). On the other hand, the effect on blurring between tissue and cavity boundaries is not examined directly since outlining LV cavity on real human datasets is not only a laborious but a highly subjective and many times erroneous process. Instead, the effect of ***Temporal Compounding*** on tissue boundaries is investigated by performing routine clinical measurements of tissue structures and cavities (Section 3.6) on the original and the processed databases. The quantitative analysis of such clinical measurements provides sufficient and relevant information indicating whether the boundary blurring introduced has a clinically limiting effect on the compounded datasets.

#### 3.7.2.1. Effect on tissue SNR, cavity SNR, tissue/cavity contrast and SDNR

A range of compounded images were generated using ***Temporal Compounding*** on frame sequences of an increasing number of cardiac cycles. Two 11x11 pixels square ROIs corresponding to the IVS and the RV cavity were manually defined on each of the 32 patient datasets. The pixel intensity values within each ROI were used to estimate the tissue and cavity *SNRs* on the original B-mode data as well as a series of compounded images:

$$SNR = \overline{M} / SD \qquad [3.22]$$

where $\overline{M}$ and $SD$ referred to the mean and standard deviation (*SD*) of the corresponding ROI intensity values (Burckhardt, 1978; Kruger, 2000). In a similar manner, the tissue/cavity Contrast (*C*) (Peli, 1990; Kruger, 2000) and Signal Difference to Noise Ratio (SDNR) also referred to as detectability index (Kruger, 2000; Mohamed & Kadah, 2008) were derived as:

$$C = \frac{\left|\overline{M}_T - \overline{M}_C\right|}{\left(\overline{M}_T + \overline{M}_C\right)/2} \qquad [3.23]$$

$$SDNR = \frac{\left|\overline{M}_T - \overline{M}_C\right|}{SD_C} \qquad [3.24]$$

where $\overline{M}_T$ and $\overline{M}_C$ corresponded to the mean intensity level within the tissue and cavity ROIs respectively. $SD_C$ corresponded to the standard deviation of the intensity values

within the cavity ROI. Figure 3.13.a displays multiple SNR curves, each representing a different dataset, illustrating the effect of the number of cardiac cycles utilised during ***Temporal Compounding*** on speckle and noise on cardiac tissue structures. Similarly, Figure 3.13.b displays the corresponding RV cavity SNR curves. The mean SNR curves, averaging the SNR curves of all 32 datasets, are also displayed in each of the plots providing representative SNR profiles for tissue and cavity. A direct comparison between the mean tissue and cavity SNR profiles is provided in Figure 3.14. Furthermore, Figure 3.15 displays a mean profile, for all 32 datasets, illustrating the effect of ***Temporal Compounding*** for an increasing number of cardiac cycles on tissue/cavity detectability index (SDNR). The SDNR curves for each individual dataset were omitted since they demonstrate a very similar trend to the corresponding SNR curves. Table 3.5 illustrates the mean percentage change on each of the four quantitative measures between the original unprocessed data and ***Temporal Compounded*** data generated using an increasing number of cardiac cycles. Tables 3.6 to 3.9 summarise the variations on those four quantitative measures between the original and the compounded datasets (using 12 cardiac cycles) elucidating the effect of ***Temporal Compounding*** on the imaged cardiac structures.

#### 3.7.2.2. Visual effect on cardiac ultrasound data

Figures 3.16 to 3.21 display six example ED frames before and after ***Temporal Compounding*** is applied on their corresponding multi-cycle datasets. Datasets covering a range of image and diagnostic qualities (3 low, 2 average and 1 high) were selected in order to best illustrate the effect on ***Temporal Compounding*** on cardiac ultrasound data. The plot in Figure 3.22 provides an example of the variations of the rigid spatial transformations applied on temporally aligned ED frames from consecutive cardiac cycles. More detailed information on the mean and maximum rotation and translation transformations applied in each individual dataset were also derived. Table 3.10 summarises the derived information, listing the minimum, maximum, mean and standard deviation of the mean and maximum rigid spatial transformations applied over the 32 patient datasets. Figures 3.23 and 3.24 display two examples of original, unprocessed ED frames along with their corresponding compounded frames with and without spatial registration performed prior to spatial averaging. Both images illustrate the visual effects of accurate spatial alignment in ***Temporal Compounding.*** Optimal acquisition and compounding parameters were applied on all the displayed images. More processed datasets can be found in the accompanying DVD-1.

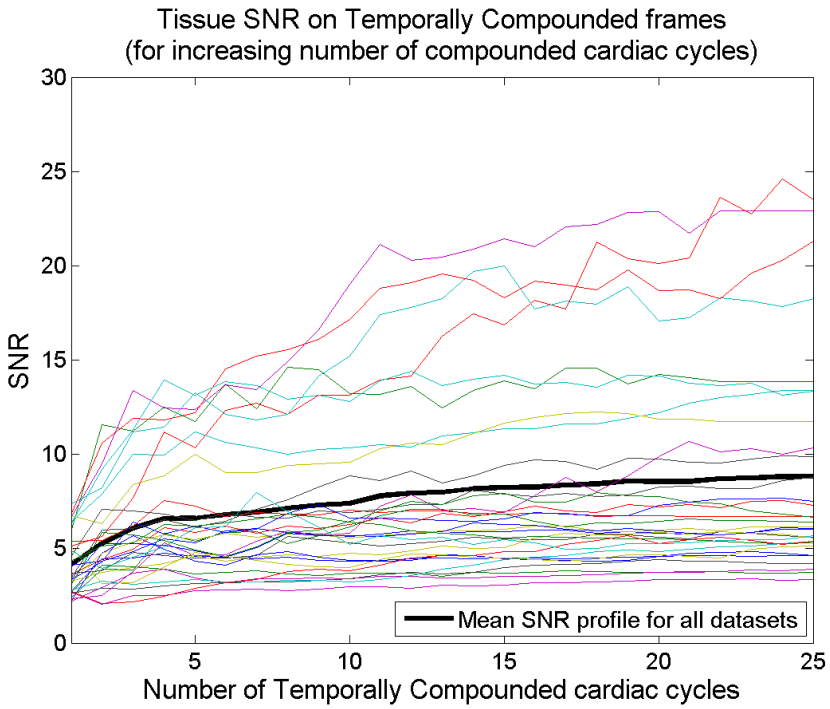


**(a)**

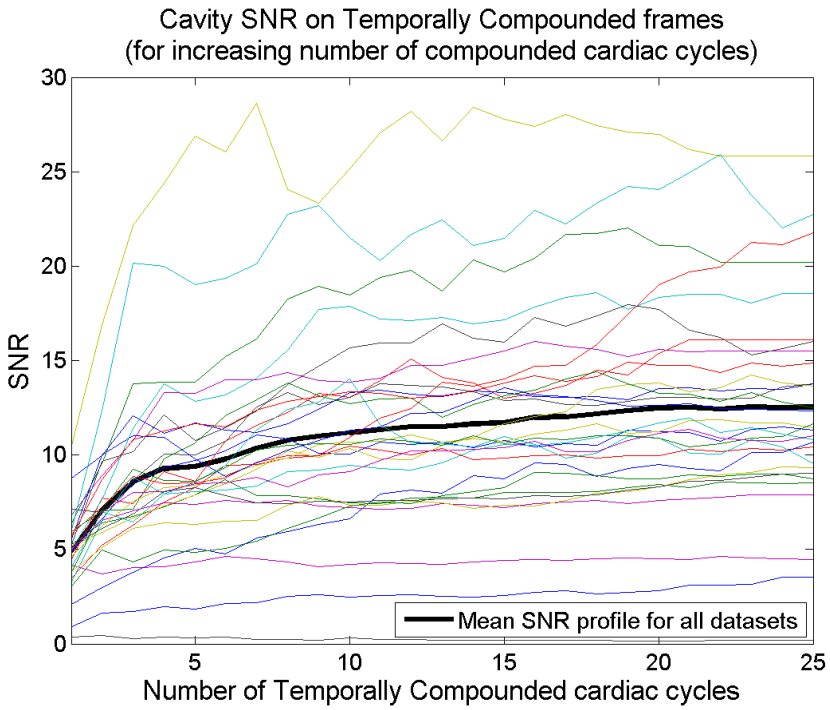


**(b)**

**Figure 3.13.** The effect of ***Temporal Compounding*** on (a) tissue and (b) cavity SNR for increasing number of compounded cardiac cycles. The mean SNR changes are also displayed.

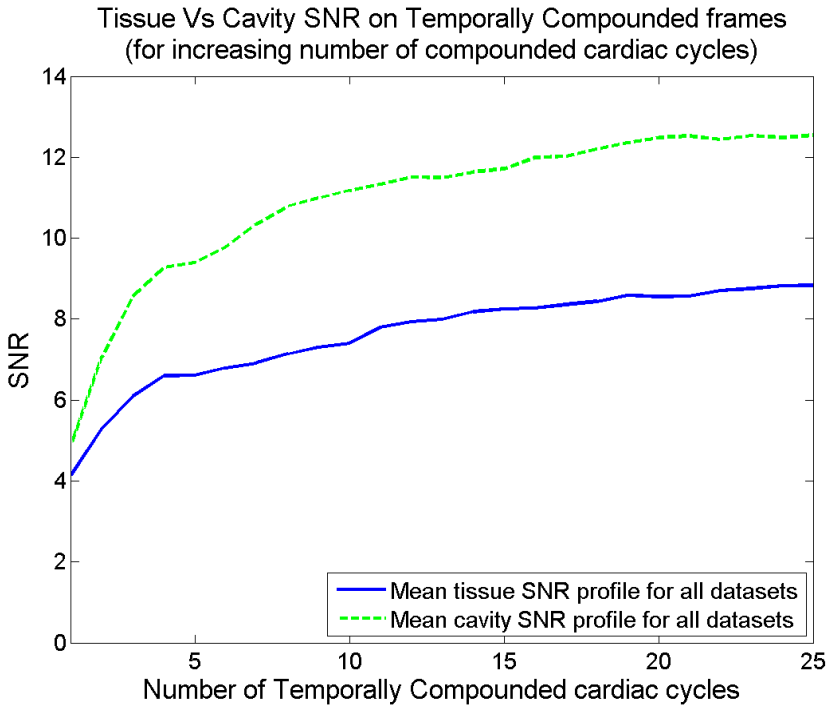


**Figure 3.14.** A direct comparison between the effect of ***Temporal Compounding*** for increasing number of cardiac cycles on tissue and cavity SNR.

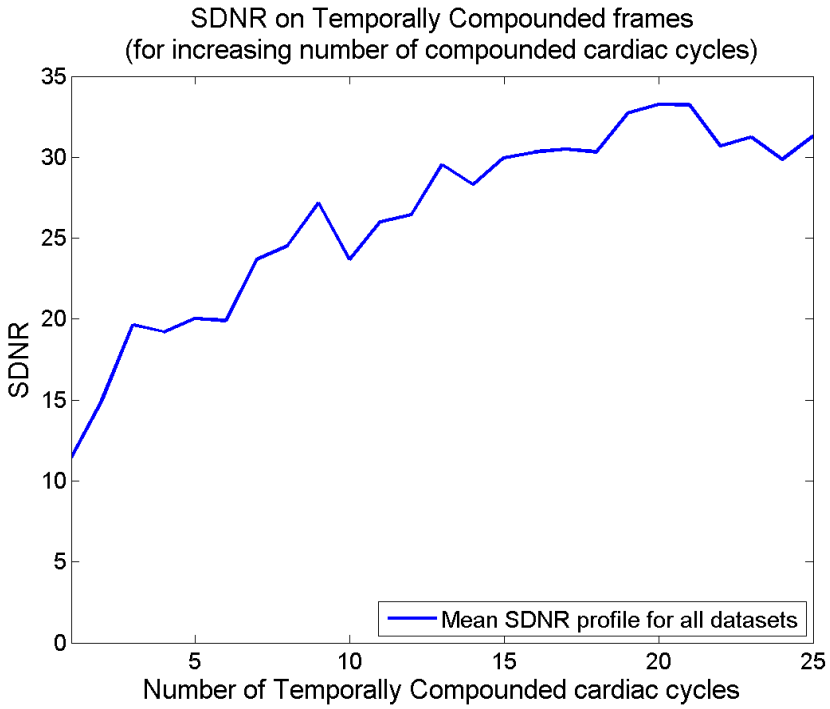


**Figure 3.15.** The effect of ***Temporal Compounding*** for increasing number of cardiac cycles on tissue/cavity SDNR.

**Table 3.5.** Mean overall effect of ***Temporal Compounding*** (percentage change between original and processed data) on four quantitative measures for increasing number of compounded cardiac cycles.

| Cardiac Cycles | Tissue SNR | Cavity SNR | Contrast | SDNR |
|---|---|---|---|---|
| **2** | 29.2% | 47.7% | -2.98% | 39.7% |
| **4** | 58.7% | 91.6% | -4.36% | 76.5% |
| **6** | 60.1% | 102.8% | -4.05% | 86.5% |
| **8** | 69.9% | 126.7% | -4.25% | 107.2% |
| **10** | 74.3% | 136.0% | -4.12% | 118.4% |
| **12** | 87.1% | 143.1% | -3.14% | 128.6% |
| **14** | 91. 6% | 147.0% | -3.47% | 130.1% |
| **16** | 95.0% | 156.5% | -4.63% | 134.0% |
| **18** | 98.5% | 160.4% | -4.99% | 134.7% |
| **20** | 103.0% | 169.0% | -4.79% | 142.9% |
| **22** | 106.4% | 169.3% | -5.69% | 137.1% |
| **24** | 108.0% | 173.3% | -5.50% | 141.4% |

**Table 3.6.** Effect of ***Temporal Compounding*** on tissue SNR. Results for 12 cardiac cycles.

| | Original | Compounded | Improvement |
|---|---|---|---|
| **Min** | 2.22 | 2.90 | 8.0% |
| **Max** | 7.37 | 20.31 | 233.1% |
| **Mean** | 4.15 | 7.94 | 87.1% |
| **SD** | 1.59 | 4.73 | 63.0% |

**Table 3.7.** Effect of ***Temporal Compounding*** on cavity SNR. Results for 12 cardiac cycles.

| | Original | Compounded | Improvement |
|---|---|---|---|
| **Min** | 0.89 | 2.59 | 1.7% |
| **Max** | 10.44 | 28.22 | 289.2% |
| **Mean** | 5.05 | 11.89 | 143.1% |
| **SD** | 1.86 | 5.26 | 75.0% |

**Table 3.8.** Effect of ***Temporal Compounding*** on tissue/cavity Contrast. Results for 12 cardiac cycles.

| | Original | Compounded | Improvement |
|---|---|---|---|
| **Min** | 0.17 | 0.06 | -64.4% |
| **Max** | 2.00 | 2.00 | 25.9% |
| **Mean** | 0.83 | 0.81 | -3.1% |
| **SD** | 0.56 | 0.55 | 16.4% |

**Table 3.9.** Effect of ***Temporal Compounding*** on tissue/cavity SDNR. Results for 12 cardiac cycles.

| | Original | Compounded | Improvement |
|---|---|---|---|
| **Min** | 0.90 | 0.5 | -50.3% |
| **Max** | 35.39 | 98.16 | 320.9% |
| **Mean** | 6.79 | 15.84 | 128.6% |
| **SD** | 7.47 | 19.2 | 85.1% |

### 3.7.2.3. Effect on clinical measurements performed on patient data

A Bland Altman approach (Bland & Altman, 1986) was then used for the quantitative assessment of the effect of ***Temporal Compounding*** on the clinical measurements described in Section 3.6 (Figures 3.25 and 3.26). The Bland Altman approach derives the level of repeatability (*Coefficient of Repeatability – CR*) of clinical measurements performed on either the original or on the compounded data (Bland & Altman, 1986). In addition, the technique also estimates the level of agreement (*CR*) between measurements performed on original and on compounded datasets (Bland & Altman, 1986). In both cases the lower the *CR* the higher the measurement repeatability and measurement agreement. The *Mean Difference* indicates the presence of any bias while the $-2SD$ and $+2SD$ intervals provide the lower and upper limits of agreement between the compared measurements (Bland & Altman, 1986). In measurement repeatability plots, since the same datasets are used in both of the compared measurements, the *Mean Difference* is expected to be approximately around zero. Furthermore, 95% of the measurement differences should lie between the $\pm 2SD$ limits. Figures 3.25 and 3.26 display measurement repeatability and measurement agreement Bland Altman plots combining all clinical measurements performed by each echocardiographer. Individual plots, one for each clinical measurement, were also derived. Table 3.11 summarises the bias, similarity measurements and agreement coefficients derived from the individual plots. Tables 3.12 and 3.13 display the clinical measurements omitted by each echocardiographer on the original and compounded datasets.

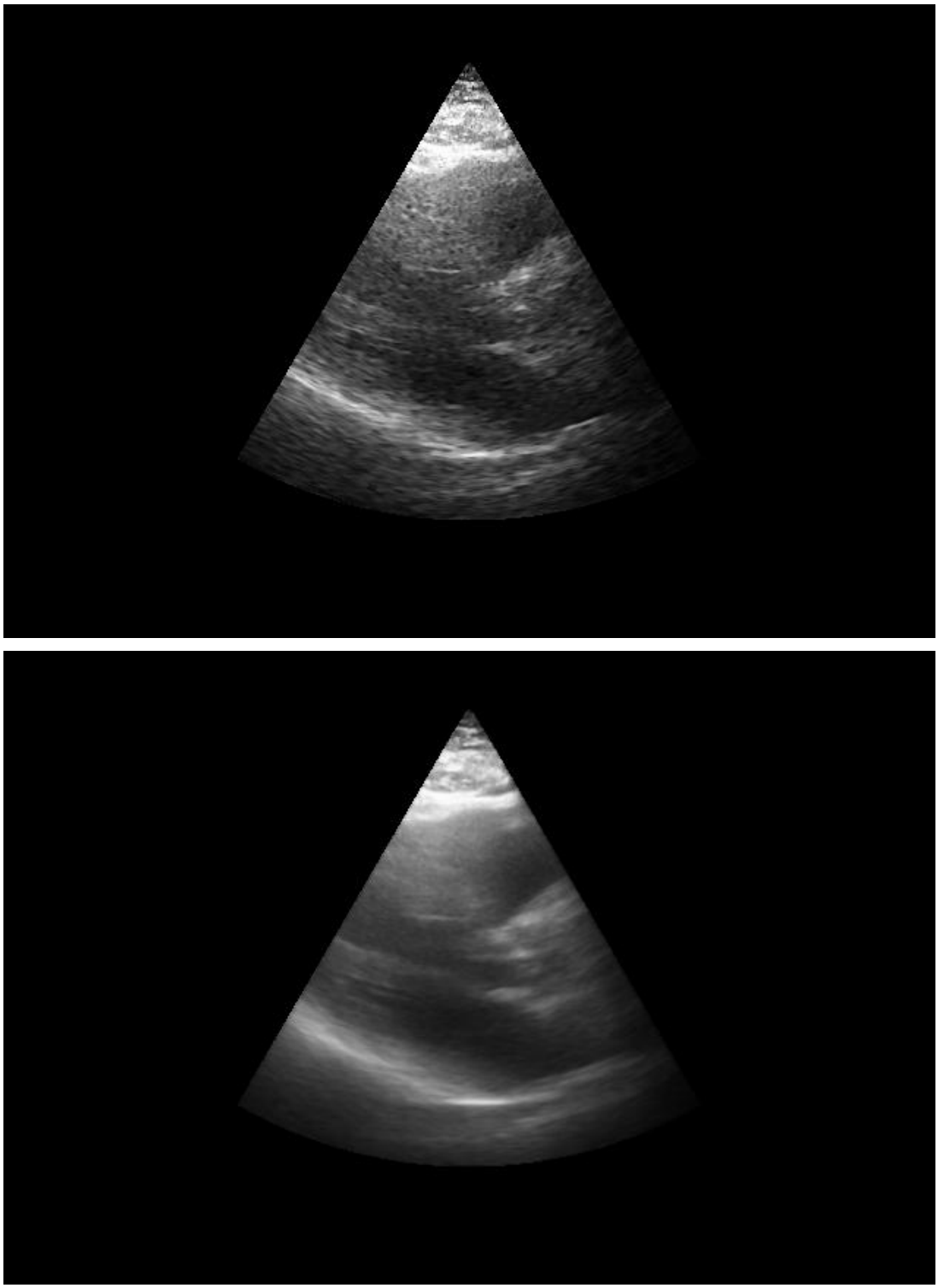

**Figure 3.16.** Original (top) and compounded (bottom) ED frames of low diagnostic value. (Patient 24)

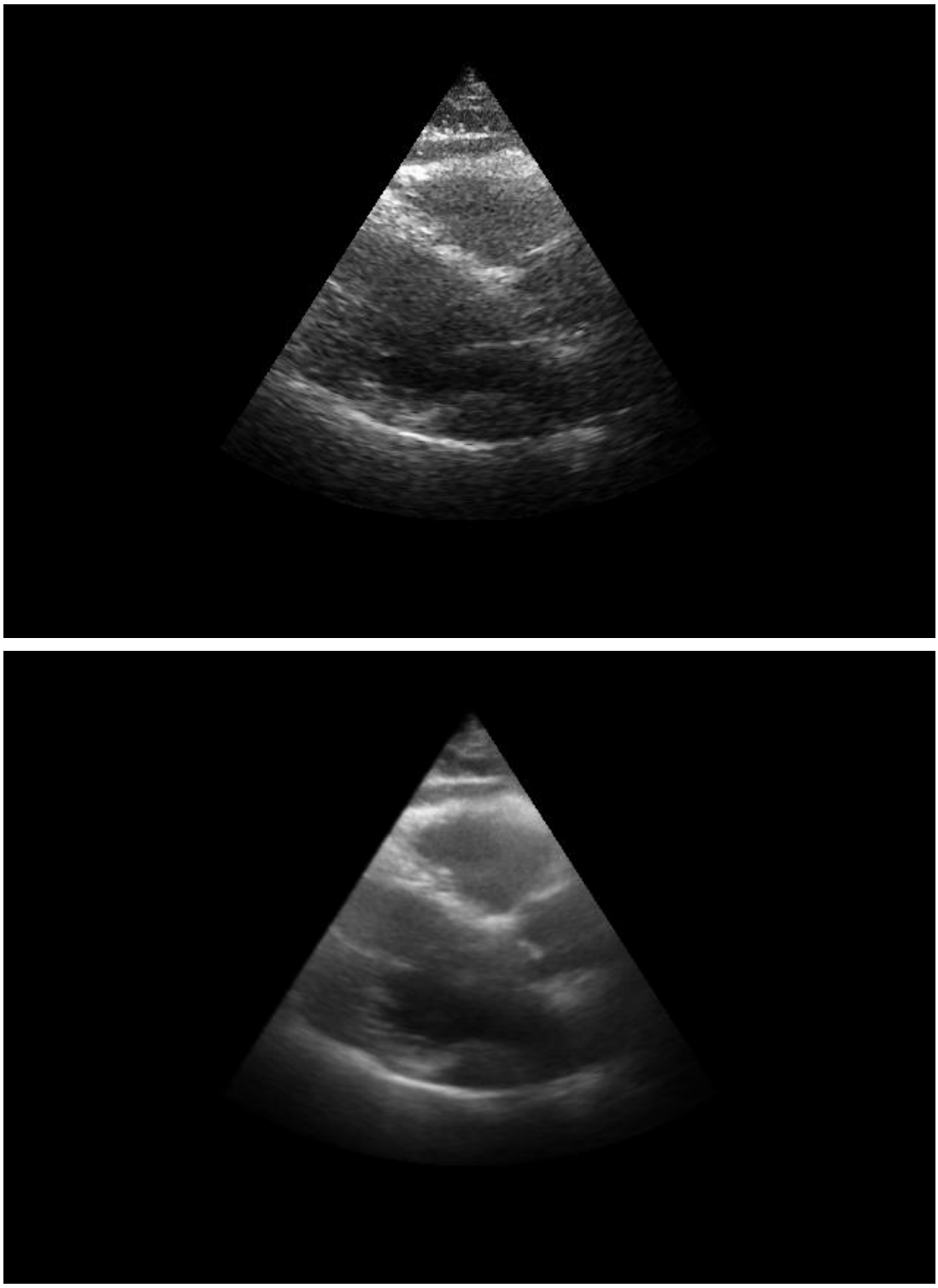

**Figure 3.17.** Original (top) and compounded (bottom) ED frames of low diagnostic value. (Patient 4)

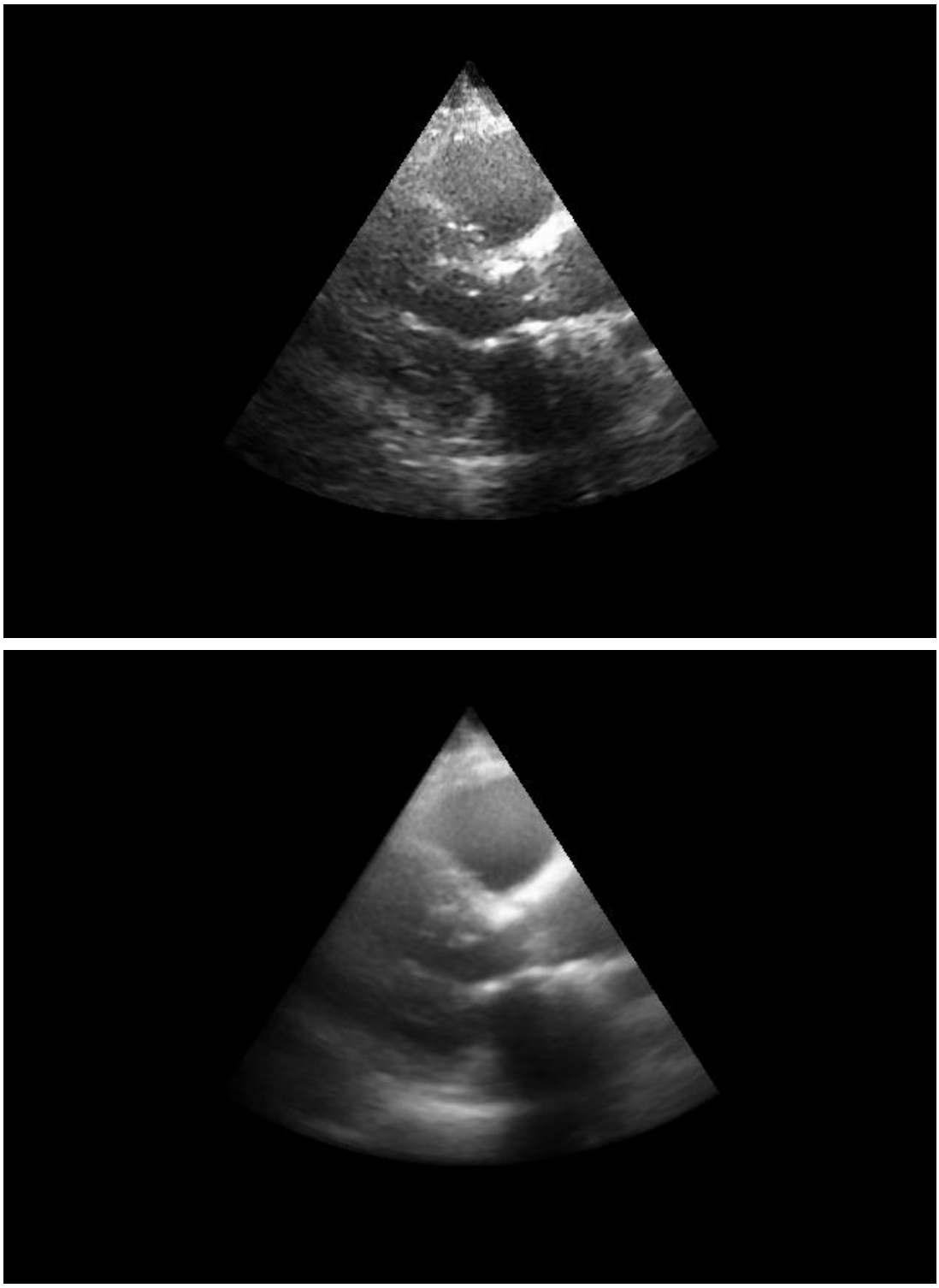

**Figure 3.18.** Original (top) and compounded (bottom) ED frames of low diagnostic value. (Patient 6)

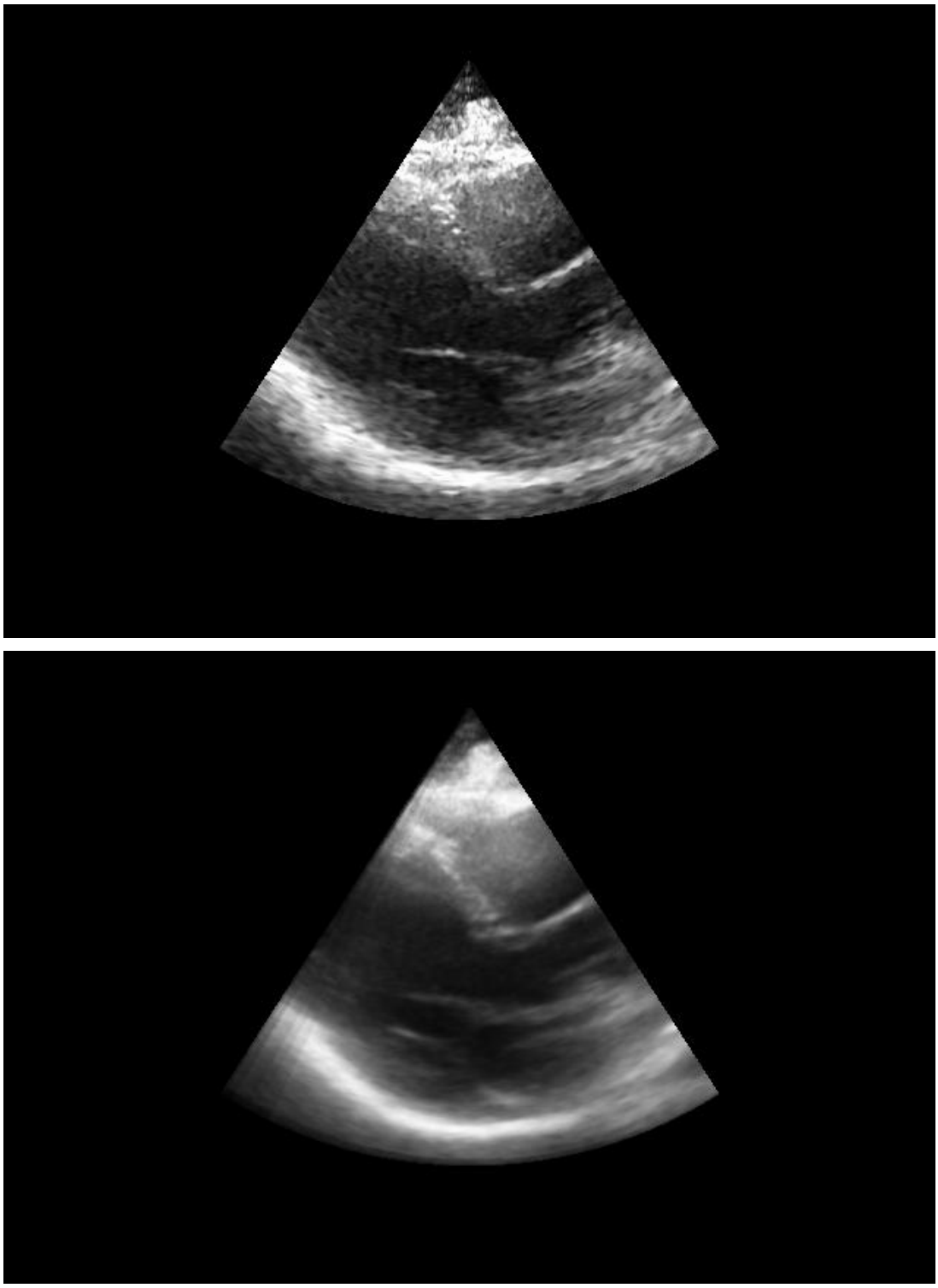

**Figure 3.19. .** Original (top) and compounded (bottom) ED frames of average diagnostic value. (Patient 11)

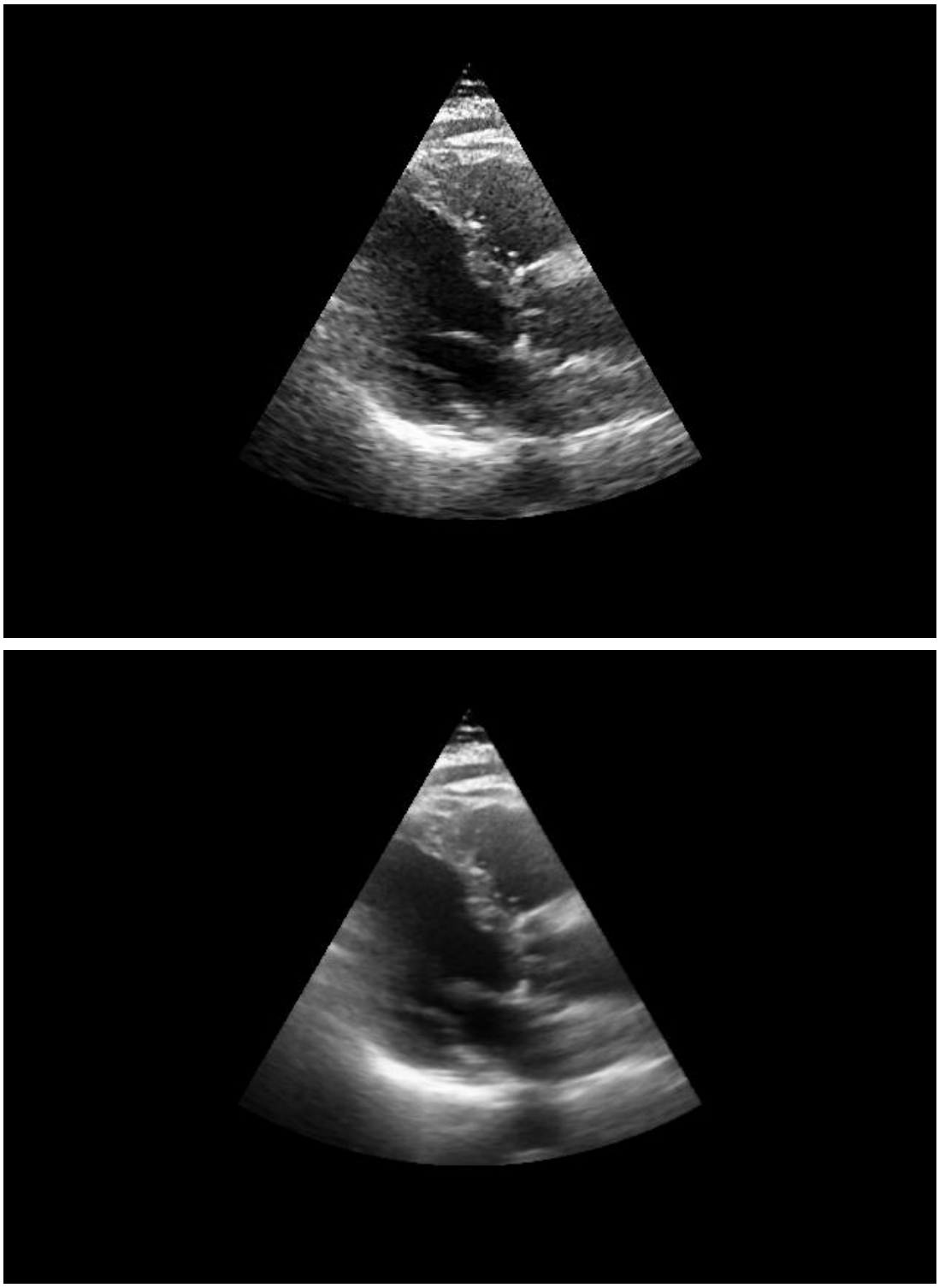

**Figure 3.20.** Original (top) and compounded (bottom) ED frames of average diagnostic value. (Patient 22)

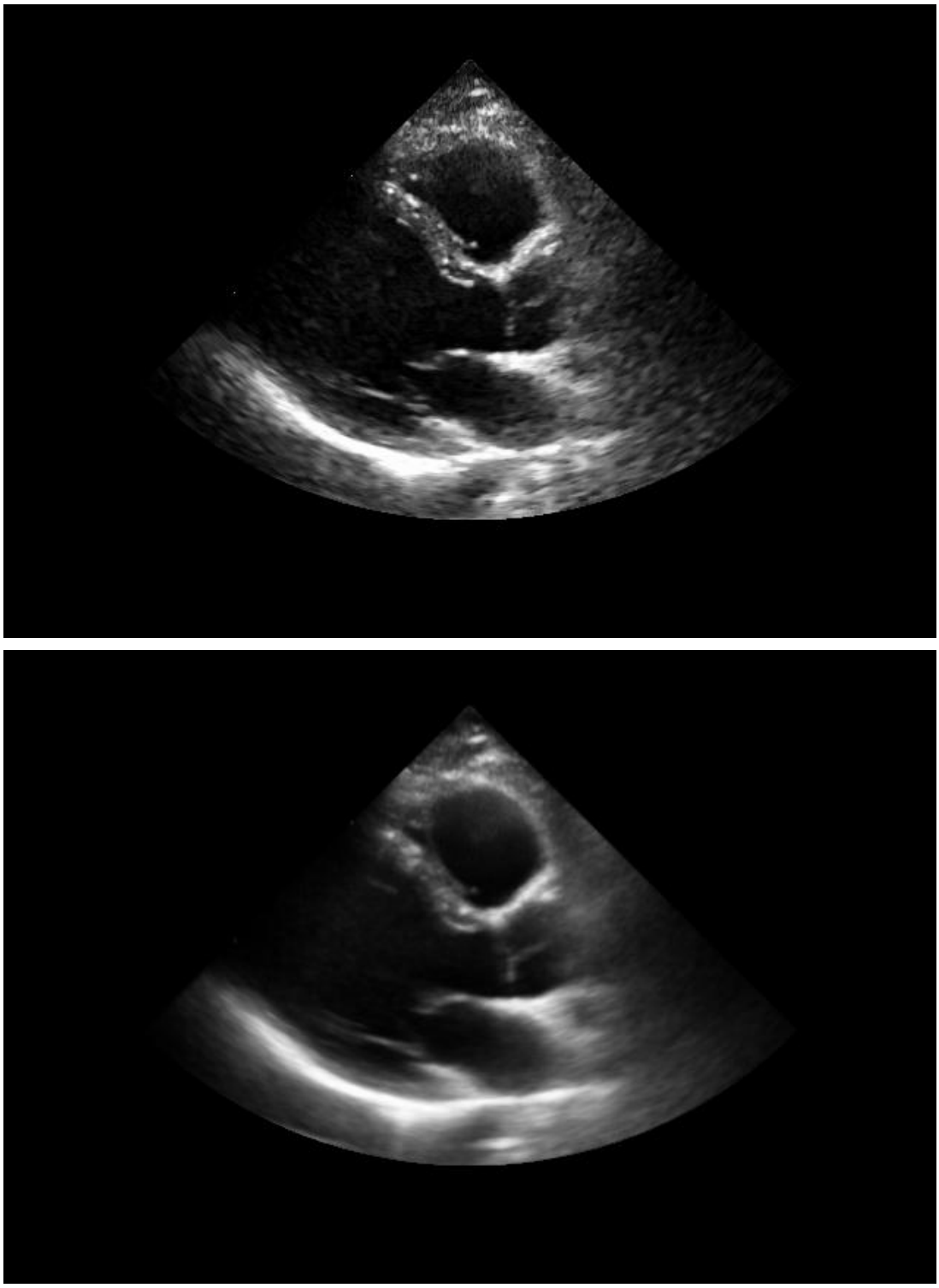

**Figure 3.21.** Original (top) and compounded (bottom) ED frames of high diagnostic value. (Patient 29)

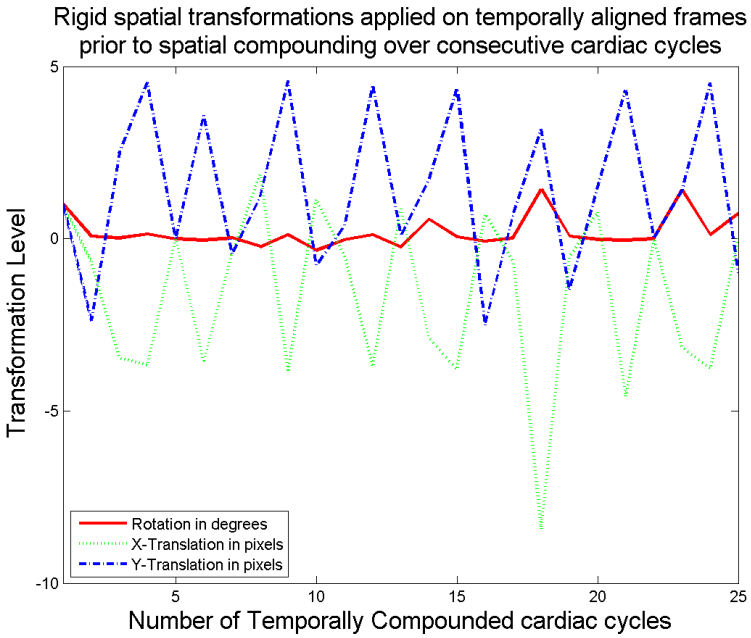


**Figure 3.22.** Plot of rigid spatial transformations applied on temporally aligned ED frames from consecutive cardiac cycles prior to spatial compounding. (Patient 25)

**Table 3.10.** Ranges of maximum and mean spatial transformations applied to each of the 32 patient datasets prior to spatial compounding.

| | $\theta$ | | $t_x$ | | $t_y$ | |
|---|---|---|---|---|---|---|
| **Dataset** | **max** | **mean** | **max** | **mean** | **max** | **mean** |
| **Mean** | 2.23 | 0.61 | 7.92 | 2.62 | 3.53 | 1.35 |
| **SD** | 1.17 | 0.33 | 4.24 | 1.43 | 1.91 | 0.83 |
| **Max** | 7.10 | 1.50 | 22.30 | 7.40 | 7.90 | 4.40 |
| **Min** | 1.00 | 0.20 | 3.10 | 1.0 | 1.0 | 0.40 |

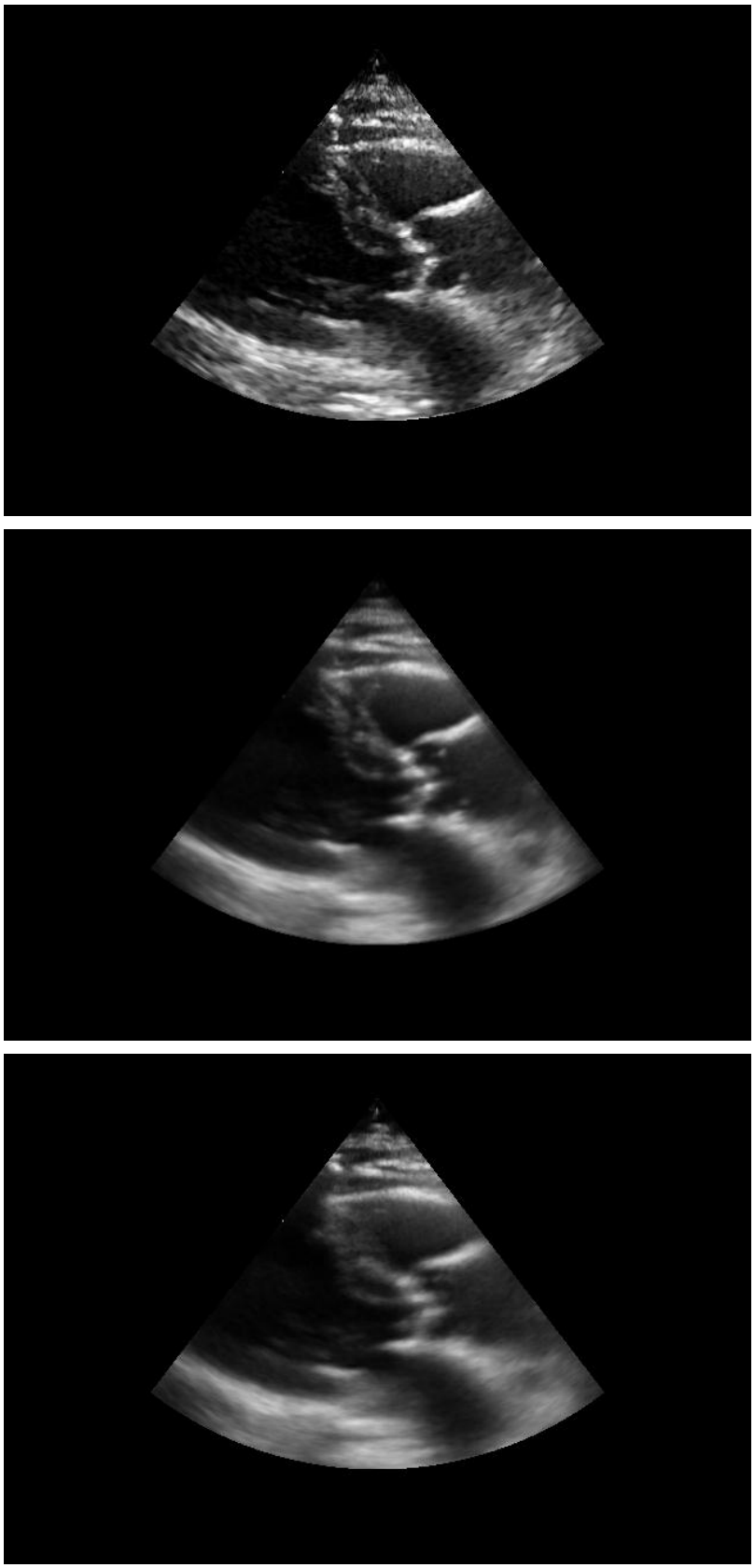

**Figure 3.23.** Original ED frame of average diagnostic value (top) and corresponding compounded frames with (middle) and without (bottom) spatial registration prior to spatial averaging. (Patient 17)

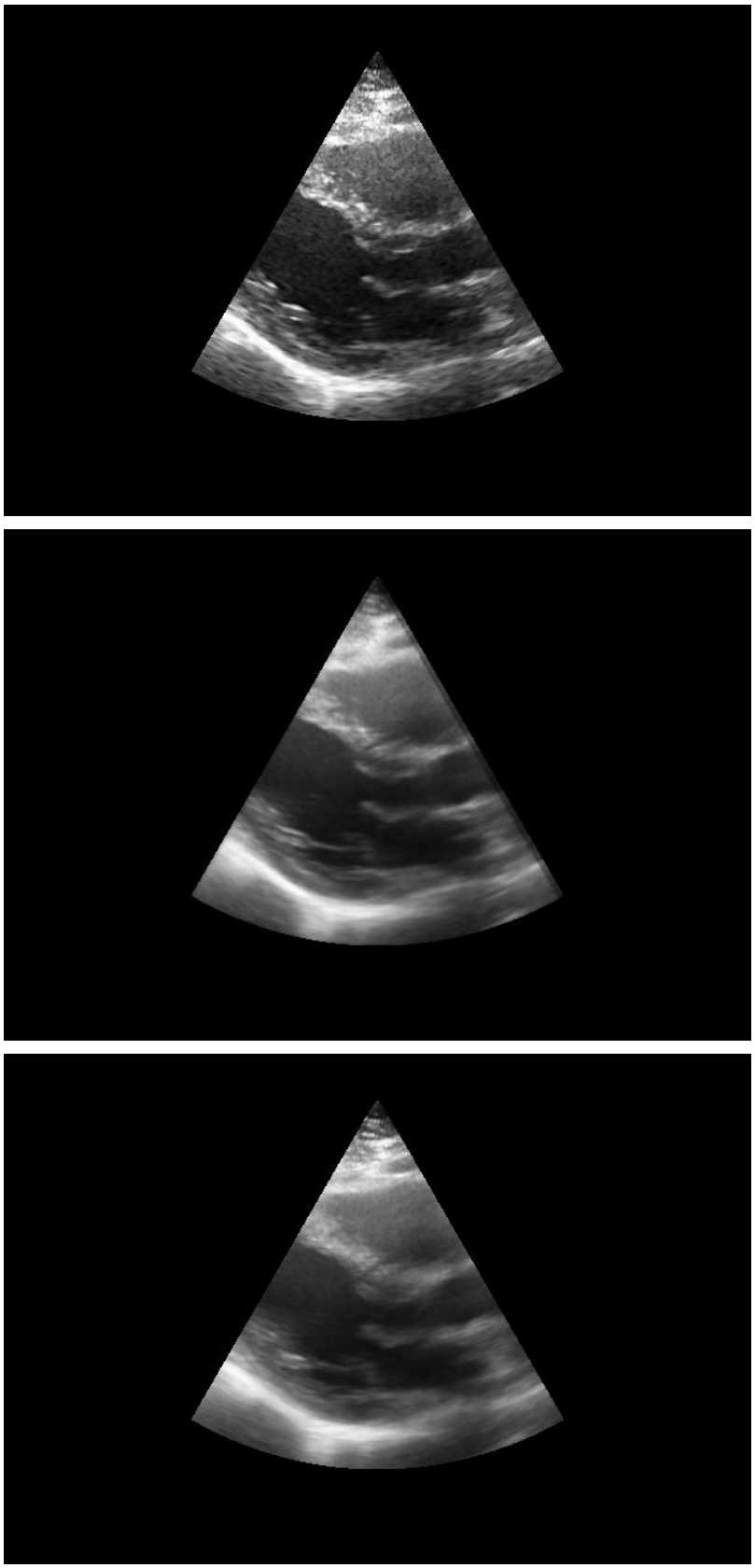

**Figure 3.24.** Original ED frame of average diagnostic value (top) and corresponding compounded frames with (middle) and without (bottom) spatial registration prior to spatial averaging. (Patient 25)

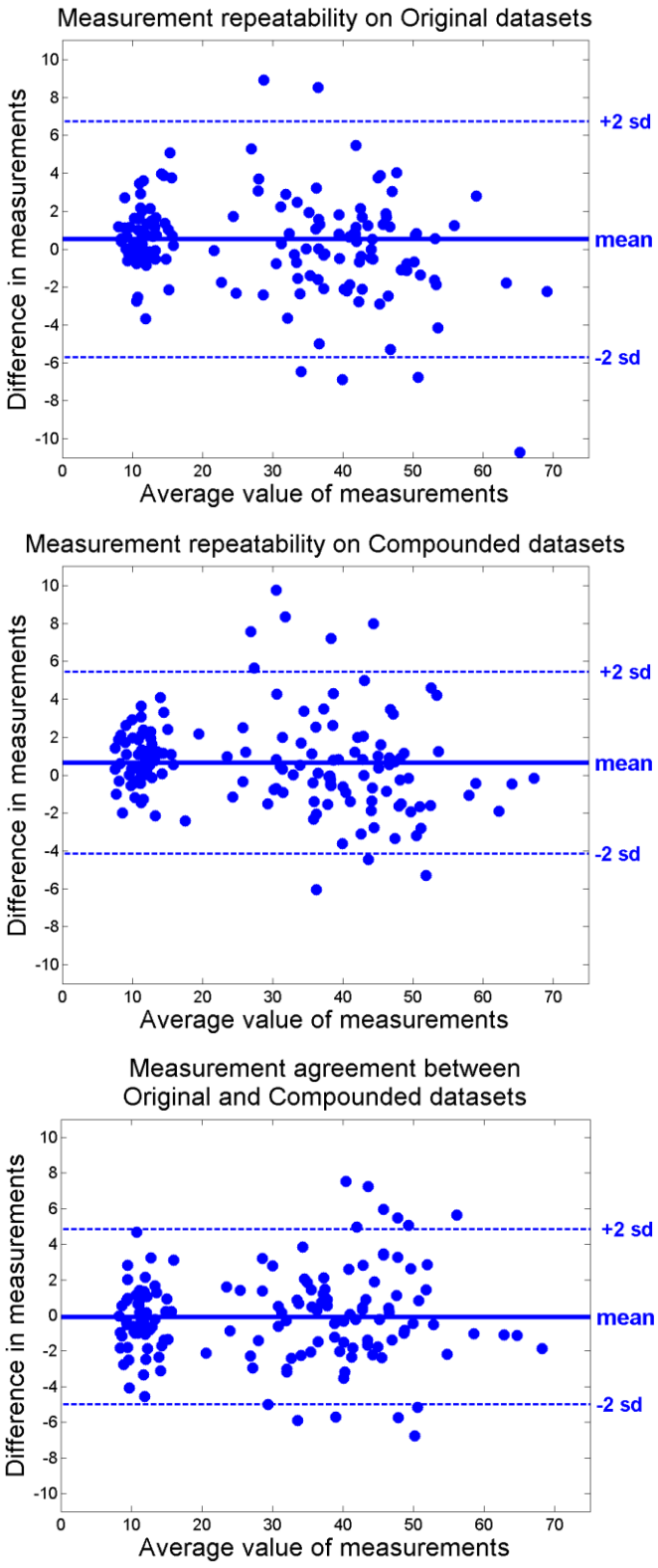


**Figure 3.25.** Bland Altman plots for the repeatability of measurements on original (top) and compounded (middle) datasets as well as the agreement between measurements on original and compounded datasets (bottom). Measurements performed by Echocardiographer 1. Bias (mean), as well as upper/lower limits of agreement are also included.

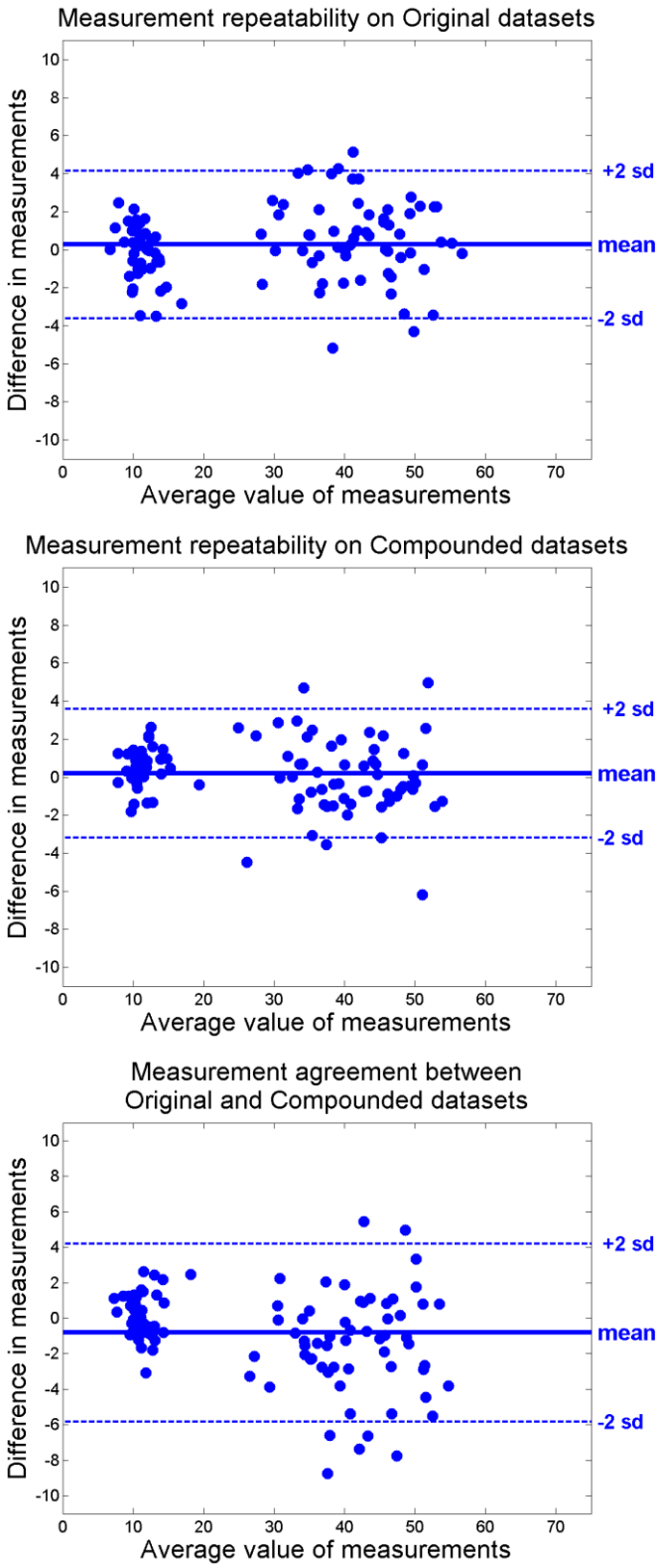


**Figure 3.26.** Bland Altman plots for the repeatability of measurements on original (top) and compounded (middle) datasets as well as the agreement between measurements on original and compounded datasets (bottom). Measurements performed by Echocardiographer 2. Bias (mean), as well as upper/lower limits of agreement are also included.

**Table 3.11.** Measurement repeatability and agreement coefficient for individual clinical measurements.

| Measure | Original | | | | Compounded | | | | Agreement | | | |
|---|---|---|---|---|---|---|---|---|---|---|---|---|
| (mm) | Mean Diff | +2sd | -2sd | CR | Mean Diff | +2sd | -2sd | CR | Mean Diff | +2sd | - 2sd | CR |
| **Echocardiographer 1** | | | | | | | | | | | | |
| **IVSd** | 1.12 | 4.44 | -2.19 | 3.31 | 0.54 | 3.46 | -2.39 | 2.93 | -0.36 | 3.27 | -3.99 | 3.63 |
| **LVIDd** | -1.06 | 5.99 | -8.12 | 7.06 | -0.25 | 4.48 | -4.98 | 4.73 | 0.19 | 7.36 | -6.98 | 7.17 |
| **LVPWd** | 0.35 | 3.34 | -2.64 | 2.99 | 1.11 | 3.60 | -1.38 | 2.49 | -0.24 | 3.12 | -3.61 | 3.37 |
| **LADs** | -0.31 | 3.86 | -4.48 | 4.17 | 0.27 | 5.91 | -5.37 | 5.64 | 0.48 | 4.41 | -3.46 | 3.94 |
| **LVIDs** | 2.82 | 11.57 | -5.93 | 8.75 | 1.67 | 7.90 | -4.55 | 6.23 | -0.57 | 4.57 | -5.70 | 5.13 |
| **Combined** | **0.52** | **6.74** | **-5.70** | **6.22** | **0.64** | **5.44** | **-4.16** | **4.80** | **-0.08** | **4.83** | **-5.00** | **4.92** |
| **Echocardiographer 2** | | | | | | | | | | | | |
| **IVSd** | -0.40 | 2.64 | -3.45 | 3.05 | 0.21 | 2.38 | -1.97 | 2.18 | -0.24 | 2.35 | -2.82 | 2.59 |
| **LVIDd** | 0.55 | 4.37 | -3.27 | 3.82 | -0.25 | 1.90 | -2.41 | 2.16 | -0.34 | 4.66 | -5.33 | 5.00 |
| **LVPWd** | 0.01 | 2.71 | -2.69 | 2.70 | 0.83 | 2.22 | -0.57 | 1.40 | 0.64 | 2.73 | -1.46 | 2.10 |
| **LADs** | 0.16 | 4.12 | -3.79 | 3.96 | -0.80 | 3.24 | -4.85 | 4.04 | -1.79 | 3.69 | -7.28 | 5.48 |
| **LVIDs** | 1.59 | 6.52 | -3.33 | 4.93 | 2.02 | 5.17 | -1.13 | 3.15 | -2.50 | 3.80 | -8.79 | 6.30 |
| **Combined** | **0.28** | **4.15** | **-3.60** | **3.88** | **0.20** | **3.59** | **-3.19** | **3.39** | **-0.82** | **4.20** | **-5.83** | **5.02** |

**Table 3.12.** List of measurements omitted by Echocardiographer 1 on each individual dataset.

| | IVSd | | LVIDd | | LVPWd | | LVIDs | | LADs | |
|---|---|---|---|---|---|---|---|---|---|---|
| **Dataset** | **Or** | **Com** | **Or** | **Com** | **Or** | **Com** | **Or** | **Com** | **Or** | **Com** |
| **7** | o | o | o | o | N/A | o | o | o | o | o |
| **18** | o | o | o | o | o | o | N/A | o | o | o |
| **20** | o | o | o | o | o | o | o | N/A | o | o |
| **21** | o | o | o | o | o | o | o | N/A | o | o |
| **24** | o | N/A | o | N/A | o | N/A | o | o | o | o |
| **26** | o | o | o | o | o | o | o | o | N/A | o |
| **Total** | 0 | 1 | 0 | 1 | 1 | 1 | 1 | 2 | 1 | 0 |

**Table 3.13.** List of measurements omitted by Echocardiographer 2 on each individual dataset.

| | IVSd | | LVIDd | | LVPWd | | LVIDs | | LADs | |
|---|---|---|---|---|---|---|---|---|---|---|
| **Dataset** | **Or** | **Com** | **Or** | **Com** | **Or** | **Com** | **Or** | **Com** | **Or** | **Com** |
| **2** | o | N/A | o | N/A | o | N/A | o | N/A | o | o |
| **4** | o | o | o | o | o | o | N/A | N/A | o | o |
| **5** | N/A | N/A | N/A | N/A | N/A | N/A | N/A | o | o | o |
| **6** | N/A | N/A | N/A | N/A | N/A | N/A | N/A | N/A | N/A | o |
| **7** | o | o | o | o | o | o | o | N/A | o | o |
| **8** | o | o | N/A | o | o | o | o | o | o | o |
| **10** | o | o | o | o | o | o | N/A | o | o | o |
| **11** | N/A | o | N/A | o | N/A | o | N/A | o | o | o |
| **16** | o | o | o | o | o | o | N/A | o | o | o |
| **17** | o | o | o | N/A | o | o | o | o | o | o |
| **18** | N/A | o | N/A | o | N/A | o | N/A | o | o | o |
| **19** | N/A | o | N/A | o | N/A | o | N/A | o | o | o |
| **20** | N/A | N/A | N/A | N/A | N/A | N/A | N/A | N/A | o | o |
| **24** | N/A | N/A | N/A | N/A | N/A | N/A | N/A | N/A | o | o |
| **26** | o | o | o | o | o | o | N/A | o | N/A | o |
| **27** | N/A | o | N/A | o | N/A | o | N/A | o | N/A | N/A |
| **28** | N/A | N/A | N/A | N/A | N/A | N/A | N/A | o | o | o |
| **30** | N/A | o | N/A | o | N/A | o | o | o | o | o |
| **31** | o | o | o | o | o | o | o | o | N/A | o |
| **32** | o | o | o | o | o | o | N/A | o | o | o |
| **Total** | 10 | 6 | 11 | 7 | 10 | 6 | 14 | 6 | 4 | 1 |

## 3.8. Discussion

### 3.8.1. Temporal alignment

The results presented in Section 3.7.1 suggest that the proposed methods (Section 3.5.1) can generate an accurate and robust temporal alignment adequately representing each of the seven independent stages of a cardiac cycle. The accurate temporal alignment of all data prior to averaging is vital to effective ***Temporal Compounding***. Insufficient temporal alignment will cause the averaging of frames corresponding to different stages within the cardiac cycle, resulting in tissue/cavity boundary blurring and therefore degradation on the clinical value of the processed data.

#### 3.8.1.1. Identification of ED and ES frames

The plots in Figure 3.10 provide an example illustrating the effect of using *CCC* as opposed to *NXC* as a similarity measure between the reference ED and ES frame pair and the remaining frames in the multi-cycle dataset. By comparing the three plots, it is evident that *CCC* can generate a very smooth curve with only a few, clearly distinguishable local maxima (representing ED frames) and local minima (representing ES frames). On the other hand, *NXC* generates curves with higher levels of noise and a higher number of local maxima and minima, i.e. candidates for ED and ES frames. For high quality datasets, both *CCC* and *NXC* can produce equally reliable results. However, for low quality datasets, such as the example illustrated in Figure 3.10, using *CCC* can generate a more robust ED and ES identification.

Currently there is no gold standard for the accurate and robust identification of the ED and ES frames over consecutive cardiac cycles. Even manual identification encounters a number of challenges due to high levels of noise and shadowing, making it difficult and sometimes impossible to identify and track specific cardiac structures over consecutive frames. This is why four distinct cues were utilised during the manual identification of ED and ES (Section 3.7.1.1), making the process very laborious and highly subjective. The results presented in Tables 3.1 and 3.2, comparing the manual identification to the representative reference ED and ES frames, indicate that only 81.5% of the ED frames and 53.9% of the ES frames were consistently identified over all three repetitions. For high quality data, up to 100% of the ED frames were consistently identified. On the other hand, the consistency in manual ES identification over three repetitions ranged from as low as 4%, for low quality data, to as high as 88%, for high quality data. The presented findings indicate two things. First, the variations in ED and ES identification over successive repetitions indicate that manual

identification is subjective and cannot be considered as gold standard. Second, the manual ES identification, especially for low quality datasets, is more challenging than the corresponding ED identification. This is due to the fact that the ECG cannot provide reliable information on the ES state while the Aortic Valve, whose opening signifies the end of systolic phase, is in most datasets hard to identify and track. Alternatives such as the periodic motion of LV and RV and the opening of the Mitral Valve were therefore utilised.

The automatic ED and ES identification described in Sections 3.5.1.1 displays very similar behaviour with the corresponding manual ED and ES identification. The mean percentage of the automatically identified ED and ES frames that were consistent with the corresponding reference frames was about 80% of the equivalent manual level. This percentage rose to about 91% of the equivalent manual level for automatically identified ED and ES frames that lay within one frame of the corresponding reference frames. The difference between the manual and automatic identification dropped even further for frames that lay within two frames of the corresponding reference frames. Furthermore, the linear regressions for both manual and automatically identified ED and ES frames indicated high levels of correlation with the corresponding reference frames ($R^2 \approx 1$) as well as low mean RMSE of less than one frame.

While the manual ED and ES identification outperformed the automatic method suggested in this chapter, the results are still very promising. Acquiring datasets with 25% more cardiac cycles can increase the number of automatically identified frames that are consistent with the corresponding reference frames to levels similar to manual identification. Similarly, datasets with only 10% more cardiac cycles can increase the number of automatically identified frames that lie within one frame from corresponding reference frames to levels similar to manual identification. As described in Section 3.5.1.3, in cases where the derivation of clear local maxima throughout the search for additional temporal control points is obstructed, the corresponding cardiac cycle is discarded throughout ***Temporal Compounding***. Moreover, as described in Section 3.5.3, the mean ($M$) and the standard deviation ($SD$) in the similarity between the reference frame and all the corresponding spatio-temporally aligned frames is derived. Frames with similarity outside the $M \pm SD$ region are discarded in order to avoid the compounding of dissimilar frames resulting in tissue/cavity boundary blurring. As a result, acquiring additional cardiac cycles ensures that the most accurate of the automatically identified ED and ES frames will be utilised in ***Temporal Compounding***. Finally, consideration should be given to the fact that the reference ED and ES frames are just representative frames derived from a series of manual identifications. They do not provide

definite representation of all ED and ES states in the dataset. Feeding the automatic algorithm with a representative pair of manually identified ED and ES frames guarantees the identification of all frames in the B-mode sequence demonstrating maximum similarity to the seed ED and ES frames. For reasons such as low temporal resolution, some automatically identified frames may lie close while not exactly representing the corresponding ED and ES states. Nevertheless, they will provide the best ED and ES representatives in the corresponding cardiac cycle that can be used during ***Temporal Compounding***.

#### 3.8.1.2. Temporal interpolation

Figure 3.12 provides four representative example variations of the temporal cardiac behaviour (with respect to the reference cardiac cycle) over consecutive cardiac cycles. Such variations can be large (Figure 3.12.a) or small (Figure 3.12.b). Moreover, they can follow similar patterns (Figure 3.12.c) or variable, independent patterns (Figure 3.12.d). Correcting these variations through temporal alignment ensures that the resulting temporally compounded images are largely unaffected by the temporal behaviour of the patient's heart. Selecting a representative reference cardiac cycle (Section 3.5.3) minimises the overall temporal deformations required over a dataset.

Figure 3.11 provides examples of the temporal interpolation (to the reference cardiac cycle) curves for four cardiac cycles within a multi-cycle dataset. Each plot displays six curves, each corresponding to one of the six temporal interpolation methods proposed in Section 3.5.1.4. In the first example, small temporal variations with respect to the reference cardiac cycle were observed. In such cases, representing a cardiac cycle with as low as 2 or 3 control points can produce temporal alignment of sufficient accuracy. In the second example, large variations were observed during the cardiac diastole while variations in the systole were kept to a minimum. Similarly, in the third example, large independent variations were observed during both the cardiac diastole and the systole. In such cases, it is apparent that characterising a cardiac cycle with as low as 2 or 3 control points is not sufficient and therefore introducing additional control points (Section 3.5.1.3) is required. Both 5 and 7 control points generate temporal alignments with comparable accuracy levels. Finally, in the fourth example, large variations were observed only during a subsection of the diastole phase while variations in the remaining of the cardiac cycle were kept to a minimum. In such cases 5 control points are inadequate and 7 control points are required to generate temporal alignment of sufficient accuracy. As mentioned earlier in this chapter, a cardiac cycle consists of 7 independent stages demonstrating individual temporal behaviour over consecutive cardiac cycles. Therefore, it is strongly believed that defining the 7 stages and

utilising them as control points can generate accurate temporal alignment in most cases independent to the nature of the temporal variation.

The quantitative results in Table 3.3 verify the observations obtained through the four examples in Figure 3.11. There were cases where using 2, 3 or 5 control points would generate identical temporal interpolation to the corresponding 7 point interpolation. Moreover, introducing additional control points in the interpolation process increased the range of temporal variations that could be characterised and corrected during the temporal alignment process. However, even when using between 5 and 7 control points there were a considerable number of frames (mean of 37.1% within each dataset) that were misaligned during interpolation with the potential disparity reaching up to 9 frames. Such large differences may introduce severe blurring in the temporally compounded data limiting their clinical usability. Considering that the introduction of additional control points in temporal alignment is not a computational intensive process, it is strongly believed that 5 control points does not provide a satisfactory alternative to the corresponding 7 point interpolation. Furthermore, the corresponding interpolation curves in Figure 3.11 along with the quantitative results in Table 3.4 indicate that temporal alignment using linear and B-Spline interpolation generated largely identical results, suggesting that both methods can be used interchangeably. However, B-Splines generated smooth, $2^{nd}$ order continuous curves providing a closer representation of the temporal cardiac characteristics when compared to the corresponding piecewise linear curves.

### 3.8.2. Temporal compounding

The results presented in Section 3.7.2 enable the derivation of the optimal number of cardiac cycles utilised during ***Temporal Compounding***. They also illustrate the visual effect of ***Temporal Compounding*** on patient data. The accurate spatial alignment of all data prior to averaging is essential in order to avoid boundary blurring and consequently degradation of the clinical value of the processed images. The enhancement of the processed datasets is finally illustrated by the increase in the measurement repeatability during a series of clinical measurements performed by experienced echocardiographers.

#### 3.8.2.1. Effect on tissue SNR, cavity SNR, tissue/cavity contrast and SDNR

Figure 3.13 illustrates the effect of ***Temporal Compounding*** on the tissue and cavity SNR for an increasing number of compounded cardiac cycles. SNR increased with an increase in the number of cardiac cycles utilised during compounding. However, the compounding effect varied significantly between different datasets ranging from negligible (around 1%) to

very substantial (more than 250%). Variations in the initial SNR amongst the unprocessed datasets can be attributed to many reasons such as different levels of static and dynamic noise, shadowing and non-optimal acquisition set-up. A wide range of artifacts can also appear in a real cardiac ultrasound scan. Such artifacts, along with variations on the ROI location and amongst the movement range during data acquisition, can attribute to the fluctuation on SNR increase achieved by compounding on different datasets. The mean SNR profile (Figures 3.13 and 3.14) provides a fairer representation of the effect of ***Temporal Compounding*** on cardiac tissue and cavity. Figure 3.14 enables the direct comparison of the mean tissue and cavity SNR profiles. Comparing the mean tissue and cavity SNR profiles, it is apparent that cavity SNRs demonstrated a higher initial value as well as larger ranges. The higher SNR ranges are due to the absence of speckle in cardiac cavities. Speckle constitutes a major contributor in the lower initial SNR values observed in cardiac tissue. Furthermore, due to the nature of speckle, a higher level of decorrelation between the compounded frames is required for its suppression when compared to the noise present in cardiac cavities.

Similar profiles for each of the 32 datasets were derived in order to assess the effect of ***Temporal Compounding*** on the tissue/cavity detectability index (SDNR) and contrast. In a like manner to the SNR profiles, the mean SNDR and contrast profiles provided fair representations of the effect of ***Temporal Compounding*** on the distinction between cardiac tissue and cavity. Figure 3.15 illustrates the corresponding mean SDNR profile. Moreover, Table 3.5 illustrates the mean percentage increase in tissue SNR, cavity SNR, SDNR and Contrast achievable through ***Temporal Compounding*** with an increasing number of cardiac cycles. As expected, ***Temporal Compounding*** resulted in a modest, and relatively unaffected by the number of utilised cardiac cycles, decrease in contrast between cardiac tissue and cavity. However, considerable increase in SNR and SDNR were achieved. By investigating the profile curvatures in Figures 3.14 and 3.15, as well as the percentage increases in Table 3.5, the mean SNR and SDNR profiles can be divided into three segments. In the first segment, observed during the compounding of the first 4-5 cardiac cycles, the SNR and SDNR increase was very large. In the second segment, observed during the compounding of up to 12-13 cardiac cycles, the SNR and SDNR increase was more moderate but still considerable. In the final segment, for compounding of more than 13 cardiac cycles, the SNR and SDNR increase was further reduced to very modest levels. This behaviour is attributed to the decrease in new information introduced by increasing the number of cardiac cycles utilised during ***Temporal Compounding***. The initial cardiac cycles introduce considerable decorrelated information. By introducing additional cardiac cycles the decorrelation between the new and the existing information decreases. In order to maintain the high SNR and

SNDR increases, a higher level of decorrelation, achieved through larger movements during acquisition, is required. However, large movements during acquisition can result in severe blurring of the tissue/cavity boundary and should therefore be avoided. After 12-13 cardiac cycles the decorrelation is minimal and the marginal SNR and SDNR increase is mainly attributed to the compounding and suppression of random dynamic noise present in cardiac ultrasound data.

After a thorough examination on the findings for all 32 datasets, it is believed that 12 cardiac cycles can introduce a sufficient noise suppression and tissue/cavity detectability increase during ***Temporal Compounding***. Tables 3.6 to 3.9 demonstrate the quantitative effect of ***Temporal Compounding*** using 12 cardiac cycles on tissue SNR, cavity SNR, tissue/cavity Contrast and detectability index SDNR. The effect of ***Temporal Compounding*** may vary amongst the 32 datasets. Nevertheless, the overall effect of ***Temporal Compounding*** on each quantitative measure seems to follow a similar trend for all datasets with the mean value providing a fair representation of it. More precisely, tissue and cavity SNRs as well as the SDNR are substantially increased by an average of 87.1%, 143.1% and 128.6% respectively. On the other hand a moderate contrast decrease of an average 3.1% is introduced. 12 cardiac cycles provide a considerable reduction in resources when compared to the 20 cardiac cycles suggested by (Abiko et al., 1997). Reducing the number of cardiac cycles utilised during ***Temporal Compounding*** can considerably reduce the acquisition and computational requirements as well as the resulting tissue/cavity boundary blurring introduced to the compounded datasets. More cardiac cycles may be required for low quality datasets where temporal alignment is challenging. Finally, for patients that the acquisition of 12 consecutive cardiac cycles is not feasible, ***Temporal Compounding*** can be utilised on less cardiac cycles while still generating considerable SNR and SDNR increases.

#### 3.8.2.2. Visual effect on cardiac ultrasound data

Figures 3.16 to 3.21 display six example ED frames, before and after ***Temporal Compounding*** is applied on their corresponding multi-cycle datasets. These figures provide characteristic examples of the effects of ***Temporal Compounding*** on clinical data over a range of image qualities and diagnostic values. Frames from 12 consecutive cardiac cycles were utilised during the ***Temporal Compounding*** process in all six examples.

Figure 3.16 displays two ED frames corresponding to a dataset with very low image quality and diagnostic value. The first image is an original unprocessed frame, while the second is the corresponding temporally compounded frame. The original image suffered from a high

level of noise and very limited contrast between cardiac cavities and tissue. The low data quality limited the visual delineation of the majority of cardiac structures including the RV, LV, IVS, PW and RA. Furthermore, the high noise and low contrast levels limited, and very possibly restricted, the suitability of the displayed dataset for most post-processing algorithms such as image segmentation and image registration. ***Temporal Compounding*** substantially suppressed the noise level in cavities as well as the speckle in tissue structures. While the quality of the dataset remained low, structures such as the RV cavity and the IVS were marginally enhanced making them easier to detect and outline. Figure 3.17 displays two ED frames corresponding to a dataset with low image quality and diagnostic value. Similarly to the previous example, the original image suffered from high noise levels making it hard to outline structures such as the IVS, LA and the LVPW. However, the effect of ***Temporal Compounding*** was more noticeable. More precisely, along with the apparent noise and speckle reduction, cardiac tissue structures such as the LV cavity, IVS, LV and the LVPW were moderately enhanced making them easier to detect and outline. The improvement of the processed data is believed to further enhance the post-processing and diagnostic value of the dataset. Figure 3.18 displays two ED frames corresponding to the last of the three datasets with low image quality and diagnostic value. The original dataset suffered from high a level of noise, which in combination with shadowing masked out clinically vital cardiac structures such as segments of the IVS, the PW and the lower end of the LA. As expected, ***Temporal Compounding*** substantially suppressed the noise level in cavities as well as the speckle in tissue structures. However, ***Temporal Compounding*** also compensated for some of the masked out structures, substantially enhancing the IVS and LA and therefore enabling the delineation of the IVS as well as RV, LV and LA cavities.

Figure 3.19 displays two ED frames corresponding to the first dataset with an average image quality and diagnostic value. The original dataset suffered from noise within cardiac cavities and tissue structures. While most cardiac structures were distinguishable, high noise levels masked out segments of the IVS in a way similar to the dataset in Figure 3.18. Furthermore, the delineation of structures such as the LVPW and the LA was challenging. Similar to the previous examples, ***Temporal Compounding*** reduced the speckle/noise level throughout the image and moderately enhanced structures such as the IVS and the PW. While the enhanced (previously masked out) sections of the IVS were not fully restored, they enabled a moderately improved delineation of the structure. On the other hand, small blurring was introduced around the mitral valve and the LA tissue/cavity boundaries. The blurring effect is partially due to image misalignment prior to spatial compounding and partially due to quantification errors as a result of the limited acquisition temporal resolution. Increasing the

temporal resolution (from 25 Hz utilised in the available acquisition setup) is expected to considerably decrease the level of the tissue/cavity boundary blurring introduced by ***Temporal Compounding***. Figures 3.20 and 3.21 provide examples of datasets with average and high image quality and diagnostic value respectively. While, the original data in Figure 3.20 demonstrated a moderately higher level of cavity noise and lower level of tissue/cavity contrast with respect to the original data in Figure 3.21, in both datasets cardiac structures were clearly distinguishable. Nevertheless, ***Temporal Compounding*** considerably suppressed tissue speckle as well as the existing low levels of cavity noise. The effect was predominantly noticeable around the IVS and RV cavity. Similarly to the example illustrated in Figure 3.19 small blurring was introduced around the mitral valve.

Figure 3.22 provides an example of the variations of the rigid spatial transformations applied on temporally aligned ED frames over 25 consecutive cardiac cycles. From the three curves displayed in Figure 3.22 it is apparent that the spatial transformations demonstrated a periodic behaviour with repetition periods ranging around 2 to 4 cardiac cycles. This periodic behaviour is attributed to the respiration movements of the patient's chest during the multi-cycle data acquisition. Table 3.10 summarises the detailed information on the mean and maximum rotation and translation transformations applied in each individual dataset. The results contradict the assumption made by (Abiko et al., 1997) that no rotation or translation along the X-axis is required prior to the compounding of multi-cycle datasets. Translation along the X-axis was the most dominant transformation over the 32 patient datasets. Moreover, the rotation levels were lower than the corresponding X and Y translations levels. However, the effect of rotation is proportional to the distance from the centre of rotation (centre of scanning sector). Therefore, even modest rotation may have a considerable effect on the edges of the scanning region (top and bottom edges). Figures 3.23 and 3.24 provide two examples illustrating the effect of spatial alignment on ***Temporal Compounding***. Noise suppression was at comparable levels in compounded data derived from both spatially aligned and non-aligned frames. However, for non-aligned data high levels of blurring on tissue structures, such as the Aortic Valve (Figure 3.23), the IVS (Figures 3.23 and 3.24), the Mitral Valve (Figure 3.24) and the LVPW (Figure 3.24), were introduced. Additional tissue blurring may reduce the clinical usability of a compounded dataset by making cardiac structures harder to delineate as well as making the identified structures appear larger than they actually are.

A thorough visual examination of the 32 compounded patient datasets of a range of image qualities and diagnostic values suggests that ***Temporal Compounding*** can significantly

reduce tissue speckle as well as dynamic noise in cardiac tissue and cavities. It can also enhance cardiac structures whose boundaries are hard to delineate due to high levels of noise. On the other hand, ***Temporal Compounding*** may introduce modest tissue/cavity boundary blurring. Blurring is mostly observed around fast moving structures, such as valves, with some blurring cases identified along cavity walls. It is strongly believed that part of the blurring is due to quantification errors and minor inaccuracies in the spatio-temporal alignment. A considerable proportion of the potential blurring is diminished by the accurate and robust spatio-temporal alignment techniques presented in this chapter.

#### 3.8.2.3. Effect on clinical measurements performed on patient data

The results presented in Figures 3.25 and 3.26 along with Tables 3.11 to 3.13 enable the evaluation of the effect of ***Temporal Compounding*** on clinical measurements performed on routine cardiac ultrasound examinations. In all plots (Figures 3.25 and 3.26), two point clusters were distinguished. The first narrower cluster, with average measurement values ranging around 10mm, corresponded to wall thickness measurements, such as the IVSd and LVPWd. The second wider cluster, with average measurement values ranging around 40mm, corresponded to cavity measurements, such as the LVIDd, LVIDs and LADs. Each cluster lay in a specific range which appeared to be largely unaffected by whether measurements were performed on the original or the compound datasets. Similarly, no major variations were observed between the limits of agreement (±2SD) for measurements performed on the original or the compounded datasets. Given the fact that no major outliers were identified in the repeatability and agreement plots, it appears that repeated measurements on original and compound data tend to be relatively similar. Furthermore, the mean measurement difference in each plot lay very close to zero, indicating that no significant or systematic bias is observed within each measurement method or between the two measurement methods (utilising original or compound datasets). A thorough inspection of the results presented in the plots indicates a strong potential for the original and compounded data to be interchangeable when performing clinical cardiac ultrasound measurements.

Table 3.11 enables a more thorough investigation on the effect of ***Temporal Compounding*** on clinical measurements performed on routine cardiac ultrasound examinations. The repeatability and agreement coefficients of a clinical measurement depended both on the type of clinical measurement performed as well as the echocardiographer making the measurement. For both echocardiographers the overall level of agreement between clinical measurements performed on original and compounded data lay in levels very similar to the corresponding repeatability coefficients with no substantial or systematic bias being

observed. Echocardiographer 1 displayed a confident yet sometimes adventurous approach on making clinical measurements. Furthermore, comfortable with new technologies, Echocardiographer 1 expressed approval towards the diagnostic quality of the new compounded datasets, something that was verified by the overall improvement in measurement repeatability observed on the compounded datasets. More precisely, the repeatability coefficient of the measurements on compounded data increased by 11%, 33%, 17% and 29% for the IVSd, LVIDd, LVPWd and LVIDs measurements respectively. On the other hand, the repeatability coefficient of the LADs measurement on compounded datasets demonstrated a 35% drop. Nevertheless, when considering all clinical measurements, a considerable overall 23% improvement on the repeatability coefficient was introduced to measurements performed on compounded data compared to those performed on the original unprocessed data. Echocardiographer 2, being more hesitant with new technologies, adopted a more thorough and conservative approach to making clinical measurements and indicated reluctance towards the diagnostic quality of the compounded datasets. Such a measurement approach was apparent by the higher repeatability and agreement levels displayed on the clinical measurements when compared with those of Echocardiographer 1. Such higher repeatability and agreement levels in the original data reduced the scope for improvement by using the processed data. The repeatability coefficient of measurements performed on compounded data increased by 29%, 44%, 48% and 36% for the IVSd, LVIDd, LVPWd and LVIDs measurements respectively. On the other hand, there was a marginal 2% decrease on the repeatability coefficient of the LADs measurements for measurements performed on compounded data. Despite Echocardiographer 2's reluctance towards compounded datasets, when considering all clinical measurements a considerable overall improvement of 13% was introduced on the repeatability coefficient of measurements performed on compounded data compared to those performed on the original unprocessed data.

Tables 3.12 and 3.13 indicate whether a clinical measurement was performed or omitted by each echocardiographer on the original and compounded datasets. Both echocardiographers chose to abstain from making some clinical measurements. Similar to the results displayed in Table 3.11, the more conservative approach adopted by Echocardiographer 2 on making clinical measurements, when compared to Echocardiographer 1, was apparent. Echocardiographer 1 chose to attempt the majority of the clinical measurements while Echocardiographer 2 omitted measurements, taking fewer risks on challenging datasets. Avoiding clinical measurements on challenging datasets reduced the scope for improvement in the repeatability and agreement levels introduced by using the processed data. Nevertheless, a considerable percentage (63%) of the measurements omitted by

Echocardiographer 1 was also omitted by Echocardiographer 2. Furthermore, 88% of the measurements omitted by Echocardiographer 1 occurred in datasets where Echocardiographer 2 omitted at least one measurement. Visual inspection of the omitted datasets demonstrated high levels of corruption on the measured cardiac structures either by high noise or shadowing levels. For datasets where the IVS was masked out due to heavy artifact levels, measurements such as the IVSd, LVIDd and LVIDs were omitted. Similarly, for datasets on which the PW was heavily corrupted measurements such as the LVPW, LVIDd and LVIDs were omitted. The increase in the LVIDs measurements omitted by Echocardiographer 2 when compared to the corresponding LVIDd measurements is attributed to the enhanced difficulty to accurately delineate the PW boundaries in ES frames. While not very common, there were measurements omitted only on compounded datasets. This behaviour can be attributed to the high level of familiarity of echocardiographers with conventional, unprocessed cardiac ultrasound data. Both echocardiographers have been working for many years with challenging cardiac ultrasound data and have developed procedures utilising subtle features that enable them to perform the required clinical measurements. Currently, both echocardiographers lack the confidence to make some challenging clinical measurements on the compounded datasets which were presented to them for the first time during this study. Nevertheless, especially for Echocardiographer 2, there was still a noticeable drop (approximately 47%) in the number of omitted measurements when utilising compounded datasets. This drop is attributed to the enhancement of structures masked out by heavy artifacts, such as the IVS, introduced by ***Temporal Compounding***.

The results on the effect of ***Temporal Compounding*** on routine clinical measurements are very promising. The fact that the measurement agreement lay in levels very similar to the corresponding measurement repeatability coefficient, with no substantial or systematic bias identified, indicates that original and compounded datasets can be interchangeable when performing clinical measurements on cardiac ultrasound data. Furthermore, performing ***Temporal Compounding*** can reduce the number of omitted clinical measurements as well as enhance the repeatability of the performed measurements. Compounding datasets acquired using a higher frame rate would remove some of the tissue/cavity boundary blurring introduced due to quantification errors. Reduced tissue/cavity boundary blurring can further improve clinical measurement repeatability. Moreover, operator confidence and consequently measurement repeatability is expected to increase as the familiarity of the echocardiographers with the compounded data increases. Therefore, ***Temporal Compounding*** demonstrates great potential for the further improvement in the repeatability

of routine clinical measurements on cardiac ultrasound data. ***Temporal Compounding*** can act as a beneficial alternative to conventional B-mode imaging for clinical measurements.

## 3.9. Conclusions

In this chapter, a novel and effective implementation of ***Temporal Compounding***, a simple method for enhancing the image quality and diagnostic value of cardiac ultrasound data, was introduced and quantitatively evaluated. The accurate and robust spatio-temporal alignment of multi-cycle cardiac data acquired from a single acoustic window is a key process for effective ***Temporal Compounding***. Insufficient spatio-temporal alignment would result in the intensity averaging of frames corresponding to different cardiac phases, introducing severe tissue/cavity boundary blurring to the processed datasets. A 7 control-point interpolating B-Spline was found to provide an accurate representation of the temporal variations between consecutive cardiac cycles. Furthermore, a rigid spatial registration was found to correct for spatial misalignments between temporally aligned frames caused mostly by the patient's respiration motion during data acquisition.

A number of multi-cycle patient cardiac ultrasound datasets were utilised for the quantitative assessment of the effect of ***Temporal Compounding*** on image quality and diagnostic value. Optimal acquisition parameters such as the number of compounded cardiac cycles were identified. Compounding data from 12 cardiac cycles were found to provide the best tradeoff between data enhancement and acquisition time. However, if the acquisition of 12 cardiac cycles is not feasible then ***Temporal Compounding*** data of 4 cardiac cycles or more can still generate considerable data enhancement. Data enhancement includes suppressing tissue speckle and cavity noise substantially, increasing the corresponding SNR as well as the tissue/cavity detectability index (SDNR). Furthermore, by averaging decorrelated instances of the same structure, ***Temporal Compounding*** can enhance tissue structures that are masked out by heavy levels of noise and shadowing. However, ***Temporal Compounding*** was found to have no noteworthy effect on the limited tissue/cavity contrast experienced in cardiac ultrasound data. Moreover, minor spatio-temporal misalignments combined with high noise levels may result in modest tissue/cavity boundary blurring. Nevertheless, due to its effectiveness and simple nature, ***Temporal Compounding*** can act as a first step to post-processing techniques, such as segmentation and registration, whose applicability is limited and sometimes restricted by low image quality (SNR and SDNR) in cardiac ultrasound data.

Having verified the impact of ***Temporal Compounding*** on cardiac ultrasound image quality, its effect on diagnostic value was investigated by assessing the impact on repeatability levels

between routine clinical measurements performed by two experienced echocardiographers. The effect of ***Temporal Compounding*** varied depending on the echocardiographer and the clinical measurement performed. Nevertheless, unlike other noise suppression methods, ***Temporal Compounding*** improved considerably the repeatability level as well as the number of omitted clinical measurements (due to heavy data corruption) when compared to the original unprocessed data. Taking into consideration that both echocardiographers were presented for first time with the processed data, it is strongly believed that there is further scope for improvement as the familiarity of the echocardiographers with the processed data increases. Consequently, ***Temporal Compounding*** has a strong potential to provide a valuable alternative to B-mode data for improving clinical cardiac measurements.

# Chapter 4

# 3D-to-2D Compounding

This chapter extends the notion of spatial compounding of cardiac ultrasound data acquired through a single acoustic window, which is presented in Chapter 3. ***3D-to-2D Compounding*** is introduced as a novel method for the suppression of speckle/noise by averaging spatially adjacent (along the elevation plane), partially decorrelated, 2D slices of the heart. The 2D slices are extracted as a thin angular sub-sector of a volumetric pyramid scan. A human left ventricle phantom is utilised as a controlled environment in order to examine the effect of the angular range of the volumetric sector utilised during ***3D-to-2D Compounding*** on (i) quantitative image quality metrics such as tissue SNR, cavity SNR, tissue/cavity Contrast and detectability index (SDNR) as well as (ii) the tissue/cavity boundary blurring introduced to the imaged structure. Optimal acquisition parameters, such as 3D angular sector width and angular inter-slice displacement, are derived. Human volunteer data, acquired applying optimal acquisition parameters, are then utilised to examine the effect of ***3D-to-2D Compounding*** on image quality and diagnostic value. Diagnostic value is assessed through variations in the repeatability level of five clinical measurements performed on routine echocardiographic examinations. All data are acquired using a clinical, 2D phased array probe. 3D sectors of various angular ranges are acquired using mechanically controlled, angular probe displacement along the elevation plane.

## 4.1. Introduction

As mentioned in earlier chapters, spatial compounding on cardiac ultrasound data is challenging due to the constant, rapid heart motion and the limited acoustic windows through the patient rib cage and between the ribs and lungs. Chapter 3 introduces and evaluates *Temporal Compounding*, a method for the spatio-temporal alignment and spatial compounding of cardiac ultrasound data acquired over multiple cardiac cycles from a single acoustic window. *Temporal Compounding* provides a simple and effective method for suppressing speckle/noise while enhancing the diagnostic value of the processed data.

However, multiple cardiac cycles are required, imposing minor rules and restrictions on the data acquisition procedure.

Chapters 1 and 2 provide a review on current 3D and 4D cardiac ultrasound acquisition technologies and research. Recent advances in data acquisition technologies, such as matrix transducers (von Ramm & Smith, 1990; Sheikh et al., 1991; von Ramm et al., 1991; Wang et al., 2003), enable the acquisition of real-time, non-gated, 4D cardiac ultrasound data through a single acoustic window (Figure 4.1). Real-time 4D acquisition, though a great technological advance, has not yet established itself in clinical cardiac ultrasound examinations. The visual complexity and some time incompleteness of the volumetric cardiac data (i.e. heart too big to fit in 3D volume) currently limit its clinical usability.

Current approaches on spatial compounding of 3D/4D cardiac ultrasound data involve the acquisition, alignment and compounding of multiple volumes scanned through different acoustic windows to a single compounded volume (Grau & Noble, 2005; Soler et al., 2005; Yao & Penney, 2008; Rajpoot et al., 2009; Szmigielski et al., 2010; Yao et al., 2010). Speckle/noise is suppressed and tissue structures are in some cases enhanced. However, compounding of multiple 4D scans requires extended data acquisition time while the resulting compounded volumetric data are complex and suffer from limited clinical usability. Furthermore, compounding of multiple 4D scans is heavily dependent on the accurate and robust spatiotemporal registration of the available datasets (Rohling et al., 1997). Such registration methods are a current, challenging research subject due to the noisy nature of cardiac ultrasound data. *Elevational Spatial Compounding* (Li & O'Donnell, 1994) provides an early, preliminary attempt to use 3D data acquired by steering the imaging plane using small inclinations along the elevation plane to generate an enhanced 2D dataset. ***3D-to-2D Compounding*** extends the notion of *Elevational Spatial Compounding* by utilising real-time 4D matrix transducer technology for the acquisition of adjacent partially decorrelated cardiac slices and compounding them to an improved 2D B-mode frame sequence. ***3D-to-2D Compounding*** is also a versatile extension of the elemental *Thick Slice* functionality provided by the Philips IE33 scanner (Figure 4.1) along with the X3-1 matrix-array transducer (Yang et al., 2008).

## 4.2. Aims and contributions

The aim of this chapter is to introduce and quantitatively evaluate a novel method for acquiring (through a single acoustic window) and spatially compounding partially decorrelated instances of a cardiac structure in order to (i) suppress tissue speckle as well as

static and dynamic noise within cavities, and (ii) enhance the detectability between cardiac tissue and cavities.

The contributions of this chapter are:

- ***3D-to-2D Compounding***, a simple and novel method for acquiring and compounding adjacent (along the elevation plane), partially decorrelated cardiac slices from a single acoustic window.

- Developing a simple, easily reproducible and low cost human left ventricle phantom, using a widely accepted, non-commercial, agar-based Tissue Mimicking Material (TMM), as a controlled environment for:

    - The quantitative analysis and evaluation of the ***3D-to-2D Compounding*** method.

    - The derivation of optimal acquisition parameters, such as inter-slice angular displacement and 3D sector angular range, ensuring the clinical feasibility of ***3D-to-2D Compounding***.

- Assessing the effect of ***3D-to-2D Compounding*** (using optimal acquisition parameters) on volunteer cardiac ultrasound scans utilising quantitative measures such as tissue Signal-to-Noise Ratio (SNR), cavity SNR, tissue/cavity Contrast and Signal Difference to Noise Ratio (SDNR) also known as detectability index.

- Examining the effect of ***3D-to-2D Compounding*** on routine clinical measurements performed on patient cardiac ultrasound scans of a range of image qualities and diagnostic values.

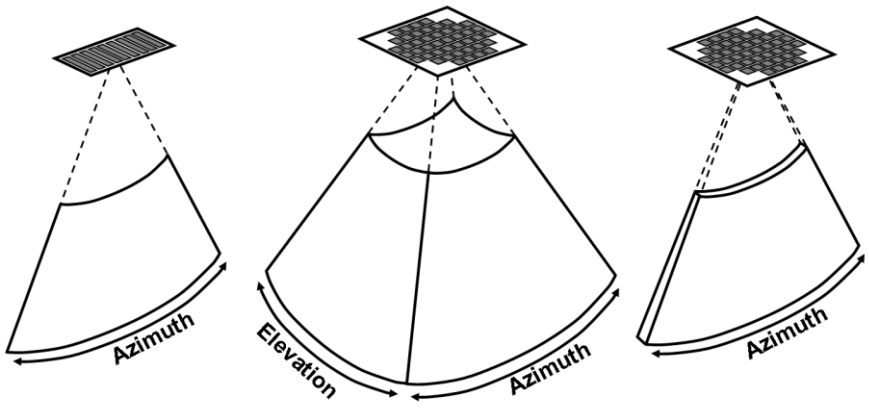


**Figure 4.1.** Left: 2D acquisition using a phased array probe. Centre: 3D acquisition using a matrix probe. Right: Thick Slice acquisition (on Philips IE33) using a matrix probe.

## 4.3. Materials

### 4.3.1. Scanning setup

B-mode frame sequences over adjacent slices (along the elevation plane) are acquired using a mechanically displaced 2D phased array cardiac probe (Figure 4.2). The 2D probe is attached to an *RS 351-4647* unipolar geared stepper motor (Figure 4.2 and Table 4.1). The motor is powered with 12 V by an *ISO-TECH IPS2302A* laboratory DC power supply and driven by a *Tektronix AFG3102* arbitrary function generator (Figure 4.3 and Table 4.2). Each slice is offset slightly from the previous one with a small angular displacement $\theta$°. The collection of adjacent slices forms a thin angular 3D sector of a volumetric pyramid scan (Figures 4.4 and 4.5). The combined B-mode frame sequences acquired over each adjacent slice form a 4D sector of the scanned cardiac structure. In a clinical setup, a 4D matrix transducer can be used for the real-time, simultaneous acquisition of the adjacent slices. However, with the available acquisition setup, a manually controlled displacement of a 2D probe enables the investigation of optimal acquisition parameters such as inter-slice angular displacement and 3D sector angular width. Such parameters have direct effect on the SNR increase as well as the tissue boundary blurring introduced to the compounded data. Moreover, wide angular sector acquisition lessens the effectiveness of ***3D-to-2D Compounding*** on patients with restricted acoustic windows through the rib cage and lungs. Therefore, the objective is to introduce as higher SNR increase as possible while keeping the acquisition sector's width to a minimum.

**Table 4.1.** *RS 351-4647* geared stepper motor attributes.

| Attribute Type | Attribute Value |
|---|---|
| Motor Step Angle | 7.5° |
| Gearbox Ratio | 125:1 |
| Steps per Revolution | 6000 |
| Holding Torque | 1000 mNm |
| Voltage | 5 V dc |
| Shaft Diameter | 4 mm |
| Length | 25 mm |
| Frame Size | 42 mm |

**Table 4.2.** *Tektronix AFG3102* setup.

| **Attribute Type** | **Attribute Value** |
|---|---|
| Function | Pulse |
| Run Mode | Burst |
| Frequency | 300 Hz (maximum for available motor) |
| Number of Cycles | 2 (0.12°) to 6 (0.36°) depending on acquisition inter-slice displacement |
| Inter-Burst Interval | Variable – duration of 2 cardiac cycles. |
| Amplitude | 0 - 5 V (2.5 V offset) |

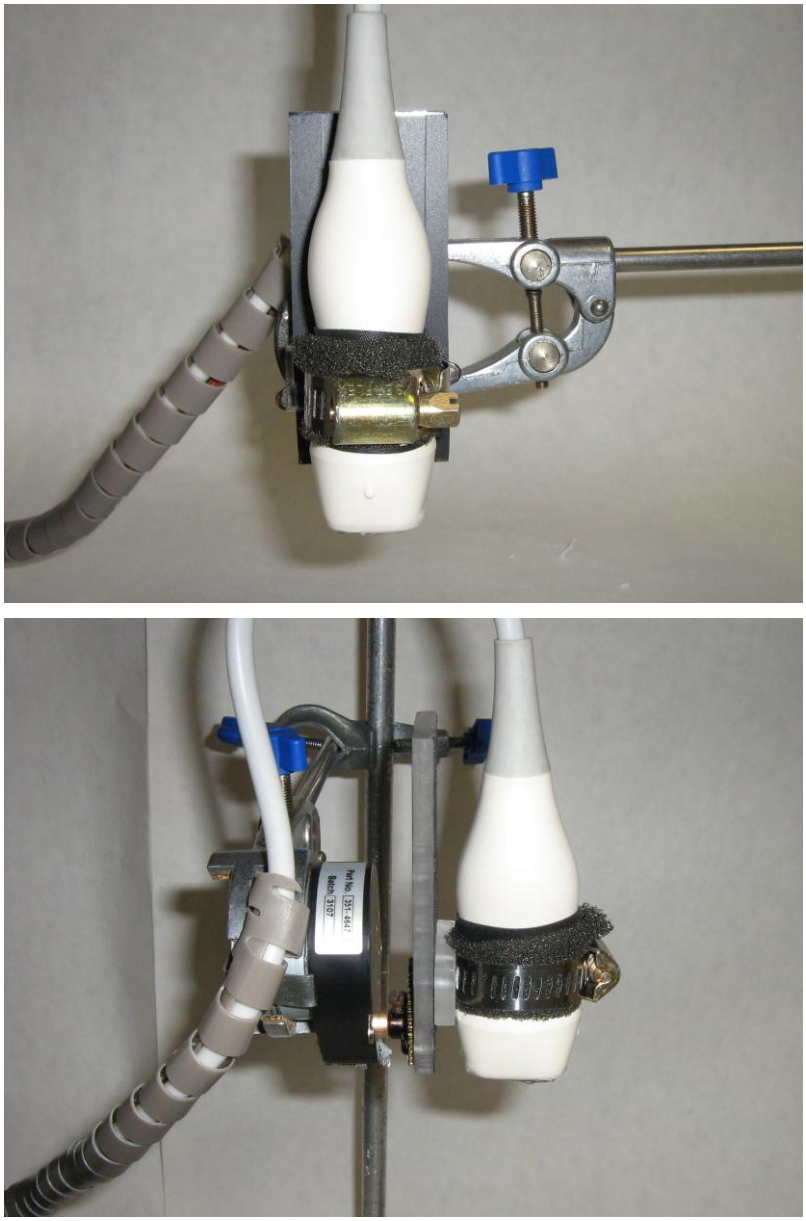

**Figure 4.2.** Close up of the motor-arm attached on the phased array probe that accommodates acquisition of adjacent slices by angular displacement of the probe.

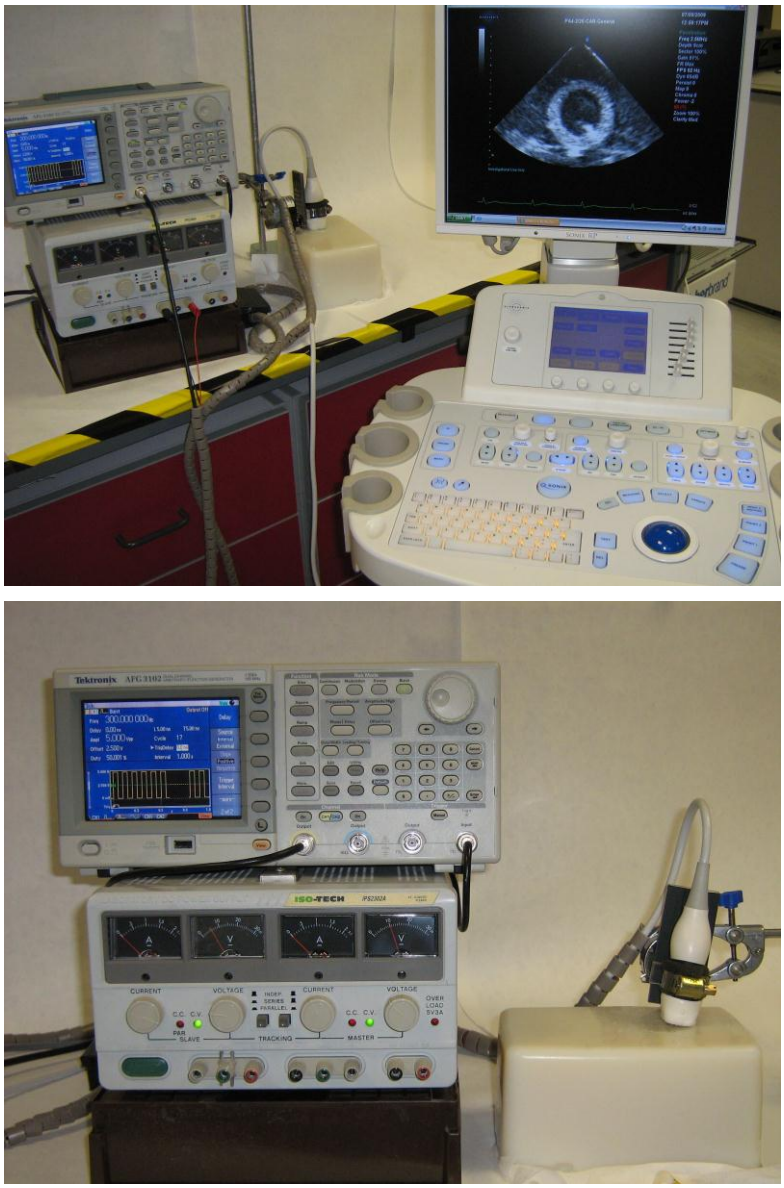


**Figure 4.3.** Top: Experimental setup including phantom, power supply, signal generator, motor-arm and cardiac ultrasound scanner Sonix-RP. Bottom: A close up to the acquisition setup.

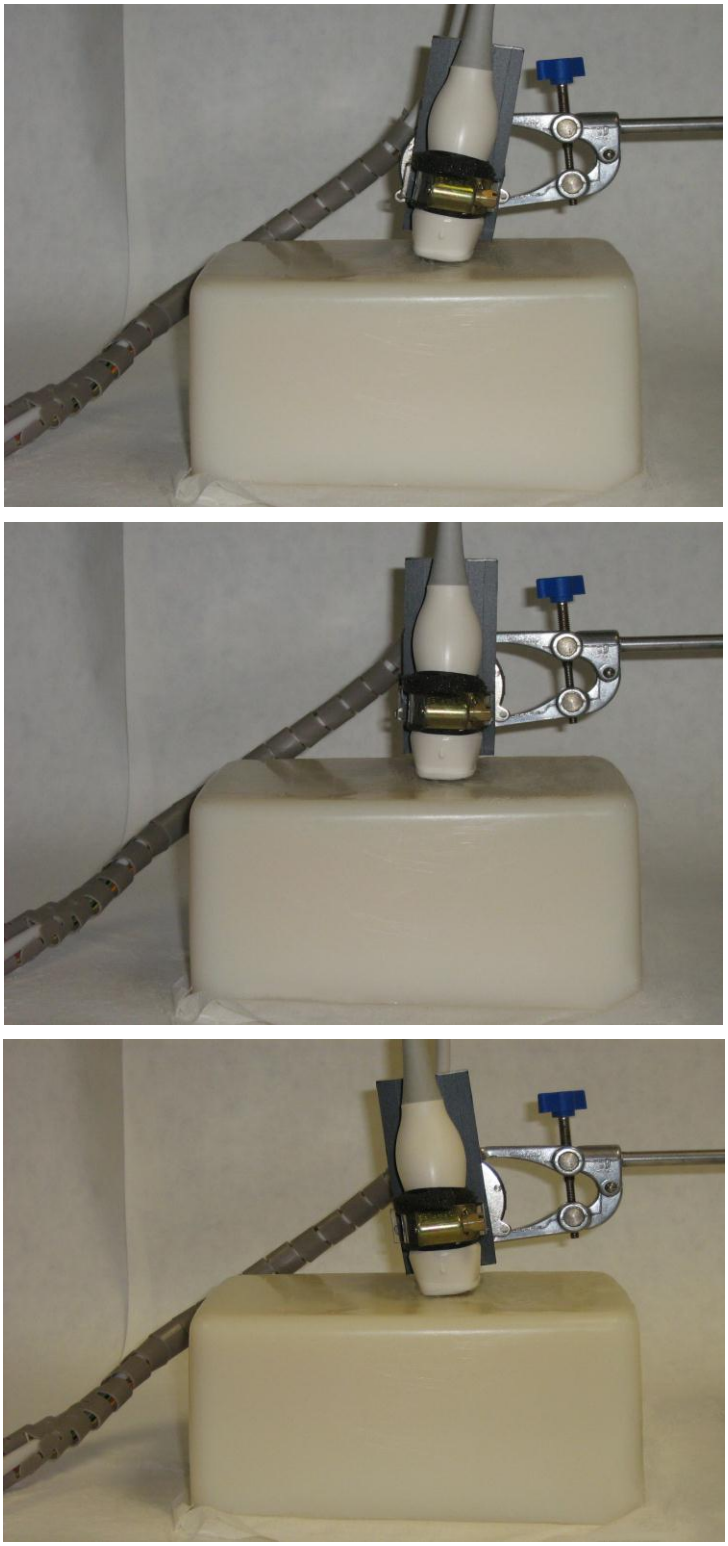

**Figure 4.4.** Example acquisition of adjacent slices. From top to bottom: negative angular displacement, centre acquisition, positive angular displacement.

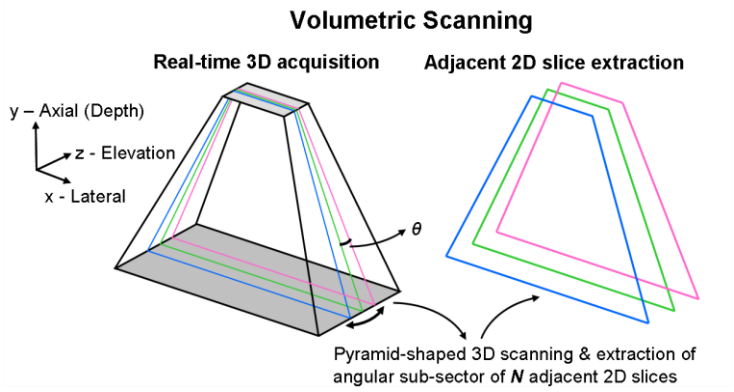


**Figure 4.5.** Diagram of volumetric ultrasound acquisition. 3D volume is formed by a series of adjacent 2D slices, each with an angular inter-slice distance $\theta$°.

### 4.3.2. Anthropomorphic left ventricle phantom

A range of anthropomorphic cardiac ultrasound phantoms have been proposed over the years (Smith & Rinaldi, 1989; Smith et al., 1993; Smith et al., 1995; Nowicki et al., 1996; Rusk et al., 2000; Hashimoto et al., 2002; Nguyen et al., 2003; Playford et al., 2003; Langeland et al., 2004). In this work a simple, easily reproducible and low cost human left ventricle (LV) phantom is designed and developed for the quantitative analysis and evaluation of ***3D-to-2D Compounding***. The test device is constructed using a solid TMM composed by an agar based gel. The TMM solution provides tissue equivalence using glycerol to match the speed of sound in human tissue (1540 m/s) as well as particles such as Silicon Carbide (SiC) and Aluminium Oxide ($Al_2O_3$) to modify the ultrasound attenuation and the backscatter generating acoustic speckle on B-mode scans. The solution is based on a widely accepted non-commercial recipe for ultrasound test devices first proposed in (Teirlinck et al., 1998).

The proposed anthropomorphic cardiac phantom provides a simple anatomic representation of an adult human LV. It consists of a cup-shaped (prolate-ellipsoid) TMM model of an adult human LV positioned along the elevation plane within a bloc of agar based gelatin (Figure 4.6). When scanned along the *x*-*y* plane, the phantom simulates a parasternal short axis slice of a blood filled adult human LV. The solution of the agar based gelatin is very similar to the TMM solution. However, the SiC and $Al_2O_3$ particles have been omitted to avoid ultrasound back-scattering and speckle formation. The LV model is located at a depth of 5cm (centre of the model), has a maximum cavity diameter of 4cm, maximum wall thickness of 1cm and a cavity depth of 6cm, typical values for a male human LV during the systole phase. Wall thickness and cavity diameter may vary at different locations similarly to a real human left ventricle. Figure 4.7 displays 3D segments as well as a 2D slice (*x*-*y* plane) of the LV phantom acquired using a clinical Philips IE33 scanner and an X3-1 matrix-array transducer.

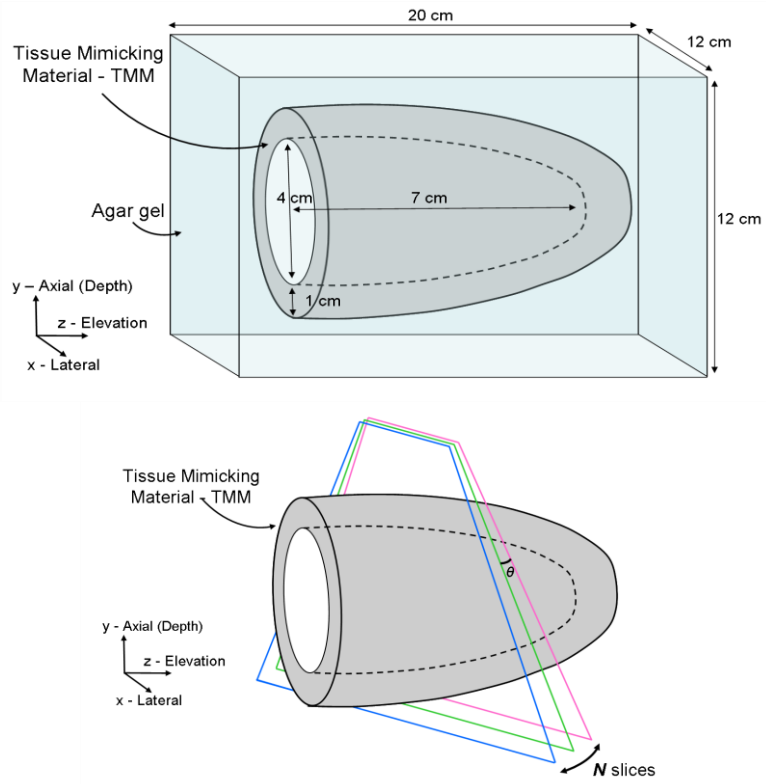


**Figure 4.6.** Left ventricle TMM phantom enclosed in an agar gelatine filled container. Scanning is performed along the *x-y* plane simulating a parasternal short axis slice of an adult human left ventricle.

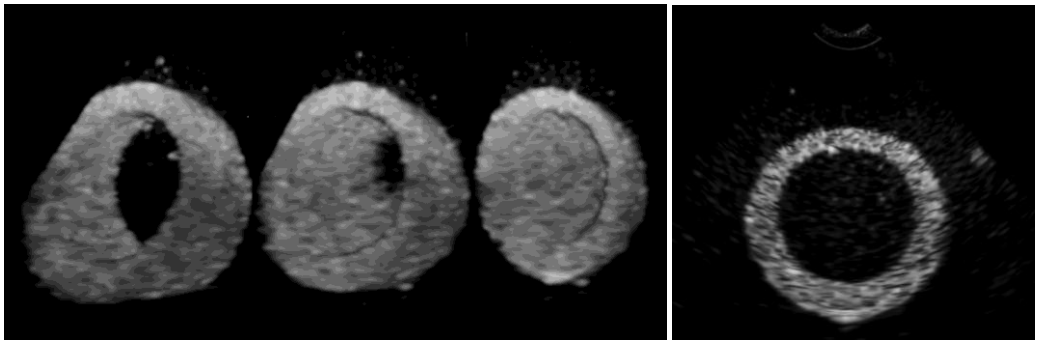

**Figure 4.7.** Left: 3D segments of the LV Phantom. Right: 2D scan of the LV Phantom. Clear boundary between the TMM structure and the agar filled container in both 3D and 2D.

## 4.4. Data acquisition

The developed LV phantom provided a controlled environment for the quantitative analysis and evaluation of the ***3D-to-2D Compounding*** method. The phantom enabled the investigation of the relation between the angular width of the volumetric scanning sector against the SNR increase and tissue boundary blurring introduced to the scanned structure during ***3D-to-2D Compounding***. It also enabled the examination of the relationship between inter-slice angular displacement and SNR increase. Consequently, the phantom facilitated

the derivation of optimal acquisition parameters that were subsequently utilised for acquiring datasets from healthy volunteers. The volunteer data were then used to examine the effect of ***3D-to-2D Compounding*** on routine clinical measurements.

### 4.4.1. Phantom data acquisition

The LV phantom was scanned using the Ultrasonix Sonix-RP ultrasound scanner along with a 2 to 4 MHz phased array cardiac probe. Due to restrictions introduced by the phantom's construction approach, all data were acquired along the x-y plane simulating a parasternal short axis slice of an adult human left ventricle. Each dataset consisted of frames acquired from adjacent slices along the elevation plane with inter-slice angular displacement of 0.12° (2 motor steps). 167 frames from adjacent slices formed the 3D acquisition sector. The angular 3D sector width was 19.92°, 9.96° from either side of the central acquisition plane. The probe frequency was set to 3.3MHz, a typical frequency for acquiring adult human cardiac data. The scanning depth and beam focus were set at 9cm and 5cm respectively ensuring optimal acquisition focusing approximately in the centre of the LV structure. Other acquisition parameters such as sector width and gain were optimally set by the operator.

### 4.4.2. Volunteer data acquisition

25 multi-cycle cardiac datasets from 5 healthy volunteers were acquired by an experienced echocardiographer in the Echocardiography department of the Western General Hospital, Edinburgh, during November 2009. All volunteers were male with an average age of 36 (ranging from 27 to 69). B-mode data of the Parasternal Long-Axis view were acquired according to the standards adopted by the British Society of Echocardiography (BSE) (Henry et al., 1980; Feigenbaum, 1994; Fuster et al., 2008). Each cardiac cycle was acquired with an angular displacement relative to the previous acquisition resulting in the acquisition of a 4D sector (Section 4.3.1). No gating was used. Instead, during each acquisition, the rate of the angular displacement was manually set to the heart rate of the scanned volunteer. Volunteers were not requested to hold their breath due to the extended duration of the multi-cycle data acquisition. Consequently, they were requested to breathe as smoothly as possible to avoid large displacements along the scan plane over the duration of the multi-cycle scan. No discomfort was reported by the participants during the acquisition due to the mechanically rotating extension to the probe.

For the data acquisition an Ultrasonix Sonix-RP ultrasound scanner was used along with a 2 to 4 MHz phased array probe at 32 frames per second (fps). The acquisition parameters such

as scanning frequency, depth, focus, sector width and gain were optimally set by the operator for each individual scan. The captured data were exported as DICOM image sequences of 600x800 pixels with no compression applied to them. Similar to the datasets used in Chapter 3, data quality was manually assessed by the operator according the visual quality and the diagnostic value of the acquired images. The image quality and diagnostic value of our datasets ranged from low (4) to average (6) and high (15). Four datasets were discarded, three of them due to the high level of noise challenging the accuracy of ***3D-to-2D Compounding*** and one due to repeated loss of contact between the probe and the patient.

## 4.5. Data processing

Similarly to *Temporal Compounding*, there are 3 steps to ***3D-to-2D Compounding***: (i) the identification of ED and ES frames within a B-mode sequence, (ii) the spatio-temporal alignment of frames from consecutive cardiac cycles and (iii) the spatial compounding of the aligned data. The first two steps are not required if the acquisition of 3D volumes is performed using a matrix-array transducer. Figure 4.8 provides a diagram for the process.

### 4.5.1. Identification of ED and ES and spatio-temporal alignment

As mentioned in Chapter 3, the temporal behaviour of the heart may vary over consecutive cardiac cycles. If the adjacent slices are acquired over consecutive cardiac cycles then the corresponding B-mode frame sequences needed to be temporally aligned prior to any spatial compounding performed on them. This step is not required if the adjacent slices are acquired using a 4D matrix transducer. However, with the current acquisition setup insufficient temporal alignment would result in compounding frames corresponding to different cardiac phases, leading to severe blurring of anatomic structures making clinical measurements inaccurate and unrepeatable. The non-linear method introduced and evaluated in Chapter 3 was used for the temporal alignment of our datasets. Initially, the inter-frame similarity coefficient (*CCC*) was used to semi-automatically identify all ED and ES frames within each frame sequence. Then a *1D interpolating cubic B-Spline* was used to temporally align all frames within the corresponding cardiac cycles acquired from each adjacent slice. Rigid spatial registration was employed to align frames prior to spatial compounding, eliminating small movements mostly due to patient respiration motion (Section 3.5.1.4).

### 4.5.2. Spatial compounding

The spatio-temporally aligned frames from adjacent slices were spatially compounded to a single B-mode frame sequence. Similar to *Temporal Compounding*, intensity averaging was

utilised as the spatial compounding method as a well established and effective method for noise suppression in ultrasound datasets. The intensity of each pixel within the resulting frame was therefore set as the average intensity value of the corresponding pixels from all the spatio-temporally aligned frames.

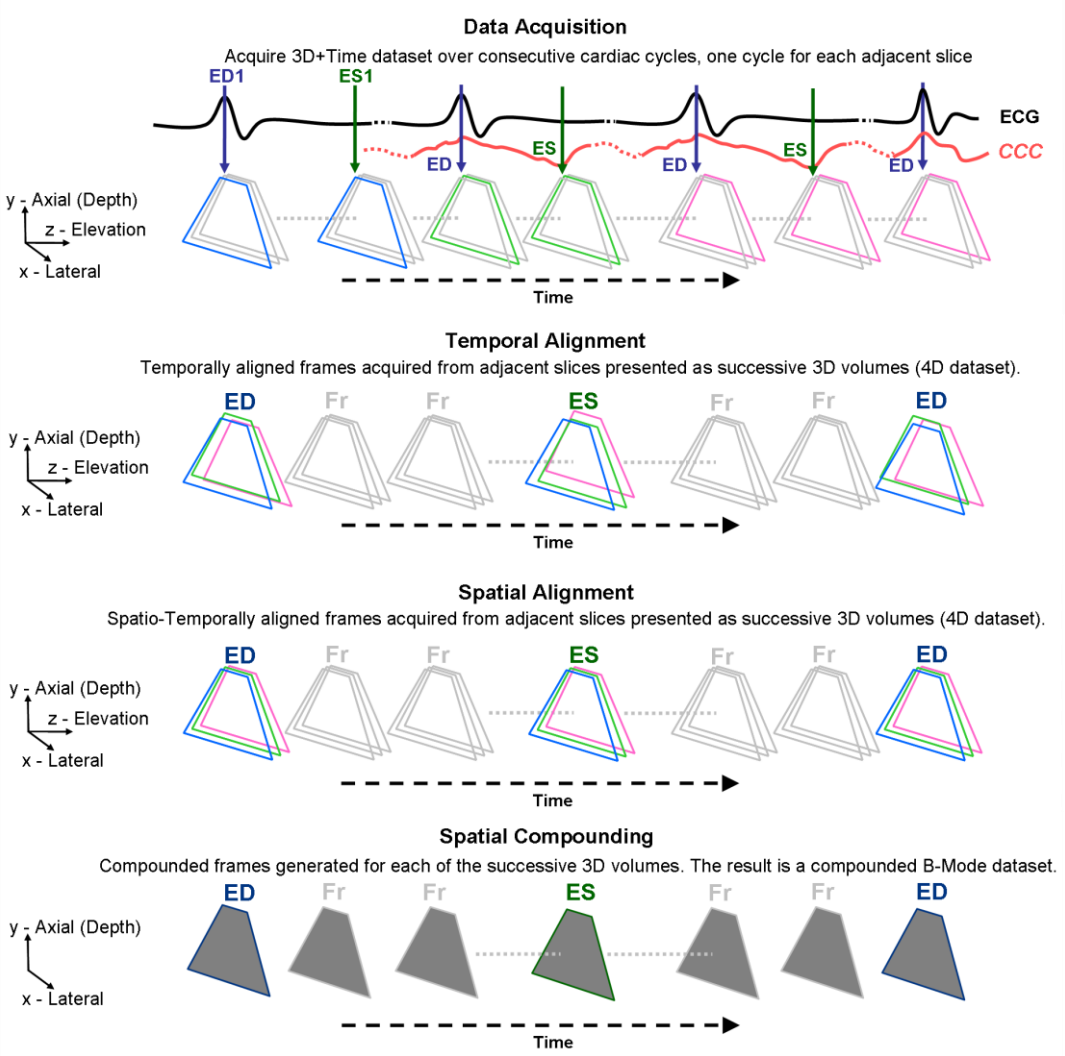


**Figure 4.8.** Diagram of the ***3D-to-2D Compounding*** process with the current data acquisition setup.

## 4.6. Data analysis and results

A range of quantitative and qualitative results are presented in order to assess ***3D-to-2D Compounding*** on cardiac ultrasound data. The main objective is identifying optimal acquisition parameters that will ensure the clinical feasibility of ***3D-to-2D Compounding*** by achieving adequate noise suppression while (i) maintaining tissue/cavity boundary blurring to a clinically acceptable level and (ii) keeping data acquisition time and processing requirements to a minimum by limiting the number of adjacent compounded slices.

### 4.6.1. Phantom study

Figure 4.9 displays a set of images acquired using the LV phantom. Figure 4.9.a provides an unprocessed, B-mode scan of the *x-y* plane of the LV Phantom. Acquisition depth was set to 9cm, sector width was set to 80% and beam focus depth was set to 5cm, approximately at the centre of the LV cavity. The remaining images in Figure 4.9 (b – f) display compounded frames for increasing 3D acquisition sector widths ranging from 2.4° to 14.4°.

#### 4.6.1.1. Effect on tissue SNR, cavity SNR, tissue/cavity contrast and SDNR

Two rectangular Regions of Interest (ROI) of 11x35 pixels each, both corresponding to cardiac tissue, were defined approximately equidistant from the scanning focal depth (Figure 4.10). The ROI on the top LV wall corresponds to the Interventricular Septum (IVS) while the ROI on the bottom LV wall corresponds to the Left Ventricle Posterior Wall (LVPW). Similarly, a third ROI was defined above the LV structure representing the RV cavity. The pixel intensity values at each ROI were used to estimate their corresponding SNR as well as the contrast and detectability index (SDNR) between cardiac tissue and cavity. Figure 4.11 displays two plots with curves representing the tissue SNR on the original and a series of compounded images derived using ***3D-to-2D Compounding*** on data acquired with increasing 3D acquisition sector width and a range of inter-slice displacements. Figure 4.11.a corresponds to SNR changes on the top tissue ROI while Figure 4.11.b corresponds to SNR changes on the bottom tissue ROI. The SNR changes on two acquisition depths are investigated since the inter-slice displacement during 3D acquisition is angular. As a result, the spatial inter-slice displacement increases with depth, possibly affecting the outcome of the compounding process. Figure 4.12 provides a direct comparison between the SNR curves from both tissue ROIs utilising an intermediate inter-slice angular displacement of 0.36°. In a similar manner, Figure 4.13 displays a number of curves representing the cardiac cavity SNR on the original and a series of compounded images derived using increasing 3D acquisition sector width and a range of inter-slice displacements. Figure 4.14 displays a curve of the tissue/cavity detectability (SDNR) on the original and a series of compounded images derived using increasing 3D acquisition sector width. While data from a range of inter-slice angular displacements were derived, the intermediate displacement of 0.36° was utilised for the illustrated SDNR curve. The remaining SDNR curves are omitted since they undergo a similar trend to the illustrated curve. Table 4.3 illustrates the percentage change on each of the five quantitative measures between the original and compounded data for an increasing 3D acquisition sector width.

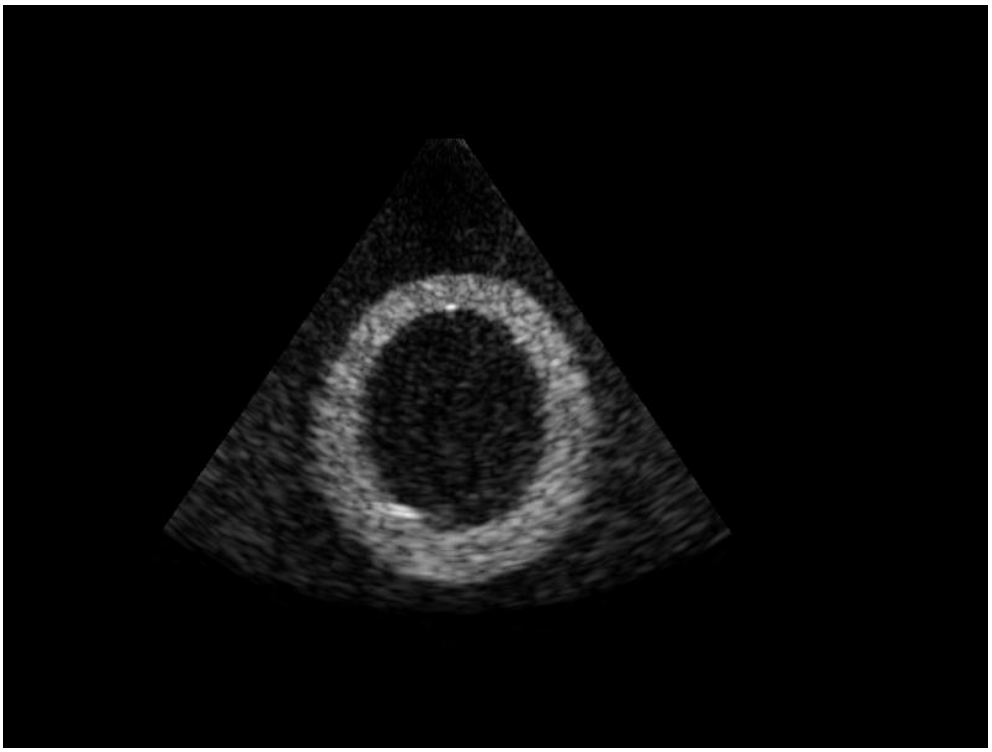

**(a)**

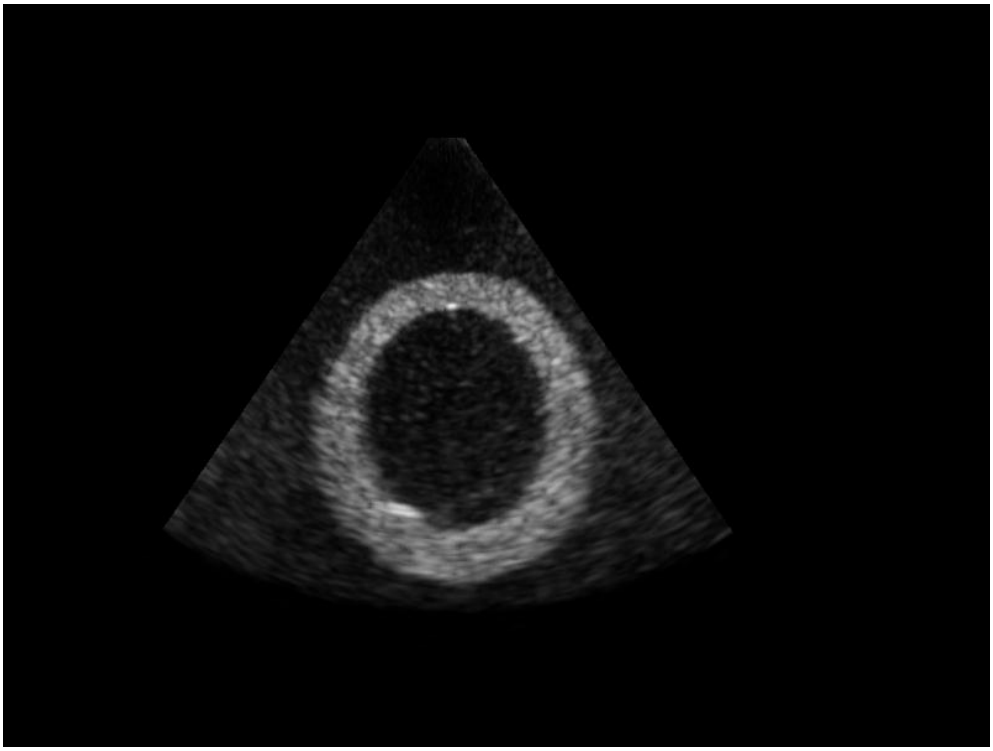

**(b)**

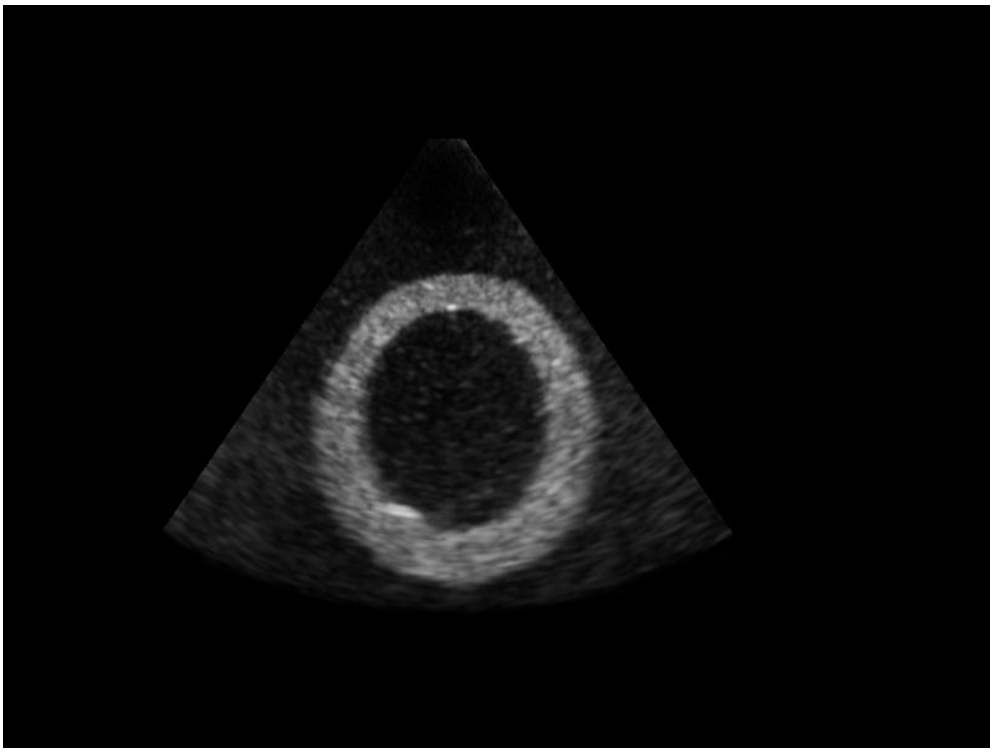

**(c)**

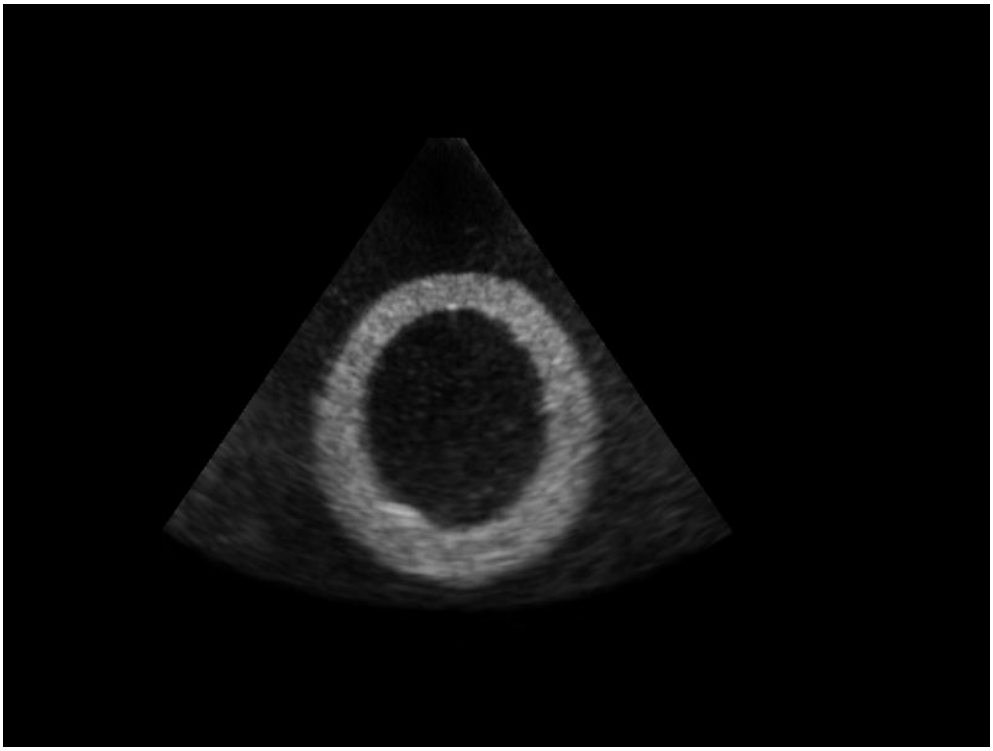

**(d)**

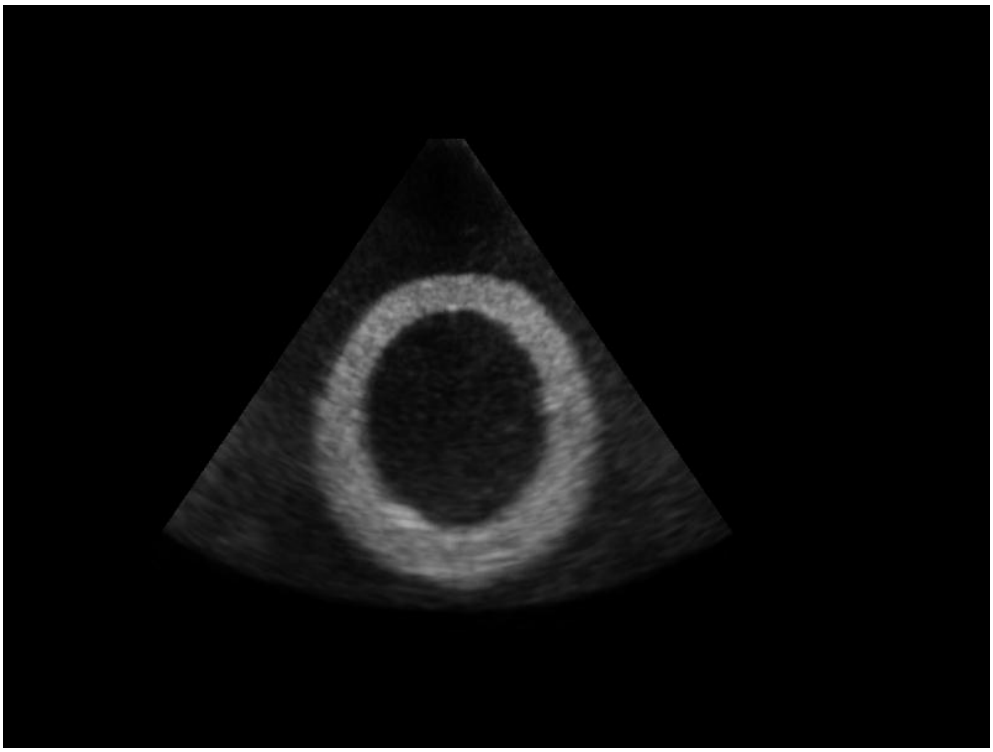

**(e)**

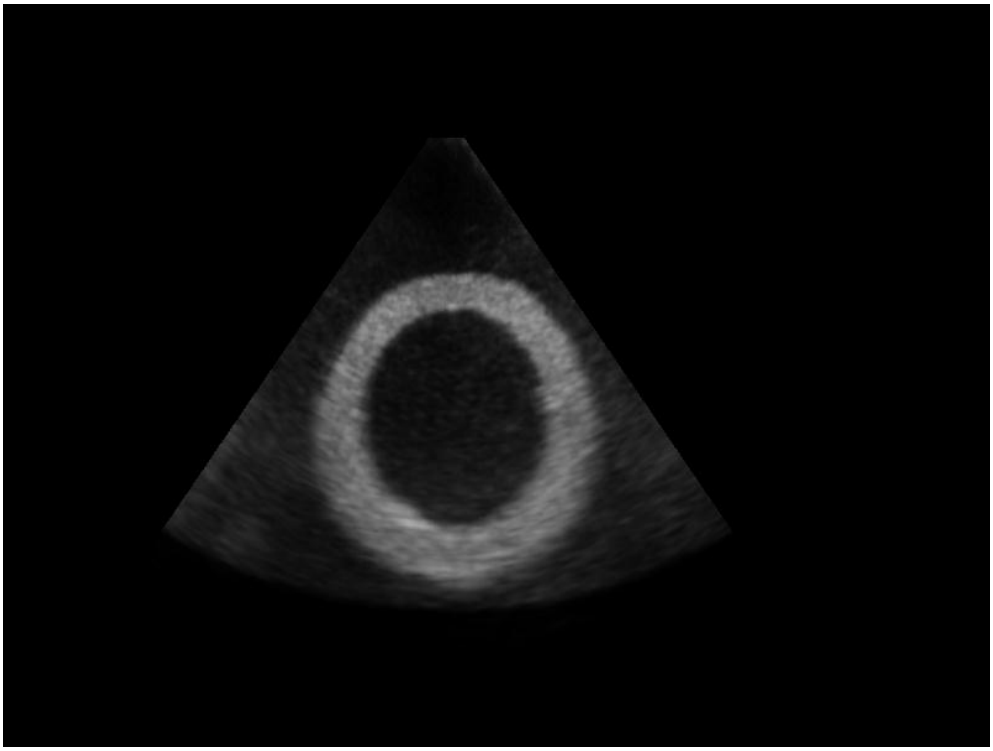

**(f)**

**Figure 4.9.** Original and compounded scans of LV phantom. (a) Original scan, (b - f) Compounded scans with 3D acquisition sector width of (b) 2.4°, (c) 3.6°, (d) 7.2°, (e) 10.8° and (f) 14.4°.

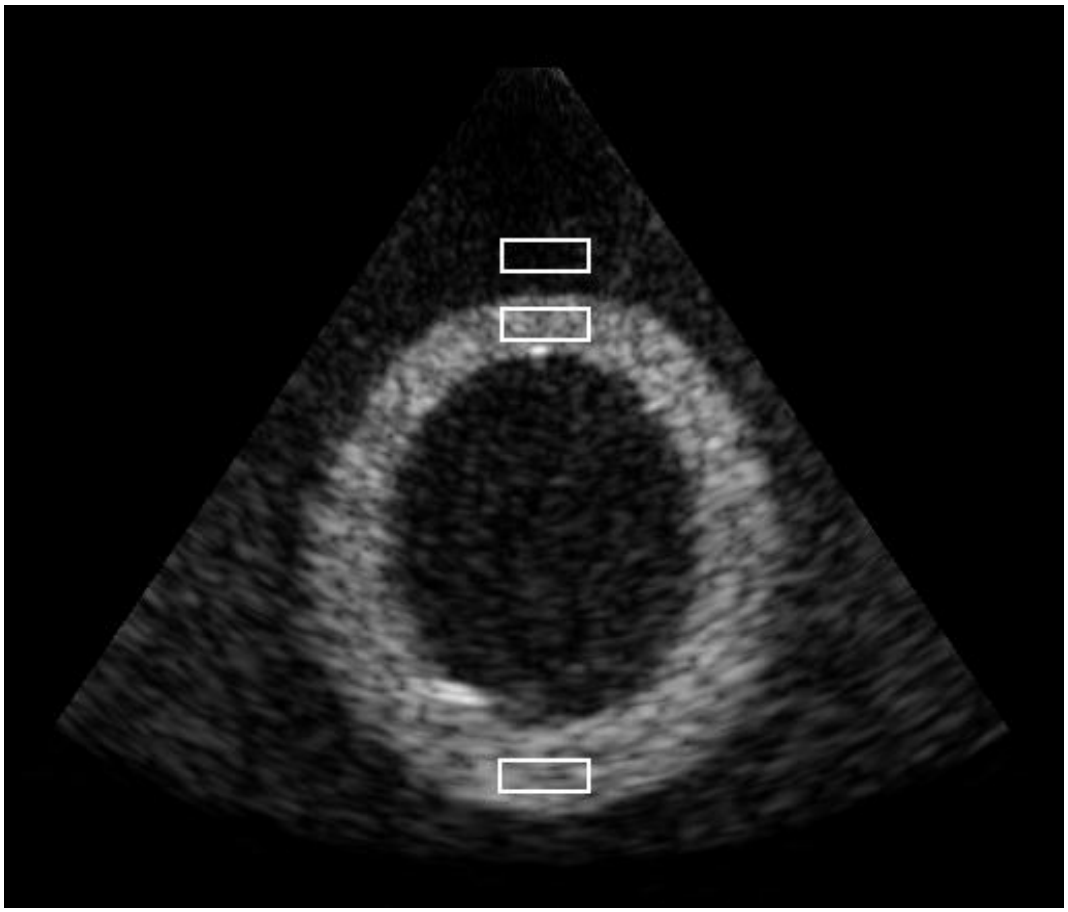

**Figure 4.10.** B-mode scan of LV phantom along with the rectangular ROIs used to derive the SNR, contrast and SNDR values.

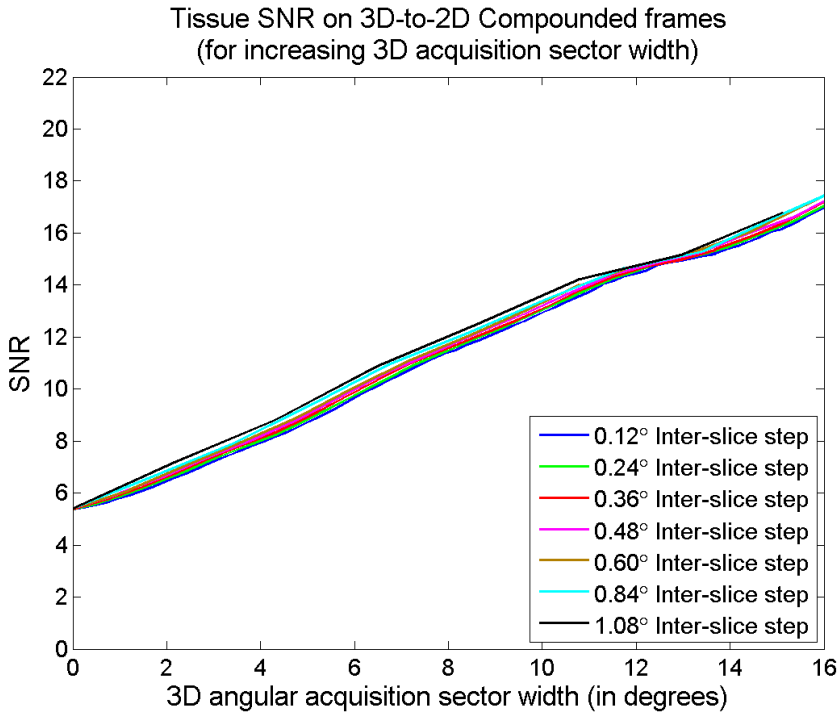


**(a)**

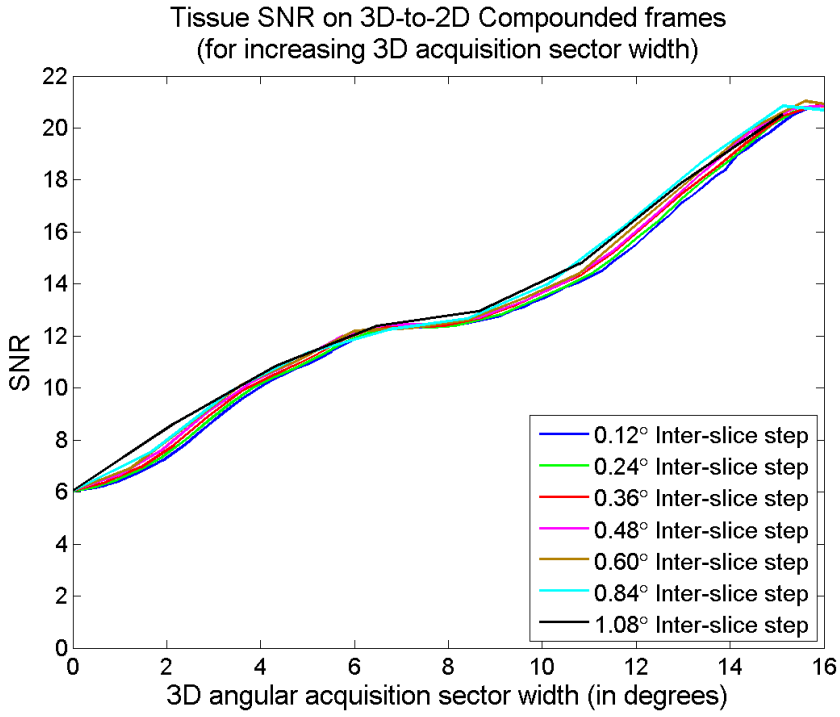


**(b)**

**Figure 4.11.** The effect of ***3D-to-2D Compounding*** on tissue SNR for increasing 3D acquisition sector width and a range of inter-slice displacements. SNR curves for ROIs representing the IVS (a) and LVPW (b) are presented.

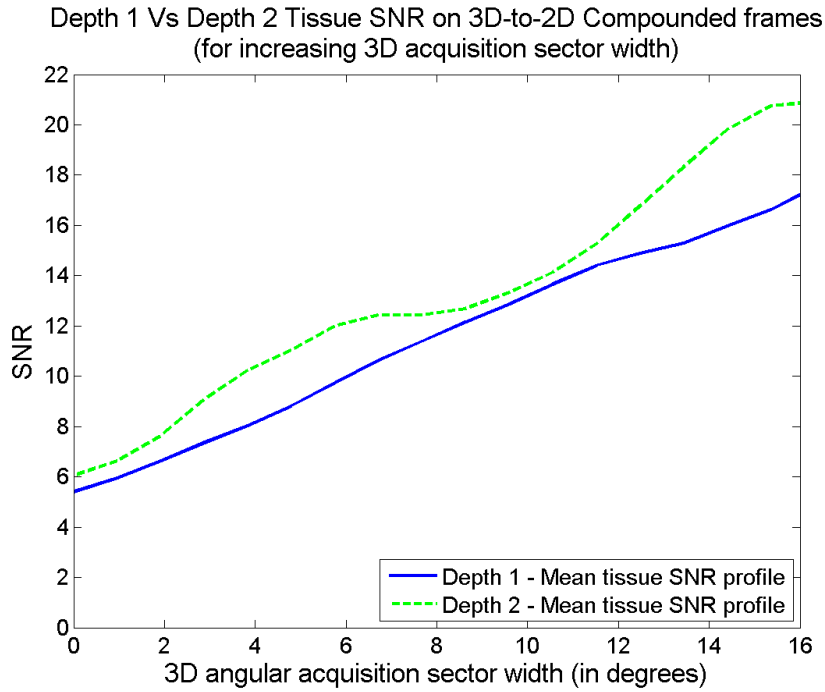


**Figure 4.12.** The effect of ***3D-to-2D Compounding*** on tissue SNR for increasing 3D acquisition sector width. SNR curves for 2 depths are displayed utilising an inter-slice angular distance of 0.36°.

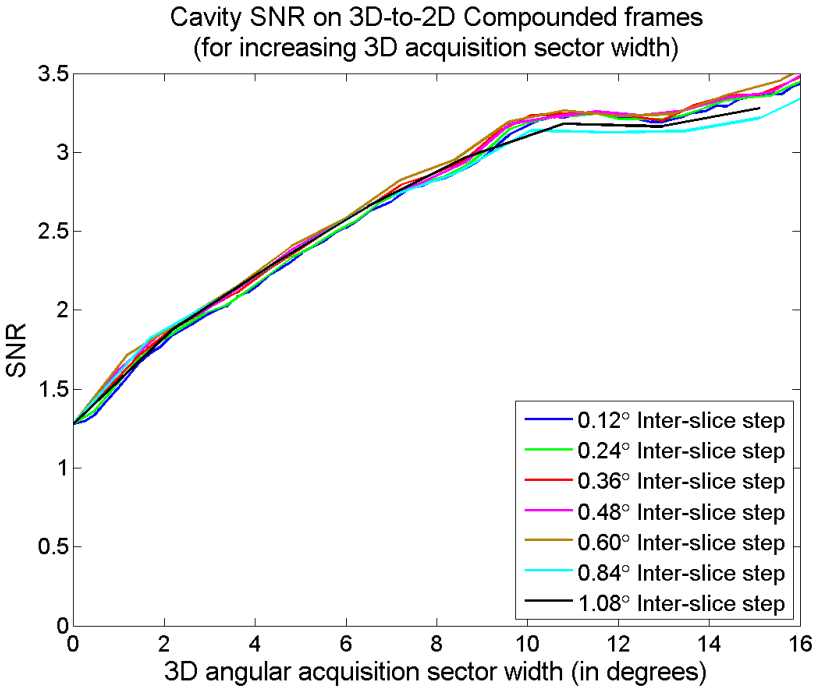


**Figure 4.13.** The effect of ***3D-to-2D Compounding*** on cavity SNR for increasing 3D acquisition sector width and a range of inter-slice displacements.

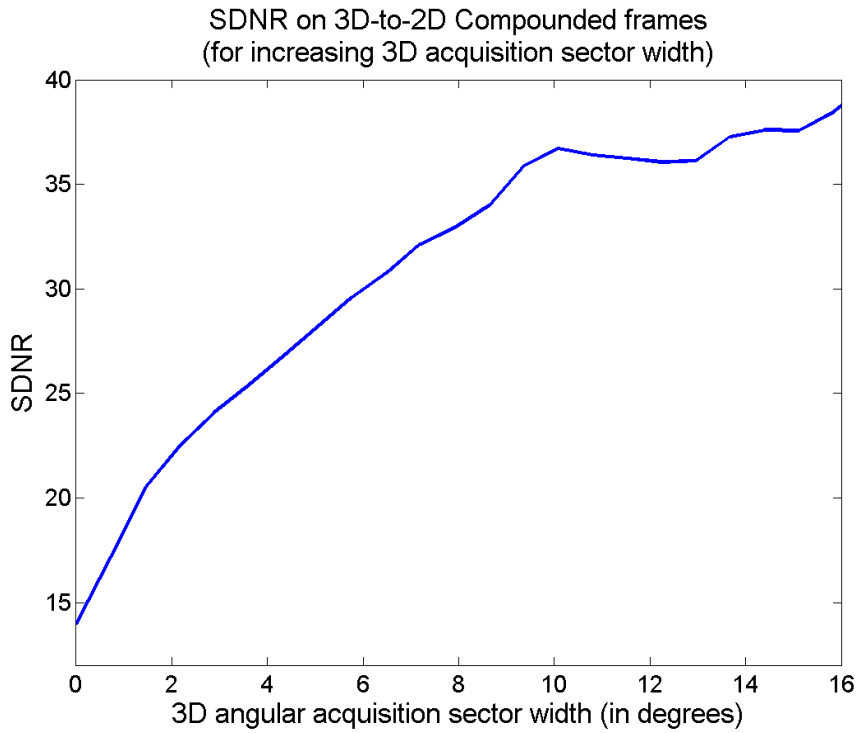


**Figure 4.14.** The effect of ***3D-to-2D Compounding*** on tissue/cavity SDNR for increasing 3D acquisition sector width. An inter-slice angular distance of 0.36° has been utilised.

**Table 4.3.** Mean overall effect of ***3D-to-2D Compounding*** on a range of quantitative measures for increasing 3D acquisition sector width.

| Sector Width | Tissue SNR (Top) | Tissue SNR (Bottom) | Cavity SNR | Contrast | SDNR |
|---|---|---|---|---|---|
| **2.2°** | 24.90% | 29.21% | 46.63% | 1.39% | 60.86% |
| **4.3°** | 54.11% | 73.86% | 76.78% | 1.22% | 91.74% |
| **6.5°** | 91.31% | 104.20% | 107.11% | 0.93% | 120.18% |
| **8.6°** | 123.41% | 109.42% | 130.60% | 0.82% | 143.40% |
| **10.8°** | 155.19% | 136.51% | 153.10% | 0.46% | 160.77% |
| **13.0°** | 177.79% | 188.51% | 149.80% | 0.54% | 158.73% |
| **15.1°** | 203.37% | 238.54% | 162.84% | 0.36% | 169.10% |

#### 4.6.1.2. Effect on tissue/cavity boundaries

The LV cavity was manually outlined over the original B-mode scan and intensity profiles were extracted at different depths and orientations along the tissue/cavity boundary. Each profile consisted of the intensity values of a 41 pixel linear segment along the normal of the outline (Figure 4.15). Equivalent intensity profiles were extracted from a series of compounded images each derived using 3D data of increasing acquisition sector width and an inter-slice displacement of 0.36°. For the quantitative analysis of tissue/cavity boundary blurring a sigmoid curve, modelled as a Generalised Logistic Function (Richards, 1959; Yin et al., 2003) was fitted through each intensity profile:

$$Y(t) = A + \frac{K - A}{1 + e^{-B(t-M)}} \qquad [4.1]$$

where, *A* is the lower asymptote, *K* the upper asymptote, *M* the pixel at which maximum intensity growth occurs and *B* the Relative Growth Rate (RGR) at *M*.

Figures 4.16 to 4.18 display 6 sample profiles along with the corresponding sigmoid curves extracted from orientations of 0°, 60°, 120°, 180°, 240° and 300° (clockwise from the top of the image). Figure 4.16 displays the intensity profiles extracted from the original B-mode frame. Figures 4.17 and 4.18 display the corresponding profiles extracted from 3D-to-2D Compounded frames derived using acquisition sector widths of 7.2° and 14.4° respectively. The plots provide a qualitative demonstration of the effect of ***3D-to-2D Compounding*** on tissue/cavity boundary blurring for increasing 3D acquisition sector widths.

The sigmoid curve parameters enable the quantitative assessment on the effect of ***3D-to-2D Compounding*** for increasing acquisition sector width on tissue/cavity boundary blurring. More precisely, *A* represents the mean cavity intensity, *K* represents the mean tissue intensity, *M* represents the point tissue/cavity intersection and *B* represents the degree of tissue/cavity boundary blurring at *M*. The goodness of fit parameters, such as linear regression ($R^2$) and Root Mean Square Error (RMSE), for each sigmoid curve also provide a quantitative assessment on the amount of noise along the tissue/cavity boundary. The better the fit the better defined the tissue/cavity boundary is. Figure 4.19 illustrates the effect of ***3D-to-2D Compounding*** on such parameters for increasing angular acquisition sector width. Each plot contains a curve for each of the 6 sample intensity profiles displayed in Figures 4.16 to 4.18.

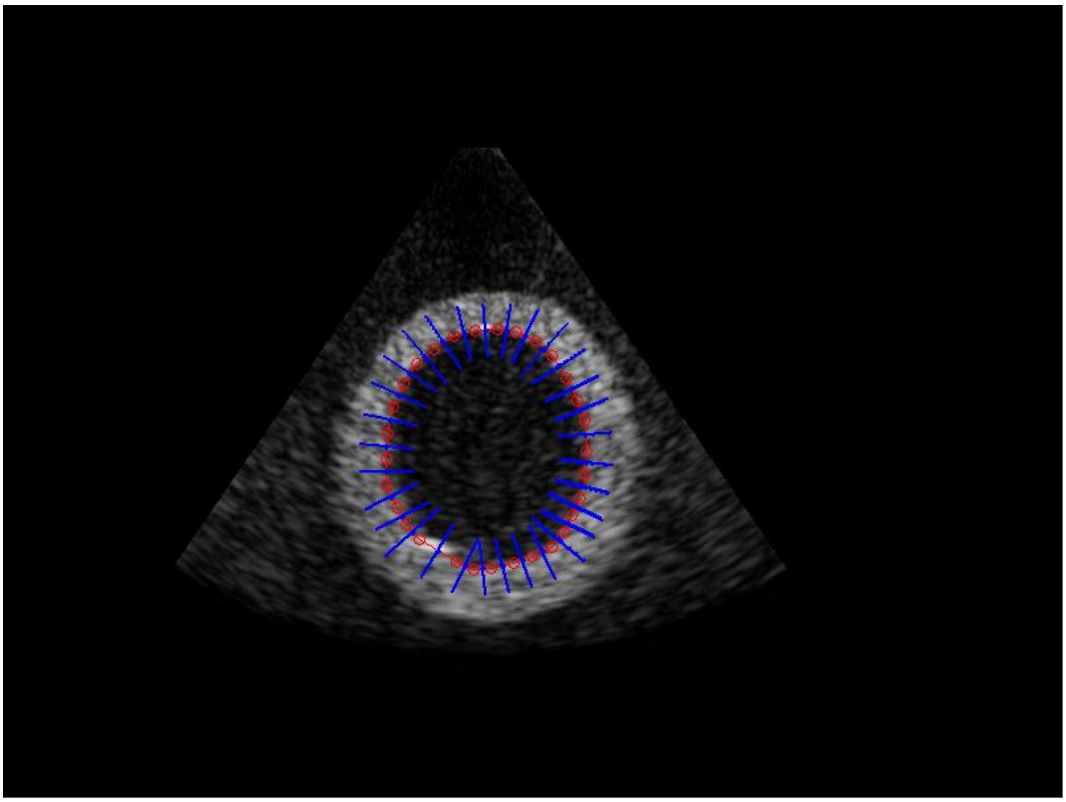

**Figure 4.15.** Manual outline of the LV cavity along with the linear segments (normal to the outline) used for the extraction of the intensity profiles necessary to examine the LV tissue boundary blurring.

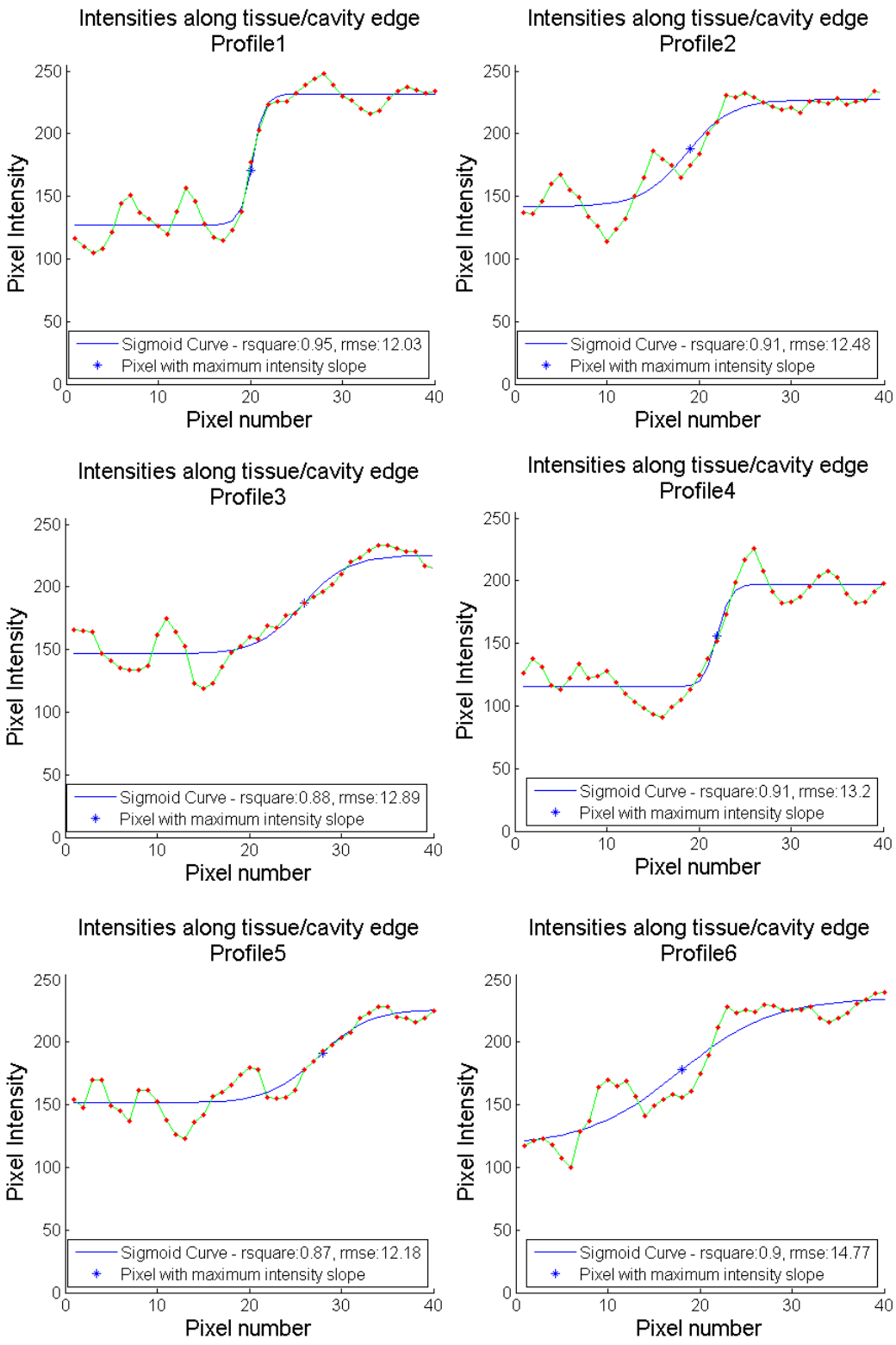


**Figure 4.16.** Intensity profiles at tissue/cavity boundary along with the corresponding sigmoid curves. Profiles 1 to 6 were extracted from the original B-mode frame at sample orientations of 0°, 60°, 120°, 280°, 240° and 300° (clockwise from top) respectively.

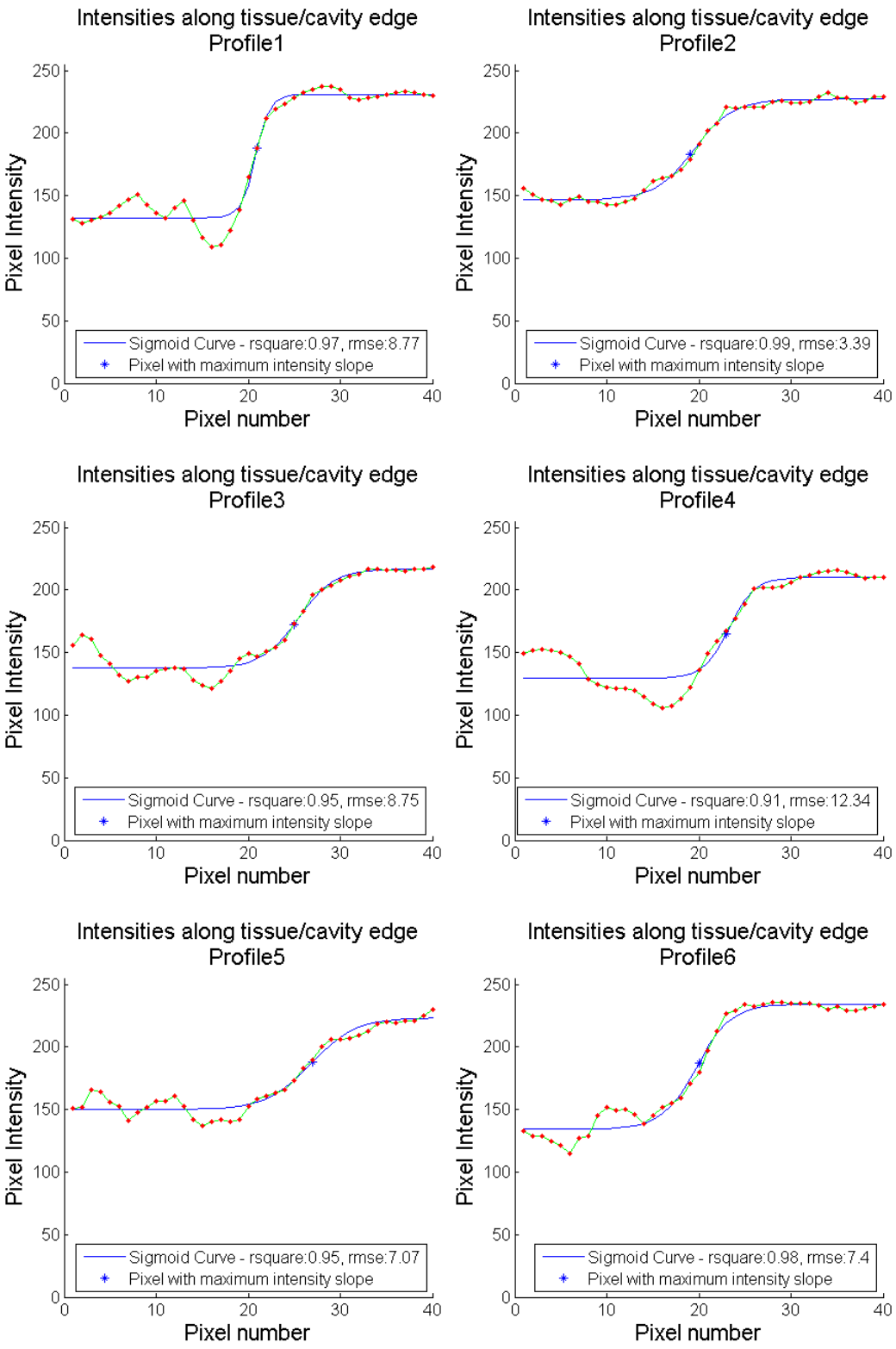


**Figure 4.17.** Intensity profiles at tissue/cavity boundary along with the corresponding sigmoid curves. Profiles 1 to 6 were extracted from a *3D-to-2D Compounded* frame (acquisition sector width of 7.2°) at sample orientations of 0°, 60°, 120°, 280°, 240° and 300° (clockwise from top) respectively.

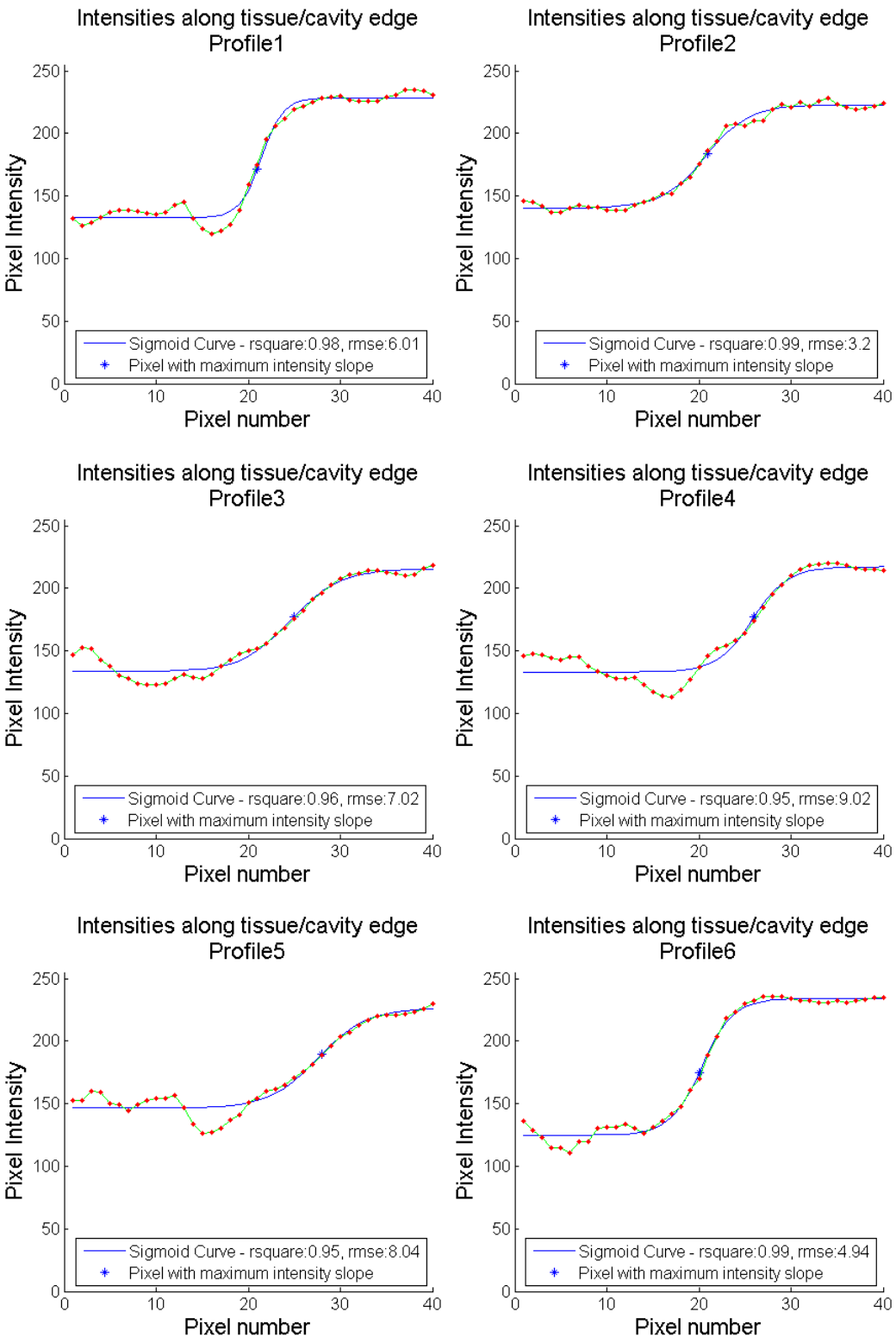


**Figure 4.18.** Intensity profiles at tissue/cavity boundary along with the corresponding sigmoid curves. Profiles 1 to 6 were extracted from a *3D-to-2D Compounded* frame (acquisition sector width of 14.4°) at sample orientations of 0°, 60°, 120°, 280°, 240° and 300° (clockwise from top) respectively.

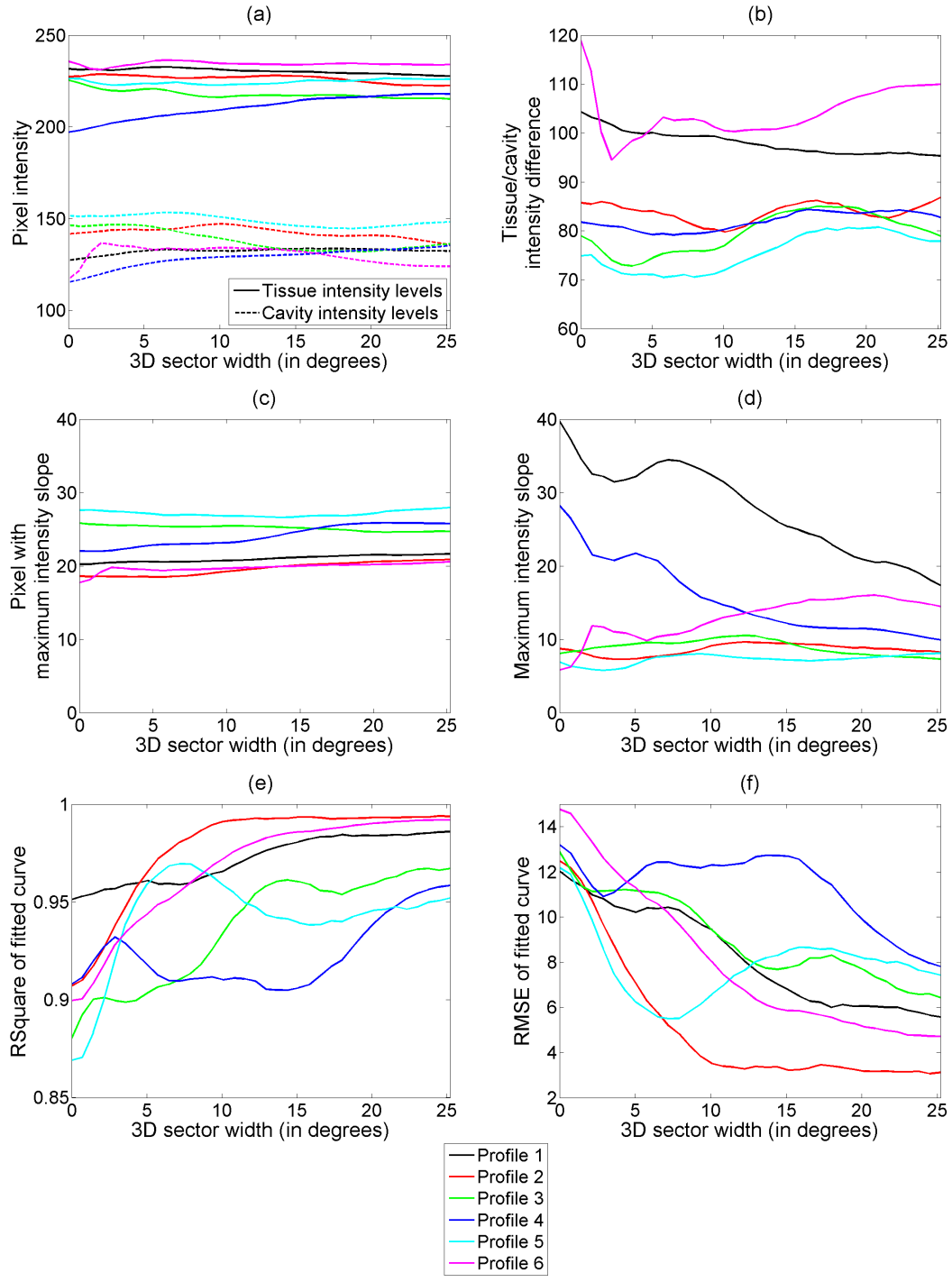


**Figure 4.19.** Effect of ***3D-to-2D Compounding*** for increasing acquisition sector width on sigmoid curve parameters: (a) Tissue vs. Cavity intensity level, (b) Tissue/cavity intensity difference, (c) Position of pixel with maximum tissue/cavity intensity slope, (d) Maximum slope, (e) Goodness of fit of sigmoid curve, (e) RMSE between original data and fitted curve. Parameters for intensity profiles 1 to 6.

### 4.6.2. Volunteer study

The effect of the acquisition sector width during ***3D-to-2D Compounding*** on cardiac tissue structures is investigated by examining the SNR, contrast and SDNR changes on the IVS and cardiac cavities. On the other hand, the effect on blurring between tissue and cavity boundaries is not examined directly since outlining the LV cavity on real human datasets is not only a laborious but a highly subjective and variable process. Instead, the effect of ***3D-to-2D Compounding*** on tissue boundaries is investigated by performing routine clinical measurements of tissue structures and cavities. Such measurements provide sufficient information to indicate whether the boundary blurring introduced has a limiting impact on clinical measurements performed on the compounded datasets.

Figures 4.20 to 4.22 display three example ED frames before and after ***3D-to-2D Compounding***. Datasets over a range image qualities and diagnostic values (low, average and high) are selected in order to best illustrate the effect on ***3D-to-2D Compounding*** on cardiac ultrasound data. More examples can be found in the accompanying DVD-2.

#### 4.6.2.1. Effect on tissue SNR, cavity SNR, tissue/cavity contrast and SDNR

Similar to the process utilised on the phantom datasets, two 11x11 pixels ROIs corresponding to the IVS and the RV cavity (equivalent to the top two phantom ROIs) were manually defined on each of 20 volunteer datasets. The pixel intensity values at the ROI were used to estimate the tissue SNR, cavity SNR, the tissue/cavity Contrast and detectability index SDNR on the original B-mode image as well as a series of compounded images. The compounded images were derived using ***3D-to-2D Compounding*** on data acquired with an increasing 3D angular sector width.

Figure 4.23.a displays multiple SNR curves, each representing a different dataset, illustrating on the effect of the acquisition sector width during ***3D-to-2D Compounding*** on the speckle as well as static and dynamic noise on cardiac tissue structures. Similarly, Figure 4.23.b displays the corresponding RV cavity SNR curves. The mean SNR curves, averaging the SNR curves of all 20 datasets, are also displayed in each of the plots providing representative SNR profiles for tissue and cavity. A direct comparison between the mean tissue and cavity SNR profiles is provided in Figure 4.24. Furthermore, Figure 4.25 displays a mean profile, for all 20 datasets, illustrating the effect of ***3D-to-2D Compounding*** for an increasing number of cardiac cycles on tissue/cavity detectability index (SDNR). The SDNR curves for each individual dataset were omitted since they demonstrate a very similar trend to the corresponding SNR curves. An intermediate inter-slice angular displacement of 0.36° was

utilised during the derivation of each curve in Figures 4.23 to 4.25. Finally, Tables 4.4 to 4.7 summarise the variations on the four quantitative measures between the original and the compounded datasets (using a 6.5° sector with a 0.36° inter-slice angular displacement) elucidating the effect of ***3D-to-2D Compounding*** on the imaged cardiac structures.

#### 4.6.2.2. Effect on clinical measurements performed on patient data

Similar to the process described in Section 3.6, two experienced echocardiographers were asked to perform routine clinical measurements on ED and ES frames from both the original B-mode as well as the 3D-to-2D compounded data. A sequence of ED frames was presented and the IVSd, LVIDd and LVPWd measurements were performed on each frame. Similarly, a sequence of ES frames was presented and the LVIDs and LADs measurements were performed on each frame. Each frame sequence contained one original and one averaged frame for each of the datasets (40 frames in total). The order of the frames was randomised to ensure no bias in the results. The echocardiographers had the option to abstain from a clinical measurement if they considered there were no sufficient visual cues for an accurate measurement of a structure in the displayed image. All clinical measurements were performed twice, in accordance with the standards adopted by the BSE (Henry et al., 1980; Feigenbaum, 1994; Fuster et al., 2008), to enable the examination of measurement agreement and repeatability (Bland & Altman, 1986).

A Bland Altman approach (Bland & Altman, 1986) was then used for the quantitative assessment of the effect of ***3D-to-2D Compounding*** on clinical measurements. The Bland Altman approach (i) analyses the repeatability of clinical measurements performed on either the original or on the contrast enhanced data, and (ii) compares the agreement between clinical measurements performed on original and measurements performed on contrast enhanced datasets. Figures 4.26 and 4.27 display Bland Altman plots combining all clinical measurements performed by each echocardiographer. Individual plots, one for each clinical measurement, were also derived. Table 4.8 summarises the bias, similarity measurements and agreement coefficients derived from the individual plots. Tables 4.9 and 4.10 display which clinical measurements were omitted by each echocardiographer on the original and compounded datasets. More information on Bland Altman plots is provided in Section 3.7.2.3.

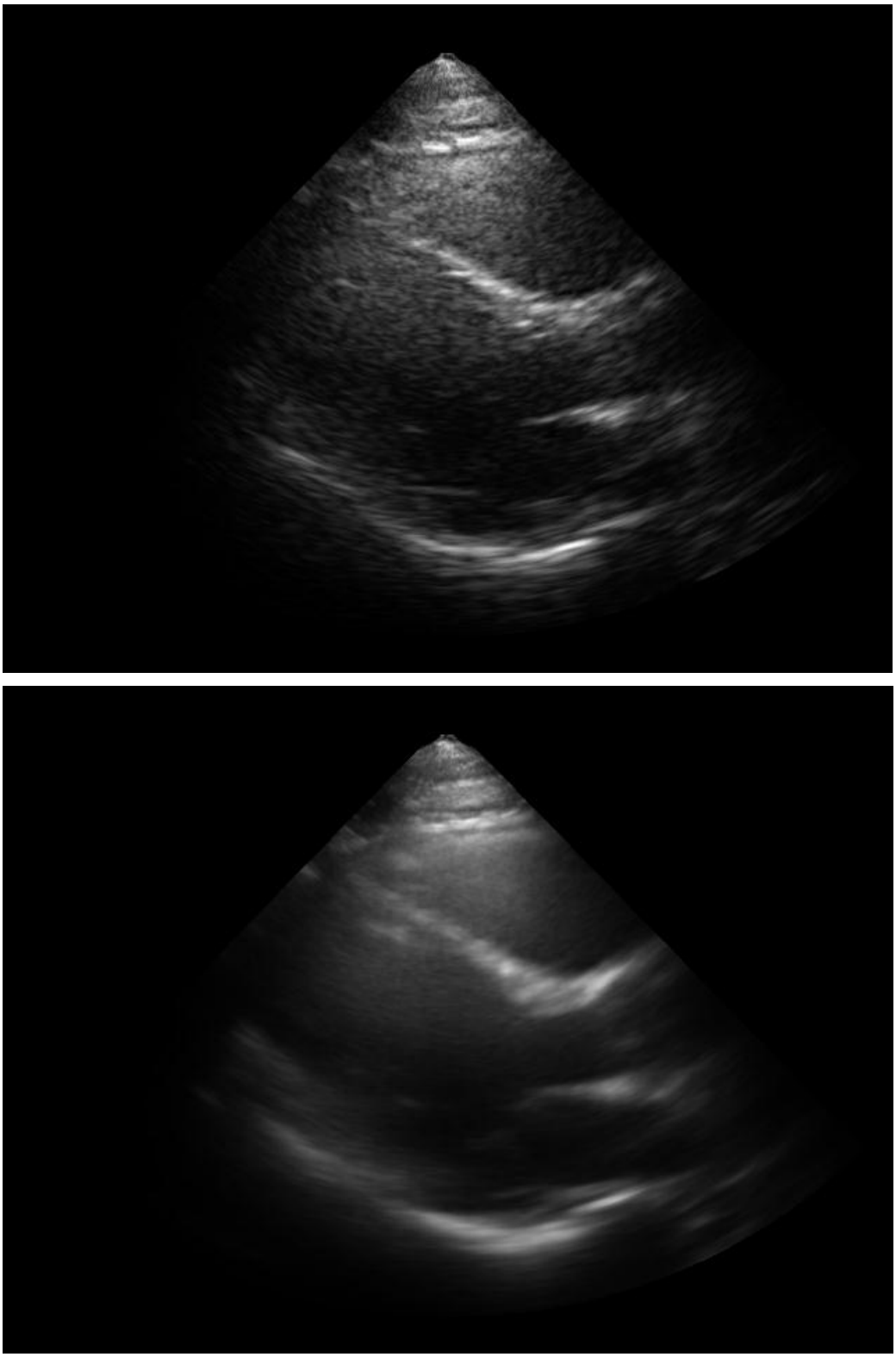

**Figure 4.20.** Original (top) and compounded (bottom) ED frames of low image quality and diagnostic value. (Volunteer 1, dataset 3)

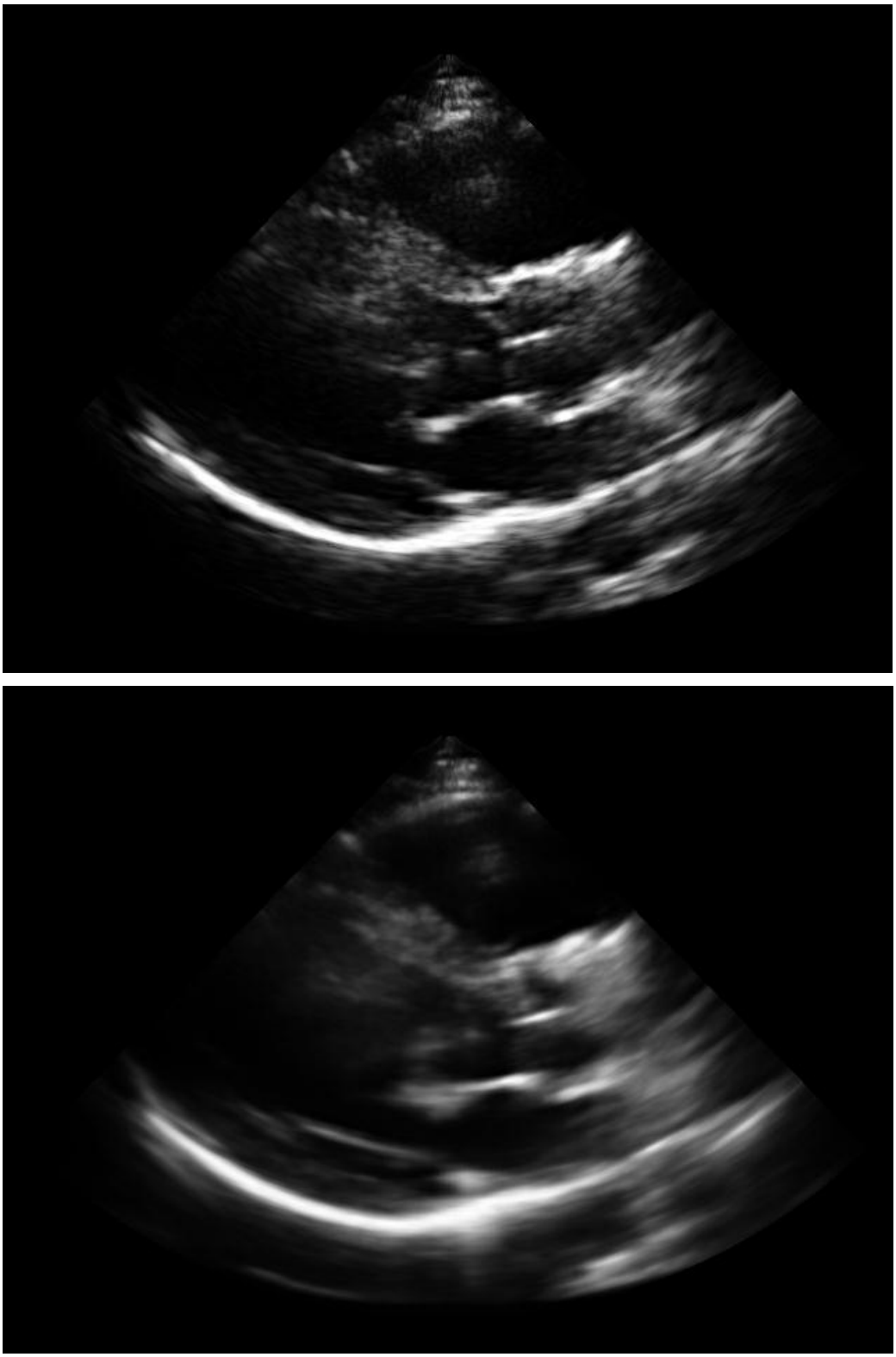

**Figure 4.21.** Original (top) and compounded (bottom) ED frames of average image quality and diagnostic value. (Volunteer 3, dataset 4)

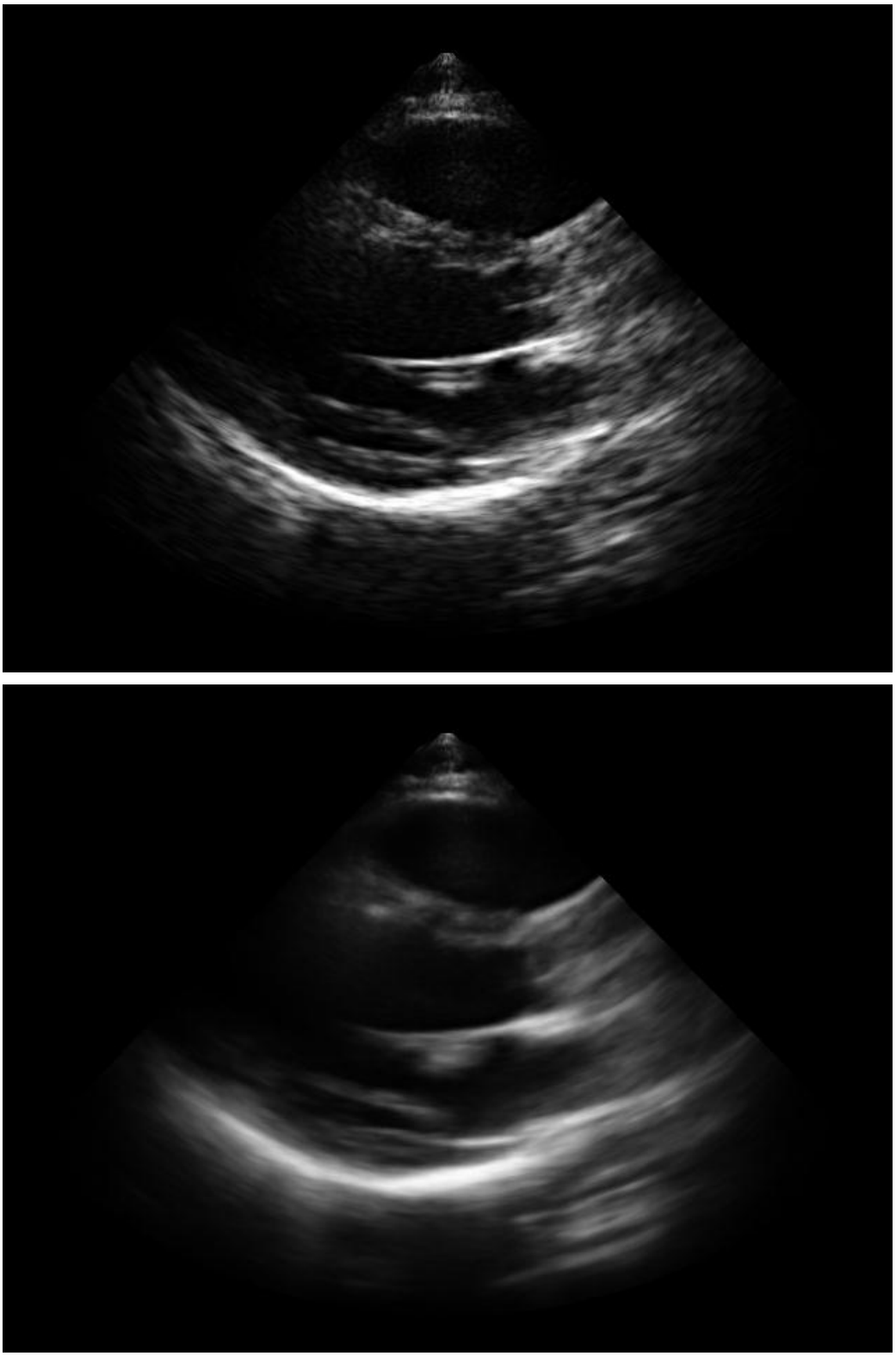

**Figure 4.22.** Original (top) and compounded (bottom) ED frames of high image quality and diagnostic value. (Volunteer 5, dataset 1)

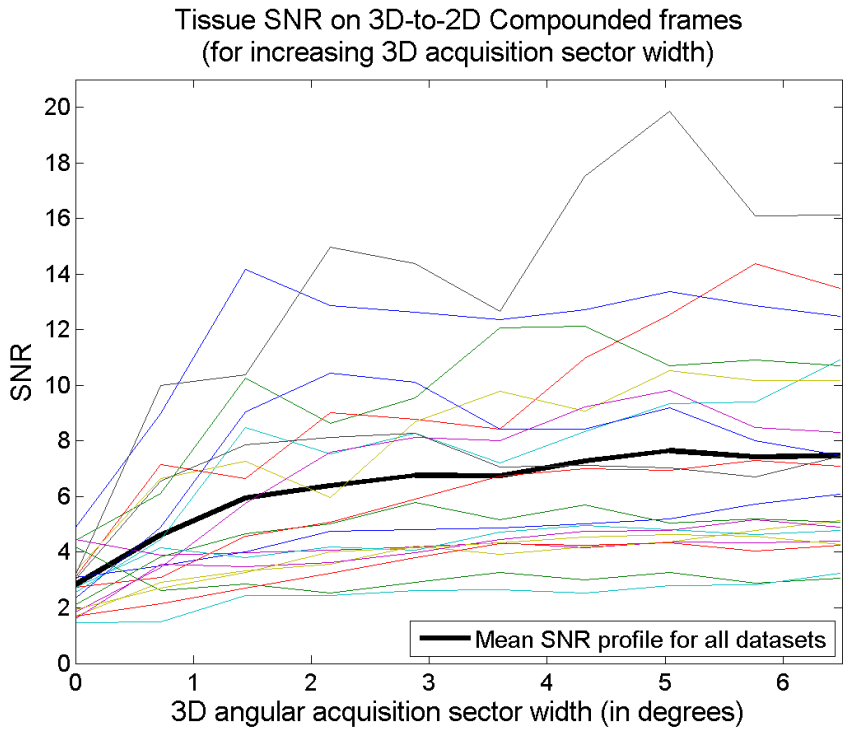


**(a)**

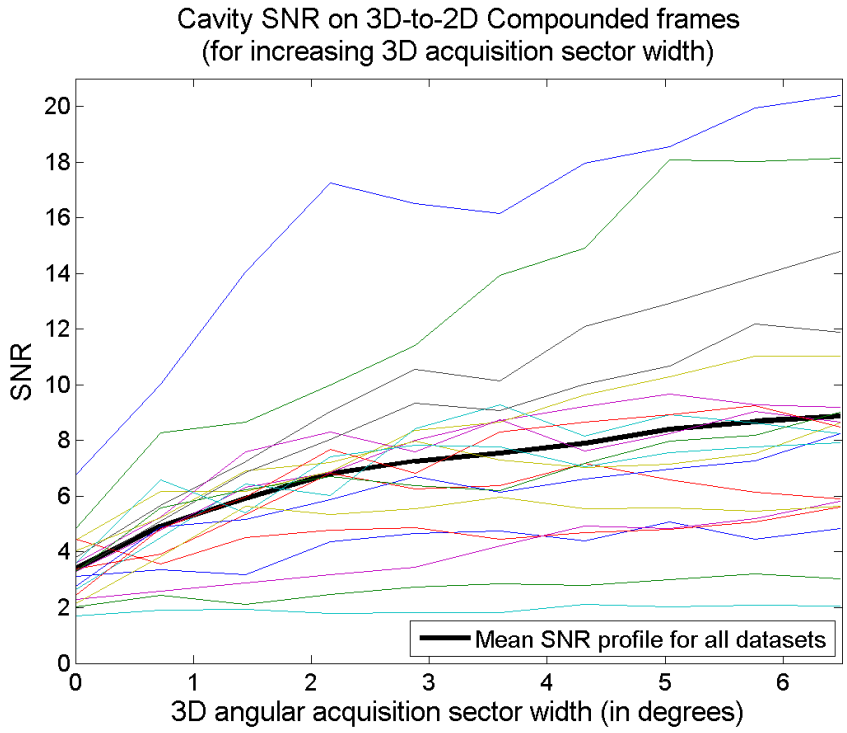


**(b)**

**Figure 4.23.** The effect of ***3D-to-2D Compounding*** on (a) tissue and (b) cavity SNR for increasing 3D acquisition sector width. The mean SNR changes are also displayed.

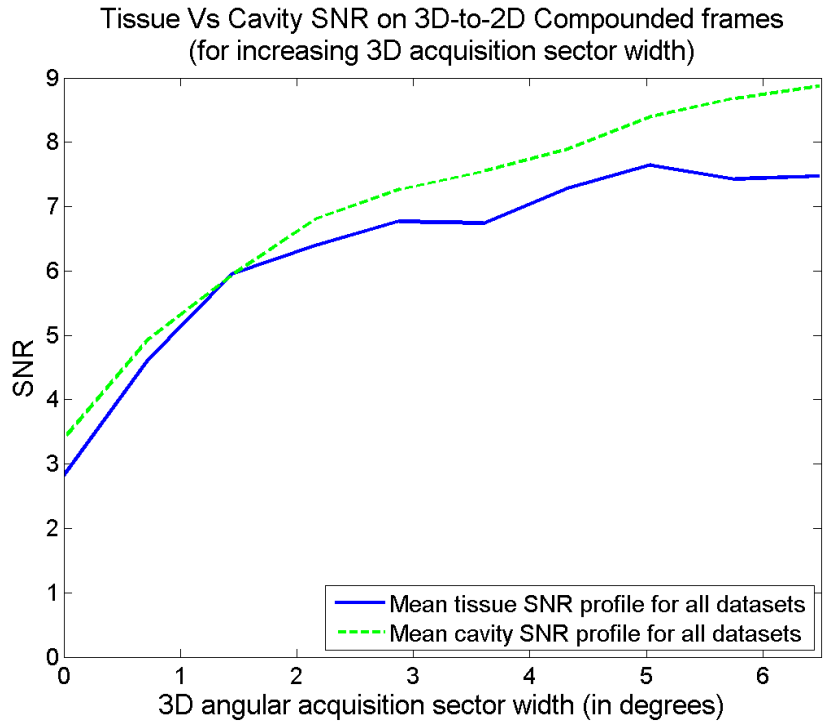


**Figure 4.24.** A direct comparison between the effect of ***3D-to-2D Compounding*** for increasing 3D acquisition sector width on tissue and cavity SNR.

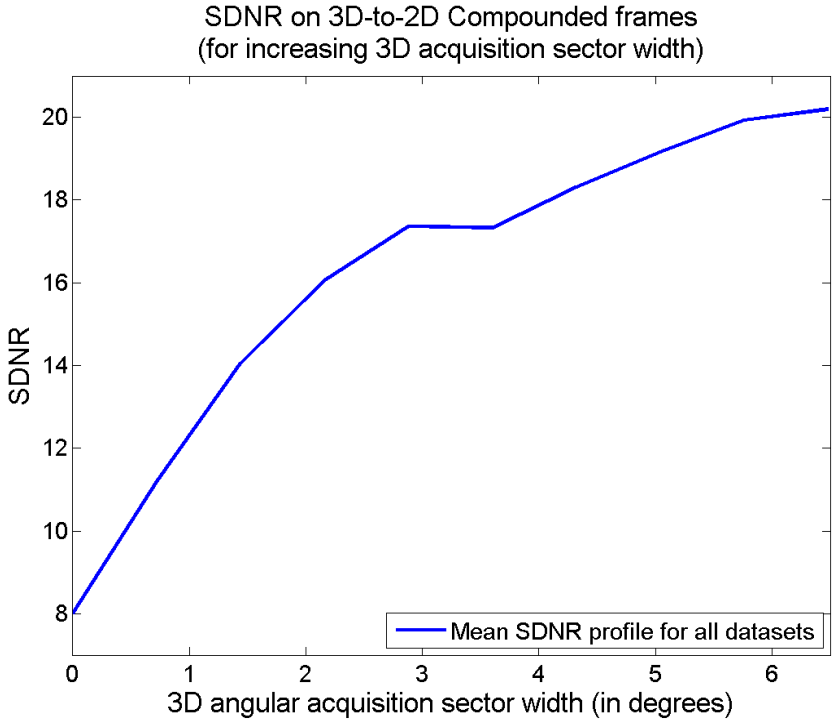


**Figure 4.25.** The effect of ***3D-to-2D Compounding*** for increasing 3D acquisition sector width on tissue/cavity SDNR.

**Table 4.4.** Effect of ***3D-to-2D Compounding*** on tissue SNR. Results for a 6.5° sector.

| | **Original** | **Compounded** | **Improvement** |
|---|---|---|---|
| **Min** | 1.48 | 3.07 | -26.96% |
| **Max** | 4.89 | 16.14 | 405.2% |
| **Mean** | 2.82 | 7.48 | 176.39% |
| **STD** | 1.03 | 3.71 | 111.19% |

**Table 4.5.** Effect of ***3D-to-2D Compounding*** on cavity SNR. Results for a 6.5° sector.

| | **Original** | **Compounded** | **Improvement** |
|---|---|---|---|
| **Min** | 1.69 | 2.06 | 21.98% |
| **Max** | 6.76 | 20.39 | 288.33% |
| **Mean** | 3.40 | 8.88 | 155.11% |
| **STD** | 1.16 | 4.62 | 81.11% |

**Table 4.6.** Effect of ***3D-to-2D Compounding*** on tissue/cavity Contrast. Results for a 6.5° sector.

| | **Original** | **Compounded** | **Improvement** |
|---|---|---|---|
| **Min** | 0.01 | 0.21 | -58.76% |
| **Max** | 1.82 | 1.50 | 146.29% |
| **Mean** | 0.93 | 0.95 | 12.74% |
| **STD** | 0.46 | 0.39 | 42.72% |

**Table 4.7.** Effect of ***3D-to-2D Compounding*** on tissue/cavity SDNR. Results for a 6.5° sector.

| | **Original** | **Compounded** | **Improvement** |
|---|---|---|---|
| **Min** | 0.02 | 1.34 | -79.61% |
| **Max** | 33.42 | 49.42 | 721.91% |
| **Mean** | 8.01 | 20.20 | 229.94% |
| **STD** | 7.59 | 16.46 | 203.11% |

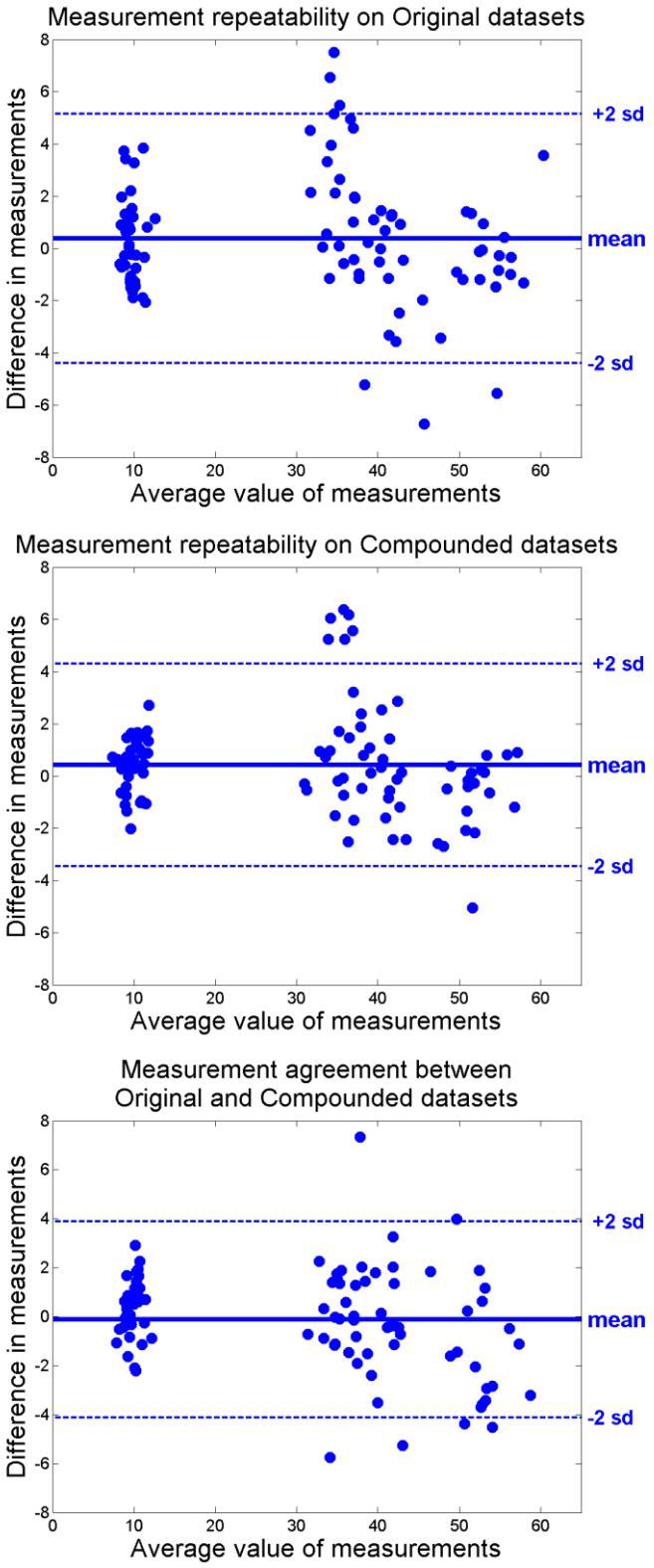


**Figure 4.26.** Bland Altman plots for the repeatability of measurements on original (top) and compounded (middle) datasets as well as the agreement between measurements on original and compounded datasets (bottom). Measurements performed by Echocardiographer 1. Bias (mean), as well as upper/lower limits of agreement are also included.

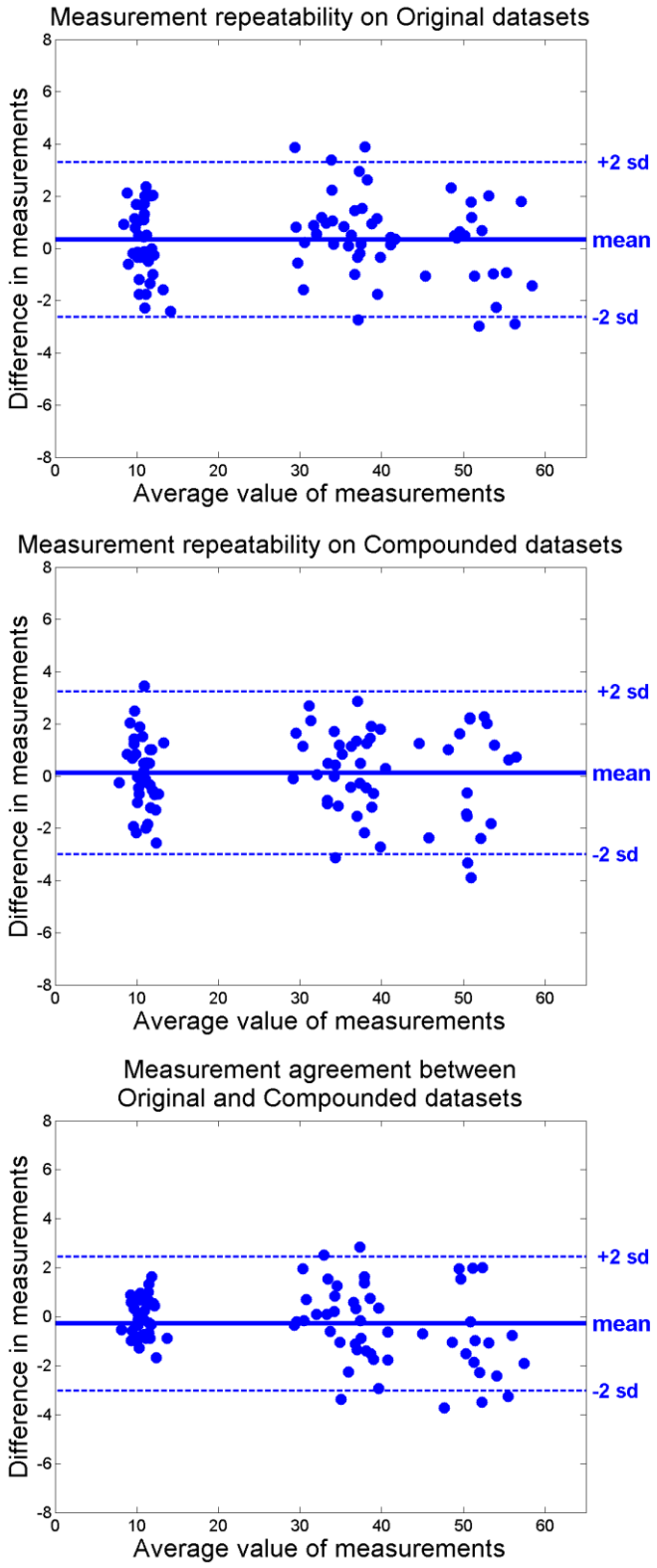


**Figure 4.27.** Bland Altman plots for the repeatability of measurements on original (top) and compounded (middle) datasets as well as the agreement between measurements on original and compounded datasets (bottom). Measurements performed by Echocardiographer 2. Bias (mean), as well as upper/lower limits of agreement are also included.

**Table 4.8.** Measurement repeatability and agreement coefficient for clinical measurements.

| Measure | Original | | | | Compounded | | | | Agreement | | | |
|---|---|---|---|---|---|---|---|---|---|---|---|---|
| (mm) | Mean Diff | +2sd | -2sd | CR | Mean Diff | +2sd | -2sd | CR | Mean Diff | +2sd | - 2sd | CR |
| **Echocardiographer 1** | | | | | | | | | | | | |
| **IVSd** | -0.23 | 1.98 | -2.43 | 2.20 | 0.50 | 2.75 | -1.75 | 2.25 | 0.51 | 2.60 | -1.59 | 2.10 |
| **LVIDd** | -0.63 | 3.10 | -4.36 | 3.73 | -0.82 | 2.14 | -3.79 | 2.97 | -1.34 | 3.37 | -6.05 | 4.71 |
| **LVPWd** | 0.82 | 4.42 | -2.79 | 3.61 | 0.34 | 2.17 | -1.50 | 1.83 | 0.17 | 2.58 | -2.23 | 2.40 |
| **LADs** | -1.14 | 3.10 | -5.37 | 4.23 | 0.03 | 3.99 | -3.93 | 3.96 | -0.08 | 3.79 | -3.95 | 3.87 |
| **LVIDs** | 3.19 | 7.34 | -0.97 | 4.15 | 2.11 | 7.01 | -2.79 | 4.90 | 0.16 | 5.14 | -4.82 | 4.98 |
| **Combined** | **0.39** | **5.17** | **-4.39** | **4.78** | **0.43** | **4.31** | **-3.45** | **3.88** | **-0.12** | **3.89** | **-4.13** | **4.01** |
| **Echocardiographer 2** | | | | | | | | | | | | |
| **IVSd** | -0.08 | 2.97 | -3.13 | 3.05 | -0.45 | 2.08 | -2.99 | 2.53 | 0.09 | 1.83 | -1.64 | 1.74 |
| **LVIDd** | -0.10 | 3.13 | -3.33 | 3.23 | -0.13 | 3.87 | -4.13 | 4.00 | -0.99 | 2.61 | -4.59 | 3.60 |
| **LVPWd** | 0.46 | 2.48 | -1.57 | 2.03 | 0.58 | 3.08 | -1.92 | 2.50 | -0.22 | 1.16 | -1.61 | 1.39 |
| **LADs** | 0.67 | 3.76 | -2.42 | 3.09 | 0.78 | 3.01 | -1.46 | 2.24 | -0.37 | 2.00 | -2.73 | 2.37 |
| **LVIDs** | 0.79 | 3.61 | -2.04 | 2.83 | -0.33 | 2.86 | -3.52 | 3.19 | 0.14 | 3.52 | -3.23 | 3.37 |
| **Combined** | **0.34** | **3.30** | **-2.62** | **2.96** | **0.12** | **3.23** | **-3.00** | **3.12** | **-0.29** | **2.44** | **-3.02** | **2.73** |

**Table 4.9.** List of measurements omitted by Echocardiographer 1 on each individual dataset.

| | IVSd | | LVIDd | | LVPWd | | LVIDs | | LADs | |
|---|---|---|---|---|---|---|---|---|---|---|
| **Dataset** | **Or** | **Com** | **Or** | **Com** | **Or** | **Com** | **Or** | **Com** | **Or** | **Com** |
| **8** | o | N/A | o | N/A | o | N/A | N/A | N/A | o | o |
| **Total** | 0 | 1 | 0 | 1 | 0 | 1 | 1 | 1 | 0 | 0 |

**Table 4.10.** List of measurements omitted by Echocardiographer 2 on each individual dataset.

| | IVSd | | LVIDd | | LVPWd | | LVIDs | | LADs | |
|---|---|---|---|---|---|---|---|---|---|---|
| **Dataset** | **Or** | **Com** | **Or** | **Com** | **Or** | **Com** | **Or** | **Com** | **Or** | **Com** |
| **1** | o | o | o | o | o | o | o | N/A | o | o |
| **2** | o | o | o | o | o | o | N/A | N/A | o | o |
| **3** | o | o | N/A | N/A | N/A | N/A | o | N/A | o | o |
| **8** | N/A | N/A | o | N/A | o | o | o | o | o | o |
| **9** | o | N/A | o | o | o | o | o | o | o | o |
| **13** | o | o | o | o | o | o | o | o | N/A | o |
| **18** | o | o | o | o | o | o | o | o | o | N/A |
| **19** | o | N/A | o | o | o | o | o | N/A | o | o |
| **20** | o | o | o | o | o | o | o | N/A | o | o |
| **Total** | 1 | 3 | 1 | 2 | 1 | 1 | 1 | 5 | 1 | 1 |

## 4.7. Discussion

The results on the phantom based study enable optimal 3D acquisition parameters such as inter-slice angular displacement and angular sector width to be identified. However, note that the phantom provides a controlled environment with optimal scanning conditions. The absence of cardiac movement along with the fact that the longitudinal curvature (short axis scan) can be smaller than the circumferential one (long axis scan) may induce a favourable bias in the results. Consequently, the findings of the phantom study provided best case scenario results, which were then used as a starting point for the volunteer based study.

### 4.7.1. Phantom study

Through a visual inspection on the images displayed in Figure 4.9, it is apparent that ***3D-to-2D Compounding*** reduced the speckle and noise both in tissue, as well as cavity areas of our LV phantom. Compounded data derived using wider 3D acquisition sectors displayed larger speckle and noise suppression. However, tissue/cavity boundary blurring was almost

negligible on data derived using narrow 3D acquisition sectors (Figure 4.9 a-c) while it became more apparent as the 3D acquisition sector width increased (Figure 4.9 d-f). Tissue/cavity boundary blurring is more noticeable at larger depths since for a given angular acquisition width, the corresponding spatial acquisition width increases with depth.

#### 4.7.1.1. Effect on clinical measurements performed on patient data

The curves in Figures 4.11 to 4.14 along with the results in Table 4.3 allow the thorough investigation of the effect of 3D acquisition sector width and inter-slice displacement during ***3D-to-2D Compounding*** on tissue speckle and cavity noise as well as the contrast and detectability between tissue and cavity. Rectangular ROIs of 11x35 pixels were utilised for the derivation of the quantitative image quality measures such as SNR, Contrast and SDNR. The ROIs were considerably larger than the 11x11 square ROIs utilised during *Temporal Compounding*. The larger nature of the speckle observed in the cardiac phantom, when compared to speckle in patient datasets utilised in Chapter 3, along with the limited spatial resolution (especially along the x-axis, lateral resolution) of the acquisitions setup dictated for larger, rectangular ROIs. Direct comparison between the current results and the corresponding *Temporal Compounding* results is beyond the scope of this study. The main objective is the derivation of general trends in quantitative image quality metrics introduced on cardiac ultrasound data by ***3D-to-2D Compounding***. As a result, utilising distinct ROIs throughout this study is considered acceptable and beneficial.

Similar to *Temporal Compounding*, ***3D-to-2D Compounding*** had no noteworthy effect on tissue/cavity contrast. On the other hand, Figure 4.11 illustrates that SNR on phantom tissue increased almost linearly with the 3D angular acquisition width utilised during ***3D-to-2D Compounding***. A substantial SNR increase of more than 90% was generated with a 6.5° sector, increasing to more than 200% for a 15° sector. Small variations on the SNR curves, such as the small curvature on Figure 4.11.a and the flattened region on Figure 4.11.b, are attributed to inhomogeneities in the 3D acquisition introduced due to small errors in the mechanical motor-driven probe displacement. Furthermore, the SNR curves for compounded data derived using different inter-slice angular distance followed almost identical paths. However, for a given 3D angular acquisition width, curves acquired with a larger inter-slice step demonstrated slightly larger SNR than the curves of smaller inter-slice displacement. Such behaviour can be anticipated since for small angular acquisition sectors, such as the sectors examined in this study, not much new information is introduced by further reducing the inter-slice acquisition distances. Compounding additional highly correlated slices may

reduce the mean intensity value and therefore the resulting SNR for a given 3D angular acquisition width.

Figure 4.12 enables a direct comparison between the SNR corresponding to the two distinct tissue acquisition depths. An intermediate inter-slice distance of 0.36° was used. Both curves exhibited similar behaviour with respect to the increasing 3D angular acquisition sector width. On the original unprocessed data, the SNR at depth 2 was just marginally larger than the corresponding SNR at depth 1. However, when increasing the acquisition angle the SNR curves appeared to deviate with the curve corresponding to larger acquisition depth displaying considerably larger SNR values (of up to 18%) than the curve corresponding to smaller acquisition depth. This curve deviation can be attributed to the fact that 3D acquisition is angular. As a result, for a given angular acquisition width, the corresponding spatial acquisition width increases with depth. Larger spatial acquisition width implies that the compounded slices will be less correlated, resulting in an increased SNR.

Figure 4.13 illustrates that similar to tissue, cavity SNR increased with the 3D angular acquisition width utilised during ***3D-to-2D Compounding***. However, while for small acquisition widths the SNR increase was substantial and almost linear (107% for 6.5° and 153% for 10.8°); it levelled out as the 3D acquisition width increased (163% for 15.1°). A very similar behaviour was also observed on tissue/cavity detectability (SDNR) illustrated in Figure 4.14. This behaviour is attributed to the fact that unlike tissue, no new information on cardiac cavity is introduced by each new adjacent slice. The noise suppression is solely based on random intensity variations present in cardiac ultrasound noise. Compounding of adjacent slices averages out such intensity variations and therefore generates homogeneous cardiac cavities. Having achieved the intensity uniformity within cardiac cavities, compounding of additional slices has a minimal effect on the corresponding SNR and SDNR.

#### 4.7.1.2. Effect on tissue/cavity boundaries

Figures 4.16 to 4.18 provide a qualitative demonstration of the effect of ***3D-to-2D Compounding*** on tissue/cavity boundary blurring for increasing 3D acquisition sector widths. Profiles 1 and 4 represent the tissue/cavity intensity transition of the top (IVS) and bottom (LVPW) wall of the LV phantom. The tissue/cavity boundary on the unprocessed data was steep and well defined for profiles 1 and 4 while it appeared vaguer for the rest of the profiles demonstrating the lower spatial resolution of the acquisition system along the x-axis. ***3D-to-2D Compounding*** increased the goodness of fit between the tissue/cavity

boundary profiles and their corresponding sigmoid curves resulting in better defined boundaries. However, while compounding using narrow angular acquisition sector widths (Figure 4.17) appeared to make the tissue/cavity intensity transition steeper, compounding using wider angular acquisition sector widths (Figure 4.18) moderated the slope of the tissue/cavity transition, introducing tissue/cavity boundary blurring.

Examining the individual parameters monitored in the plots displayed in Figure 4.19 facilitate a better, quantitative understanding of the effect of ***3D-to-2D Compounding*** on tissue/cavity boundaries. Plots (a), (b) and (c) (Figure 4.19) indicate that ***3D-to-2D Compounding*** had a minor effect on the mean tissue and cavity intensities as well as the point of tissue/cavity intersection. The variations in the corresponding curves were minimal with no clinical relevance. Furthermore, from plots (e) and (f) (Figure 4.19) it can be seen that the goodness of fit between the intensity profile and the corresponding sigmoid curve improved along with the increase of the angular acquisition sector width utilised in ***3D-to-2D Compounding***. Improved goodness of fit implies better defined, less noisy tissue/cavity boundaries. However, in all profiles except profile 4, about 90% of the improvement was achieved for narrow acquisition sectors of 5° to 9° leveling out for wider acquisition sectors.

Examining the maximum intensity slope plots (Figure 4.19.d) two distinctive behaviours can be identified. For profiles with steep tissue/cavity intensity transitions, such as profiles 1 and 4, compounding with increasing 3D angular acquisition sector moderated the intensity transitions considerably and therefore introduced tissue/cavity boundary blurring. After an initial small slope drop, 23% for profile 1 and 33% for profile 4, the tissue/cavity transition slope remained almost unchanged for narrow angular acquisition sectors of up to 6° and 5° for profiles 1 and 4 respectively. An insignificant boundary blurring was introduced during this small slope drop. For wider angular acquisition sectors there was a considerable drop in the slope of approximately 56% for profile 1 and 64% for profile 4. The stronger effect of ***3D-to-2D Compounding*** on profile 4, which lies at a larger depth than profile 1, is apparent. On the other hand, for profiles with smooth tissue/cavity intensity transitions, such as profiles 2, 3, 5 and 6 (Figure 4.19.d), compounding with increasing 3D angular acquisition sector slightly increased the slope of the intensity transition. The increase on the tissue/cavity transition slope peaked at angular acquisition sector width between 6° and 7° generating slope increases of 10%, 30%, 14% and 230% on profiles 2, 3, 5 and 6 respectively. When compounding data using wider angular acquisition sectors the tissue/cavity intensity transition slope flattened out and in some cases slightly decreased.

The derived quantitative results verify the qualitative observations on the compounded datasets using increasing 3D angular acquisition sector widths presented in Figure 4.9. ***3D-to-2D Compounding*** reduces speckle and noise over the tissue/cavity boundary of the acquired data. Noise reduction increases linearly with the width of the 3D sector utilised during ***3D-to-2D Compounding***. The noise and speckle reduction results in better defined transitions between tissue and cavity and can also help enhance heavily corrupted tissue/cavity edges by increasing the corresponding intensity transition slopes. On the other hand, ***3D-to-2D Compounding***, by averaging adjacent and slightly deformed slices of a structure, can possibly introduce tissue/cavity boundary blurring. For narrow 3D sectors, the tissue boundary blurring appears to be negligible with no negative effect on the tissue/cavity edge enhancement introduced due to noise reduction. However, for wider 3D sectors, the compounding of distant slices, where larger anatomic structure deformations occur, introduces tissue/cavity boundary blurring that counteracts the initial benefits introduced by the ***3D-to-2D Compounding*** of narrow acquisition sectors.

### 4.7.2. Volunteer study

The phantom provided a controlled environment to assess speckle/noise reduction and tissue/cavity boundary blurring. The findings should be treated as a best case scenario since additional challenges arise in real cardiac ultrasound scans. Therefore, a sector of up to 6.5° was found to provide a good trade-off between the speckle/noise suppression and tissue/cavity boundary blurring introduced by ***3D-to-2D Compounding***. Furthermore, inter-slice displacement had no substantial effect in the noise suppression introduced by ***3D-to-2D Compounding***. As a result, an intermediate inter-slice distance of 0.36° may reduce acquisition resources, such as time and processing, while accommodating flexibility in the acquisition of small 3D segments when it is required. For example, acquisition and compounding of narrower 3D sectors may be required when there is a narrow acoustic window through the rib cage or a smaller heart, such as with younger people or women. All acquisition and compounding on volunteer datasets was performed with an inter-slice step of 0.36° and angular sector width of up to 6.58°. Figures 4.20 to 4.22 display ED frames, original and compounded, acquired using these parameters. They provide characteristic examples on the effects of ***3D-to-2D Compounding*** on clinical data over a range of image and diagnostic qualities.

Figure 4.20 displays two ED frames corresponding to a dataset with low image quality and diagnostic value. The first image is an original unprocessed frame, while the second is the corresponding compounded frame. The original image suffered from high noise levels

making it hard to outline structures such as the IVS and the LVPW. The speckle and noise reduction is apparent in the compounded frame. In addition, both the IVS and LVPW were enhanced making them easier to detect and outline. Figure 4.21 displays two ED frames corresponding to a dataset with average image quality and diagnostic value. Noise levels were much lower than the dataset displayed in Figure 4.20. However, high noise levels around the IVS made the delineation of the structure challenging. Similar to the previous example, ***3D-to-2D Compounding*** reduced the speckle/noise level throughout the image and enhanced the existing structures making the IVS detectable. On the other hand, small blurring was introduced around the mitral valve, which is expected since the valve is a very fast moving structure. Figure 4.22 displays two ED frames corresponding to a dataset with high image quality and diagnostic value. The noise levels in the original image were very low and the cardiac structures were easily distinguishable. Nevertheless, ***3D-to-2D Compounding*** suppressed tissue speckle. However, small tissue/cavity boundary blurring was introduced around the LA tissue/cavity boundaries.

A thorough visual examination on the available volunteer datasets suggests that ***3D-to-2D Compounding*** can significantly reduce noise and speckle on datasets of a range of image qualities and diagnostic values. It can enhance noisy structures but may also introduce moderate tissue/cavity boundary blurring. It is strongly believed that part of the blurring is due to quantification errors (on fast moving structures), small inaccuracies in the temporal alignment and small patient movements during multi-cycle data acquisition. It is believed that a considerable proportion of the blurring can be reduced by acquiring and compounding 3D data using a real-time 4D matrix transducer. As mentioned in Section 4.4.2, three datasets were discarded due to the high noise levels obstructing the identification of ED and ES frames and therefore prohibiting the application of ***3D-to-2D Compounding***. Another dataset was not considered due to repeated loss of contact between the probe and the subject over the multi-cycle data acquisition. Both problems would be avoided if the datasets were acquired using a real-time 4D matrix transducer. Finally, there was a dataset discarded during the quantitative evaluation of ***3D-to-2D Compounding***. The dataset corresponds to the fifth volunteer where the scanning plane was altered during acquisition visualising different cardiac structures. Such behaviour can be attributed either to patient movement during the scan or to the acquisition of a large 3D sector of the scanned cardiac structure. The behaviour was not observed on any of the remaining scans performed on the same subject. However, it provides an indication that flexibility on the 3D acquisition sector width can be beneficial.

#### 4.7.2.1. Effect on tissue SNR, cavity SNR, tissue/cavity contrast and SDNR

Figure 4.23 illustrates the effect of ***3D-to-2D Compounding*** on tissue and cavity SNR for increasing compounding sector width. Moreover, Tables 4.4 and 4.5 summarise the variations on both measures between the original and the compounded datasets (using an acquisition sector of 6.5°). Similar to the results from the phantom study, SNR increased with the increase of the angular sector width utilised during compounding. However, the effect varied significantly between different datasets ranging from modest to very substantial (over 400%). Variations in the original SNR can be attributed to many reasons, such as different levels of static and dynamic noise, shadowing and non-optimal acquisition set-up. A wide range of artifacts can also appear in a real cardiac ultrasound scan. Such artifacts along with variations in the depth of the sampled tissue, small errors in the mechanical motor-driven probe displacement and small subject movements during scanning account for the variations in SNR increase achieved by compounding on different datasets. There was an attempt to limit such sources of SNR inaccuracies to a minimum. However, with the current acquisition set-up it was not feasible to fully eliminate them. Compounding of real time 4D data acquired using a matrix transducer would eliminate all SNR variations due to patient and probe movements during acquisition. The mean SNR profile (Figures 4.23 and 4.24) provides a fair representation of the effect of 3***D-to-2D Compounding*** on cardiac tissue. A compounding sector width of 6.5° generated considerable mean tissue and cavity SNR increases of 176% and 155% respectively. Figure 4.24 enables the direct comparison of the mean tissue and cavity SNR profiles. Comparing the mean tissue and cavity SNR profiles, it is apparent that cavity SNRs tend to have higher initial values as well as increased ranges. This behaviour was also observed during ***Temporal Compounding***. The higher SNR ranges were due to the absence of speckle in cardiac cavities. Speckle constitutes a major contributor in the lower initial SNR values observed in cardiac tissue. Furthermore, due to the nature of speckle, a higher level of decorrelation between the compounded frames is required for its suppression when compared to the noise present in cardiac cavities. Hence the lower SNR increase range observed for cardiac tissue.

Similar profiles for each of the 20 datasets were derived in order to assess the effect of ***3D-to-2D Compounding*** on the tissue/cavity detectability index (SDNR) and contrast. In a like manner to the SNR profiles, the mean SNDR and contrast profiles provide fair representations of the effect of ***3D-to-2D Compounding*** on the distinction between cardiac tissue and cavity. Figure 4.25 illustrates the corresponding mean SDNR profile. Moreover, Tables 4.6 and 4.7 summarise the variations on both measures between the original and the

compounded datasets (using an acquisition sector of 6.5°). As expected, ***3D-to-2D Compounding*** resulted in a very modest, relatively unaffected by the width of the acquisition sector, increase in contrast between cardiac tissue and cavity. However, a considerable increase in SDNR was achieved through ***3D-to-2D Compounding***.

By investigating the profile curvatures in Figures 4.23 to 4.25, the mean SNR and SDNR profiles can be divided into two segments. In the first segment, observed during the compounding of 2-3° 3D angular sectors, the SNR and SDNR increase introduced was very large. In the second segment, observed during the compounding of larger sectors, the SNR and SDNR increase was more moderate but still considerable. This behaviour is attributed to the decrease of new information introduced by increasing the number of adjacent slices utilised during ***3D-to-2D Compounding***. The initial slices introduce considerable decorrelated information. By introducing additional slices the decorrelation between the new and the existing information decreases. In order to maintain the high SNR and SNDR increases, a higher level of decorrelation, achieved through larger inter-slice distances and acquisition sector widths, are required. However, larger acquisition sector widths introduce blurring on the tissue/cavity boundary and should therefore be avoided. Furthermore, on the derived mean cavity SNR curve, a third segment (for sectors larger than 5°) is observed where the SNR increase is negligible. A similar behaviour was observed in the corresponding phantom study earlier in this chapter. This behaviour is attributed to the fact that unlike tissue, no new information on cardiac cavity is introduced by each new adjacent slice. The noise suppression is solely based on random intensity variations present in cardiac ultrasound noise. Compounding of adjacent slices averages out such intensity variations and therefore generating homogeneous cardiac cavities. Having achieved the intensity uniformity within cardiac cavities, compounding of additional slices has a minimal effect on the corresponding SNR. It is believed that the utilised 6.5° sector width provides a good trade-off, introducing sufficient noise suppression and tissue/cavity detectability increase while maintaining tissue/cavity boundary blurring to a minimum.

#### 4.7.2.2. Effect on clinical measurements performed on patient data

The results presented in Figures 4.26 and 4.27 along with Tables 4.8 to 4.10 enable the evaluation of the effect of ***3D-to-2D Compounding*** on clinical measurements performed on routine cardiac ultrasound examinations. Each point cluster (representing different types of clinical measurements) as well as the corresponding limits of agreement (±2SD) lay in a specific range which was largely unaffected by whether measurements were performed on the original or the compound datasets. Furthermore, the mean measurement difference in

each plot lay very close to zero, indicating that no significant or systematic bias was observed within each measurement method or between the two measurement methods. Finally, no major outliers were identified in the repeatability and agreement plots. Consequently, the results presented in the plots indicate a strong potential for the original and compounded data to be interchangeable when performing clinical cardiac ultrasound measurements.

Tables 4.8 and 4.10 enable a more thorough investigation on the effect of ***3D-to-2D Compounding*** on clinical measurements performed on routine cardiac ultrasound examinations. The repeatability of a clinical measurement appears to depend both on the type of clinical measurement performed as well as the echocardiographer making the measurement. The more confident Echocardiographer 1 demonstrated an overall improvement in the repeatability for measurements performed on the compounded datasets. More precisely, the repeatability coefficient of the measurements on compounded data increased by 20%, 49% and 6% for the LVIDd, LVPWd and LADs measurements respectively. On the other hand, the repeatability coefficient of the IVSd measurement remained consistent between original and compounded data while the LVIDs measurements demonstrated an 18% drop in the repeatability coefficient for compounded datasets. Nevertheless, when considering all clinical measurements, a considerable overall 19% improvement on the repeatability coefficient was introduced to measurements performed on compounded data compared to those performed on the original unprocessed data. The more conservative Echocardiographer 2 indicated reluctance on the diagnostic quality of the compounded datasets. The more thorough measurement approach utilised by Echocardiographer 2 is apparent by the higher repeatability and agreement levels displayed on the clinical measurements when compared with those of Echocardiographer 1. The repeatability coefficient of measurements performed on compounded data decreased by 24%, 23% and 13% for the LVIDd, LVPWd and LVIDs measurements respectively. On the other hand, there was a considerable increase of 17% and 28% on the repeatability coefficients of the IVSd and LADs measurements respectively for measurements performed on compounded data. Despite Echocardiographer 2's reluctance towards compounded datasets, when considering all clinical measurements, a modest, marginal overall decline of 5% was introduced on the repeatability coefficient of measurements performed on compounded data compared to those performed on the original unprocessed data. Throughout this study all 4D cardiac volumes were acquired as a collection of adjacent 2D slices over consecutive cardiac cycles by mechanical displacement of a 2D probe. As a result, this drop on the repeatability is mainly attributed to minor tissue/cavity boundary blurring introduced due to quantification

errors and small inaccuracies during the spatio-temporal alignment of the adjacent slices. Compounding 4D datasets acquired in real-time using a matrix transducer would remove such tissue/cavity boundary blurring. Reduced tissue/cavity boundary blurring can improve clinical measurement repeatability. Nevertheless, as the repeatability level of Echocardiographer 2 on both the original and processed datasets is very high, substantially higher than the corresponding level for Echocardiographer 1, it would be very challenging to considerably improve on it.

Tables 4.9 and 4.10 indicate whether a clinical measurement was performed or omitted by each echocardiographer on the original and compounded datasets. Both echocardiographers chose to abstain from making some clinical measurements. Similar to the results displayed in Table 4.8, the more conservative approach adopted by Echocardiographer 2 on making clinical measurements is apparent when compared to Echocardiographer 1. Echocardiographer 1 chose to attempt the majority of the clinical measurements while Echocardiographer 2 omitted measurements, taking fewer risks on challenging datasets. Avoiding clinical measurements on challenging datasets reduced the scope for improvement in the repeatability and agreement levels introduced by using the processed data. Visual inspection of the omitted datasets demonstrated high levels of corruption on the measured cardiac structures either by high noise or shadowing levels. As a result, measurements involving the corrupted structures were omitted. Some measurements were omitted by both echocardiographers on both the original and the compounded data of specific challenging datasets. For example, on Dataset 8, a large section of the IVS was corrupted by shadowing making performing measurements related to the IVS (IVSd, LVIDd, LVIDs) very challenging. Both echocardiographers omitted measurements on Dataset 8. However, there were some measurements omitted only on compounded datasets. Both echocardiographers have been working for many years with challenging cardiac ultrasound data and have developed procedures utilising subtle features that enable them to perform the required clinical measurements. Data processing may modify such features preventing the echocardiographers from making some challenging clinical measurements on the processed datasets that were presented to them for the first time during this study. The number of omitted measurements on the compounded data is expected to drop as the familiarity of the echocardiographers with the compounded data increases.

The results on the effect of ***3D-to-2D Compounding*** on clinical measurements performed on routine cardiac ultrasound examinations were very promising. The fact that the measurement agreement lay in levels very similar to the corresponding measurement repeatability

coefficient with no substantial or systematic bias identified indicates that original and compounded datasets can be interchangeable when performing clinical measurements on cardiac ultrasound data. Compounding 4D datasets acquired in real-time using a matrix transducer would remove some of the tissue/cavity boundary blurring introduced during the multi-cycle data acquisition. Reduced tissue/cavity boundary blurring can further improve clinical measurement repeatability. Moreover, operator confidence as well as measurement repeatability is expected to increase as the familiarity of the echocardiographers with the compounded data increases. Therefore, ***3D-to-2D Compounding*** demonstrates potential for the improvement in the repeatability of routine clinical measurements on cardiac ultrasound data. ***3D-to-2D Compounding*** could possible act as a beneficial adjunct to conventional B-mode imaging for clinical measurements.

## 4.8. Conclusions

In this chapter, ***3D-to-2D Compounding***, a method for the acquisition and compounding of adjacent partially decorrelated cardiac slices to an improved B-mode frame sequence, was introduced. A number of multi-cycle patient cardiac ultrasound datasets were utilised for the quantitative assessment on the effect of ***3D-to-2D Compounding*** on image quality and diagnostic value. 3D data acquisition parameters such as maximum angular acquisition sector width and angular inter-slice distance have a direct effect on the SNR and SDNR increase as well as the tissue/cavity boundary blurring introduced to the compounded data. Optimal acquisition parameters were derived using a LV phantom. Volunteer cardiac data were then acquired and compounded using the derived optimal acquisition parameters. A 3D acquisition sector of 6.5° along with an inter-slice distance of 0.36° was found to provide a good trade-off between SNR increase and tissue/cavity boundary blurring. However, if the acquisition of a 6.5° sector is not feasible then compounding data from a 3D sector of 2.5° more can still generate considerable data enhancement. Data enhancement generated using ***3D-to-2D Compounding*** includes suppressing tissue speckle and cavity noise, substantially increasing the corresponding SNR as well as the tissue/cavity detectability index (SDNR). Furthermore, by averaging decorrelated instances of the same structure, ***3D-to-2D Compounding*** can enhance tissue structures that are masked out by heavy levels of noise and shadowing. However, ***3D-to-2D Compounding*** was found to have no noteworthy effect on the limited tissue/cavity contrast experienced in cardiac ultrasound data. Due to its effectiveness and simple nature, ***3D-to-2D Compounding*** can act as a first step for post-processing techniques, such as image segmentation and registration, whose effectiveness is

limited and sometimes restricted by low image quality (SNR and SDNR) in cardiac ultrasound data.

Having verified the impact of ***3D-to-2D Compounding*** on cardiac ultrasound image quality, its effect on diagnostic value was investigated by assessing the impact on repeatability levels between routine clinical measurements performed by two experienced echocardiographers. The effect of ***3D-to-2D Compounding*** varies depending on the echocardiographer and the clinical measurement performed. ***3D-to-2D Compounding*** predominantly induces a considerable improvement in the repeatability of clinical measurements performed by Echocardiographer 1 and a modest, marginal drop in the repeatability of clinical measurements performed by Echocardiographer 2. Compounding 4D datasets acquired in real-time using a matrix transducer will remove some of the tissue/cavity boundary blurring introduced during the multi-cycle acquisition of 3D datasets. Reduced tissue/cavity boundary blurring can further improve clinical measurement repeatability. Taking into consideration that both echocardiographers were presented with the processed data for first time, it is strongly believed that there is further scope for improvement as the familiarity of the echocardiographers with the processed data increases. Consequently, ***3D-to-2D Compounding*** demonstrates potential to provide a valuable adjunct to B-mode data for improving cardiac measurements.

# Chapter 5

# Dynamic Histogram Based Intensity Mapping

This chapter introduces ***Dynamic Histogram Based Intensity Mapping* (*DHBIM*),** a novel and fully automated method for suppressing noise in cardiac cavities while enhancing information in cardiac tissue structures. During ***DHBIM*** the temporal variations within the individual frame histograms over consecutive multi-frame cardiac cycles are analysed in order to derive any underutilised intensity values as well as the tissue/cavity intensity threshold. Thereupon, piecewise intensity mapping (contrast stretching) applied on each frame in the B-mode frame sequence (i) increases the cardiac tissue intensity dynamic range and (ii) suppresses cavity noise information therefore, enhancing the diagnostic information within the imaged cardiac structure. ***DHBIM*** is quantitatively assessed using 32, multi-cycle, patient cardiac ultrasound datasets providing a representative range of image qualities and diagnostic values. Optimal acquisition parameters, such as the optimal number of cardiac cycles for accurate and robust tissue/cavity threshold extraction, are derived. Furthermore, the effect of ***DHBIM*** on the noise and contrast within the imaged cardiac structures is quantitatively assessed utilising measures such as tissue SNR and cavity SNR, as well as tissue/cavity Contrast and detectability index SDNR. Finally, similar to the two previous chapters, this study examines the effect of ***DHBIM*** on five clinical measurements performed during routine echocardiographic examinations.

## 5.1. Introduction

As described in Chapters 1 and 2, cardiac ultrasound data suffer, amongst many other artifacts, from high levels of noise as well as low contrast between tissue and cavity structures. High noise and low contrast levels limit both the quality of the acquired images as well as their diagnostic value. Low image quality further limits and sometimes restricts (i) the application of common post-processing methods, such as image segmentation and registration, on cardiac ultrasound data, and (ii) the ability to perform accurate and repeatable clinical measurements. As described in Chapter 2, the limitations of cardiac

ultrasound have long been identified, and over the last 30 years there has been a wide range of studies attempting to address some of these limitations. The vast majority of these studies has identified speckle and noise as the most important limitations and has focused on developing reliable speckle/noise suppression techniques. Chapters 3 and 4 introduced and evaluated two methods that succeed in suppressing speckle as well as dynamic noise in cardiac ultrasound data by spatially compounding spatio-temporally aligned data acquired from a single acoustic window. Unlike other noise suppression methods, both techniques managed to substantially suppress noise while considerably increasing the detectability between tissue and cavity. However, like most studies attempting to enhance cardiac ultrasound data, they did not generate any noteworthy effect in enhancing the contrast between cardiac tissue and cavity structures. Furthermore, while tissue speckle suppression, caused by spatial compounding, may be advantageous for some image post-processing, it restricts the application of other commonly employed cardiac ultrasound methods such as *Speckle Tracking*. As a result, a method that suppresses noise in cardiac cavities while enhancing the contrast and detectability between cardiac tissue and cavity structures as well as the speckle detail in cardiac tissue is desirable.

In order to be able to distinguish between tissue and cavity pixels and apply corresponding gray level transformations to them, a method to derive a representative tissue/cavity threshold is required. The process of identifying an intensity threshold between individual structures, such as tissue and cavity, within an image is known as thresholding. Over the years there has been a wide range of thresholding methods. Due to its intuitive properties, simplicity of implementation and low computational requirements, image thresholding is commonly used during image segmentation algorithms (Gonzalez & Woods, 2001; Shrimali et al., 2009). (Sahoo et al., 1988) and (Sezgin & Sankur, 2004) provided two very thorough surveys on image thresholding techniques. Moreover, (Noble & Boukerroui, 2006; Shrimali et al., 2009) provided two reviews on thresholding methods that have been utilised with medical ultrasound data. (Hammoude, 1998) provided a review on thresholding for cardiac ultrasound data. (Sezgin & Sankur, 2004) categorised thresholding methods, based on the type of information manipulated by their corresponding algorithm, into six groups: (i) histogram shape, (ii) clustering, (iii) entropy, (iv) image attributes, (v) spatial information, and (vi) local characteristics. Clustering techniques can also be used along with gray-level histograms for image thresholding. Histogram based methods are very popular due to their simplicity and efficiency. For an 8-bit gray scale image, a histogram based method processes data within a 256 element vector. This can considerably reduce the processing requirements when compared to processing a 434 x 636 element matrix storing a moderately sized cardiac

ultrasound image. Taking into consideration the multi-frame nature of cardiac ultrasound data (approximately 100 frames per second on state of the art scanners) makes histogram based thresholding methods even more appealing.

(Abdullah-Al-Wadud et al., 2007) and (Ibrahim & Kong, 2007) provided thorough reviews on contrast enhancement techniques applied in low contrast images. Furthermore (Abdullah-Al-Wadud et al., 2007) introduced Dynamic Histogram Equalisation (DHE), a contrast enhancement technique that analysed the shape of the histogram and partitioned (thresholds) it based on local minima. It then assigned specific gray-level ranges to each partition before performing histogram equalisation on them individually. Histogram equalisation is a commonly used image enhancement technique that, based on the probability distributions of the input gray levels, generates a gray-level mapping which linearises the cumulative histogram of the output image (Gonzalez & Woods, 2001). (Ibrahim & Kong, 2007) provided an extension to DHE referred to as Brightness Preserving Dynamic Histogram Equalisation (BPDHE). BPDHE partitioned the histogram based on local maxima instead of local minima used by DHE. It then assigned specific gray-level ranges to each partition before performing histogram equalisation on each individually. Finally, BPDHE normalised the output intensities in order to maintain the mean brightness of the original image. Both techniques performed well in low contrast images. However, the high levels of noise and therefore more complex histograms in cardiac ultrasound data impose a great limitation on the potential of similar histogram-shape based techniques (Hammoude, 1998). Nevertheless, there have been some early attempts (Ohyama et al., 2000) utilising gray-level histogram shape information in order to derive thresholds between cardiac tissue and cavity structures.

(Zwirn & Akselrod, 2004, 2005) introduced a very interesting technique for the automatic adjustment of the gray-levels used in cardiac ultrasound data, aiming to enhance cardiac tissue visualisation and tracking. The technique was referred to as Adaptive Brightness Transfer Function (ABTF) and was an example of clustering thresholding methods. ABTF was based on the assumption that the gray-level histogram of cardiac ultrasound images can be approximated by the sum of three non-overlapping normal distribution functions (Gaussians). Each Gaussian represented a different cardiac structure with the low intensity Gaussian representing cardiac cavities and the medium and high intensity Gaussians representing low and high intensity cardiac tissue structures respectively. The intersection between these three Gaussians would act as thresholds defining the intensity range of the three image segments. Each section of the histogram was then processed individually using a number of techniques including histogram equalisation, specification and scaling amongst

others. Histogram specification is a commonly used process, similar to histogram equalisation, which generates the output image assimilating to a pre-specified histogram (Gonzalez & Woods, 2001). (Zwirn & Akselrod, 2006) later used the histogram based thresholding method as a post-processing step for an automatic cluster rejection procedure on cardiac ultrasound data.

(Zwirn & Akselrod, 2004, 2005) data enhancement approach, while very promising, suffered from a number of limitations. Like all the histogram-shape based approaches described earlier, ABTF made a very strong assumption about the shape of the gray-level histograms of the processed cardiac ultrasound data. While the assumption holds in some datasets there is still a considerable number of datasets for which this assumption does not hold. Furthermore, ABTF assumed constant tissue and cavity brightness throughout the scanned structure. This has long been identified as a potential problem in many thresholding approaches (Gonzalez & Woods, 2001; Xiao et al., 2002). Adaptive thresholding methods divide the image in a number of sub-sections and proceed with the extraction of a corresponding threshold for each sub-sector (Gonzalez & Woods, 2001). A number of studies have employed adaptive thresholding method techniques (Sahoo et al., 1988; Xiao et al., 2002; Sezgin & Sankur, 2004). In addition, ABTF made no use of temporal information on the moving cardiac structures contained in a sequence of consecutive cardiac ultrasound frames. The potential value of such temporal information has been previously identified (Herlin & Ayache, 1992; Mulet-Parada & Noble, 2000; Achmad et al., 2009). Finally, while mostly a criticism and not a limitation, ABTF made use of complicated histogram equalisation and specification techniques even though a simple piecewise-linear intensity mapping would suffice.

***Histogram Based Intensity Mapping* (*DHBIM*)** aims to provide a simple, efficient and fully automated method for suppressing cavity noise, enhancing tissue speckle and increasing tissue/cavity contrast and detectability. The ***DHBIM*** method employs and extends a lot of the ideas introduced over the years. In the first instance, ***DHBIM*** utilises dynamic variations from a sequence of cardiac frames in order to derive the tissue/cavity threshold as well as any unutilised/underutilised intensity levels at the lower and higher end of the available gray-level range. Having identified all possible intensity thresholds, a simple piecewise-linear intensity transfer function is defined, providing a mapping between the intensity values in the original data and their corresponding intensity values in the processed data. In order to accommodate for any variations in the illumination, both the threshold derivation and intensity mapping are performed on a sequence of non-overlapping regions along the y-axis of the cardiac ultrasound scan.

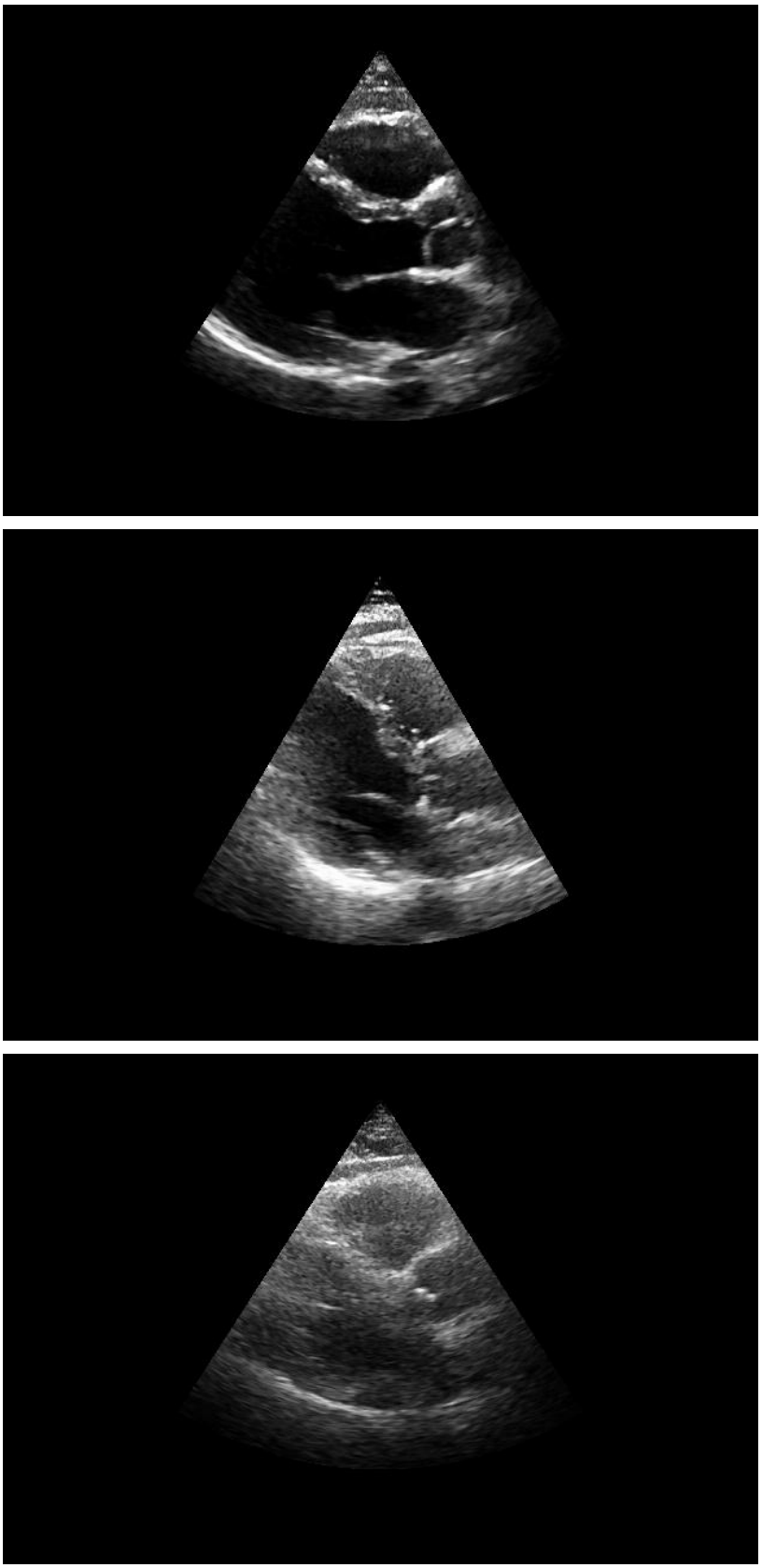

**Figure 5.1.** Examples from the original, unprocessed ED frames of (top) high (patient 12), (middle) average (patient 22) and (bottom) low (patient 4) image quality and diagnostic value.

## 5.2. Aims and contributions

The aim of this chapter is to introduce a fully automated method that utilises gray-level histogram information from multi-cycle cardiac B-mode datasets in order to suppress cavity noise, increase tissue intensity dynamic range and enhance the contrast and detectability between tissue and cavity.

The contributions of this chapter are:

- The development of ***Dynamic Histogram Based Intensity Mapping* (*DHBIM*)**, a novel and fully automated method for suppressing noise in cardiac cavities while enhancing cardiac tissue information by:
    - Analysing the dynamic temporal variations within image histograms of consecutive cardiac ultrasound frames in order to identify any unutilised/underutilised intensity levels as well as to derive the cardiac tissue/cavity intensity threshold.
    - Performing a piecewise intensity mapping (contrast stretching) on each individual frame in order to suppress the cavity while enhancing the tissue intensity dynamic ranges respectively.
- Assessing the effect of ***DHBIM*** on patient cardiac ultrasound scans using a range of quantitative measures such as tissue Signal-to-Noise Ratio (SNR), cavity SNR, tissue/cavity Contrast and Signal Difference to Noise Ratio (SDNR), also known as detectability index. Optimal acquisition parameters are identified ensuring the clinical feasibility of ***DHBIM***.
- Examining the effect of ***DHBIM*** on routine clinical measurements performed on patient cardiac ultrasound scans over a range of image qualities and diagnostic values.

## 5.3. Data acquisition and manual analysis

The 32 multi-cycle patient datasets (18 male, 14 female, ages ranging from 21 to 88 years with an average age of 60 years) described in Chapter 3 were utilised during the development and the assessment of the ***DHBIM*** algorithm. All datasets (25 cardiac cycles of the Parasternal Long-Axis view) were acquired according to the BSE standards (Henry et al., 1980; Feigenbaum, 1994; Fuster et al., 2008) by an experienced echocardiographer in the

Echocardiography department of the Western General Hospital, Edinburgh, during January of 2009. Prior to any processing each dataset was manually labeled as high (12), average (12) or low (8) according to the visually observed quality as well as the diagnostic value of its images (Figure 5.1).

## 5.4. Data processing

There are 4 steps to ***Dynamic Histogram Based Intensity Mapping*** **(*DHBIM*)**: (i) the identification of unutilised and underutilised intensity levels within the frame sequence, (ii) the suppression of the unutilised/underutilised intensity levels, (iii) the derivation of the cardiac tissue/cavity intensity threshold and (iv) the contrast enhancement between cardiac tissue and cavity structures. From experience, the level of cavity noise as well as the tissue/cavity contrast varied considerably between different segments of the imaged structure. Such variations could be attributed to the variable interaction of each structure with the transmitted ultrasound signal, as well as a non-optimal Time Gain Control (TGC) employed by the echocardiographer during data acquisition. As a result of the noise and contrast variations, the derived tissue/cavity threshold would be representative of the largest but not necessarily of all the cardiac structures imaged in the sector. Consequently, each step was performed on a number of non-overlapping sub-sectors along the *y*-axis of the cardiac scan (Figure 5.2) compensating for such large contrast variations. Each non-overlapping sector would act as a binary mask with no information outside the sector being used throughout the ***DHBIM*** process. A prerequisite for each sub-sector was to contain both cardiac tissue and cavity structures so that temporal histogram variations could generate a representative tissue/cavity threshold. Identifying a suitable number of sub-sectors was essential for the effectiveness and efficiency of the ***DHBIM*** process. For example, for a high number of sub-sectors, it would be very likely that some sectors would consist exclusively of cavity or tissue pixels making the derivation of tissue cavity threshold infeasible. On the other hand, using a low number of sectors, it would be very likely that each sector would contain a number of cardiac structures. The sectors where therefore empirically selected to represent different sections of a parasternal long axis cardiac ultrasound scan. The size of each sub-sector increased with the y-axis compensating for the size increase of the imaged cardiac structures. Finally, linear interpolation between the extracted thresholds was employed through the boundaries of each sector in order to avoid any intensity level discontinuities.

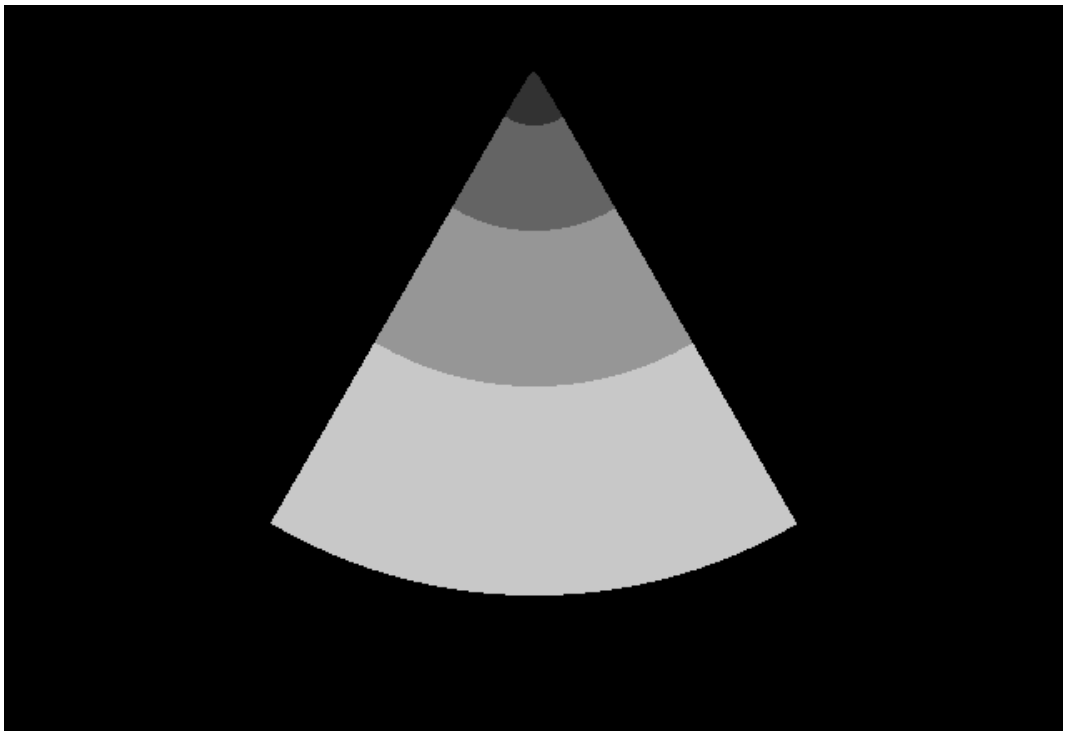

**Figure 5.2.** Partition of scan in four of non-overlapping sub-sectors along the y-axis.

A B-mode cardiac cycle can be described by an ordered sequence of *n* 2D images $S_k(x, y)$ with a fixed field of view $\Omega_{S_k}$ and an acquisition time $t_k$, where $t_k < t_{k+1}$, in the temporal direction. The resulting image sequence can be viewed as 2D+time structure $S(x, y, t)$ defined on the spatio-temporal domain $\Omega_{S_k} \times [t_1, t_n]$. The goal in this chapter is to derive an intensity transformation function *T* of the form:

$$T : S(x, y, t) \rightarrow S'(x, y, t) \qquad [5.1]$$

where $S(x, y, t)$ represents the gray level of the original image at point *(x, y)* and time *t* while $S'(x, y, t)$ represents the gray level on the processed image at point *(x, y)* and time *t*. Transformation *T* maps the intensity level $S(x, y, t)$ at any point in an image sequence into a corresponding intensity level $S'(x, y, t)$. The enhancement at any point within the image depends only on the gray level at that point. The values of such a transformation function are typically stored in a one-dimensional array while the intensity mappings are implemented via look-up tables (Gonzalez & Woods, 2001). For the 8-bit gray-level cardiac ultrasound images utilised in this study, a lookup table containing the values of intensity mapping *T* requires 256 entries $[0,255]$.

Throughout this chapter, any parameters required in order to define the intensity transfer function $T$ (intensity mapping) were automatically derived by analysing the dynamic variations in the image histograms along a sequence of consecutive cardiac ultrasound frames. The histogram of a digital image with gray levels in the range $[0,255]$ is a discrete function (Gonzalez & Woods, 2001):

$$H(r_k) = n_k \qquad [5.2]$$

where $r_k$ is the $k$th gray level and $n_k$ is the number of pixels in the image having gray level $r_k$. Figure 5.3 provides the histogram of an example ED cardiac ultrasound frame. A histogram can be normalised by dividing each of its values by the total number of pixels in the image, denoted by $n$ (Gonzalez & Woods, 2001):

$$p(r_k) = n_k / n \qquad [5.3]$$

for $k \in [0,255]$ (i.e. $p(r_k)$ denotes the probability of occurrence of gray level $r_k$).

Histograms provide useful image statistics and as a consequence they act as the basis for numerous spatial domain processing techniques such as image enhancement, segmentation and compression. Moreover, histograms are simple to calculate and efficient to operate on, making them a popular tool for real-time image processing.

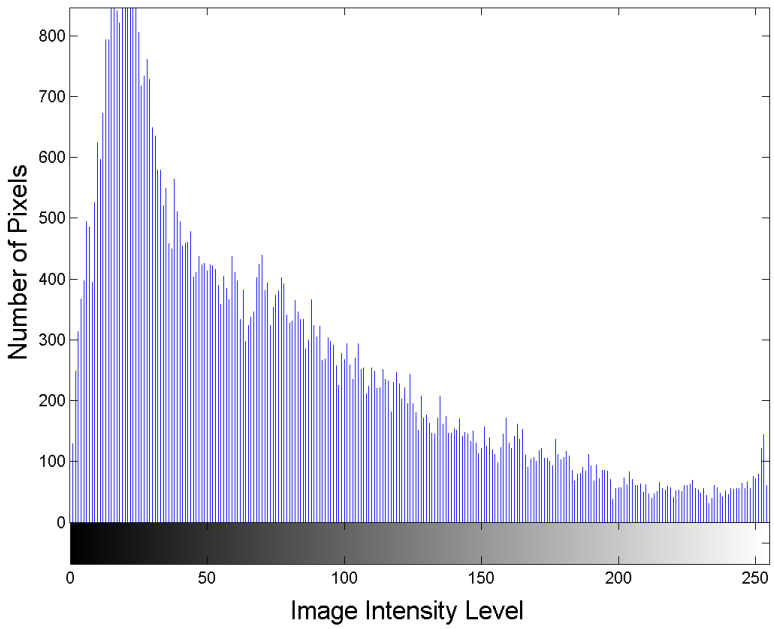


**Figure 5.3.** Example of a typical histogram of an ED cardiac ultrasound frame.

### 5.4.1. Identify unutilised/underutilised intensities within the frame sequence

Unutilised and underutilised intensity levels within the B-mode frame sequences were identified by analysing the dynamic temporal variations in the image histograms corresponding to a sequence of consecutive cardiac ultrasound frames. A normalised histogram was generated for each frame in the B-mode sequence:

$$p(r_k, t) = n_k(t) / n \qquad [5.4]$$

where $r_k$ was the *k*th gray level, $n_k(t)$ was the number of pixels in the image having gray level $r_k$ at time *t* and *n* total number of pixels in the image. The standard deviation (SD) of the variations in each intensity level over consecutive frames was then derived:

$$\sigma(r_k) = \sqrt{\frac{1}{N}\sum_{t=1}^{N}(p(r_k, t) - \mu)^2} \qquad [5.5]$$

where *N* was the total number of frames and $\mu$ was the mean $p(r_k)$ value over the B-mode frame sequence. The derived SD profiles highlighted any intensity levels for which $p(r_k)$ underwent negligible variations over the B-mode frame sequence. More precisely, the SD profiles demonstrated roughly a Skew Normal Distribution with intensity levels indicating limited or no variation (over the frame sequence) being observed in the bottom and top end of the intensity range. Such intensity levels are either not utilised within the frame sequence, hence the absence of variation, or they correspond to pixels within a cavity or tissue structure that was largely unaffected by the constant, rapid cardiac motion. In either case, intensity levels with negligible or no variations do not correspond to clinically critical information. A heuristic threshold set as less than 1% of the maximum value observed over the derived SD profile was utilised in order to identify such unutilised and underutilised intensity levels:

$$\begin{aligned} th_l &= i, \quad \text{where} \quad \sigma(r_0) \to \sigma(r_i) < 1\% * \max[\sigma(r_k)] \\ th_t &= j, \quad \text{where} \quad \sigma(r_j) \to \sigma(r_{255}) < 1\% * \max[\sigma(r_k)] \end{aligned} \qquad [5.6]$$

### 5.4.2. Suppress unutilised/underutilised intensity levels

Having identified the lower and upper thresholds ($th_l$ and $th_t$) defining the predominantly utilised intensity range within the B-mode frame sequence, it was possible to enhance the corresponding information (dynamic range) within the imaged cardiac structure. This study utilised a simple piecewise-linear transformation function as an intensity mapping between

the original and the processed frame sequences. A piecewise linear function is a contrast-stretching transformation that increases the dynamic range of the gray levels in the image being processed (Gonzalez & Woods, 2001) (Figure 5.4.a). The shape of the transformation was controlled by thresholds $th_l$ and $th_t$. In this study, the piecewise-linear transformation function $f_1$ was defined as (Figure 5.4.b):

$$f_1(r_k) = \begin{cases} 0, & \text{if } k \le th_l; \\ 255, & \text{if } k \ge th_t; \\ a * r_k + b, & \text{if } th_l < k < th_t \end{cases} \qquad [5.7]$$

where $r_k$ was the *k*th intensity level, *a* represented the slope of the linear contrast stretching $\left(a = 255 \big/ th_t - th_l\right)$ and *b* represented its *y*-intercept $\left(b = 255 * th_l \big/ th_t - th_l\right)$. The defined transformation compressed all intensity levels below or equal to $th_l$ to the single intensity value of 0. This process is known as black level expansion. Similarly, the transformation compressed all intensity levels above or equal to $th_t$ to the single intensity value of 255. This process is known as white level expansion. As a result, intensity levels between $th_l$ and $th_t$, that were predominately utilised in the processed frame sequence, were linearly stretched to the full 8-bit gray-scale range of [0-255] increasing the dynamic range of the imaged cardiac structure.

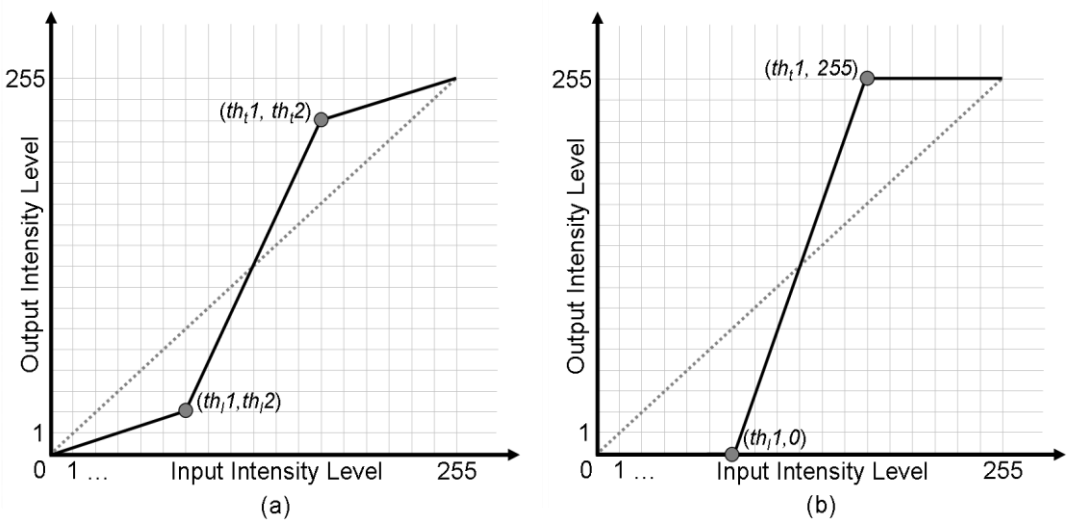


**Figure 5.4.** (a) A typical example of a piecewise-linear transformation function used for contrast stretching. (b) An example of the type of intensity mapping utilised in this study.

### 5.4.3. Identify tissue/cavity intensity threshold

Similar to Section 3.5.1, the cardiac tissue/cavity intensity threshold, $th_{ct}$, was identified by analysing the dynamic temporal variations in the image histograms over a sequence of consecutive cardiac ultrasound frames. The novel approach proposed in this study was based on some basic observations in cardiac ultrasound data. Let $n_c(d)$ and $n_c(s)$ represent the number of cardiac cavity pixels within an ED and an ES frame respectively. Moreover, $diff_cDS$ represents the difference in the number of cavity pixels between ED (where ventricular cavities reach maximum volume) and ES (where ventricular cavities reach minimum volume):

$$diff_cDS = n_c(d) - n_c(s). \qquad [5.8]$$

If $th_r$ represents an arbitrarily selected tissue/cavity gray-level threshold then there are three possible cases. In the first case, $th_r$ is set lower than the actual tissue/cavity threshold ($th_r < th_{ct}$). As a result:

$$\begin{aligned} diff_rDS &= n_r(d) - n_r(s) \\ &= \left(n_c(d) - n_{fn}(d)\right) - \left(n_c(s) - n_{fn}(s)\right) \\ &= \left(n_c(d) - n_c(s)\right) - \left(n_{fn}(d) - n_{fn}(s)\right) \\ &= diff_cDS - \left(n_{fn}(d) - n_{fn}(s)\right) \end{aligned} \qquad [5.9]$$

where, $n_r(d)$ and $n_r(s)$ are the total number of "cavity" pixels identified (i.e. pixels with intensity less than threshold $th_r$) while $n_{fn}(d)$ and $n_{fn}(s)$ are the number of cavity pixels falsely identified as tissue pixels in the ED and ES frames respectively. Given that the number of cavity pixels reaches its maximum in ED and its minimum in ES, $\left(n_{fn}(d) - n_{fn}(s)\right)$ is expected to be greater than 0 and therefore $diff_rDS$ less than $diff_cDS$. In the second case, $th_r$ is set higher than the actual tissue/cavity threshold ($th_r > th_{ct}$) and therefore:

$$\begin{aligned} diff_rDS &= n_r(d) - n_r(s) \\ &= \left(n_c(d) + n_{fp}(d)\right) - \left(n_c(s) + n_{fp}(s)\right) \\ &= \left(n_c(d) - n_c(s)\right) + \left(n_{fp}(d) - n_{fp}(s)\right) \\ &= diff_cDS + \left(n_{fp}(d) - n_{fp}(s)\right) \end{aligned} \qquad [5.10]$$

where, $n_r(d)$ and $n_r(s)$ are the total number of "cavity" pixels identified while $n_{fp}(d)$ and $n_{fp}(s)$ are the number of tissue pixels falsely identified as cavity pixels in the ED and ES frames respectively. Given that the number of tissue pixels reaches its minimum in ED and its maximum in ES, $\left(n_{fp}(d) - n_{fp}(s)\right)$ is expected to be less than 0 and therefore $diff_r DS$ less than $diff_c DS$. Consequently, in the third and last case where $th_r$ is equal to the actual tissue/cavity threshold ($th_r = th_{ct}$) $diff_r DS$ attains its maximum value which is equal to $diff_c DS$. Determining the intensity level for which $diff_r DS$ attains its maximum value is therefore required for the derivation of the tissue/cavity intensity threshold.

In this study, the number of identified "cavity" pixels $n_r(k)$ for a given threshold $th_r$ (pixel intensities less than threshold $th_r$) was derived over the full range of possible threshold values (i.e. [0-255]) utilising a cumulative image histogram:

$$cH(r_k) = \sum_{i=0}^{k} n_i \qquad [5.11]$$

where $r_k$ was the *k*th gray level and $n_i$ was the number of pixels in the image having gray level $r_i$. Considering the high noise level along with other artifacts (such as shadowing) present in cardiac ultrasound data, a more robust measure of determining the variation in the number of cavity pixels between ED and ES (compared to $diff_r DS$) was required. As a result, the Standard Deviation (SD) of the population variations over consecutive frames for each intensity level within the cumulative histogram was utilised:

$$\sigma(r_k) = \sqrt{\frac{1}{N}\sum_{t=1}^{N}(cH(r_k,t) - \mu)^2} \qquad [5.12]$$

where *N* was the total number of frames and $\mu$ was the mean $cH(r_k)$ value over the B-mode frame sequence. Similar to $diff_r DS$, the SD was expected to demonstrate a maximum value for $th_r$ equal to the actual tissue/cavity threshold ($th_r = th_{ct}$):

$$th_{ct} = k : \max_{k=0}^{255}\left(\sigma(r_k)\right). \qquad [5.13]$$

In order to further enhance the robustness of the approach, making it less susceptible to outliers than the suggested Equation 5.8, data from multiple ED-ES sequences were utilised during the derivation and allocation of the maximum SD value.

### 5.4.4. Enhance contrast between cardiac tissue and cavity structures

Having identified threshold $th_{ct}$ defining the intensity levels corresponding to cardiac cavity and tissue, it was possible to utilise a new piecewise-linear transformation function (intensity mapping) in order to (i) suppress noise in cardiac cavities, (ii) increase the displayed dynamic range in cardiac tissue, enhancing the available tissue speckle information, and (iii) enhance the contrast between cardiac tissue and cavity. The shape of the transformation $f_2$ was controlled by threshold $th_{ct}$ and was defined as (Figure 5.5):

$$f_2(r_k) = \begin{cases} r_k / 2, & \text{if } k \le th_{ct}; \\ a * r_k + b, & \text{if } k > th_{ct} \end{cases} \quad [5.14]$$

where $r_k$ was the *k*th intensity level, *a* represented the slope of the linear contrast stretching $\left( a = 1 + \frac{th_{ct}}{2*(255 - th_{ct})} \right)$ and *b* represented its *y*-intercept $\left( b = -\frac{255 * th_{ct}}{2*(255 - th_{ct})} \right)$. The defined transformation compressed all intensity levels below or equal to $th_{ct}$ by 50%, suppressing cavity noise. Furthermore, intensity levels above $th_{ct}$ (representing cardiac tissue in the processed frame sequence) were linearly stretched to the gray-scale range of $\left[ \frac{th_{ct}}{2}, 255 \right]$, increasing the tissue dynamic range within the imaged cardiac structure.

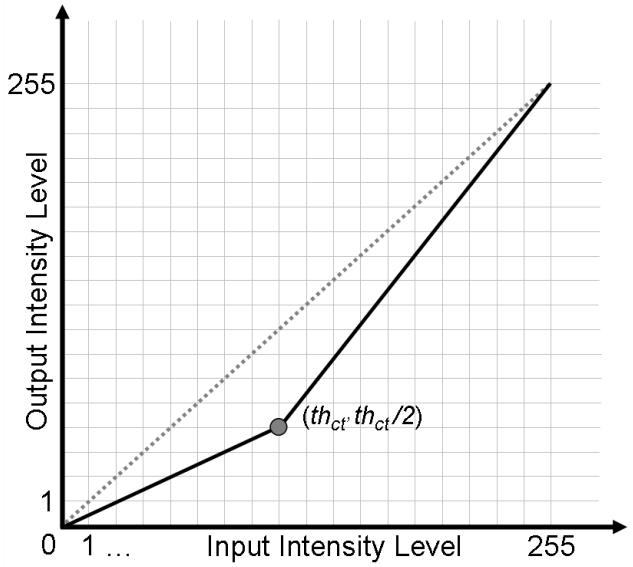


**Figure 5.5.** Example of intensity transformation function utilised in order to suppress cavity noise and enhance the dynamic range within tissue speckle as well as the cardiac tissue/cavity contrast.

## 5.5. Data analysis and results

Similarly to the previous two chapters, a range of quantitative and qualitative results are presented in order to assess the effect of ***Dynamic Histogram Based Intensity Mapping* (*DHBIM*)** on cardiac ultrasound data. The main objective was to identify optimal parameters that will ensure the clinical feasibility of ***DHBIM*** by achieving adequate cavity noise suppression as well as contrast enhancement between cardiac tissue and cavity while (i) maintaining tissue information within the processed B-mode data to a clinically acceptable level and (ii) keeping data acquisition time and processing requirements to a minimum by limiting the number of utilised cardiac cycles.

### 5.5.1. Identify unutilised/underutilised intensities within the frame sequence

Figure 5.6 illustrates two examples of the histogram variations within cardiac B-mode datasets over consecutive frames. Consecutive frames of three cardiac cycles were utilised as they were found to provide robust intensity thresholds, largely unaffected by outliers, without requiring considerable increase in processing resources. For each image intensity level, the corresponding SD representing histogram variation over time was derived. The obtained SD profile for each of the two example datasets is also illustrated. The first example is representative of datasets utilising all the available levels within the [0-255] intensity range. The second example is representative of datasets that do not utilise all the available levels within the [0-255] intensity range. More precisely, the given example contains unutilised/underutilised intensity levels both at the low and top end of the [0-255] intensity range. Table 5.1 enumerates the datasets identified demonstrating un-utilised/underutilised gray levels within the image intensity range. Furthermore, Table 5.2 provides the range, mean and SD of (i) the derived thresholds $th_l$ and $th_t$, and (ii) the total number of unutilised/underutilised intensity levels within the 32 patient cardiac ultrasound datasets. The automatic threshold identification algorithm was independently executed in four non-overlapping sub-sectors along the *y*-axis of each cardiac scan. The results are therefore derived and presented for each of these four sectors.

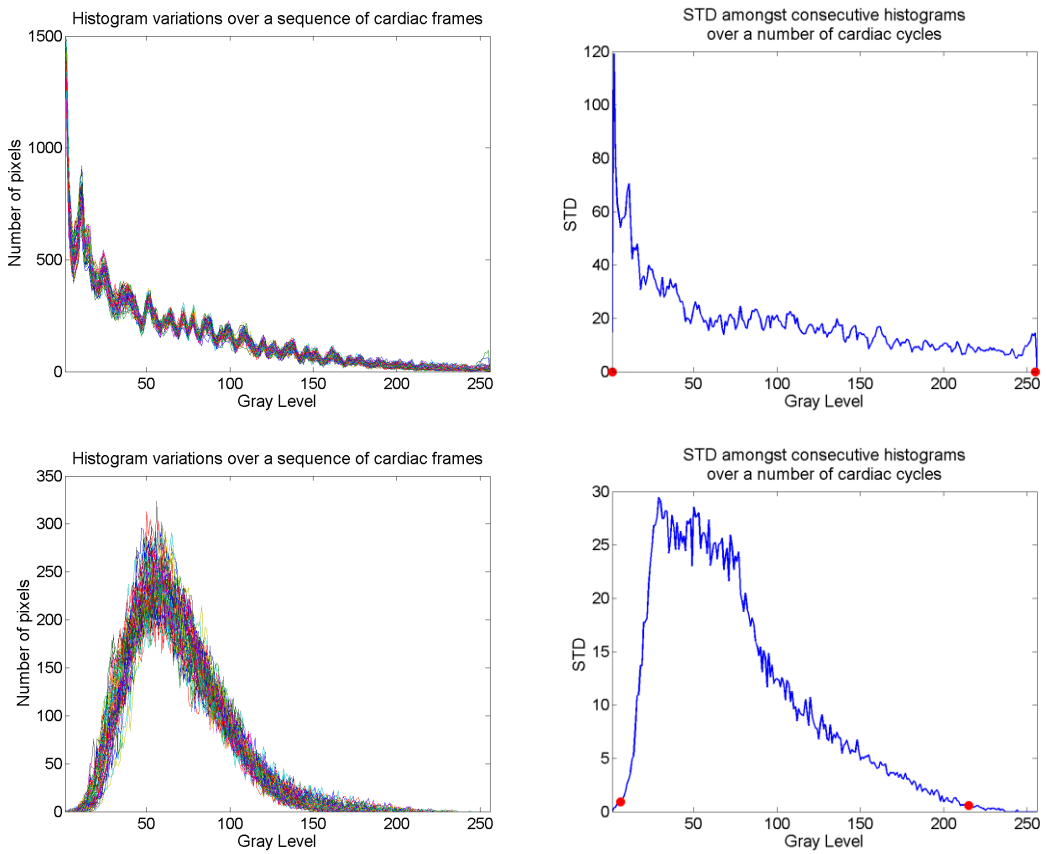


**Figure 5.6.** Variations on image histograms over two example sequences of B-mode cardiac frames along with their corresponding SD profiles. Top: frame sequence utilising all intensity levels. Bottom: frame sequence with unutilised/underutilised intensity levels both in the lower and top regions of the [0-255] gray-level range.

**Table 5.1.** Enumeration of identified datasets demonstrating unutilised/underutilised gray levels within the image intensity range of the 32 patient cardiac ultrasound datasets.

| | **Number of datasets with $th_l > 0$** | **Number of datasets with $th_t < 255$** | **Number of datasets with underutilised intensities** |
|---|---|---|---|
| **Sector 1** | 14 (43.8%) | 7 (21.9%) | 18 (56.3%) |
| **Sector 2** | 22 (68.8%) | 6 (18.8%) | 26 (81.3%) |
| **Sector 3** | 9 (28.1%) | 19 (59.4%) | 25 (78.1%) |
| **Sector 4** | 5 (15.6%) | 11 (34.4%) | 13 (40.6%) |
| **Total** | 50 (39.1%) | 43 (33.6%) | 82 (64.1%) |

**Table 5.2.** The range, mean and SD of (i) the derived bottom and top thresholds indicating un-utilised/underutilised gray levels and (ii) the total number of unutilised/underutilised intensity levels within the 32 patient cardiac ultrasound datasets.

| | **Lower Threshold ( $th_l$ )** | **Upper Threshold ( $th_t$ )** | **Underutilised Intensity Levels** |
|---|---|---|---|
| **Min** | 0 | 109 | 0 |
| **Max** | 51 | 255 | 125 |
| **Mean** | 8 | 210 | 28 |
| **SD** | 11 | 39 | 34 |

### 5.5.2. Suppress unutilised/underutilised intensity levels

Figures 5.7 and 5.8 display two example ED frames before and after automatic increase in the dynamic range of the imaged cardiac structure is applied to their corresponding multi-cycle datasets. The dataset in Figure 5.7 demonstrates unutilised/underutilised gray-levels on the top end of the image intensity range. The increase in the dynamic range by suppressing the identified underutilised gray-levels (white level expansion) intensified the tissue information, increasing the contrast between cardiac tissue and cavity. Similarly, the dataset utilised in Figure 5.8 demonstrates unutilised/underutilised gray-levels on the low end of the image intensity range. The increase in the dynamic range by suppressing the identified underutilised gray-levels (black level expansion) attenuated the cavity information, increasing the contrast between cardiac tissue and cavity. The effect of the linear contrast stretching of intensities between $th_l$ and $th_t$ (predominately utilised in the frame sequence) to the full 8-bit gray-scale range was quantitatively assessed using the approach introduced for ***Temporal Compounding***. As described in Section 3.7.2.1., two (11x11 pixels) ROIs corresponding to the IVS and the RV cavity had been previously defined on each of the 32 patient datasets. The pixel intensity values at each ROI were used to estimate the tissue SNR, cavity SNR, the tissue/cavity Contrast and the detectability index SDNR on an original as well as a processed ED frame for each of the datasets. Tables 5.3 to 5.6 summarise the variations on those four quantitative measures between the original and the processed datasets, illustrating the effect of dynamic range increase on the imaged cardiac structures.

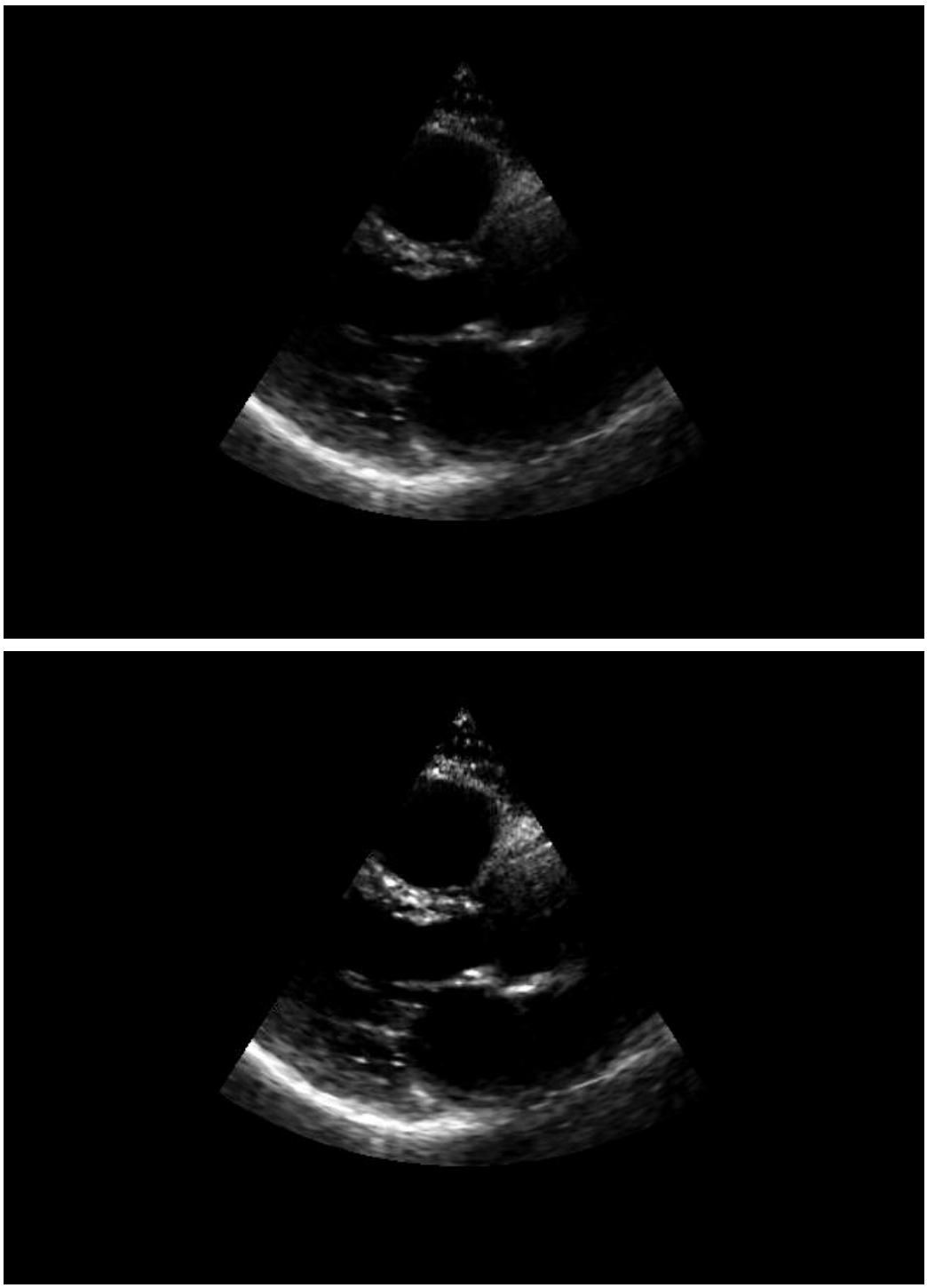

**Figure 5.7.** Example of original and contrast enhanced image where there is noticeable increase in contrast (utilising unused intensity levels on top of [0-255] range). (Patient 14)

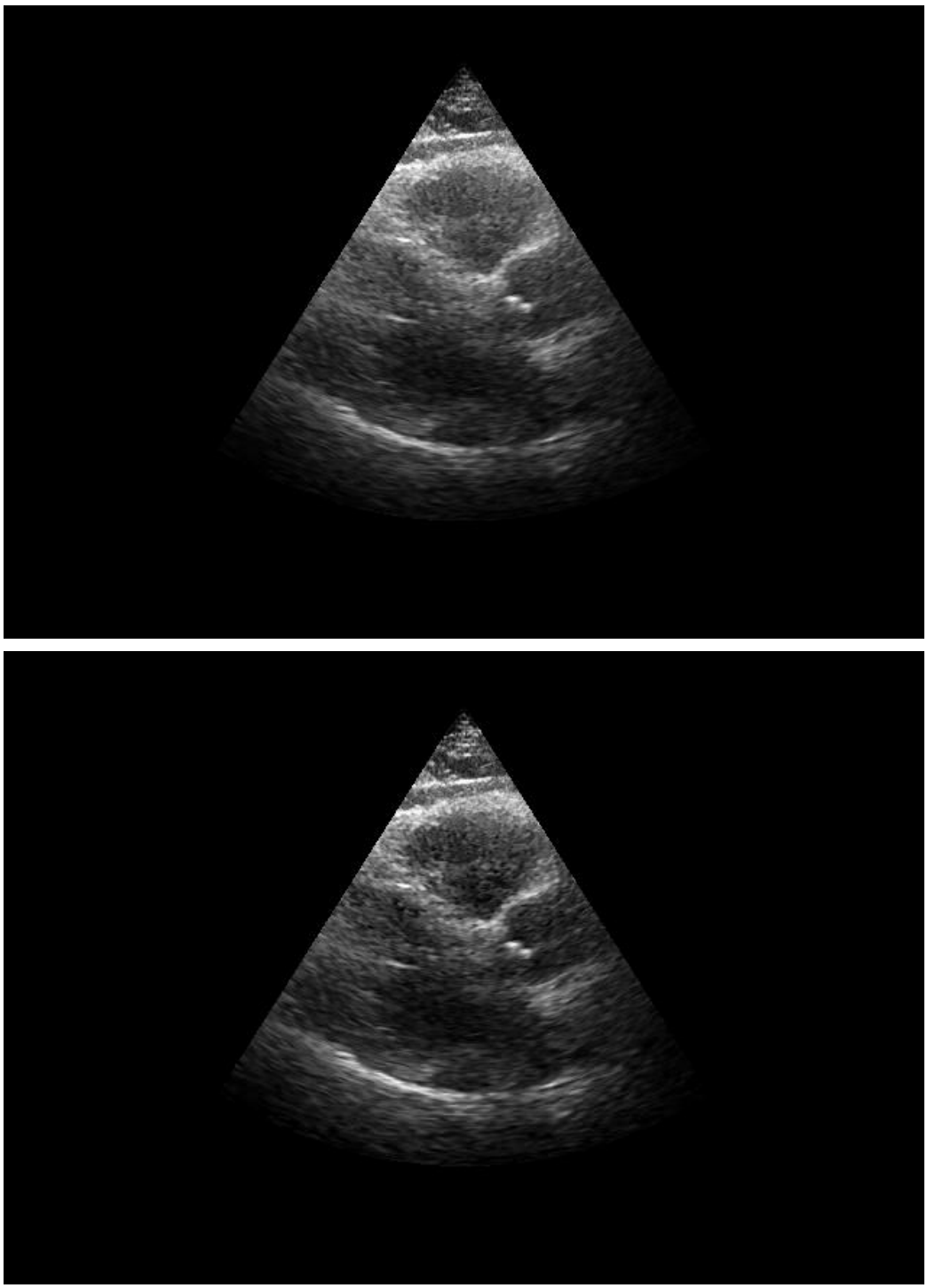

**Figure 5.8.** Example of original and contrast enhanced image where there is noticeable increase in contrast (utilising unused intensity levels on bottom of [0-255] range). (Patient 4)

**Table 5.3.** Effect of contrast enhancement on tissue SNR.

| | Original | Contrast Stretched | Improvement |
|---|---|---|---|
| **Min** | 2.22 | 2.14 | -33.9% |
| **Max** | 7.37 | 7.33 | 2.4% |
| **Mean** | 4.15 | 3.81 | -6.2% |
| **SD** | 1.59 | 1.28 | 8.6% |

**Table 5.4.** Effect of contrast enhancement on cavity SNR.

| | Original | Contrast Stretched | Improvement |
|---|---|---|---|
| **Min** | 0.89 | 0.61 | -40.0% |
| **Max** | 10.44 | 8.50 | -2.3% |
| **Mean** | 5.05 | 4.41 | -13.2% |
| **SD** | 1.86 | 1.76 | 12.4% |

**Table 5.5.** Effect of contrast enhancement on tissue/cavity contrast.

| | Original | Contrast Stretched | Improvement |
|---|---|---|---|
| **Min** | 0.17 | 0.18 | 0.0% |
| **Max** | 2.00 | 2.00 | 90.6% |
| **Mean** | 0.83 | 0.89 | 11.1% |
| **SD** | 0.56 | 0.56 | 18.4% |

**Table 5.6.** Effect of contrast enhancement on tissue/cavity SDNR.

| | Original | Contrast Stretched | Improvement |
|---|---|---|---|
| **Min** | 0.90 | 0.86 | -14.0% |
| **Max** | 35.39 | 36.24 | 44.4% |
| **Mean** | 6.79 | 7.17 | 3.5% |
| **SD** | 7.47 | 8.56 | 11.6% |

### 5.5.3. Identify tissue/cavity intensity threshold

Figure 5.9 provides a cumulative histogram example for a single cardiac ultrasound frame as well as an example plot of the cumulative histogram variations over consecutive cardiac frames. The SD within each intensity level was calculated in order to represent the

corresponding cumulative histogram variations over time, generating a SD profile. Figure 5.10 illustrates the effect of using an increasing number of cardiac cycles during the derivation of the corresponding SD profile. The tissue/cavity threshold was identified as the intensity level demonstrating maximum SD within the derived profile. Investigating the variations in the derived tissue/cavity threshold using an increasing number of cardiac cycles it became apparent that, for all datasets, the tissue/cavity threshold settled to characteristic intensity level after a few cardiac cycles. The mean intensity threshold derived using 18 to 20 cardiac cycles was considered as a representative, but not necessarily a definite, value of the characteristic threshold $th_r$ for each dataset. Moreover, the absolute difference between the current threshold $th_c$, derived using an increasing number of cardiac cycles, and $th_r$ was calculated and a mean profile for all 32 datasets was derived. Figure 5.11 displays the mean difference profile for each of the four non-overlapping sectors defined along the y-axis of the cardiac scans. For each dataset, when the absolute threshold difference ($|th_c - th_r|$) dropped and remained below 5 intensity levels, the threshold was considered settled. Table 5.7 enumerates the datasets for which threshold settled within 5, 7 and 9 cardiac cycles. For all settled datasets, the mean and SD of the absolute threshold difference ($|th_c - th_r|$) are also provided. Finally, as mentioned earlier, all datasets settled to a characteristic threshold by utilising information from an increasing number of cardiac cycles. However, in some datasets when using a large number of cardiac cycles a considerable and sudden change in the characteristic threshold occurred. Table 5.7 also enumerates datasets demonstrating such behaviour.

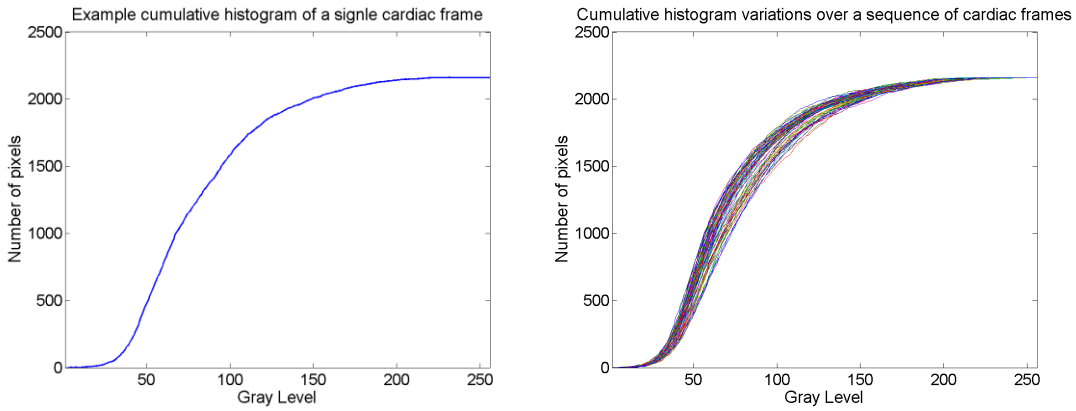


**Figure 5.9.** Example cumulative histogram (left) and cumulative histogram variations over time (right). (dataset 1, level 2)

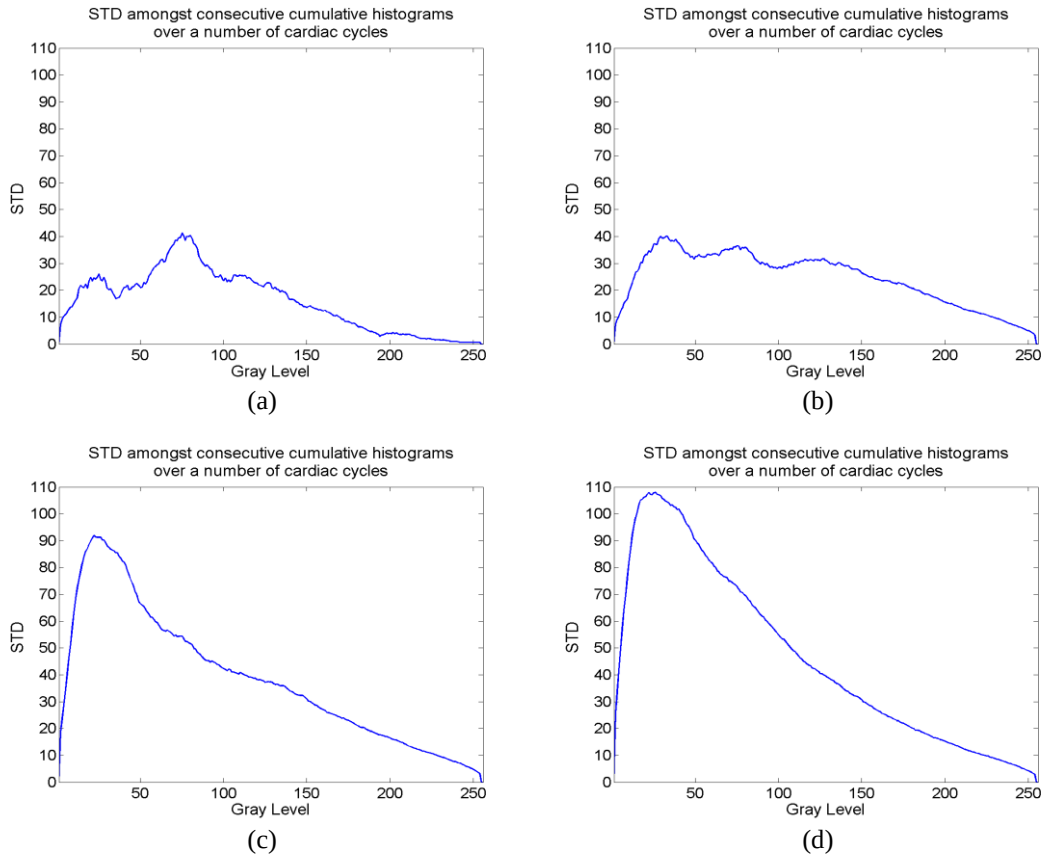


**Figure. 5.10.** Example SD profile of the cumulative histogram variations derived using data from an increasing number of cardiac cycles: (a) 1 cardiac cycle, (b) 3 cardiac cycles, (c) 5 cardiac cycles and (d) 7 cardiac cycles. (dataset 19, level 2)

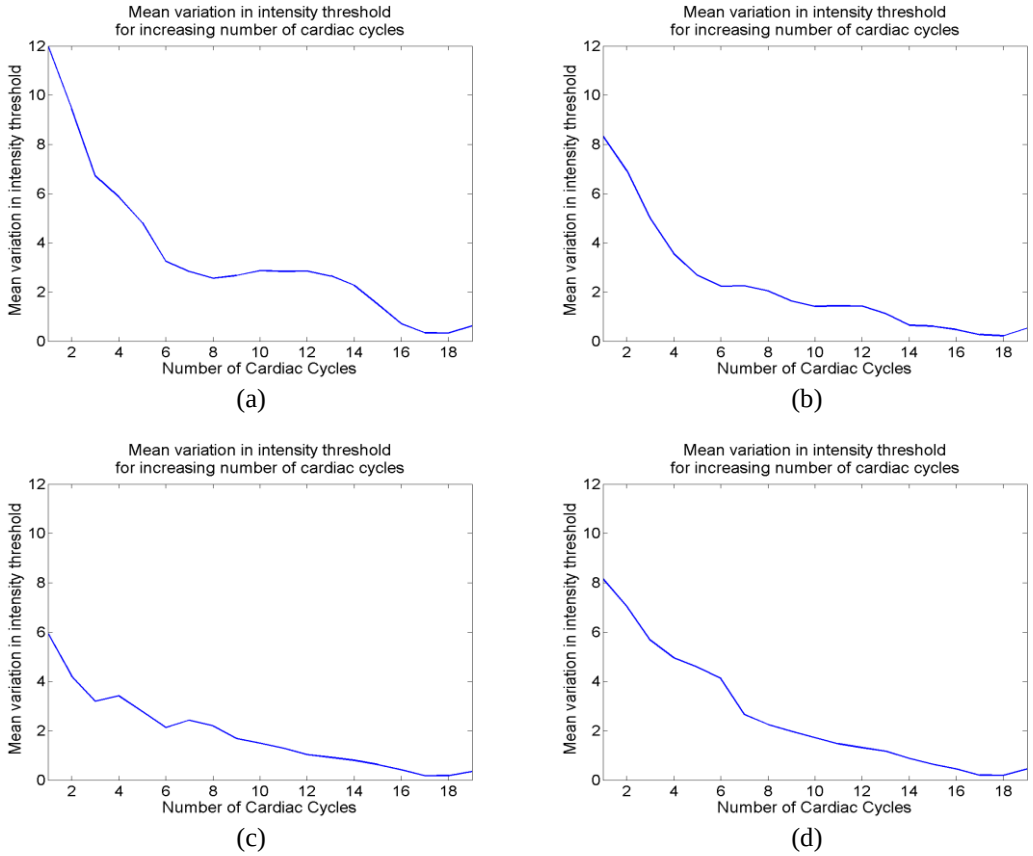


**Figure 5.11.** Mean profile of the absolute difference between the characteristic and the current threshold derived using an increasing number of cardiac cycles. Plots (a) to (d) correspond to each of the four non-overlapping sectors defined along the y-axis of the cardiac scans.

**Table 5.7.** Effect of increasing the number of cardiac cycles on the relation between current and the characteristic tissue/cavity threshold.

| | **Number of Cardiac Cycles** | | |
|---|---|---|---|
| | **5 Cardiac Cycles** | **7 Cardiac Cycles** | **9 Cardiac Cycles** |
| **Unsettled** | 20.3% (26/128) | 8.6% (11/128) | 7.0% (9/128) |
| **Settled** | 79.7% (102/128) | 91.4% (117/128) | 93.0% (119/128) |
| **Severe change** | 10.9% (14/128) | 10.9% (14/128) | 10.9% (14/128) |
| **Mean Diff (Settled)** | 1.4 | 1.7 | 1.5 |
| **SD (Settled)** | 1.2 | 1.5 | 1.4 |

### 5.5.4. Contrast enhancement between cardiac tissue and cavity structures

The effect of the complete ***DHBIM*** process on cardiac ultrasound data was investigated by examining the SNR changes at the IVS and the RV cavity, as well as contrast and SDNR changes between tissue (IVS) and cavity (RV). However, the effect on tissue/cavity thresholding and tissue information maintenance was not examined directly since outlining

cardiac tissue on clinical data is a laborious, highly subjective and many times erroneous process. Furthermore, an eminently accurate tissue/cavity segmentation was beyond the scope of this study. Instead, the effect of ***DHBIM*** on tissue/cavity boundaries was investigated by performing routine clinical measurements on tissue structures and cavities. Such measurements provided sufficient information for assessing the clinical effect of ***DHBIM*** on the processed datasets.

Figures 5.12 to 5.17 display six example ED frames before and after ***DHBIM*** is applied on their corresponding datasets. In addition, for each example an image highlighting areas identified as tissue, by demonstrating intensity greater than the derived tissue/cavity threshold, is displayed. Datasets covering a range of image and diagnostic qualities (3 low, 2 average and 1 high) were selected in order to best illustrate the effect of ***DHBIM*** on cardiac ultrasound data. More processed datasets can be found in the accompanying DVD-1.

#### 5.5.4.1. Effect on tissue SNR, cavity SNR, tissue/cavity contrast and SDNR

The effect of ***DHBIM*** on the noise and contrast within the imaged cardiac structures is quantitatively assessed using the approach introduced in Section 3.7.2.1. Two (11x11 pixels) ROIs corresponding to the cardiac IVS and the RV cavity had been previously defined on each of the 32 patient datasets. The pixel intensity values at each ROI were used to estimate the tissue SNR, cavity SNR, the tissue/cavity Contrast and the detectability index SDNR on both an original as well as a processed ED frame for each of the 32 datasets. Tables 5.8 to 5.11 summarise the variations on those four quantitative measures between the original and the processed datasets illustrating the effect of ***DHBIM*** on the imaged cardiac structures.

#### 5.5.4.2. Effect on clinical measurements performed on patient data

Similar to the process described in Section 3.6 and utilised in Chapter 4, two experienced echocardiographers were asked to perform routine clinical measurements on ED and ES frames from both the original B-mode as well as the contrast enhanced data. All clinical measurements were performed twice to enable the examination of measurement agreement and repeatability. The Bland Altman approach (Section 3.7.2.3) was then used for the quantitative assessment of the effect of ***DHBIM*** on clinical measurements. Figures 5.18 and 5.19 display Bland Altman plots combining all clinical measurements performed by each echocardiographer. Individual plots, one for each clinical measure, were also derived. Table 5.12 summarises the bias, similarity measures and agreement coefficients derived from the individual plots. Tables 5.13 and 5.14 display which clinical measurements were omitted by each echocardiographer on the original and contrast enhanced datasets.

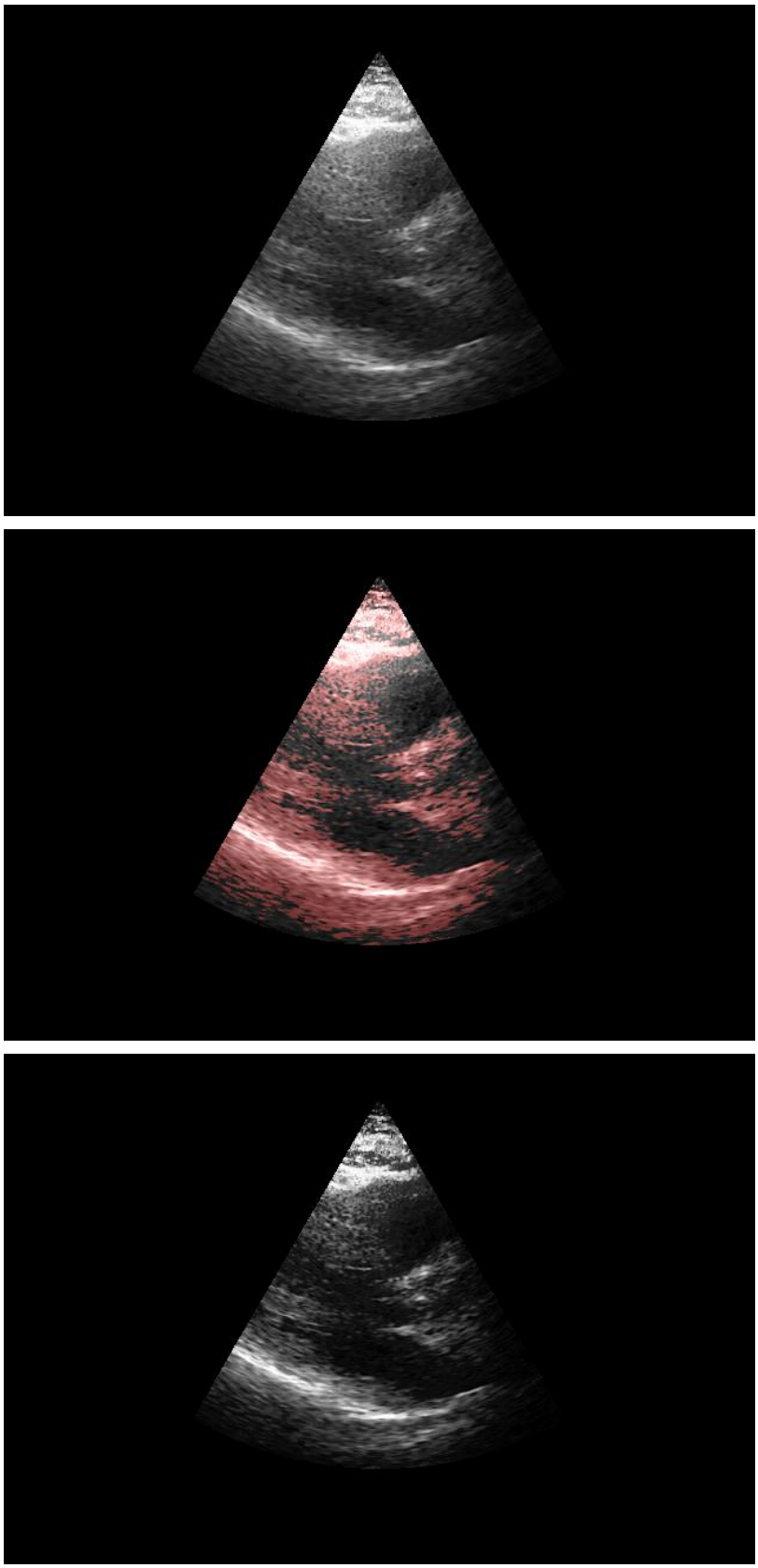

**Figure 5.12.** Original (top) and contrast enhanced (using ***DHBIM***) (bottom) ED frames of low diagnostic value. Middle image highlights areas identified as tissue. (Patient 24)

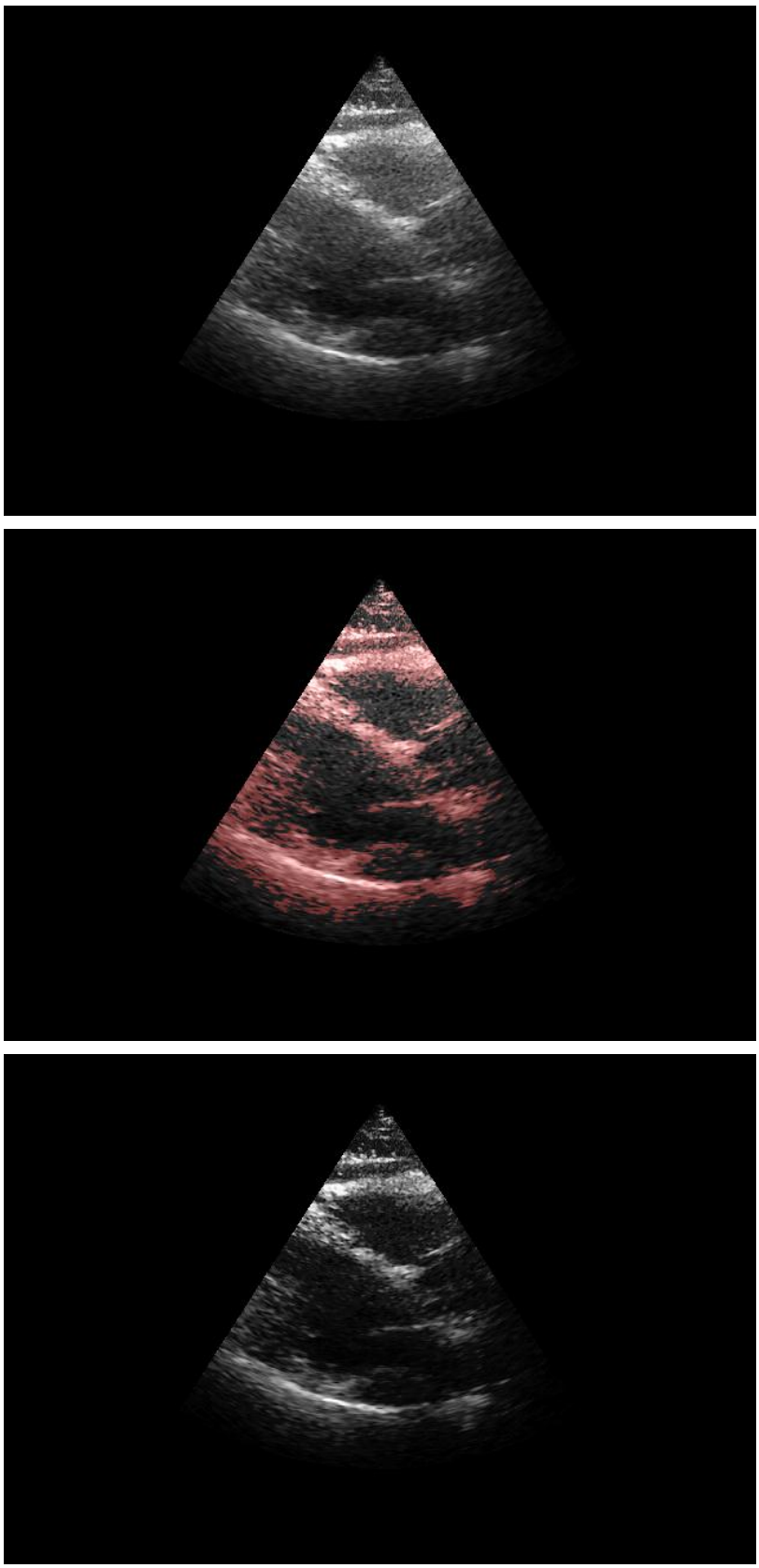

**Figure 5.13.** Original (top) and contrast enhanced (using ***DHBIM***) (bottom) ED frames of low diagnostic value. Middle image highlights areas identified as tissue. (Patient 4)

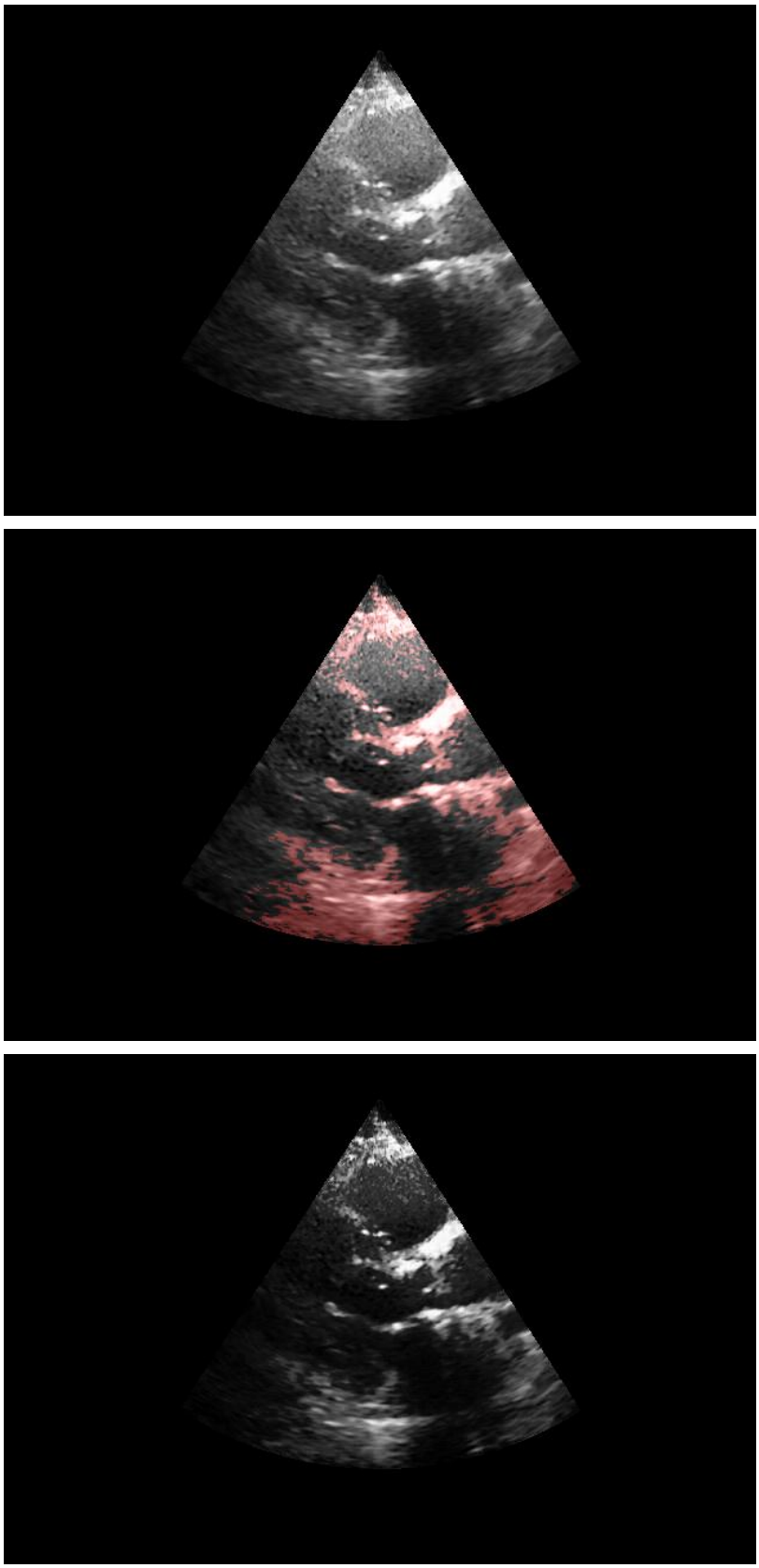

**Figure 5.14.** Original (top) and contrast enhanced (using ***DHBIM***) (bottom) ED frames of low diagnostic value. Middle image highlights areas identified as tissue. (Patient 6)

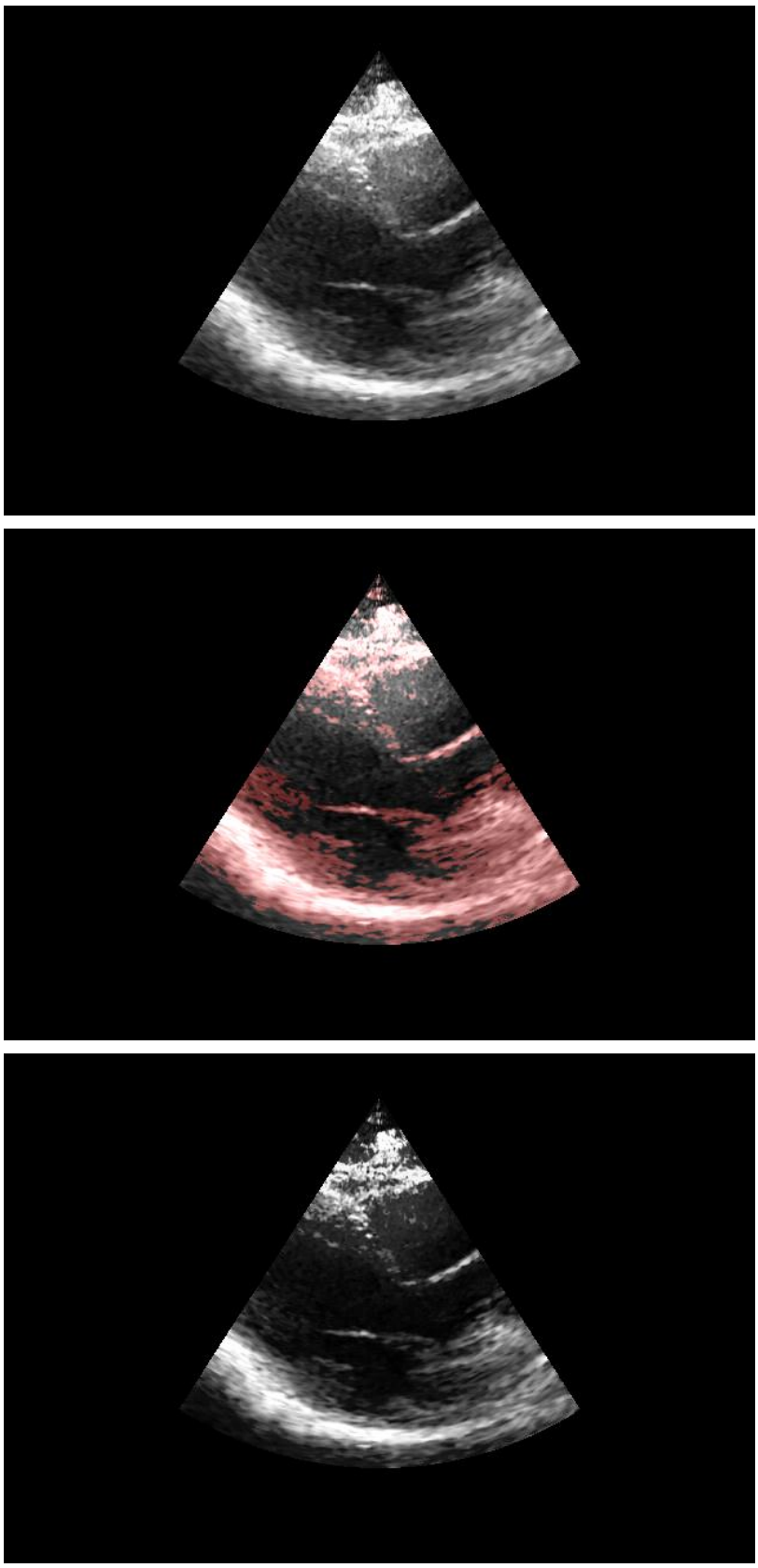

**Figure 5.15.** Original (top) and contrast enhanced (using ***DHBIM***) (bottom) ED frames of average diagnostic value. Middle image highlights areas identified as tissue. (Patient 11)

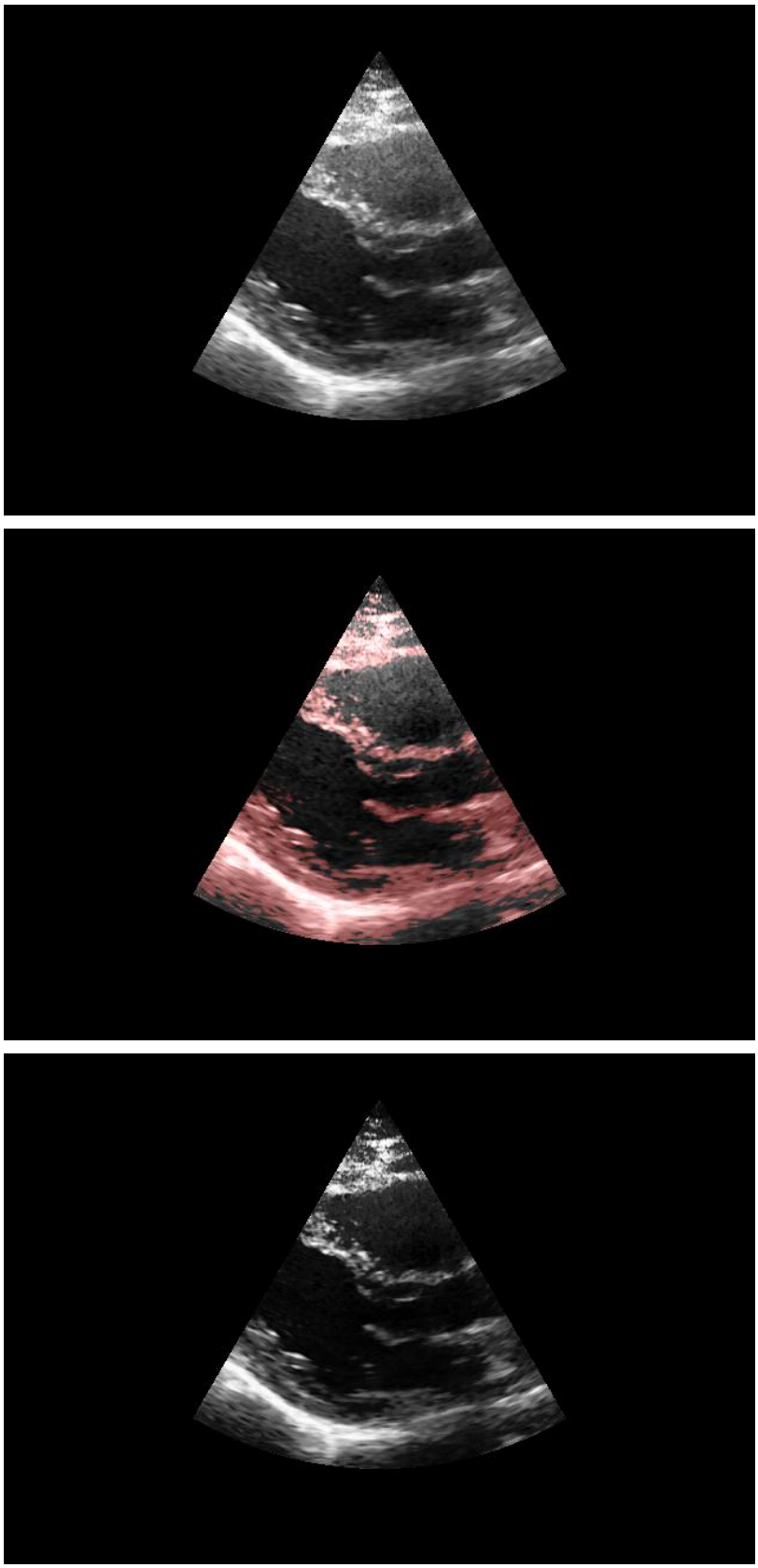

**Figure 5.16.** Original (top) and contrast enhanced (using ***DHBIM***) (bottom) ED frames of average diagnostic value. Middle image highlights areas identified as tissue. (Patient 25)

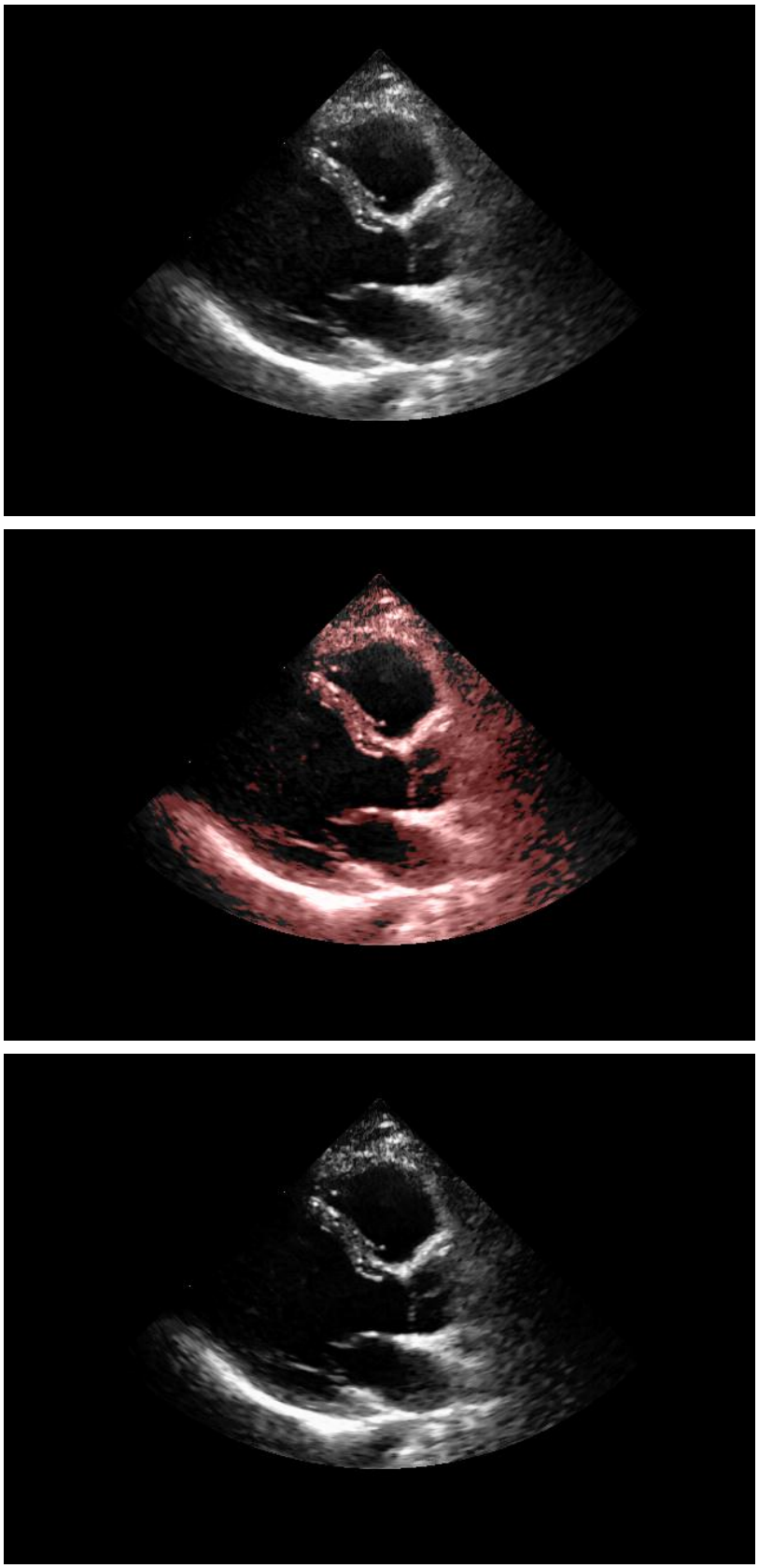

**Figure 5.17.** Original (top) and contrast enhanced (using ***DHBIM***) (bottom) ED frames of high diagnostic value. Middle image highlights areas identified as tissue. (Patient 29)

**Table 5.8.** Effect of ***DHBIM*** on tissue SNR.

| | Original | Contrast Enhanced | Improvement |
|---|---|---|---|
| **Min** | 2.22 | 1.34 | -68.1% |
| **Max** | 7.37 | 4.20 | -4.0% |
| **Mean** | 4.15 | 2.47 | -37.0% |
| **SD** | 1.59 | 0.76 | 15.9% |

**Table 5.9.** Effect of ***DHBIM*** on cavity SNR.

| | Original | Contrast Enhanced | Improvement |
|---|---|---|---|
| **Min** | 0.89 | 0.31 | -64.9% |
| **Max** | 10.44 | 8.38 | -4.3% |
| **Mean** | 5.05 | 3.71 | -26.8% |
| **SD** | 1.86 | 1.56 | 17.4% |

**Table 5.10.** Effect of ***DHBIM*** on tissue/cavity Contrast.

| | Original | Contrast Enhanced | Improvement |
|---|---|---|---|
| **Min** | 0.17 | 0.36 | 0.0% |
| **Max** | 2.00 | 2.00 | 200.2% |
| **Mean** | 0.83 | 1.22 | 73.8% |
| **SD** | 0.56 | 0.48 | 48.1% |

**Table 5.11.** Effect of ***DHBIM*** on tissue/cavity SDNR.

| | Original | Contrast Enhanced | Improvement |
|---|---|---|---|
| **Min** | 0.90 | 1.34 | -22.3% |
| **Max** | 35.39 | 90.03 | 248.1% |
| **Mean** | 6.79 | 16.44 | 120.9% |
| **SD** | 7.47 | 21.03 | 52.3% |

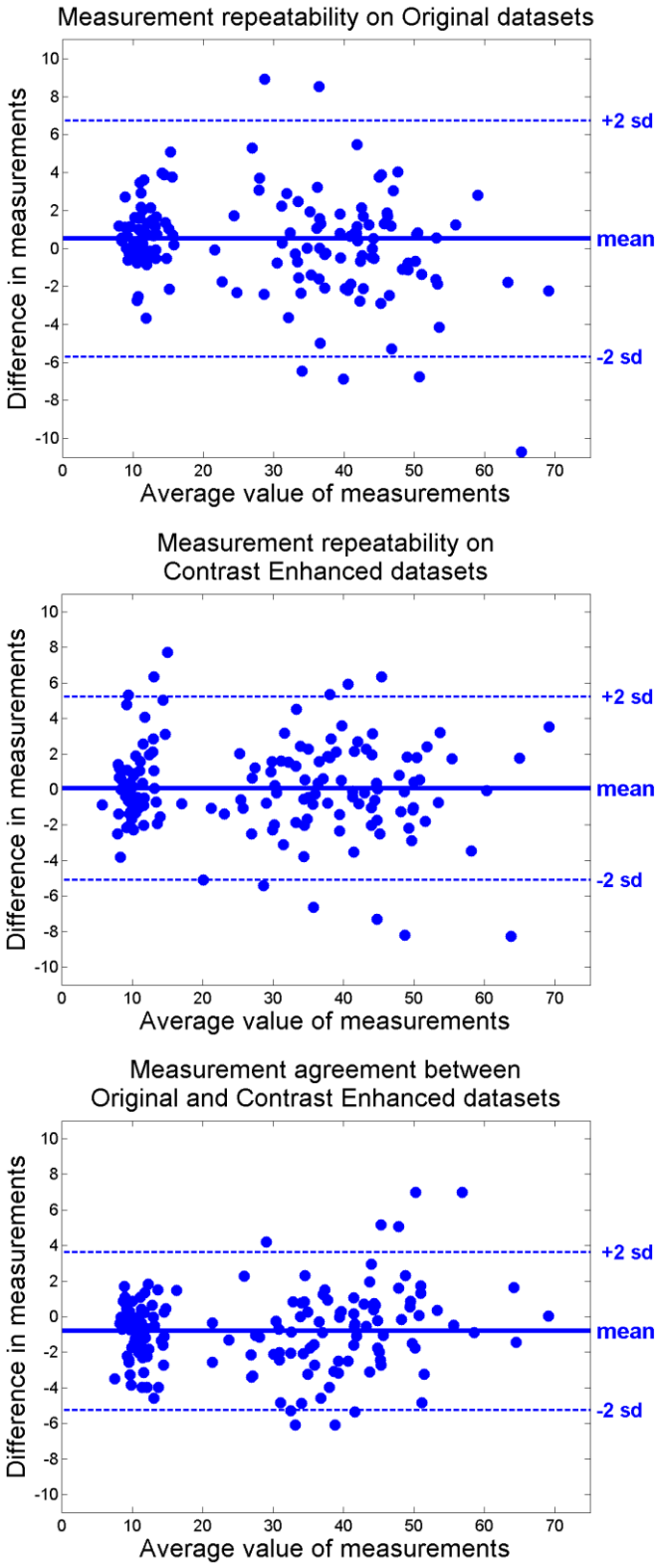


**Figure 5.18.** Bland Altman plots for the repeatability of measurements on original (top) and processed (middle) datasets as well as the agreement between measurements on original and processed datasets (bottom). Measurements performed by Echocardiographer 1. Bias (mean), as well as upper/lower limits of agreement are also included.

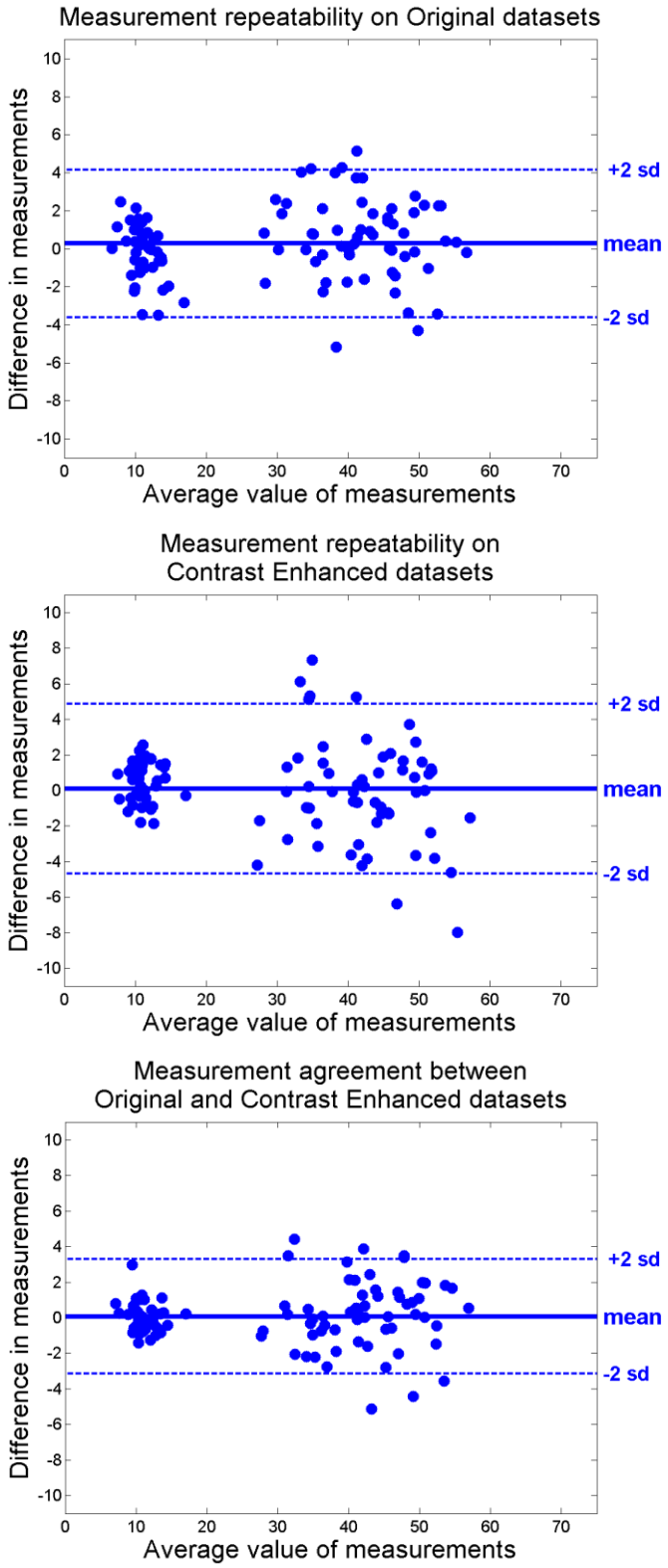


**Figure 5.19.** Bland Altman plots for the repeatability of measurements on original (top) and processed (middle) datasets as well as the agreement between measurements on original and processed datasets (bottom). Measurements performed by Echocardiographer 2. Bias (mean), as well as upper/lower limits of agreement are also included.

**Table 5.12.** Measurement repeatability and agreement coefficient for clinical measurements.

| Measure | Original | | | | Contrast Enhanced | | | | Agreement | | | |
|---|---|---|---|---|---|---|---|---|---|---|---|---|
| (mm) | Mean Diff | +2sd | -2sd | CR | Mean Diff | +2sd | -2sd | CR | Mean Diff | +2sd | - 2sd | CR |
| **Echocardiographer 1** | | | | | | | | | | | | |
| **IVSd** | 1.12 | 4.44 | -2.19 | 3.31 | -0.30 | 3.19 | -3.80 | 3.49 | -1.18 | 1.80 | -4.16 | 2.98 |
| **LVIDd** | -1.06 | 5.99 | -8.12 | 7.06 | 0.47 | 6.59 | -5.65 | 6.12 | 0.60 | 6.32 | -5.13 | 5.73 |
| **LVPWd** | 0.35 | 3.34 | -2.64 | 2.99 | 1.01 | 5.98 | -3.96 | 4.97 | -0.72 | 2.52 | -3.96 | 3.24 |
| **LADs** | -0.31 | 3.86 | -4.48 | 4.17 | 0.11 | 4.79 | -4.57 | 4.68 | -1.52 | 1.60 | -4.64 | 3.12 |
| **LVIDs** | 2.82 | 11.57 | -5.93 | 8.75 | -1.06 | 4.16 | -6.27 | 5.22 | -1.28 | 3.74 | -6.31 | 5.03 |
| **Combined** | **0.52** | **6.74** | **-5.70** | **6.22** | **0.07** | **5.23** | **-5.09** | **5.16** | **-0.81** | **3.63** | **-5.24** | **4.43** |
| **Echocardiographer 2** | | | | | | | | | | | | |
| **IVSd** | -0.40 | 2.64 | -3.45 | 3.05 | 0.64 | 3.01 | -1.74 | 2.37 | -0.15 | 1.03 | -1.33 | 1.18 |
| **LVIDd** | 0.55 | 4.37 | -3.27 | 3.82 | -0.87 | 3.54 | -5.28 | 4.41 | 0.08 | 3.14 | -2.98 | 3.06 |
| **LVPWd** | 0.01 | 2.71 | -2.69 | 2.70 | 0.30 | 2.32 | -1.72 | 2.02 | 0.07 | 2.11 | -1.98 | 2.05 |
| **LADs** | 0.16 | 4.12 | -3.79 | 3.96 | 0.30 | 6.82 | -6.22 | 6.52 | 0.19 | 4.98 | -4.60 | 4.79 |
| **LVIDs** | 1.59 | 6.52 | -3.33 | 4.93 | -0.12 | 5.63 | -5.87 | 5.75 | 0.21 | 2.97 | -2.56 | 2.77 |
| **Combined** | **0.28** | **4.15** | **-3.60** | **3.88** | **0.10** | **4.88** | **-4.68** | **4.78** | **0.08** | **3.30** | **-3.14** | **3.22** |

**Table 5.13.** List of measurements omitted by Echocardiographer 1 on each individual dataset.

| | IVSd | | LVIDd | | LVPWd | | LVIDs | | LADs | |
|---|---|---|---|---|---|---|---|---|---|---|
| **Dataset** | **Or** | **Enh** | **Or** | **Enh** | **Or** | **Enh** | **Or** | **Enh** | **Or** | **Enh** |
| **7** | o | o | o | o | N/A | o | o | o | o | o |
| **18** | o | o | o | o | o | o | N/A | o | o | o |
| **26** | o | o | o | o | o | o | o | o | N/A | o |
| **Total** | 0 | 0 | 0 | 0 | 1 | 0 | 1 | 0 | 1 | 0 |

**Table 5.14.** List of measurements by Echocardiographer 2 on each individual dataset.

| | IVSd | | LVIDd | | LVPWd | | LVIDs | | LADs | |
|---|---|---|---|---|---|---|---|---|---|---|
| **Dataset** | **Or** | **Enh** | **Or** | **Enh** | **Or** | **Enh** | **Or** | **Enh** | **Or** | **Enh** |
| **4** | o | o | o | o | o | o | N/A | N/A | o | o |
| **5** | N/A | N/A | N/A | N/A | N/A | N/A | N/A | N/A | o | o |
| **6** | N/A | N/A | N/A | N/A | N/A | N/A | N/A | N/A | N/A | N/A |
| **8** | o | o | N/A | o | o | o | o | N/A | o | o |
| **10** | o | o | o | o | o | o | N/A | o | o | o |
| **11** | N/A | N/A | N/A | N/A | N/A | N/A | N/A | o | o | o |
| **16** | o | N/A | o | N/A | o | o | N/A | o | o | o |
| **17** | o | o | o | o | o | o | o | N/A | o | o |
| **18** | N/A | N/A | N/A | N/A | N/A | N/A | N/A | N/A | o | o |
| **19** | N/A | N/A | N/A | N/A | N/A | N/A | N/A | o | o | o |
| **20** | N/A | N/A | N/A | N/A | N/A | N/A | N/A | N/A | o | o |
| **24** | N/A | N/A | N/A | N/A | N/A | N/A | N/A | N/A | o | o |
| **26** | o | o | o | o | o | o | N/A | o | N/A | N/A |
| **27** | N/A | N/A | N/A | N/A | N/A | N/A | N/A | o | N/A | N/A |
| **28** | N/A | N/A | N/A | N/A | N/A | N/A | N/A | N/A | o | o |
| **30** | N/A | o | N/A | o | N/A | o | o | N/A | o | o |
| **31** | o | o | o | o | o | o | o | o | N/A | o |
| **32** | o | o | o | o | o | o | N/A | o | o | o |
| **Total** | 10 | 10 | 11 | 10 | 10 | 9 | 14 | 10 | 4 | 3 |

## 5.6. Discussion

Each step of the algorithm was performed on a number of non-overlapping sub-sectors along the y-axis of each cardiac scan. A prerequisite for each sub-sector was to contain both cardiac tissue and cavity structures so that temporal histogram variations could generate a representative tissue/cavity threshold. After thorough examination it was concluded that 4 to 8 sectors could generate satisfactory results. During the work presented in this chapter, 4

sectors were utilised (Figure 5.2). This considerably reduced the required processing resources when compared to 8 sectors, while also providing a fair representation of the (i) near field noise, (ii) RV cavity, (iii) LV cavity and (iv) the LA cavity. Simple linear interpolation compensated for large variations between the derived tissue/cavity thresholds corresponding to neighbouring sub-sectors.

### 5.6.1. Identify unutilised/underutilised intensities within the frame sequence

A thorough examination demonstrated that the number of utilised cardiac cycles did not considerably affect the automatic identification of unutilised/underutilised intensity levels within a cardiac frame sequence. Temporal histogram variations over three cardiac cycles were employed in this study since, while they did not necessitate for a considerable increase in computational requirements, they were found to provide more robust intensity thresholds largely unaffected by outliers. Outliers occurred for intensity levels arising only in a small number of frames within a cardiac cycle. Such occurrence affected the temporal histogram variations profile derived using information from a single cardiac cycle. However, the effect on a corresponding profile derived using information from three cardiac cycles was considerably smaller.

Table 5.1 indicates that about 64% of the datasets included unutilised/underutilised intensity levels. A modest but not negligible 8.6% of the datasets demonstrated unutilised/underutilised intensity levels at both ends of the image intensity range. For the remaining datasets, the unutilised/underutilised intensity levels were spread fairly evenly in the lower (33.6%) and higher (39.1%) end of the [0-255] image intensity range. A substantial 72% of the cases demonstrating unutilised/underutilised intensity levels at the low end of the intensity range occurred on the top two non-overlapping sub-sectors along the *y*-axis of each cardiac scan (Figure 5.2). On the other hand, approximately 70% of the cases demonstrating unutilised/underutilised intensity levels at the top end of the intensity range occurred on the bottom two non-overlapping sub-sectors. This observation suggests that in most datasets the signals generated from low depth regions, corresponding to the near field noise and the RV, were over-amplified while signals from regions at a higher depth, corresponding to the LV, LA and PW were under-amplified. This behaviour can be partially attributed to non-optimal Time Gain Control (TGC) employed by the echocardiographer during data acquisition. Identifying and suppressing the unutilised/underutilised intensity levels at both the low and top ends of the intensity range can provide a partial, indirect solution to the problem.

From Table 5.2 it becomes apparent that while some datasets made use of the whole [0-255] intensity range available, some datasets disregarded a considerable number of intensity levels. For some datasets the number of unutilised/underutilised intensity levels reached up to 125 (49% of available intensity range) with a mean value of 28 intensity levels. The extent of unutilised/underutilised intensity levels was considerably larger (up to 146 intensity levels with a mean of 45) at the top end of the image intensity range when compared to the corresponding lower end (up to 51 intensity levels with a mean of 8). Such an observation was not surprising when considering the bottom heavy nature, similarly to the example illustrated in Figure 5.3, of the vast majority of histograms in the examined cardiac ultrasound data. Making use of the identified excessive intensity levels may result in a respectable contrast enhancement within the imaged cardiac structure.

### 5.6.2. Suppress unutilised/underutilised intensity levels

Figures 5.7 and 5.8 display two example ED frames before and after the dynamic range increase on their corresponding multi-cycle datasets by suppressing any identified unutilised/underutilised intensity levels. The dataset displayed in Figure 5.7 was of very high image quality and diagnostic value. The cardiac cavities demonstrated negligible levels of noise and the tissue cavity boundaries were clearly distinguishable. Nevertheless, unutilised/underutilised intensity levels were identified at the top end of the intensity range. Suppressing the unutilised/underutilised intensity levels (white level expansion) increased the dynamic range within the tissue structures as well as the contrast between cardiac tissue and cavities. On the other hand, the dataset displayed in Figure 5.8 was of low image quality and diagnostic value. High levels of noise masked out a lot of the anatomic information making the tissue detectability a challenging task. As would be expected, unutilised/underutilised intensity levels were identified at the bottom end of the intensity range. Suppressing the unutilised/underutilised intensity levels (black level expansion) increased the dynamic range within the tissue structures as well as the contrast between cardiac tissue and cavities.

Both examples in Figures 5.7 and 5.8 were representative of the potential of the dynamic range increase on cardiac ultrasound data by suppressing any identified unutilised/underutilised intensity levels. Tables 5.3 to 5.6 demonstrate the effect of the dynamic range increase by suppressing any identified unutilised/underutilised intensity levels on quantitative measures such as tissue SNR, cavity SNR, tissue/cavity Contrast and detectability index SDNR. The effect varied considerably amongst the 32 datasets, mainly due to the different level of contrast stretching applied on each. Nevertheless, the effect of

the dynamic range increase on each quantitative measure followed a similar trend for all datasets with the mean value providing a fair representation of it. More precisely, both tissue and cavity SNR were moderately decreased by a mean 6.2% and 13.2% respectively. On the other hand, tissue/cavity contrast was increased by up to 90% with a modest average increase of 11%. Similarly, tissue/cavity detectability index (SDNR) was also increased by up to 44.4% with a marginal average increase of 3.5%. The results can be described as predictable and were attributed to the increase of the dynamic range of the imaged cardiac structure. However, the SNR decrease should not be mistaken with noise increase. Tissue SNR decrease was mostly due to white level expansion resulting in speckle enhancement, which can be very beneficial during commonly used processes such as *Speckle Tracking*. Cavity SNR decrease on the other hand was mostly due to black level expansion suppressing low intensity cavity noise. The effect of suppressing unutilised/underutilised intensity levels may appear modest, and in some cases negligible. However, it provided a very simple and efficient process that increased the dynamic range in the imaged structure resulting in a more robust tissue/cavity identification (next step in ***DHBIM***). In addition, it enabled a higher level of overall cavity noise suppression as well as tissue/cavity contrast and detectability enhancement achievable during the full ***DHBIM*** process.

### 5.6.3. Identify tissue/cavity intensity threshold

The plots in Figure 5.10 provide a typical example of the effect of using information from an increasing number of cardiac cycles for the derivation of tissue/cavity threshold. Each plot contained a curve illustrating the cumulative histogram temporal variations (SD) within each intensity level over a number of cardiac cycles. As described in Section 5.4.3, the intensity level with the maximum value in the derived SD profile corresponded to the tissue/cavity intensity threshold. From the four plots it becomes apparent that utilising additional cardiac cycles can substantially change the shape of the derived SD profile. The derived profiles (for a small number of cardiac cycles) were noisy with a large number of local maxima. By introducing information from supplementary cardiac cycles, the profiles converged to a final, much smoother shape, which (most of the time) demonstrated strong global maximum values. The shape of the profile tended to be approximately that of a skew normal distribution. The skew direction was determined by the tissue/cavity intensity threshold. The number of cardiac cycles required to derive a smooth profile depended heavily on the level of noise as well as the tissue/cavity contrast and detectability in the imaged cardiac structure. A larger number of cardiac cycles were required for datasets with high levels of noise and

low contrast. However, the computational requirements increased with the utilised number of cardiac cycles and therefore a satisfactory tradeoff was desirable.

All plots displayed in Figure 5.11 demonstrated a very similar behaviour. For all 4 non-overlapping sub-sectors, the mean current threshold difference with respect to the representative threshold ($|th_c - th_r|$, Section 5.5.3) dropped by utilising information from an increasing number of cardiac cycles. While the drop varied considerably amongst the 32 cardiac datasets, ranging from 0 to more than 90 intensity levels, it was regarded that the displayed mean curves provided a fair representation. More precisely, each curve could be divided into three distinct sections. In the first section, the threshold variation introduced by utilising information from an additional cardiac cycle was sizeable. This section stretched from 0 to about 7 cardiac cycles. In the second section, which stretched from approximately 7 to 14 cardiac cycles, the threshold variation introduced by utilising information from an additional cardiac cycle was very moderate. Finally, in the last section, for more than 14 cardiac cycles, the threshold variation introduced by utilising information from an additional cardiac cycle was very limited and sometimes negligible. The above observations were verified by the results displayed in Table 5.7. Almost 80% of the dataset had "settled" to an adequately accurate and fairly static threshold by using information from 5 cardiac cycles. The percentage continued to increase rapidly reaching 91.4% when using information from 7 cardiac cycles. While the percentage of settled datasets increased by utilising additional cardiac cycles during threshold derivation, the rate of increase dropped considerably. For example, 9 cardiac cycles marginally increased the percentage of the "settled" datasets to 93%. The mean differences of the "settled" thresholds derived using 5, 7 and 9 cardiac cycles and the corresponding characteristic thresholds $th_r$ lay at a very similar and modest level ranging between 1.5 and 2 intensity levels.

For a small but not negligible number of datasets (almost 11%), while the threshold appeared "settled", a substantial and sudden drop in the derived threshold was introduced with an increasing number of cardiac cycles. Such threshold drops are a consequence of variations of the scan plane level of noise, as well as the emergence of artifacts such as shadowing that are more likely to be introduced during a prolonged period of time. All cases of sudden threshold drop were observed when using more than 10 cardiac cycles during the threshold derivation. After thorough investigation it was observed that sudden threshold variations mostly occurred (71.4%) in the first and smallest of the non-overlapping sub-sectors. The limited size of the sector made it more easily affected by variations in the imaged data and therefore more prone to outliers. Taking everything into consideration, utilising 7 cardiac

cycles appeared to provide the best tradeoff between deriving a representative tissue/cavity threshold and processing requirements.

### 5.6.4. Contrast enhancement between cardiac tissue and cavity structures

Figures 5.12 to 5.17 display six example ED frames, before and after ***DHBIM*** is applied to their corresponding multi-cycle datasets. In addition, for each of the six example datasets, an image highlighting areas identified as tissue (tissue mask), by demonstrating intensity greater than the derived tissue/cavity threshold, is displayed. These figures provide characteristic examples of the effects of ***DHBIM*** on clinical data over a range of image qualities and diagnostic values. Datasets are presented in increasing data quality ranging from very low to high (3 low, 2 average and 1 high).

Figure 5.12 displays three ED frames corresponding to a dataset with very low image quality and diagnostic value. The first image is the original unprocessed frame, while the second and third are the corresponding tissue mask and ***DHBIM*** processed frames. The original dataset suffered from very high levels of noise and very limited contrast between cardiac cavities and tissue. The low data quality limited the visual delineation of the majority of cardiac structures including the RV, LV, IVS, PW and RA. Furthermore, the high noise and low contrast levels limited, and very possibly restricted, the suitability of the displayed dataset for most post-processing algorithms. ***DHBIM*** generated a fairly representative map of tissue structures within the dataset, suppressed cavity noise and enhanced the contrast and detectability between cardiac tissue and cavity considerably. Regardless of the very low quality of the original dataset, ***DHBIM*** substantially enhanced the available information both with respect to the image quality (beneficial for data post-processing) and diagnostic value. Cardiac structures such as the RV, LV, IVS, PW and RA were distinguishable in the processed dataset and could be potentially measured accurately and robustly in a clinical setup. Figure 5.13 displays three ED frames corresponding to a dataset with low image quality and diagnostic value. Similar to the data in Figure 5.12, the original dataset suffered from very high levels of noise. However, the contrast between tissue and cavity was in some cases moderately higher, furthering the visual delineation of some structures. ***DHBIM*** generated a very similar effect to the first example, suppressing cavity noise and making cardiac structures such as the RV, LV, IVS, PW, RA and the Mitral Valve clearly distinguishable.

Figure 5.14 displays three ED frames corresponding to the last of the three datasets with low image quality and diagnostic value. Similar to the last two examples the original dataset

suffered from a high level of noise. However, it also suffered from shadowing, which combined with noise, masked clinically vital cardiac structures such as segments of the IVS, the PW and the lower end of the LA. ***DHBIM*** generated a representative map of the tissue structures imaged within the dataset, suppressed cavity noise and enhanced the contrast and detectability between cardiac tissue and cavity considerably. However, regardless of the substantial quality improvement, ***DHBIM*** did not compensate for tissue structures masked by high levels of noise and shadowing. Instead, it treated them as cardiac cavities (Figure 5.14 middle) suppressing their corresponding information. Nevertheless, the processed dataset illustrated an improvement over the original data. Figure 5.15 displays three ED frames corresponding to the first dataset with average image quality and diagnostic value. The original dataset suffered from noise and low contrast between cardiac cavities and tissue. While most cardiac structures were distinguishable, high noise and low contrast levels masked segments of the IVS in a way similar to the dataset in Figure 5.14. As expected from the previous examples, ***DHBIM*** generated a highly representative map of the tissue structures imaged within the dataset, suppressing cavity noise and making cardiac structures such as the RV, PW, RA and the Mitral Valve clearly distinguishable. Even masked segments of the IVS were enhanced, and while not fully restored, they enabled a moderately improved delineation of the structure.

Figures 5.16 and 5.17 provide examples of data with average and high image quality and diagnostic value respectively. The original image in Figure 5.16 demonstrated a moderately higher level of cavity noise and lower level of tissue/cavity contrast with respect to the original image in Figure 5.17. Nevertheless, in both datasets cardiac structures were clearly distinguishable. Like in all previous examples, ***DHBIM*** generated a highly representative map of the tissue structures and suppressed cavity noise considerably. The noise suppression was more apparent inside the RV cavity, especially at its top half. Furthermore, ***DHBIM*** increased the dynamic range within cardiac tissue, enhancing the corresponding speckle information. For both datasets processing was not required to enhance the imaged data prior to clinical measurements. However, ***DHBIM*** is expected to further improve the accuracy and robustness (repeatability) of clinical measurements performed on the processed datasets. ***DHBIM*** is also expected to improve the post-processing potential of the datasets, which is limited by the presence of cavity noise and low tissue/cavity contrast.

Overall, after a thorough examination of its effect on all 32 patient datasets, ***DHBIM*** generated a highly representative cardiac tissue mask. Reducing the intensity dynamic range of cavity pixels by half noticeably suppressed cavity noise. The noise suppression was

notable in the RV cavity. In addition, by applying the algorithm in 4 non-overlapping sectors, mostly representing different cardiac structures, reduced the variations on the mean intensity and noise level amongst cardiac structures. Furthermore, by increasing the intensity dynamic range in tissue pixels, ***DHBIM*** enhanced the contrast and detectability between cardiac tissue and cavities. Suppressing cavity noise and increasing tissue/cavity detectability can be very beneficial in post-processing techniques such as image segmentation and registration whose effectiveness is limited and sometimes restricted by high levels of noise and low contrast in cardiac ultrasound data. ***DHBIM*** also enhanced tissue speckle information, which can be very valuable for commonly used ultrasound techniques such as *Speckle Tracking*. The described effects of ***DHBIM*** were observed in a range of scales on all 32 datasets, from ones with very poor to ones with very high image quality. The only observed limitation of ***DHBIM*** was when high levels of noise, along with other artifacts such as shadowing, masked out certain cardiac structures completely. In such cases the algorithm could mis-classify the missing tissue as cardiac cavity and suppress the intensity of its corresponding pixels. While in such cases ***DHBIM*** might not always enhanced the challenging tissue structures, it was not observed to suppress vital clinical information from the original dataset. Furthermore, after observing the effect of spatial compounding (Chapters 3 and 4) on heavily corrupted cardiac tissue, it is expected that combining it with ***DHBIM*** can compensate for such a limitation.

#### 5.6.4.1. Effect on tissue SNR, cavity SNR, tissue/cavity contrast and SDNR

Tables 5.8 to 5.11 demonstrate the effect of ***DHBIM*** on quantitative measures such as tissue SNR, cavity SNR, tissue/cavity Contrast and detectability index SDNR. The quantitative results verified the observations described in Section 5.7.4. The effect of ***DHBIM*** varied amongst the 32 datasets mainly due to the different level of noise suppression and contrast enhancement required on each. Nevertheless, the overall effect of ***DHBIM*** on each quantitative measure followed a similar trend for all datasets with the mean value providing a fair representation of it. More precisely, both tissue and cavity SNRs were moderately decreased by an average of 37.0% and 26.8% respectively. However, the SNR decrease should not be interpreted as an increase in the noise level. The tissue SNR decrease was attributed to the intensity dynamic range increase for pixels identified as tissue by the ***DHBIM*** algorithm. The cavity SNR decrease was noticeably smaller than the corresponding tissue SNR change and almost 50% of it was due to the contrast enhancement introduced by suppressing unutilised/underutilised intensity levels (Table 5.4). After observing all 32 datasets, the remaining cavity SNR decrease was attributed to sparse cavity pixels with high

levels of noise identified as cardiac tissue and therefore not suppressed. Such pixels could considerably increase the SD within a ROI and as a result the corresponding cavity SNR. Therefore, the decrease in cavity SNR should not be confused with higher levels of cavity noise. After all, ***DHBIM*** suppressed cavity noise intensity values by at least 50%. On the other hand, and as expected from observing the processed images from all 32 datasets, both tissue/cavity contrast and detectability index (SDNR) were substantially increased. Tissue/cavity contrast was increased by up to 200.2% with an average increase of 73.0%. Similarly, SDNR was increased by up to 248.1% with an even larger average increase of 120.9%.

#### 5.6.4.2. Effect on clinical measurements performed on patient data

The results presented in Figures 5.18 and 5.19 along with Tables 5.12 to 5.14 enable the evaluation of the effect of ***DHBIM*** on clinical measurements performed on routine cardiac ultrasound examinations. Each point cluster (representing different types of clinical measurements) as well as the corresponding limits of agreement (±2SD) lay in a specific range which was largely unaffected by whether measurements were performed on the original or the contrast enhanced datasets. Furthermore, the mean measurement difference in each plot lay very close to zero, indicating that no significant or systematic bias was observed within each measurement method or between the two measurement methods. Finally, no major outliers were identified in the repeatability and agreement plots. Consequently, the results presented in the plots indicate a strong potential for the original and ***DHBIM*** contrast enhanced data to be interchangeable when performing clinical cardiac ultrasound measurements.

Table 5.12 enables a more thorough investigation on the effect of ***DHBIM*** on clinical measurements performed on routine cardiac ultrasound examinations. The repeatability and agreement coefficients of a clinical measurement depended both on the type of clinical measurement performed as well as the operator making the measurement. For both echocardiographers the overall level of agreement between clinical measurements performed on original and the contrast enhanced data lay in levels very similar to the corresponding repeatability coefficients with no substantial or systematic bias being observed. Echocardiographer 1 displayed a confident and sometimes adventurous approach towards making clinical measurements. More precisely, the repeatability coefficient of the measurements on contrast enhanced data increased by 13% and 40% for the LVIDd and LVIDs measurements respectively. On the other hand, the repeatability coefficient of measurements performed on contrast enhanced datasets demonstrated a marginal 5% drop

for IVSd as well as more substantial drops of 12% and 66% for LADs and LVPWd respectively. Nevertheless, when considering all clinical measurements, a considerable overall 17% improvement on the repeatability coefficient was introduced to measurements performed on contrast enhanced data, compared to those performed on the original unprocessed data. The more conservative Echocardiographer 2 indicated reluctance towards the diagnostic quality of the contrast enhanced datasets in a manner similar to the compounded datasets. The conservative measurement approach was apparent by the higher repeatability and agreement levels displayed on the clinical measurements when compared with those of Echocardiographer 1. Such higher repeatability and agreement levels in the original data reduce the scope for improvement by using the processed data. Echocardiographer 2's reluctance to the processed datasets had an effect on the repeatability level achieved on the clinical measurements, demonstrating an overall (considering all clinical measurements) repeatability coefficient drop of 23% when compared to those performed on the original unprocessed data. This drop was attributed mainly to the inability of ***DHBIM*** to compensate for some cardiac structures corrupted heavily by noise and/or shadowing (Section 5.6.4), as well as the high level of familiarity of the echocardiographer with conventional, unprocessed cardiac ultrasound data. Both echocardiographers had been working for many years with challenging cardiac ultrasound data and had developed procedures utilising subtle features that enabled them to perform the required clinical measurements. Data processing might have modified such features restraining the echocardiographers from making some challenging clinical measurements on the processed datasets that were presented to them for the first time during this study.

Tables 5.13 and 5.14 indicate whether a clinical measurement was performed or omitted by each echocardiographer on the original and ***DHBIM*** contrast enhanced datasets. Both echocardiographers chose to abstain from making some clinical measurements. Similar to the results displayed in Table 5.12, the more conservative approach adopted by Echocardiographer 2 on making clinical measurements, when compared to Echocardiographer 1, was apparent. Echocardiographer 1 chose to attempt the majority of the clinical measurements while Echocardiographer 2 omitted measurements, taking fewer risks on challenging datasets. Avoiding clinical measurements on challenging datasets reduced the scope for improvement in the repeatability and agreement levels by using the processed data. Nevertheless, a considerable percentage (67%) of the measurements omitted by Echocardiographer 1 was also omitted by Echocardiographer 2. Comparing the omitted measurements with the corresponding ones for compounded datasets (Tables 3.12 and 3.13) it became apparent that there was a high level of correlation. Visual inspection on the

omitted datasets demonstrated high levels of corruption on the measured cardiac structures either by high noise or shadowing levels. Similar to ***Temporal Compounding***, abstaining from making clinical measurements was mostly attributed to high levels of noise and shadowing making the delineation of the IVS and PW structures very challenging in some datasets. The number of omitted measurements was higher than the corresponding encountered utilising ***Temporal Compounding***. Nevertheless, the cavity noise suppression and tissue/cavity contrast enhancement introduced during ***DHBIM*** were responsible for a modest decrease when compared to the measurements omitted on the original unprocessed datasets. Such a modest drop was observed in the measurements performed by both Echocardiographers.

The results on the effect of ***DHBIM*** on clinical measurements performed on routine cardiac ultrasound examinations, while not as prolific as the corresponding ***Temporal Compounding*** results, were still very promising. The fact that the measurement agreement lay in levels similar to the corresponding measurement repeatability coefficient, with no substantial or systematic bias identified, indicates that original and contrast enhanced datasets can be interchangeable when performing clinical measurements on cardiac ultrasound data. While Echocardiographer 2 demonstrated a decrease in the measurement repeatability, the corresponding repeatability increase for Echocardiographer 1, along with the modest decrease in the number of omitted measurements, indicates the potential for ***DHBIM*** on clinical measurements. It is expected that by increasing familiarity, Echocardiographer 2 may adjust existing procedures for making measurements on challenging datasets for use with the contrast enhanced datasets. A higher confidence level in making clinical measurements on processed datasets can potentially increase the repeatability coefficient in a manner similarly to Echocardiographer 1. Furthermore, the limitation of ***DHBIM*** to compensate for heavily corrupted structures can be potentially counterpoised by combining it with spatial compounding (Chapters 3 and 4), shown to compensate for such masked out structures. Therefore, ***DHBIM*** demonstrates great potential for the further improvement in the repeatability of routine clinical measurements on cardiac ultrasound data. ***DHBIM*** either exclusively or combined with spatial compounding can possibly act as a beneficial alternative to conventional B-mode imaging for clinical measurements.

## 5.7. Conclusions

In this chapter, ***DHBIM***, a novel and fully automated method for suppressing noise in cardiac cavities while enhancing information in cardiac tissue was introduced and

quantitatively evaluated. ***DHBIM*** investigated the temporal variations within image histograms of consecutive frames in order to (i) identify any unutilised/underutilised intensity levels and (ii) derive the tissue/cavity intensity threshold within the processed frame sequence. Piecewise intensity mapping was then used to suppress cavity noise and enhance tissue information. The derivation of representative intensity thresholds was a key process for effective ***DHBIM***. Due to the noisy nature of cardiac ultrasound data, information over multiple cardiac cycles was required to derive representative intensity thresholds. Furthermore, individual thresholds for a number of non-overlapping sub-sectors along the y-axis were required in order to compensate for the non-optimal TGC employed during data acquisition.

Similar to ***Temporal Compounding***, a number of multi-cycle patient cardiac ultrasound datasets were utilised for the quantitative assessment of the effect of ***DHBIM*** on image quality and diagnostic value. Optimal acquisition parameters such as the number of utilised cardiac cycles and non-overlapping sub-sectors were identified. Information from 7 cardiac cycles along with 4 sub-sectors was found to provide the best tradeoff between data enhancement and acquisition/processing requirements. Data enhancement included cavity noise suppression, enhancement of tissue speckle information, as well as a considerable increase in tissue/cavity contrast and detectability index. While speckle enhancement may limit the accuracy of data registration, it can be advantageous for the application of other commonly employed cardiac ultrasound methods such as *Speckle Tracking*. Furthermore, due to its simple nature, by generating a fairly representative outline of cardiac tissue structures, ***DHBIM*** can act as a step prior to image processing techniques whose effectiveness is limited and sometimes restricted by high noise and low contrast levels in cardiac ultrasound data. The only observed limitation of ***DHBIM*** was when high levels of noise and shadowing masked certain tissue structures. In such cases the algorithm mis-classified the missing tissue as cardiac cavity and suppressed the intensity of its corresponding pixels. Nevertheless, ***DHBIM*** was not observed to suppress vital clinical information from the original datasets. Furthermore, after observing the effect of the compounding techniques introduced in Chapters 3 and 4 on heavily corrupted cardiac tissue, it is expected that combining ***DHBIM*** with spatial compounding can compensate for the limitation.

Having verified the impact of ***DHBIM*** on cardiac ultrasound image quality, its effect on diagnostic value was investigated by assessing the impact on repeatability levels between routine clinical measurements performed by two experienced echocardiographers. Similar to

all previous methods the effect of ***DHBIM*** depended on the echocardiographer as well as the clinical measurement performed. For both echocardiographers, the number of clinical measurements omitted using ***DHBIM*** was decreased. Furthermore, ***DHBIM*** induced a considerable overall improvement in measurement repeatability for (confident with new technologies) Echocardiographer 1. However, the more hesitant with new technologies Echocardiographer 2 demonstrated a decrease in the repeatability of clinical measurements performed utilising ***DHBIM*** when compared to the original unprocessed data. Given the diverse effect of ***DHBIM*** on clinical measurements performed by the two echocardiographers, and taking into consideration that both echocardiographers were presented for first time with the processed data, it is strongly believed that there is further scope for improvement as the familiarity of the echocardiographers with the processed data increases. Consequently, ***DHBIM*** demonstrates a strong potential to provide a valuable alternative to B-mode data for improving cardiac measurements.

# Chapter 6

# Combining *DHBIM* with Spatial Compounding

This chapter introduces a data acquisition and analysis protocol for integrating the dynamic intensity mapping (***DHBIM***) along with spatial compounding methods described in earlier chapters. The integrated method suppresses cavity noise and tissue speckle while enhancing tissue/cavity contrast as well as the delineation of cardiac cavity boundaries. Similar to Chapters 3 and 5, the integrated method is quantitatively assessed using 32, multi-cycle, patient cardiac ultrasound datasets providing a representative range of image qualities and diagnostic values. The effect of the integrated method on the noise and contrast within the imaged cardiac structures is quantitatively assessed utilising measures such as tissue SNR, cavity SNR as well as tissue/cavity Contrast and detectability index SDNR. Furthermore, similar to all previous chapters, this study examines the effect of the integrated method on five clinical measurements performed during routine echocardiographic examinations. Finally, both the qualitative and quantitative effects of each of the individual methods on cardiac ultrasound data are compared and contrasted to the corresponding effect generated by the integrated data enhancement approach.

## 6.1. Introduction

In previous chapters a number of data enhancement methods for cardiac ultrasound data have been described and quantitatively assessed. Chapters 3 and 4 introduced and evaluated two methods that succeeded in suppressing both static and dynamic noise in cardiac ultrasound data by spatially compounding spatio-temporally aligned data acquired from a single acoustic window. Unlike other noise suppression methods, both techniques managed to substantially suppress cavity noise and tissue speckle while considerably increasing the detectability between tissue and cavity. Furthermore, both techniques demonstrated potential in enhancing corrupted (either by noise or by shadowing) anatomic structures within cardiac ultrasound scans. Consequently, spatial compounding can act as a first step to clinical measurements as well as to post-processing techniques (e.g. segmentation and registration)

whose effectiveness is limited and sometimes restricted by low image quality in cardiac ultrasound data.

Most studies attempting to enhance cardiac ultrasound data have not managed to generate a noteworthy effect in enhancing the contrast between cardiac tissue and cavity structures. Low contrast between tissue and cavities is a major limitation in cardiac ultrasound data when compared to other imaging modalities. Furthermore, while tissue speckle suppression may be advantageous for some image post-processing techniques, it restricts the application of other commonly employed cardiac ultrasound methods such as *Speckle Tracking*. Chapter 5 introduced ***DHBIM***, a simple, efficient and very effective method for suppressing cavity noise while enhancing tissue speckle and increasing tissue/cavity contrast and detectability. ***DHBIM*** generated a fairly representative map of the tissue structures within the dataset and could therefore act as a first step to image segmentation whose effectiveness is limited by the low contrast between cardiac tissue and cavity in ultrasound data. In circumstances where high levels of noise masked clinically vital cardiac structures, by suppressing cavity noise and enhancing the contrast between cardiac tissue and cavity, ***DHBIM*** enhanced the visual delineation of the challenged structures. However, unlike both compounding techniques, ***DHBIM*** did not suppress tissue speckle or compensate for structures masked by shadowing.

All three methods introduced in this thesis can be applied independently in order to enhance cardiac ultrasound data. However, by observing the strengths and weaknesses identified in each approach it becomes apparent that spatial compounding appears to complement the ***DHBIM*** method. Furthermore, both techniques require multiple instances of a cardiac cycle acquired from a single acoustic window in order to attain supplementary information necessary for suppressing noise and enhancing tissue/cavity contrast. Integrating spatial compounding with ***DHBIM*** may therefore overcome, to some extent, the limitations of the individual techniques. The integrated image enhancement method has the potential to provide a post-processing solution that suppresses cavity noise and tissue speckle while enhancing tissue/cavity contrast as well as the delineation of cardiac cavity boundaries even when heavily corrupted by a range of cardiac ultrasound artifacts.

## 6.2. Aims and contributions

The aim of this chapter is to introduce a fully automated method that integrates dynamic intensity mapping along with spatial compounding in order to suppress cavity noise and tissue speckle, while enhancing tissue/cavity contrast as well as the delineation of cardiac cavity boundaries even when heavily corrupted by a range of cardiac ultrasound artifacts.

The contributions of this chapter are:

- The development of a protocol for data acquisition and analysis that integrates the key processes of ***Temporal Compounding*** and ***Dynamic Histogram Based Intensity Mapping* (*DHBIM*)** introduced in Chapters 3 and 5 respectively.
- Assessing the effect of the integrated approach on patient cardiac ultrasound scans using a range of quantitative measures such as tissue Signal-to-Noise Ratio (SNR), cavity SNR, tissue/cavity Contrast and Signal Difference to Noise Ratio (SDNR) also known as detectability index.
- Examining the effect of the integrated method on routine clinical measurements performed on patient cardiac ultrasound scans over a range of image qualities and diagnostic values.
- Comparing and contrasting the qualitative and quantitative effects on cardiac ultrasound data between the individual ***Temporal Compounding*** and ***DHBIM*** methods and the corresponding integrated approach.

## 6.3. Data acquisition and manual analysis

Multiple cardiac cycles of a section through the imaged cardiac structure are required for the successful application of both spatial compounding as well as ***DHBIM*** algorithms. The multi-cycle data can be acquired over consecutive cardiac cycles (Chapter 3 - ***Temporal Compounding***) utilising small variations in the viewing plane and therefore the speckle patterns over the prolonged acquisition. Alternatively, the multi-cycle data can be acquired as a collection of single cardiac cycles acquired from adjacent (along the elevation plane) slices of the scanned cardiac structure (Chapter 4 - ***3D-to-2D Compounding***) using a 4D matrix array transducer. For the study presented in this chapter, data acquired over consecutive cardiac cycles and therefore compounded using ***Temporal Compounding*** were utilised. As described in Chapter 3, compounding data from 12 cardiac cycles generated a substantial level of enhancement on the imaged structure. Furthermore, information from 7 to 9 cardiac cycles was sufficient in order to derive a representative tissue/cavity intensity threshold during ***DHBIM***. However, some cardiac cycles may be heavily corrupted by noise as well as other artifacts and therefore provide no constructive information for the ***Temporal Compounding*** and ***DHBIM*** algorithms. The acquisition of 15 (high quality data) to 20 (low quality data) cardiac cycles is believed to be sufficient for the requirements of the integrated method. Large probe displacements should be avoided during the multi-cycle acquisition.

The 32 multi-cycle patient data (18 male, 14 female, ages ranging from 21 to 88 with an average age of 60) described in Chapter 3 were utilised during the development and the assessment of the integrated data enhancement algorithm. All datasets (25 cardiac cycles of the Parasternal Long-Axis view) were acquired according to the BSE standards (Henry et al., 1980; Feigenbaum, 1994) by an experienced echocardiographer in the Echocardiography department of the Western General Hospital, Edinburgh, during January of 2009. Prior to any processing each dataset was manually labeled as high (12), average (12) or low (8) according to the visually observed quality as well as the diagnostic value of its images.

## 6.4. Data processing

The integrated method for enhancing cardiac ultrasound data suggested in this chapter is a simple linear combination of the ***Temporal Compounding*** and ***DHBIM*** algorithms described in Chapters 3 and 5 respectively. There are 7 steps to the integrated data enhancement approach. Steps 1 to 4 correspond to the ***DHBIM*** process: (i) the identification of unutilised and underutilised intensity levels within the frame sequence, (ii) the dynamic range increase of the imaged cardiac structure by suppressing the unutilised/underutilised intensity levels, (iii) the derivation of the cardiac tissue/cavity intensity threshold, and (iv) the contrast enhancement between cardiac tissue and cavity structures. Each step was performed on 4 non-overlapping sub-sectors along the *y*-axis of the cardiac scan (Figure 5.2) compensating for the variable interactions between different cardiac structures and the transmitted ultrasound signals as well as the inconsistent and highly objective Time Gain Control (TGC) employed by the echocardiographer. Likewise, steps 5 to 7 correspond to the ***Temporal Compounding*** process: (v) the temporal alignment of the multi-cycle data to the frames of a reference cardiac cycle, (vi) the spatial alignment of the temporally aligned frames, and (vii) the spatial compounding of the spatio-temporally aligned data. Steps 5 to 7 can be replaced by the corresponding steps required for ***3D-to-2D Compounding*** as described in Chapter 4 (Section 4.5).

### 6.4.1. Identify unutilised/underutilised intensities within the frame sequence

Unutilised and underutilised intensity levels within the B-mode frame sequences were identified by analysing the dynamic temporal variations in the image histograms corresponding to a sequence of consecutive cardiac ultrasound frames. A normalised histogram was generated for each frame in the B-mode sequence. The SD of the variations in each intensity level over consecutive frames was then derived highlighting any intensity levels that demonstrated negligible variations with respect to their corresponding number of

pixels over the B-mode frame sequence. A heuristic threshold set to less than 1% of the maximum value observed over the derived SD profile defined any unutilised and underutilised intensity levels. Such intensity levels demonstrating limited or no variation (over the frame sequence) were observed in the bottom and top end of the [0:255] intensity range and did not correspond to clinically vital information.

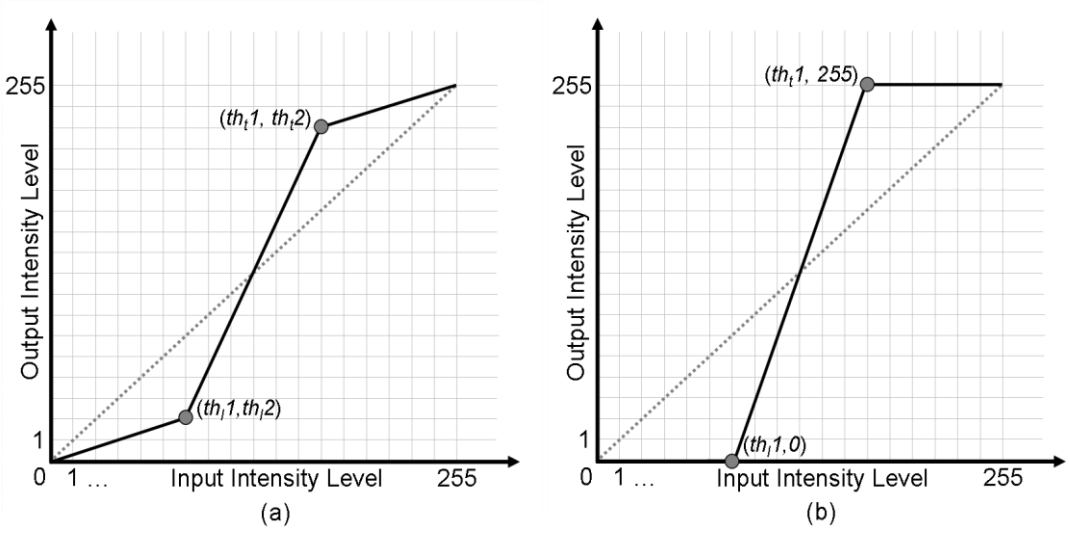


**Figure 6.1.** (a) A typical example of a piecewise-linear transformation function used for contrast stretching. (b) An example of the type of intensity mapping utilised in this study.

### 6.4.2. Suppress unutilised/underutilised intensity levels

Having identified the lower and upper thresholds ($th_l$ and $th_t$) defining the predominantly utilised intensity range within the B-mode frame sequence, it was possible to enhance the corresponding information (dynamic range) within the imaged cardiac structure. This study utilised a simple piecewise-linear transformation function as an intensity mapping between the original and the processed frame sequences. The shape of the transformation was controlled by thresholds $th_l$ and $th_t$ compressing all intensity levels below or equal to $th_l$ to 0 as well as all intensity levels above or equal to $th_t$ to 255 (Figure 6.1). As a result, the predominately utilised intensity levels were linearly stretched to the full 8-bit gray-scale range of [0:255], increasing the dynamic range and contrast of the imaged cardiac structure.

### 6.4.3. Identify tissue/cavity intensity threshold

Similar to Section 6.4.1, the cardiac tissue/cavity intensity threshold was identified by analysing the dynamic temporal variations in the image histograms over a sequence of consecutive cardiac frames. The approach employed in this study was based on some basic

observations in cardiac ultrasound data. A cumulative histogram was generated for each frame in the B-mode sequence. Furthermore, the SD of the population variations over consecutive frames for each intensity level within the cumulative histogram was derived. The tissue/cavity threshold was located at the intensity level demonstrating maximum SD.

### 6.4.4. Enhance contrast between cardiac tissue and cavity structures

Having identified intensity threshold $th_{ct}$ between cardiac cavity and tissue pixels, it was possible to utilise a new piecewise-linear transformation function in order to: (i) suppress noise in cardiac cavities, (ii) increase the dynamic range in cardiac tissue enhancing the available speckle information, and (iii) enhance the contrast between cardiac tissue and cavity. The shape of the transformation was controlled by threshold $th_{ct}$ compressing all intensity levels below or equal to $th_{ct}$ by 50% (Figure 6.2). As a result, intensity levels representing cardiac tissue were linearly stretched, increasing the tissue dynamic range and consequently the tissue/cavity contrast within the imaged cardiac structure.

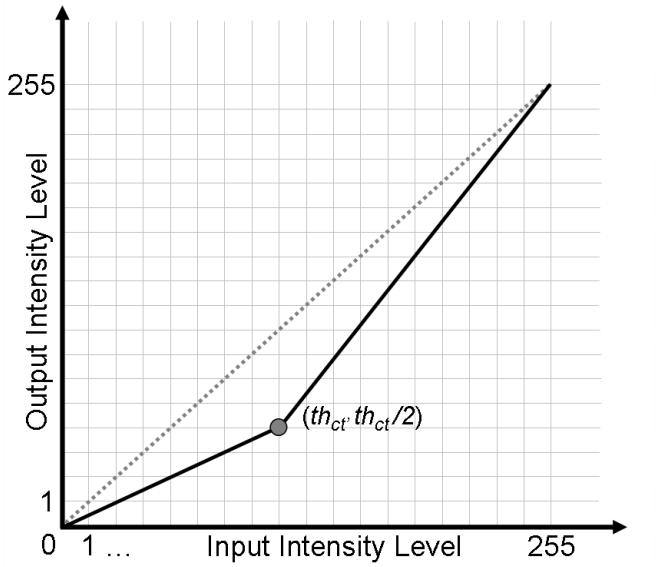


**Figure 6.2.** Example of intensity transformation function used to suppress cavity noise and enhance the dynamic range within tissue speckle as well as the cardiac tissue/cavity contrast.

### 6.4.5. Temporal alignment

Temporal alignment can be divided into four further steps: (i) the identification of all ED and ES frames within the multi-cycle dataset, (ii) the extraction of a representative reference cardiac cycle for the dataset, (iii) the identification of additional frames as control points for

a more accurate temporal alignment, and (iv) the temporal mapping between all cardiac cycles to the reference cycle of the dataset.

#### 6.4.5.1. Identification of ED and ES frames

All ED and ES frames within a multi-cycle dataset were semi-automatically identified utilising intensity information within the B-mode image sequence. The method was based on the left ventricular deformation during the cardiac cycle and required the manual identification of one ED (ED1) and one ES (ES1) frame. During systole, due to left ventricular contraction, each consecutive frame appeared less similar to ED1 and more similar to ES1. Likewise, during diastole, due to left ventricular relaxation, each consecutive frame became more similar to ED1 and less similar to ES1. A similarity coefficient based on normalised cross correlation (NXC) between each subsequent frame of a B-mode dataset and the manually identified ED1 and ES1 frames was estimated. The similarity coefficient demonstrated strong local maxima on all ED frames as well as strong local minima on all ES frames compensating for the high noise levels contained in cardiac ultrasound data.

#### 6.4.5.2. Extraction of a representative reference cardiac cycle

The derived ED and ES frames defined each cardiac cycle (ED – ES – ED sequence) and were utilised in order to extract a reference cardiac cycle, representative of the whole multi-cycle dataset. The reference cardiac cycle was automatically identified so that the temporal variations within the diastole and systole phases amongst the reference cardiac cycle and the remaining cycles of the dataset were minimised. All remaining cardiac cycles would then be temporally and spatially registered to the reference cardiac cycle prior to the final spatial compounding being applied on their corresponding frames.

#### 6.4.5.3. Identification of additional control points

Having identified the ED and ES frames defining all cardiac cycles as well as extracted a reference cardiac cycle within a multi-cycle dataset, additional frames corresponding to different stages of a cardiac cycle were identified. The additional frames would then act as control points (CPs) during the temporal interpolation process resulting in a more accurate alignment. Such frames were initially introduced at regular temporal intervals in the contraction and relaxation phases of the reference cardiac cycle. Two additional frames in each phase were introduced defining 7 independent cardiac stages, a fair representation of both the global as well as the local temporal variations within a cardiac cycle. NXC was then used in order to identify which frames within the remaining cardiac cycles corresponded

(demonstrated local maximum) to the additional CPs. In cases where high levels of noise or shadowing obstructed the derivation of a clear local maximum throughout the search, the corresponding cardiac cycle was omitted during the temporal mapping and spatial compounding stages.

#### 6.4.5.4. Interpolation process

The final stage of the temporal alignment established a temporal correspondence between the aligned and the reference frame sequences. The process was referred to as temporal interpolation and was applied between the reference cardiac cycle and all remaining cardiac cycles within a multi-cycle B-mode dataset. As mentioned in Section 3.2, cardiac temporal variations can be global such as differences in cardiac cycle lengths, as well as local such as differences in the dynamic properties of the 7 individual cardiac cycle phases. Both global and local temporal variations were addressed by decoupling the transformation into independent global and local components. The global component of the transformation was represented by an affine transformation while the local component of the transformation was modeled using a *1D relaxed uniform cubic B-Spline* curve interpolating through the corresponding CPs identified in the two frame sequences. Nearest neighbour interpolation on the transformation curve was utilised in order to allocate a corresponding frame to each frame within the reference cardiac cycle.

### 6.4.6. Spatial alignment

The last step prior to spatial compounding was the automatic spatial registration of the temporally aligned frames relating each point within an image to the corresponding point in the reference image. An intrinsic registration method utilising image intensity similarity information was employed. A rigid-body transformation consisting of rotation and translation components was used for the spatial registration of the temporally aligned frames. Moreover, bilinear interpolation was applied during the image transformation process since it has been found to provide the best trade-off between accuracy and computational complexity. Finally, Nelder-Mead's simplex optimisation strategy was used to derive an optimal transformation maximising the similarity between the registered images.

### 6.4.7. Spatial compounding

Each frame within the reference cardiac cycle was finally replaced by a compounded frame generated from the spatio-temporally aligned images, one from each cardiac cycle (Figure 6.3). The mean (*M*) as well as the standard deviation (*SD*) in the similarity (NXC) between

the reference frame and all the corresponding spatio-temporally aligned frames was derived. Frames with NXC outside the $M \pm STD$ region were discarded in order to avoid the compounding of dissimilar frames resulting in tissue/cavity boundary blurring. Intensity averaging was utilised as a well established and effective compounding method for noise suppression in ultrasound datasets. The intensity of each pixel within the compounded frame was therefore set as the average intensity value of the corresponding pixels from all the spatio-temporally aligned data (Figure 6.3).

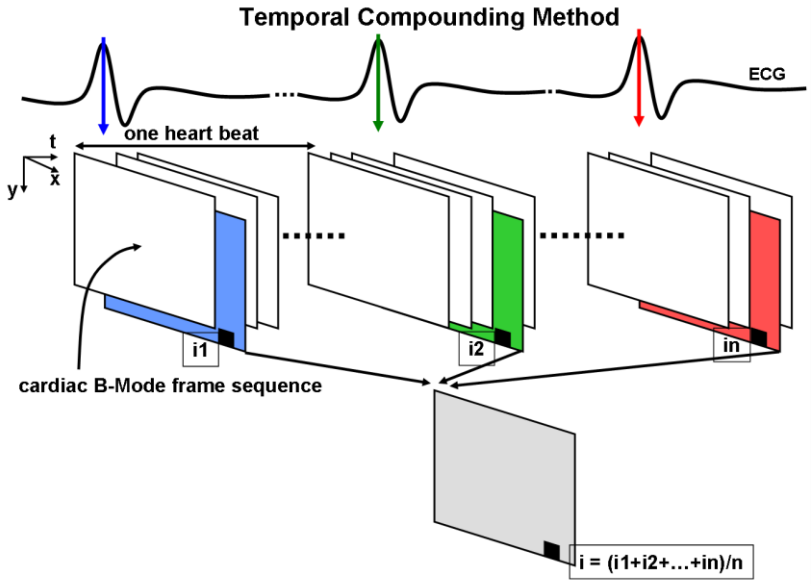


**Figure 6.3.** Intensity averaging of temporally aligned frames from consecutive cardiac cycles.

## 6.5. Data analysis and results

Similar to Chapters 3 to 5, a range of quantitative and qualitative results are presented in order to assess the effect of the integrated approach proposed on enhancing cardiac ultrasound data. The main objectives are to (i) compare and contrast the effect of the individual ***Temporal Compounding*** and ***DHBIM*** methods and the corresponding integrated approach and (ii) assess whether the integrated method compensates for the limitations encountered on each of the individual approaches. Optimal acquisition and processing parameters identified in Chapters 3 and 5 were utilised ensuring the clinical feasibility of each individual method, and as a consequence of the proposed integrated approach. Clinical feasibility encompasses the achievement of adequate noise suppression as well as contrast enhancement between cardiac tissue and cavity while (i) preserving clinically vital tissue information within the processed B-mode data, (ii) maintaining tissue/cavity boundary

blurring to a clinically acceptable level, and (iii) keeping data acquisition time and processing requirements to a minimum by limiting the number of utilised cardiac cycles.

More precisely, the effect of the integrated image enhancement process on cardiac ultrasound data is investigated by examining the SNR changes at the IVS and at the RV cavity, as well as contrast and SNDR changes between tissue (IVS) and cavity (RV). The effect on tissue/cavity thresholding and tissue/cavity blurring is not examined directly since outlining the LV cavity on real human datasets is not only a laborious, but a highly subjective and erroneous process. Instead, the effect of integrated image enhancement process on tissue/cavity boundaries is investigated by performing routine clinical measurements on tissue structures and cavities. Such measurements provide sufficient information indicating whether the information suppression and boundary blurring introduced in cardiac cavities has limiting clinical effect on the processed datasets.

### 6.5.1. Effect on tissue SNR, cavity SNR, tissue/cavity contrast and SDNR

The effect of the proposed integrated image enhancement method on the noise and contrast within the imaged cardiac structures was quantitatively assessed utilising the approach introduced in Section 3.7.2.1. Two (11x11 pixels) ROIs corresponding to the cardiac IVS and the RV cavity had been previously defined on each of the 32 patient datasets. The pixel intensity values at each ROI were used to estimate the tissue SNR, cavity SNR, the tissue/cavity Contrast and the detectability index SDNR on both an original as well as a series of processed ED frames for each of the datasets. The processed frames were generated integrating the ***DHBIM*** and ***Temporal Compounding*** methods on sequences of increasing numbers of cardiac cycles. Figure 6.4.a displays multiple SNR curves, each representing a different dataset, illustrating the effect of the number of cardiac cycles utilised during the integrated image enhancement approach on speckle and noise in cardiac tissue structures. Similarly, Figure 6.4.b displays the corresponding LV cavity SNR curves. The mean SNR curves, averaging the SNR curves of all 32 datasets, are also displayed in each of the plots providing representative SNR profiles for tissue and cavity. A direct comparison between the mean tissue and cavity SNR profiles is provided in Figure 6.5. Furthermore, Figure 6.6 displays a mean profile, for all 32 datasets, illustrating the effect of the integrated image enhancement approach for an increasing number of cardiac cycles on tissue/cavity detectability index (SDNR). The SDNR curves for each individual dataset are omitted since they demonstrate a very similar trend to the corresponding SNR curves. Tables 6.1 to 6.4 summarise the variations on the four quantitative measures between the original and the processed datasets (using 12 cardiac cycles) elucidating the effect of the integrated image

enhancement approach on the imaged cardiac structures. Finally, Figures 6.7 and 6.8 illustrate the mean SNR and SDNR curves generated using ***Temporal Compounding*** and the integrated image enhancement method for increasing numbers of cardiac cycles. In a similar way, Table 6.5 provides a direct comparison on the mean effect of the individual and integrated image enhancement methods on all 4 image quality metrics.

### 6.5.2. Visual effect on cardiac ultrasound data

Figures 6.9 to 6.20 display six examples of original and processed ED frames. Each example illustrates the effect of the individual ***Temporal Compounding*** and ***DHBIM*** methods as well as the proposed integrated image enhancement method on the corresponding multi-cycle dataset. Datasets covering a range of image and diagnostic qualities (3 low, 2 average and 1 high) were selected in order to best illustrate the processing effect on typical clinical cardiac ultrasound data. More processed datasets can be found in the accompanying DVD-1.

### 6.5.3. Effect on clinical measurements performed on patient data

Similar to the process described in Section 3.6 and utilised in Chapters 3 to 5, two experienced echocardiographers were asked to perform routine clinical measurements on ED and ES frames from both the original B-mode as well as the contrast enhanced data. All clinical measurements were performed twice to enable the examination of measurement agreement and repeatability. The Bland Altman approach was then used for the quantitative assessment of the effect of the integrated image enhancement method on clinical measurements. Figures 6.21 and 6.22 display Bland Altman plots combining all clinical measurements performed by each echocardiographer. Individual plots, one for each clinical measurement, were also derived. Table 6.6 summarises the bias, similarity measures and agreement coefficients derived from the individual plots. In a similar way, Table 6.7 provides a direct comparison on the effect of the individual and integrated image enhancement methods on the repeatability coefficient of all 5 clinical measurements performed by both echocardiographers. Tables 6.8 and 6.9 display the clinical measurements omitted by each echocardiographer on the original and contrast enhanced datasets. More information on Bland Altman plots is provided in Section 3.7.2.3.

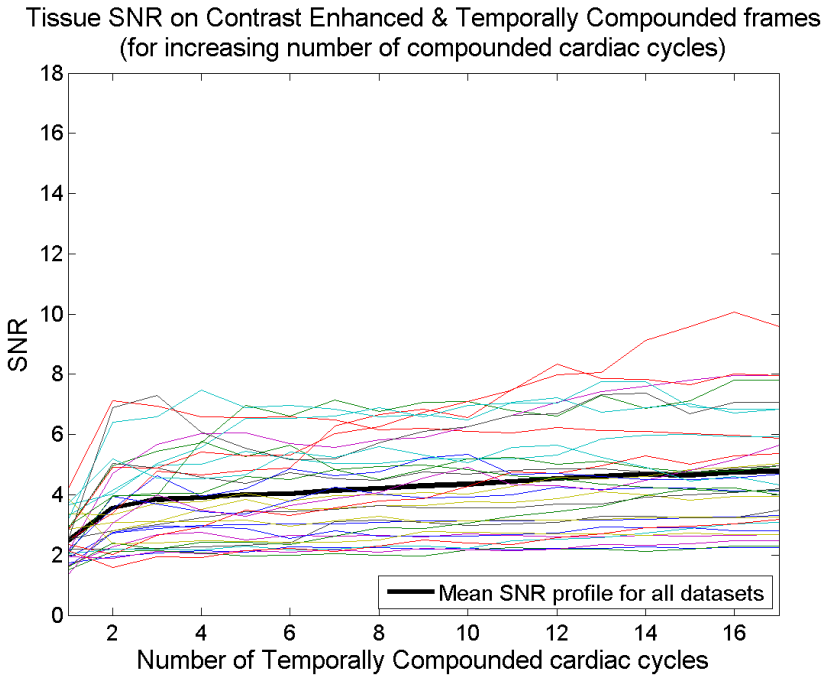


**(a)**

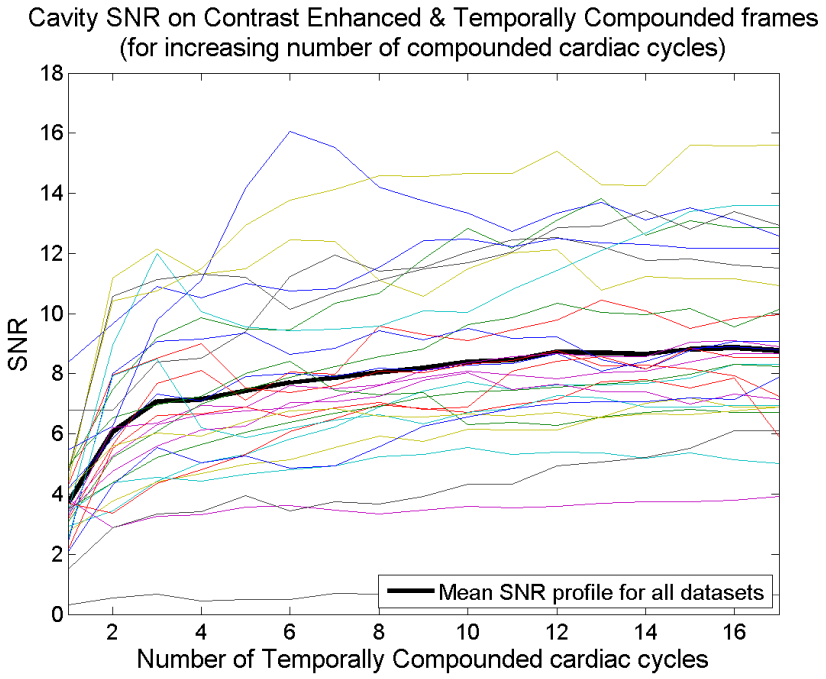


**(b)**

**Figure 6.4.** The effect of the *integrated image enhancement method* on (a) tissue and (b) cavity SNR for increasing number of compounded cardiac cycles. The mean SNR changes are also displayed.

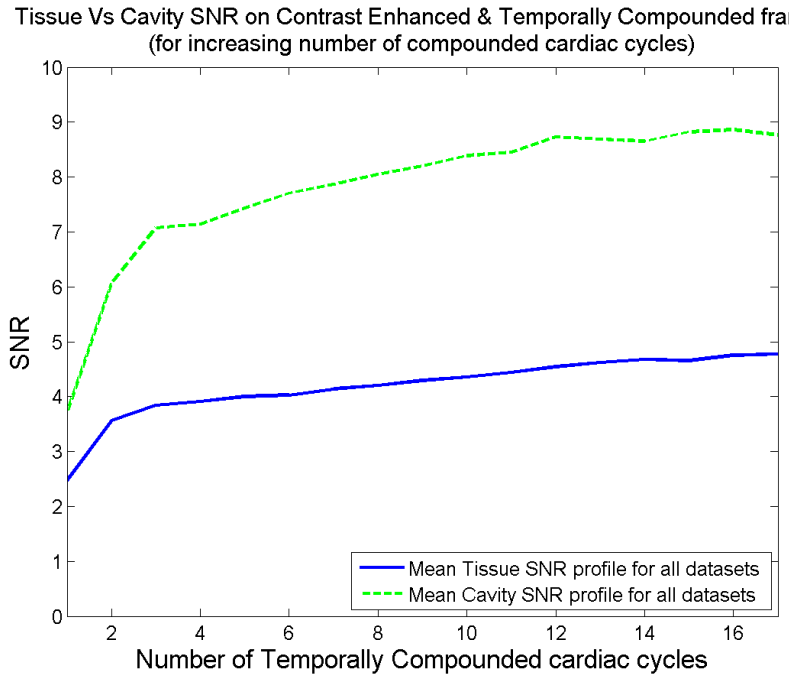


**Figure 6.5.** A direct comparison between the effect of the *integrated image enhancement method* for increasing number of cardiac cycles on tissue and cavity SNR.

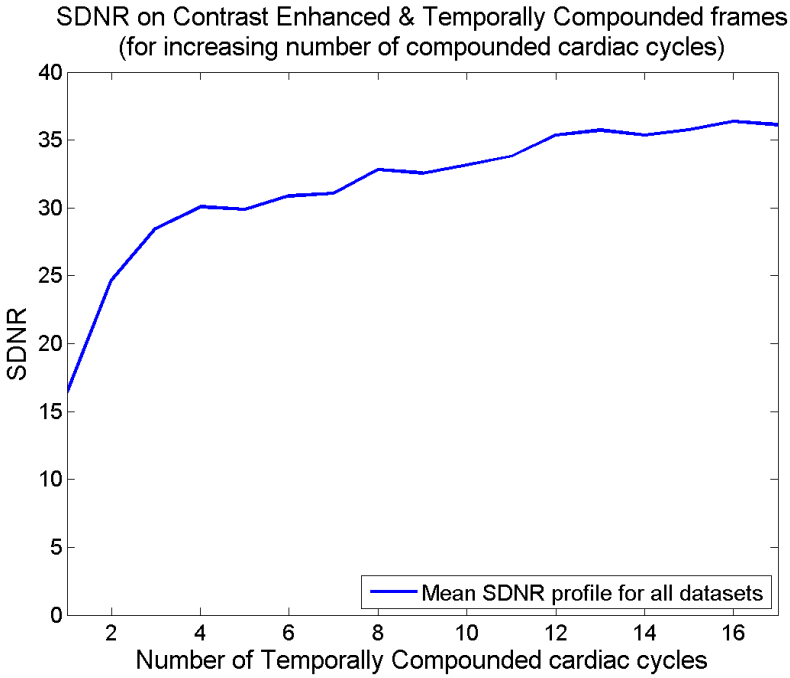


**Figure 6.6.** The effect of the *integrated image enhancement method* for increasing number of cardiac cycles on tissue/cavity SDNR.

**Table 6.1.** Effect of *integrated method* on tissue SNR. Results for 12 cardiac cycles.

| | | Contrast Enhanced & | |
|---|---|---|---|
| | **Original** | **Temporally Compounded** | **Improvement** |
| **Min** | 2.22 | 2.20 | -47.0% |
| **Max** | 7.37 | 8.33 | 107.5% |
| **Mean** | 4.15 | 4.54 | 14.1% |
| **SD** | 1.59 | 1.82 | 38.3% |

**Table 6.2.** Effect of *integrated method* on cavity SNR. Results for 12 cardiac cycles.

| | | Contrast Enhanced & | |
|---|---|---|---|
| | **Original** | **Temporally Compounded** | **Improvement** |
| **Min** | 0.89 | 0.71 | -19.7% |
| **Max** | 10.44 | 15.40 | 199.8% |
| **Mean** | 5.05 | 8.73 | 78.2% |
| **SD** | 1.86 | 3.27 | 59.7% |

**Table 6.3.** Effect of *integrated method* on tissue/cavity Contrast. Results for 12 cardiac cycles.

| | | Contrast Enhanced & | |
|---|---|---|---|
| | **Original** | **Temporally Compounded** | **Improvement** |
| **Min** | 0.17 | 0.30 | 0.0% |
| **Max** | 2.00 | 2.00 | 222.9% |
| **Mean** | 0.83 | 1.20 | 72.1% |
| **SD** | 0.56 | 0.47 | 56.4% |

**Table 6.4.** Effect of *integrated method* on tissue/cavity SDNR. Results for 12 cardiac cycles.

| | | Contrast Enhanced & | |
|---|---|---|---|
| | **Original** | **Temporally Compounded** | **Improvement** |
| **Min** | 0.90 | 1.87 | 107.9% |
| **Max** | 35.39 | 224.58 | 816.7% |
| **Mean** | 6.79 | 35.35 | 401.4% |
| **SD** | 7.47 | 45.40 | 182.3% |

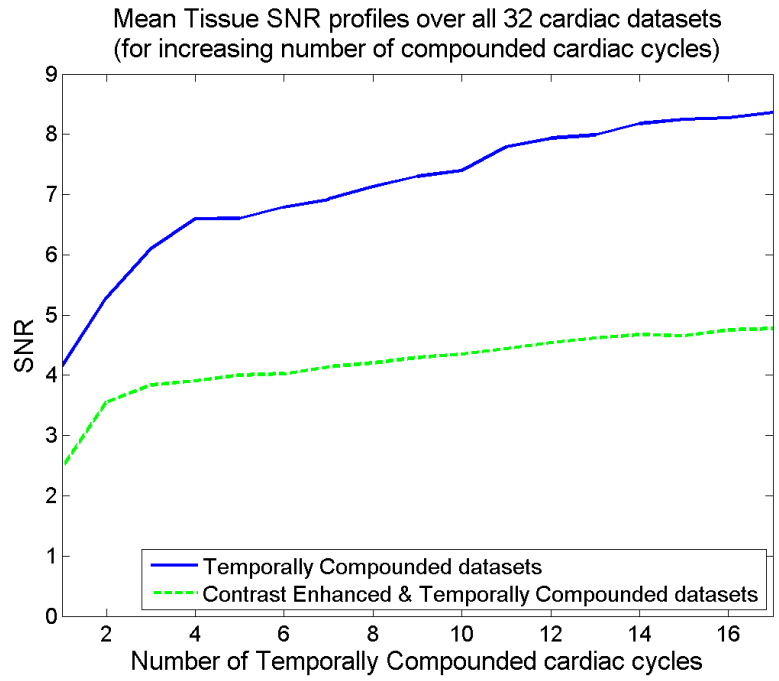


**(a)**

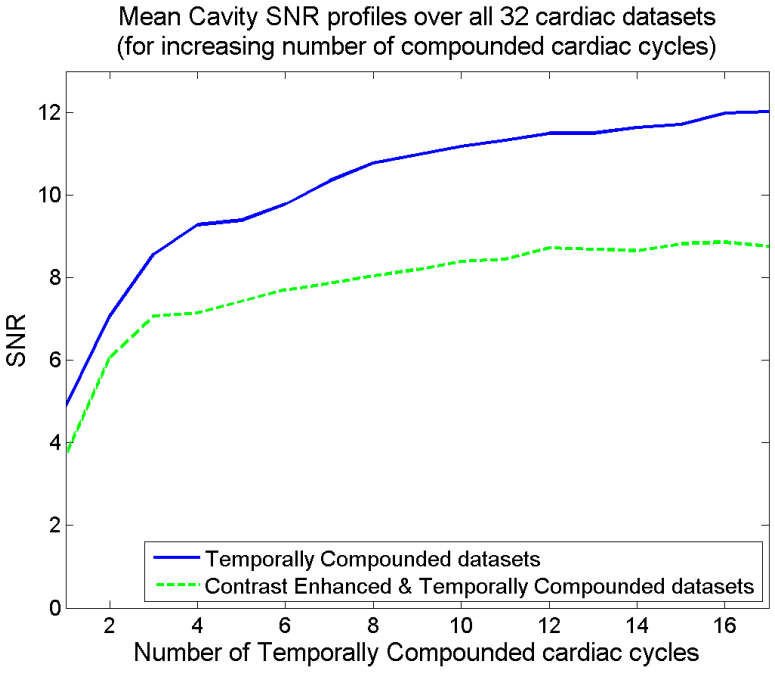


**(b)**

**Figure 6.7.** A direct comparison between the effects of *Temporal Compounding* against the *integrated image enhancement method* for increasing number of cardiac cycles on (a) tissue and (b) cavity SNR.

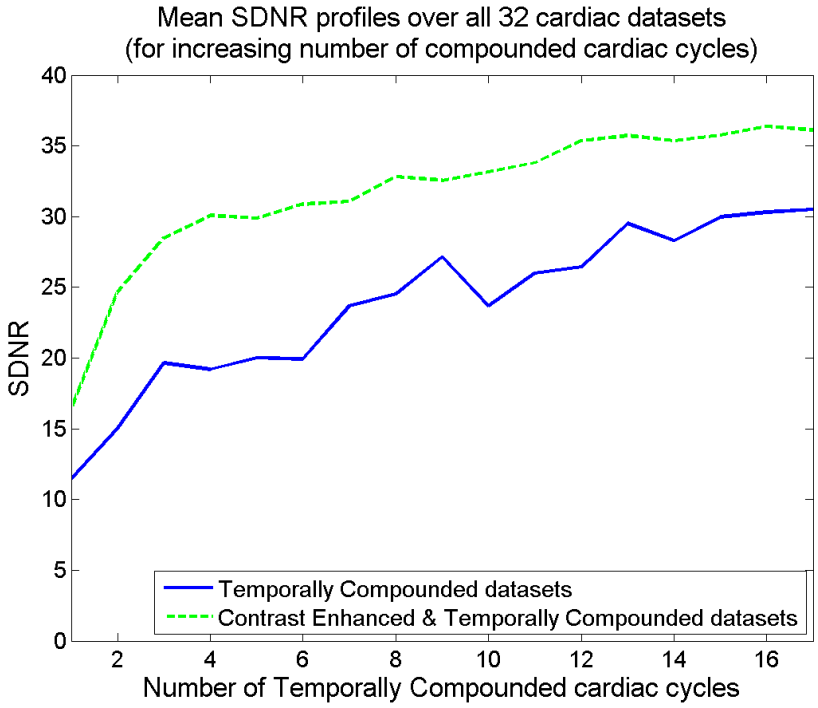


**Figure 6.8.** A direct comparison between the effects of *Temporal Compounding* against the *integrated image enhancement method* for increasing number of cardiac cycles on tissue/cavity SDNR.

**Table 6.5.** Comparing the effect of individual and integrated methods on image quality metrics.

| | **Temporally Compounded** | **Contrast Enhanced** | **Contrast Enhanced & Temporally Compounded** |
|---|---|---|---|
| **Tissue SNR** | 87.1% | -37.0% | 14.1% |
| **Cavity SNR** | 143.1% | -26.8% | 78.2% |
| **Contrast** | -3.1% | 73.8% | 72.1% |
| **SDNR** | 128.6% | 120.9% | 401.4% |

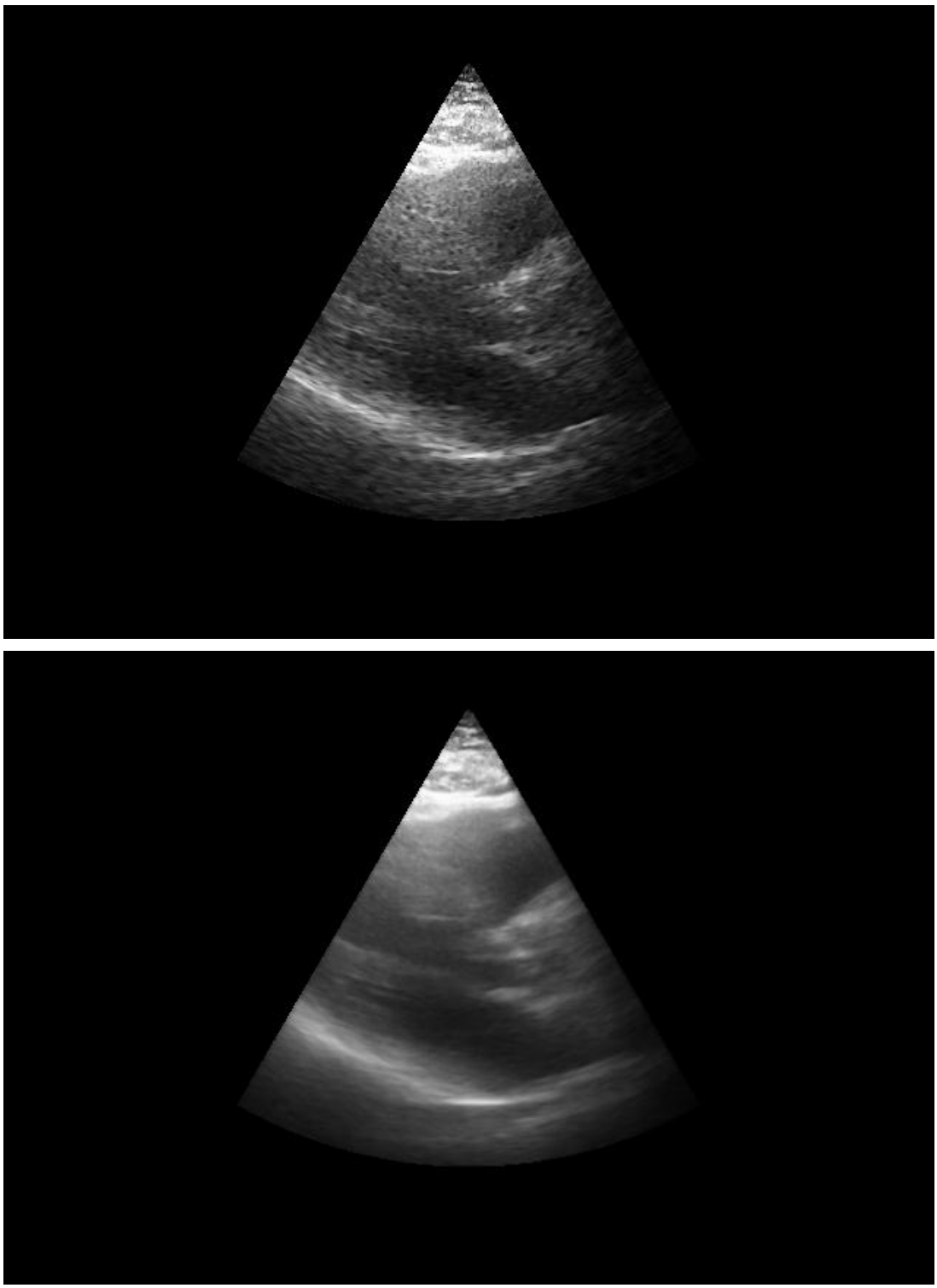

**Figure 6.9.** Original (top) and temporally compounded (bottom) ED frames of low diagnostic quality. (Patient 24)

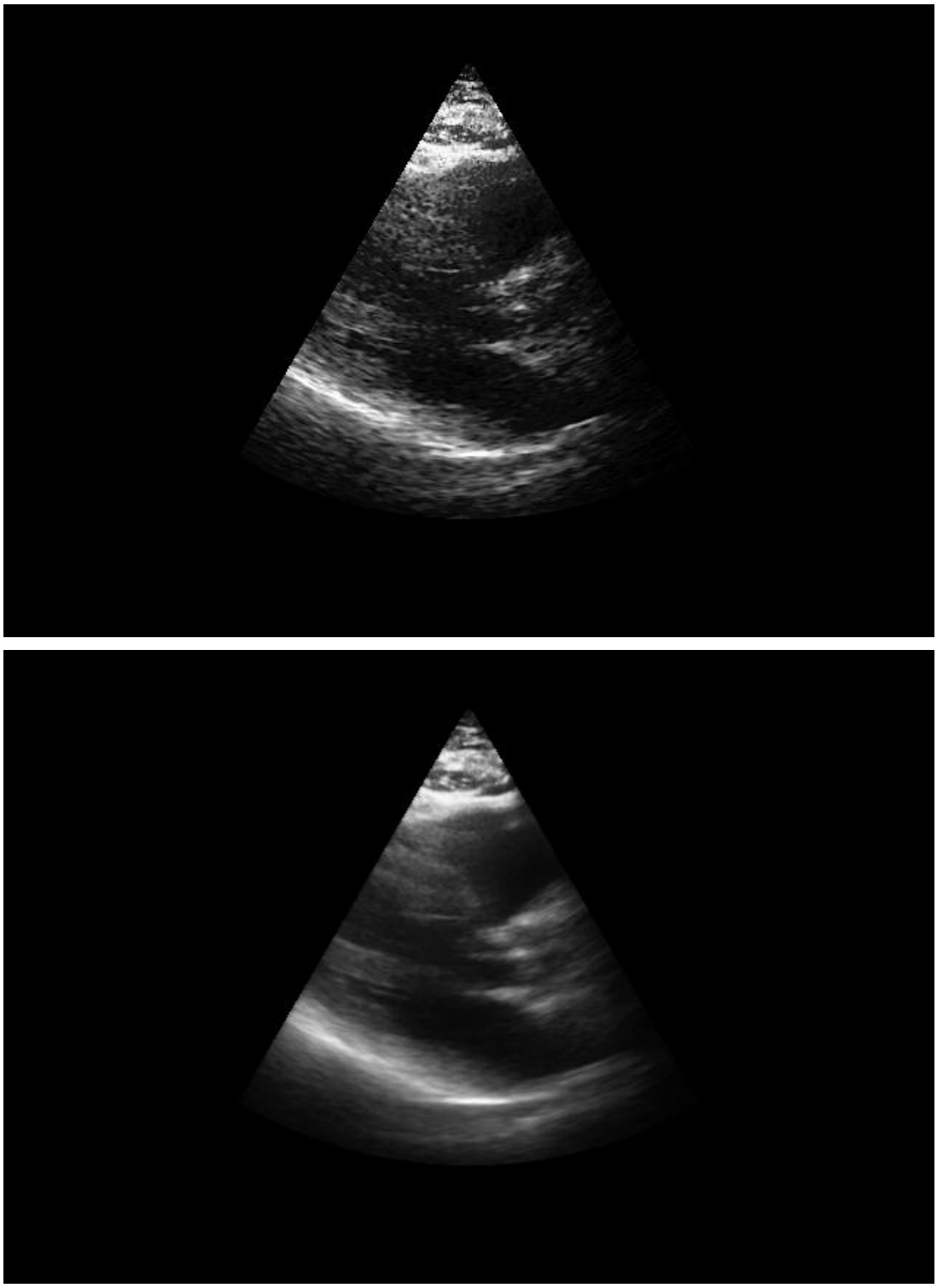

**Figure 6.10.** Contrast enhanced (using DHBIM) (top) and integrated (contrast enhanced followed by temporally compounded) (bottom) ED frames of low diagnostic quality. (Patient 24)

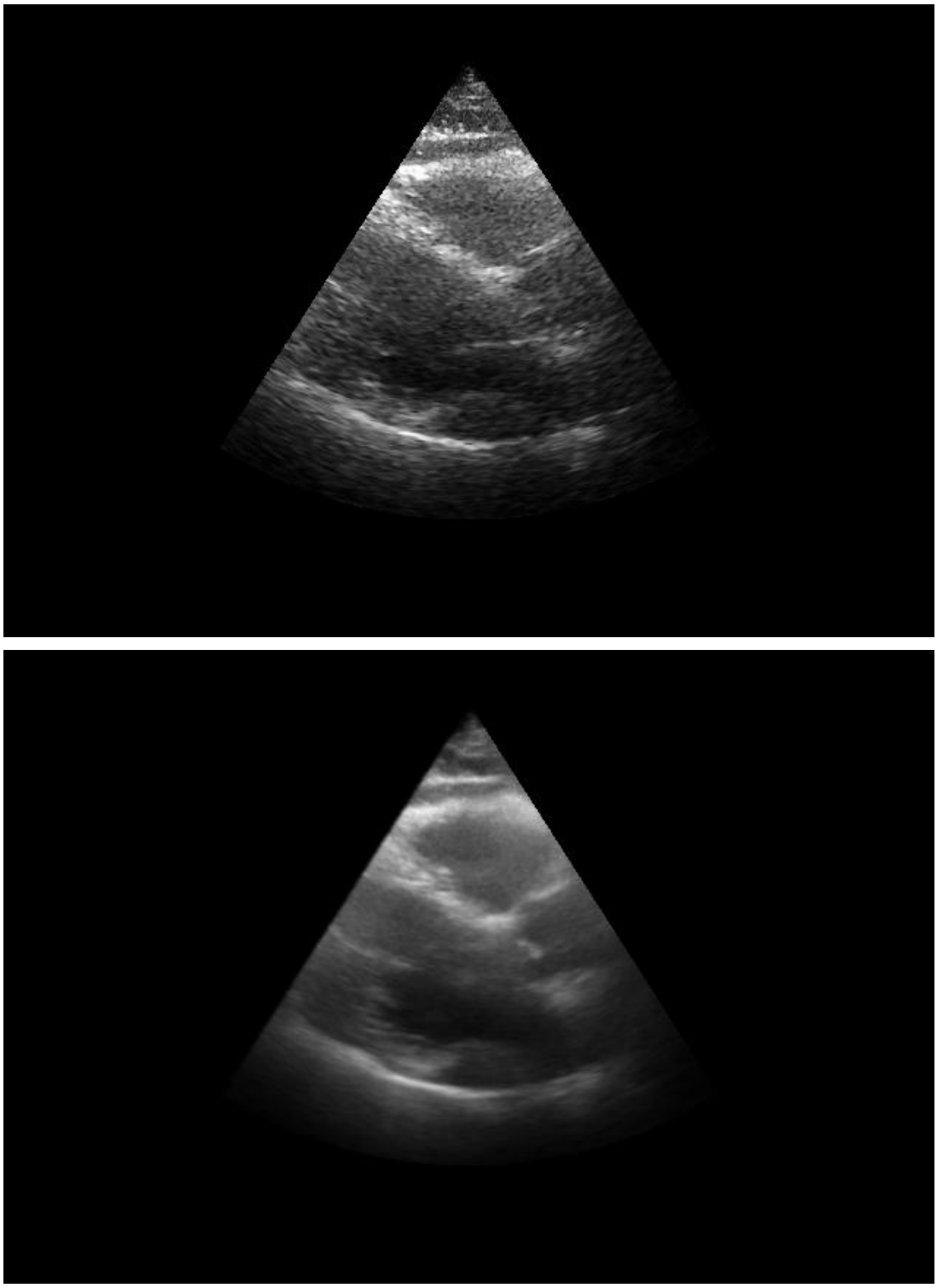

**Figure 6.11.** Original (top) and temporally compounded (bottom) ED frames of low diagnostic quality. (Patient 4)

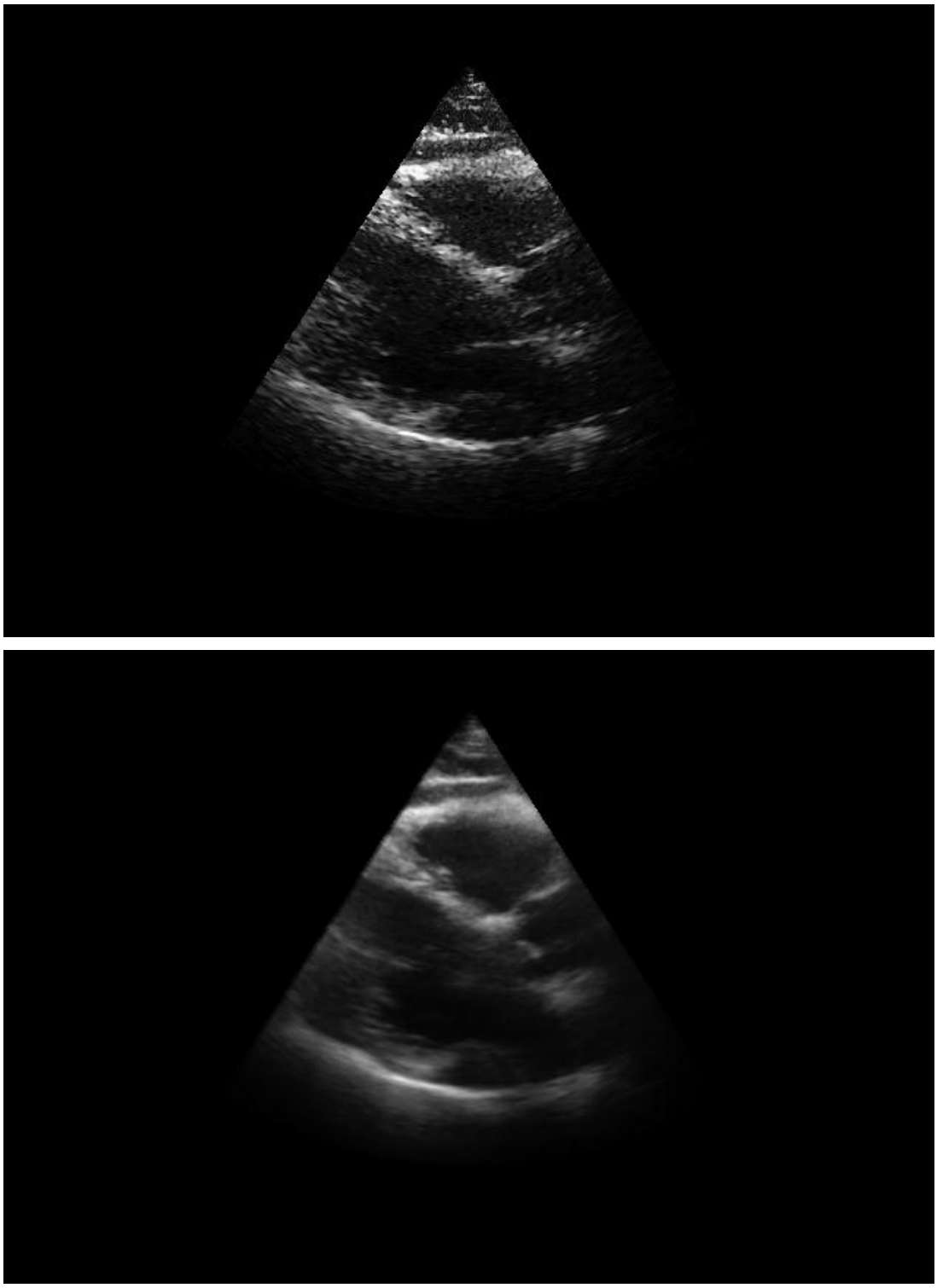

**Figure 6.12.** Contrast enhanced (using DHBIM) (top) and integrated (contrast enhanced followed by temporally compounded) (bottom) ED frames of low diagnostic quality. (Patient 4)

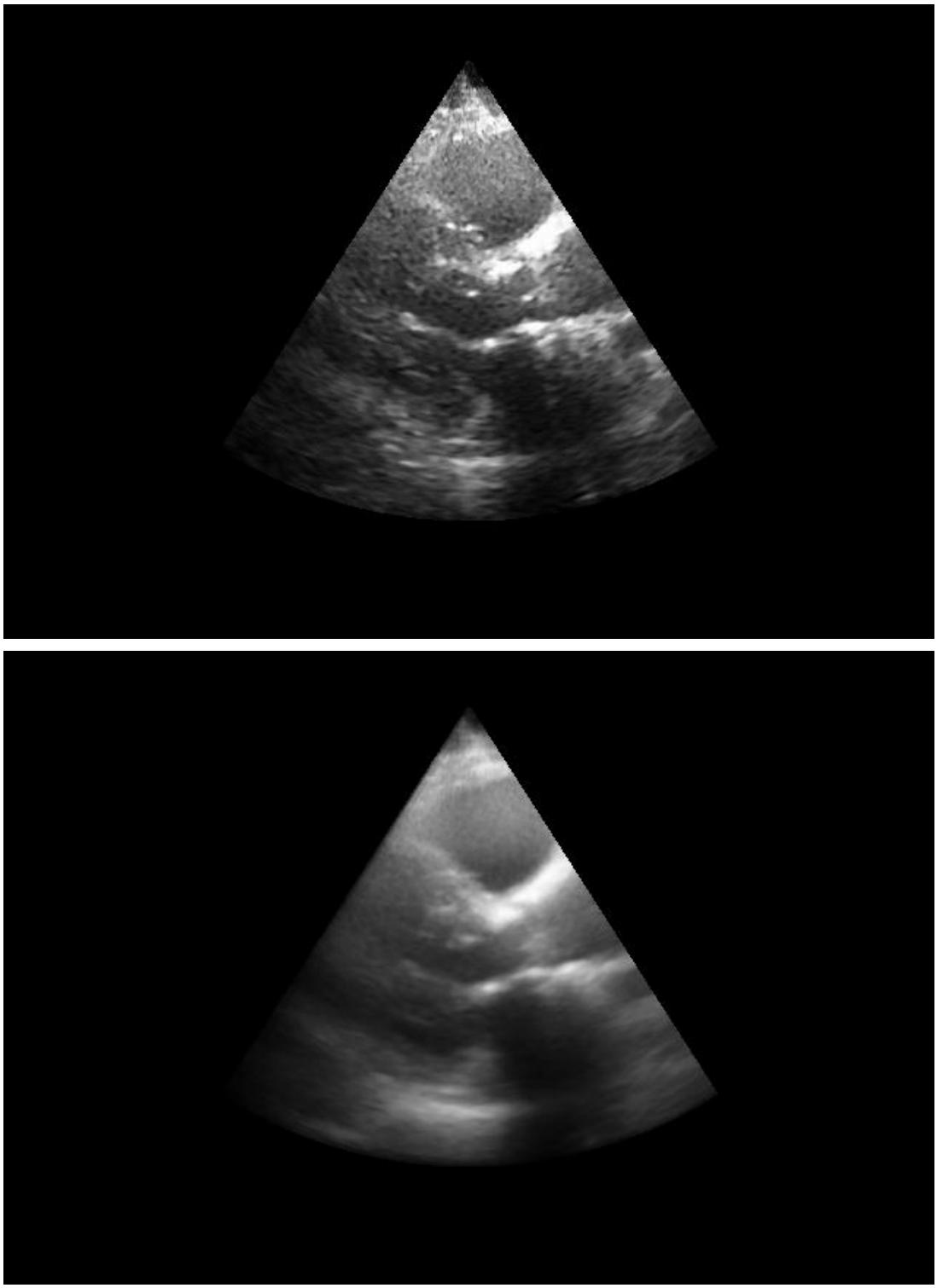

**Figure 6.13.** Original (top) and temporally compounded (bottom) ED frames of low diagnostic quality. (Patient 6)

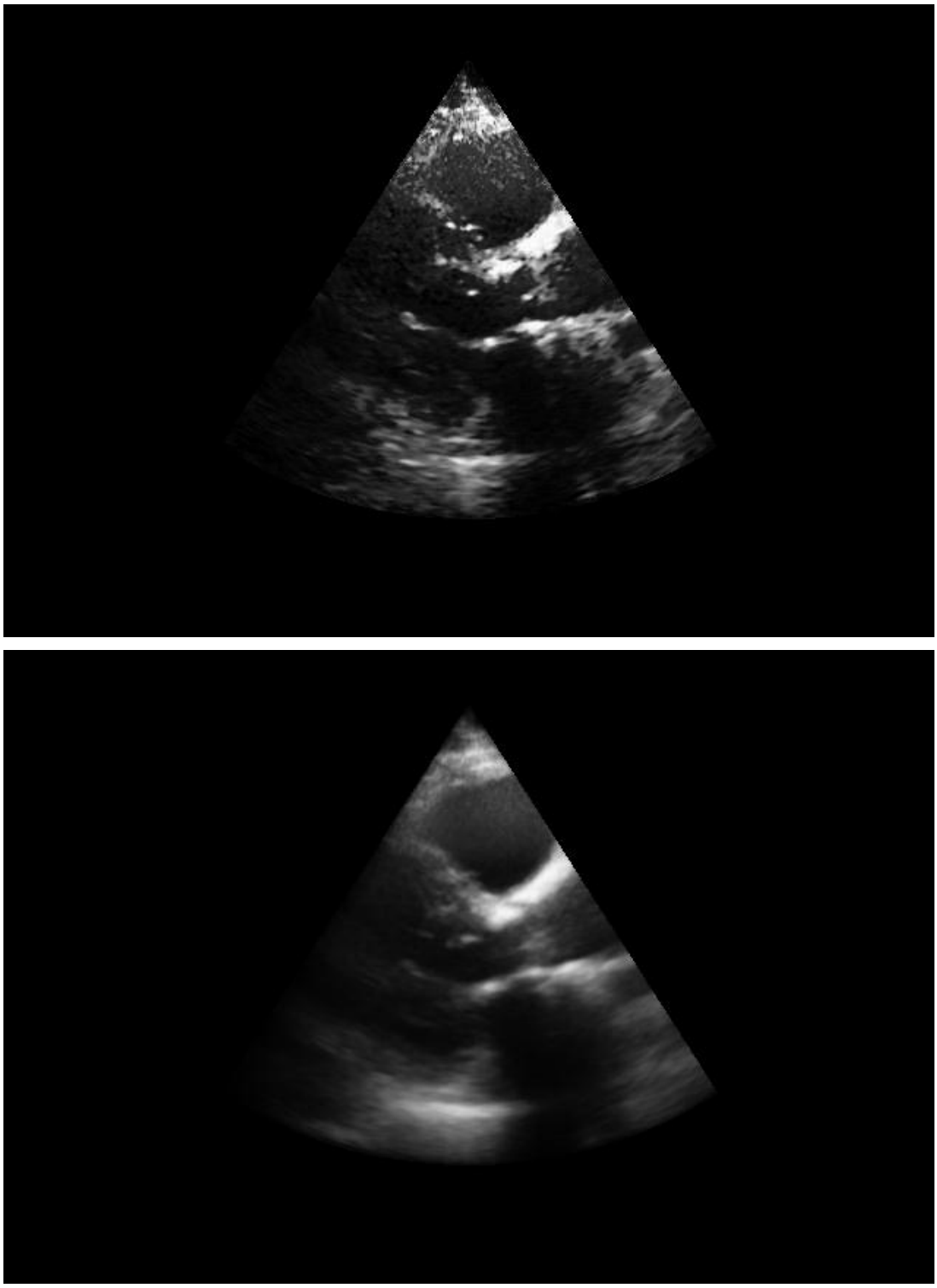

**Figure 6.14.** Contrast enhanced (using DHBIM) (top) and integrated (contrast enhanced followed by temporally compounded) (bottom) ED frames of low diagnostic quality. (Patient 6)

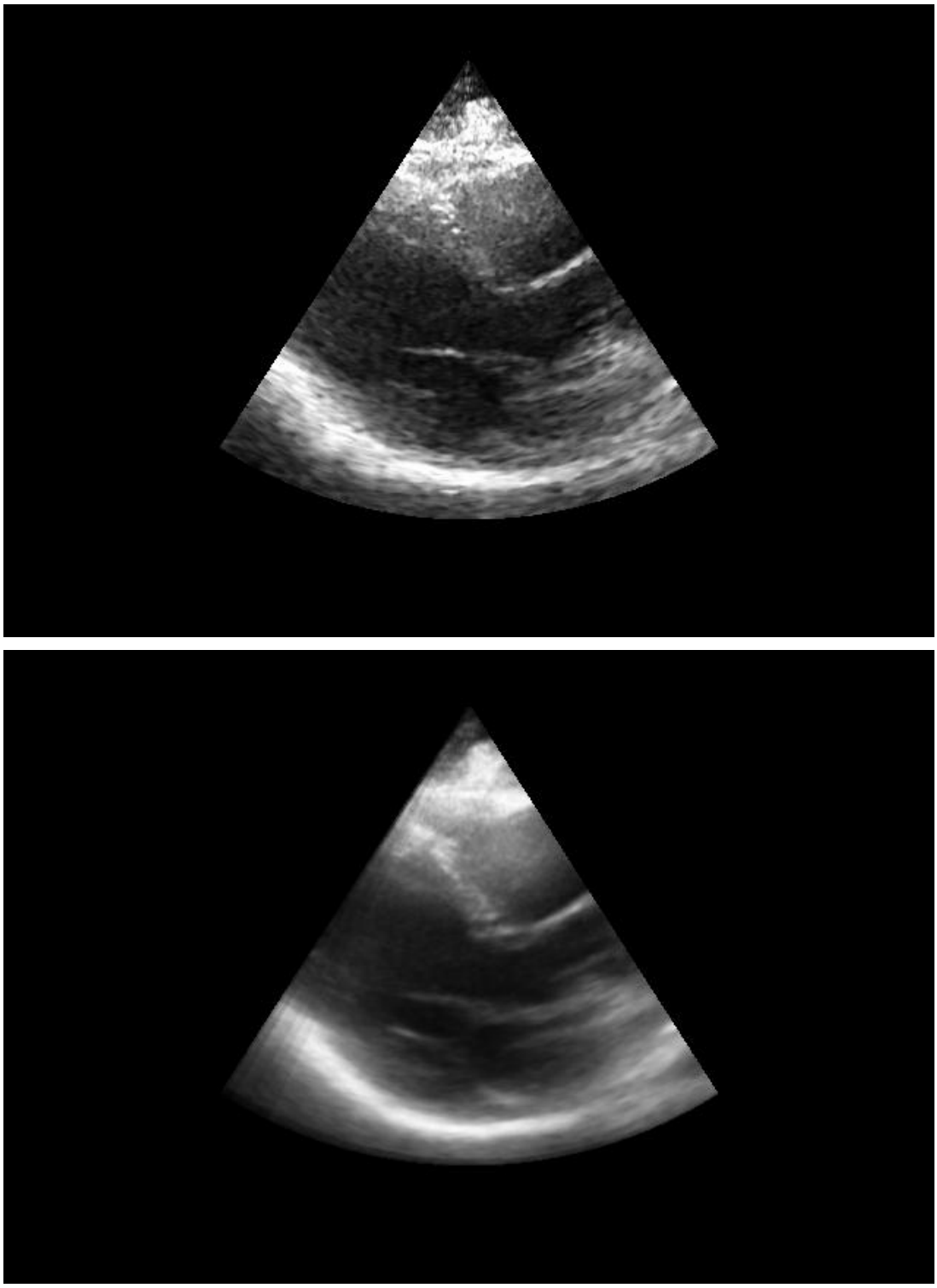

**Figure 6.15.** Original (top) and temporally compounded (bottom) ED frames of average diagnostic quality. (Patient 11)

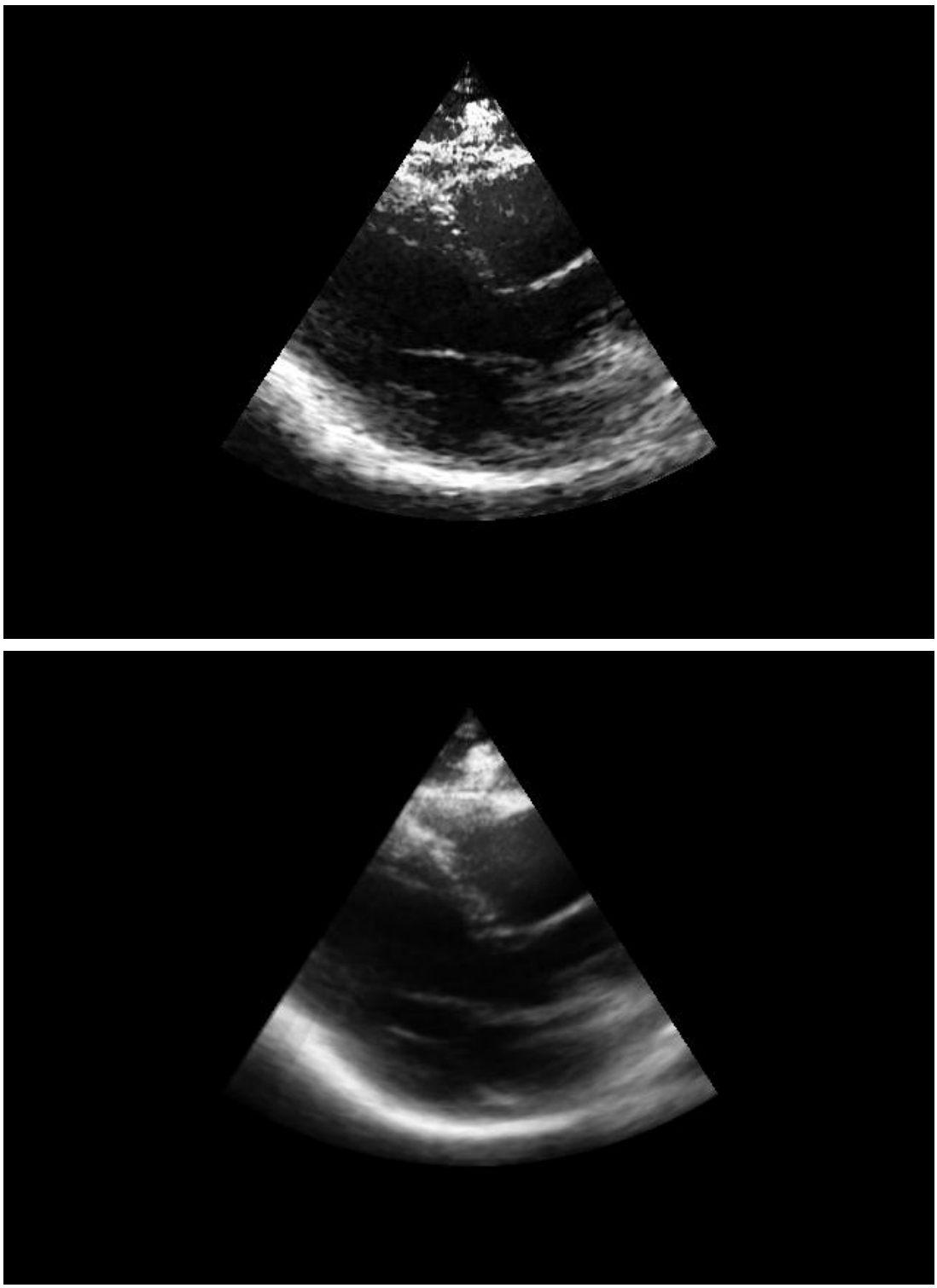

**Figure 6.16.** Contrast enhanced (using DHBIM) (top) and integrated (contrast enhanced followed by temporally compounded) (bottom) ED frames of average diagnostic quality. (Patient 11)

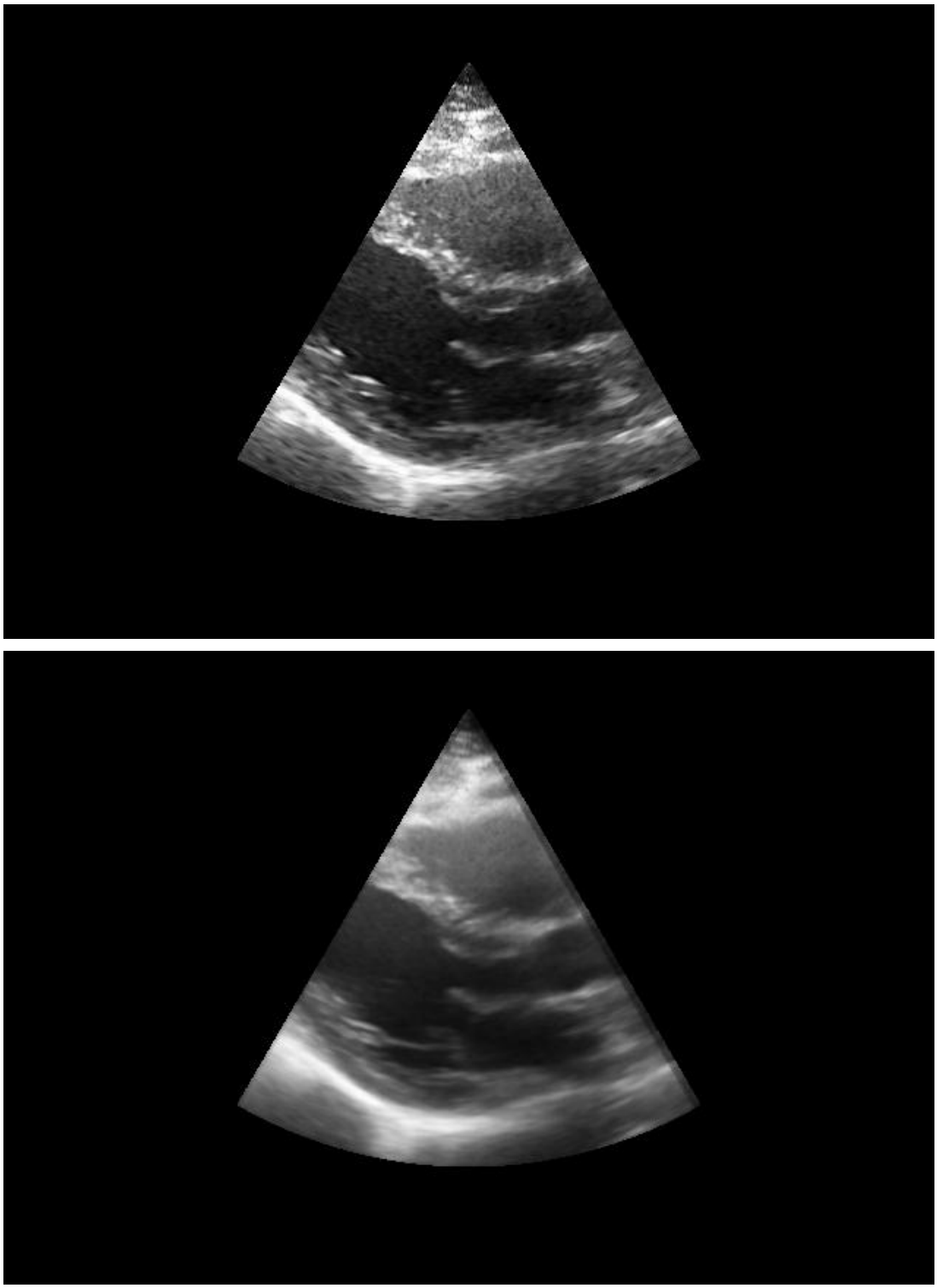

**Figure 6.17.** Original (top) and temporally compounded (bottom) ED frames of average diagnostic quality. (Patient 25)

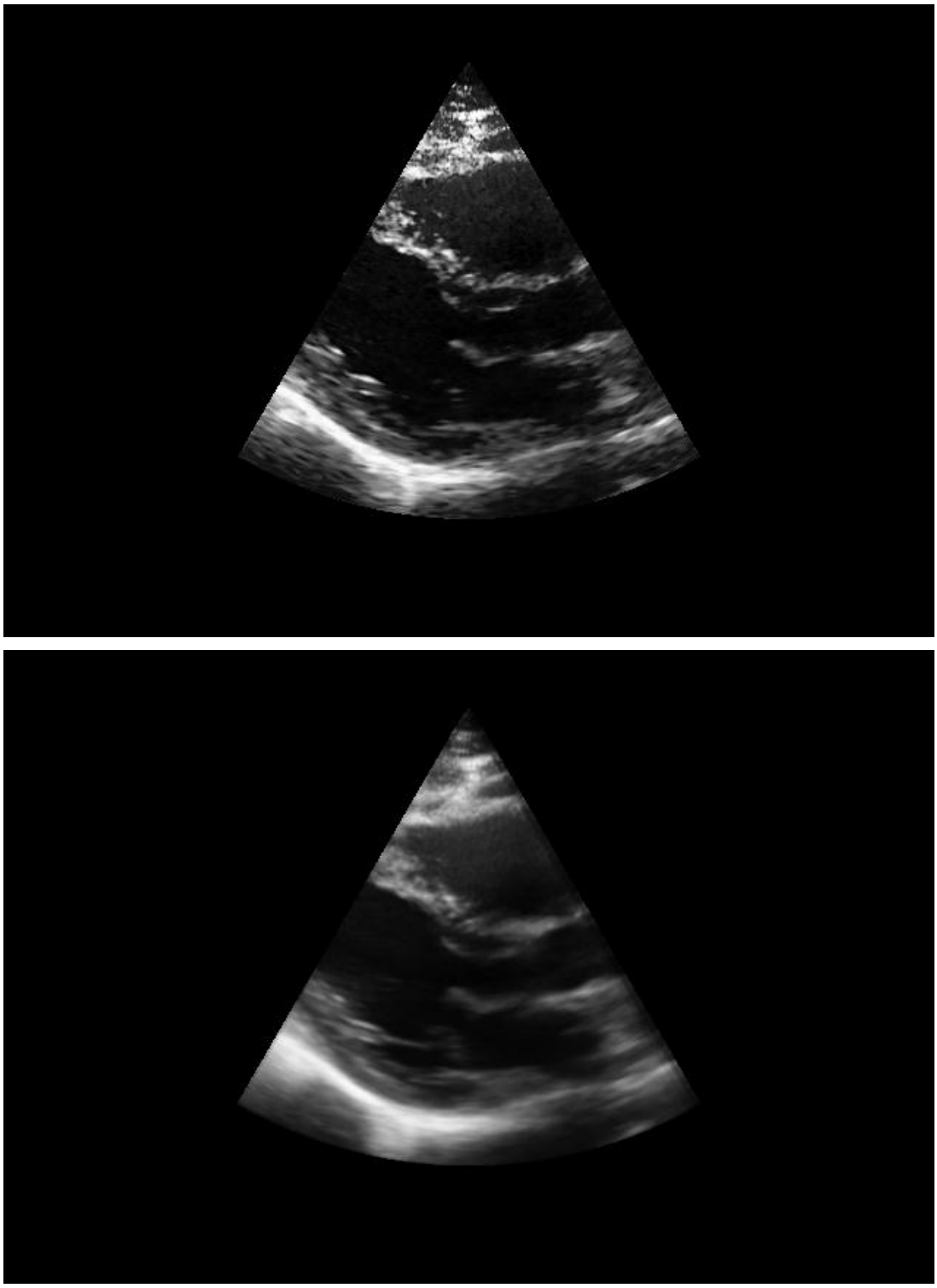

**Figure 6.18.** Contrast enhanced (using DHBIM) (top) and integrated (contrast enhanced followed by temporally compounded) (bottom) ED frames of average diagnostic quality. (Patient 25)

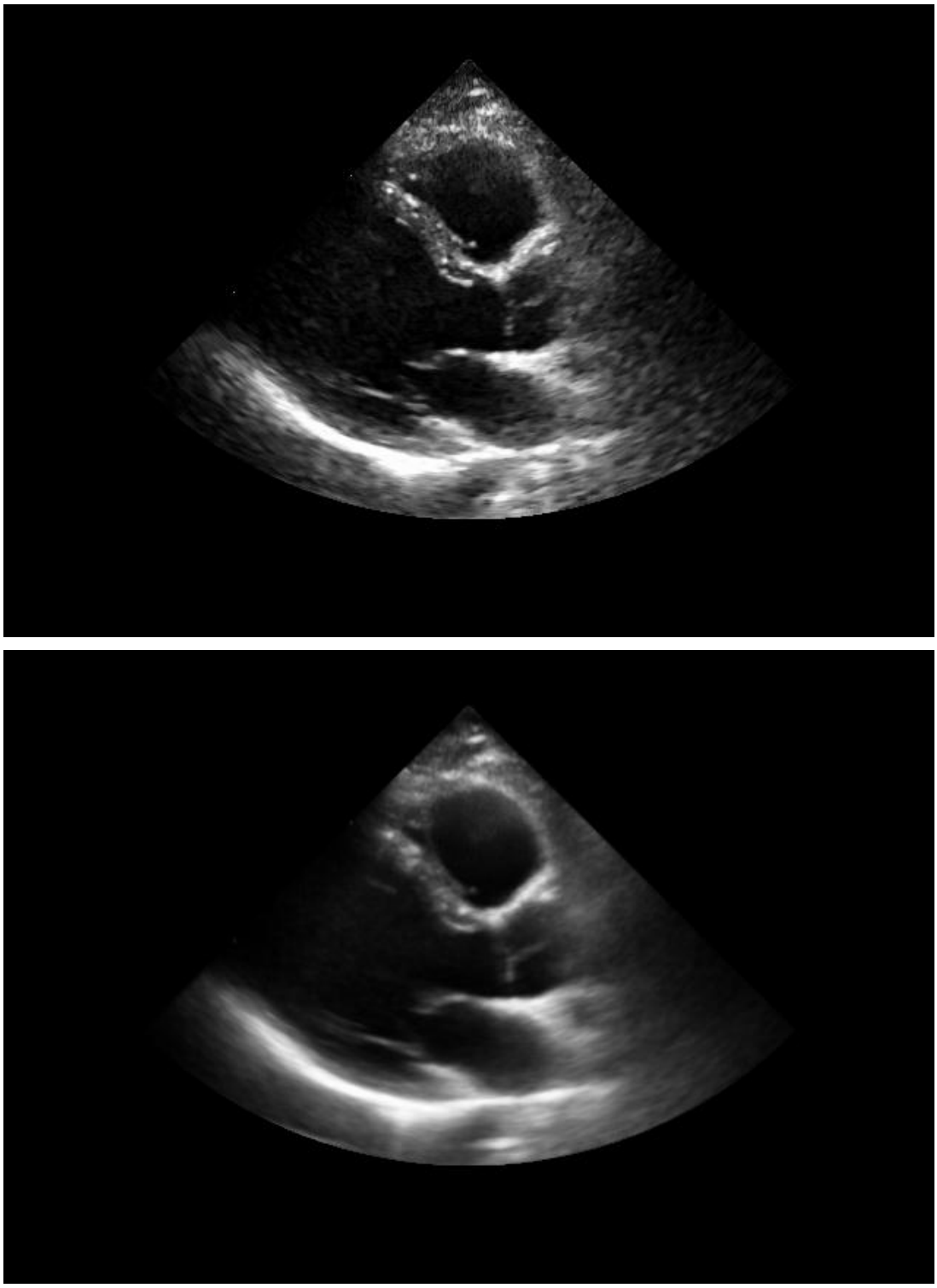

**Figure 6.19.** Original (top) and temporally compounded (bottom) ED frames of high diagnostic quality. (Patient 29)

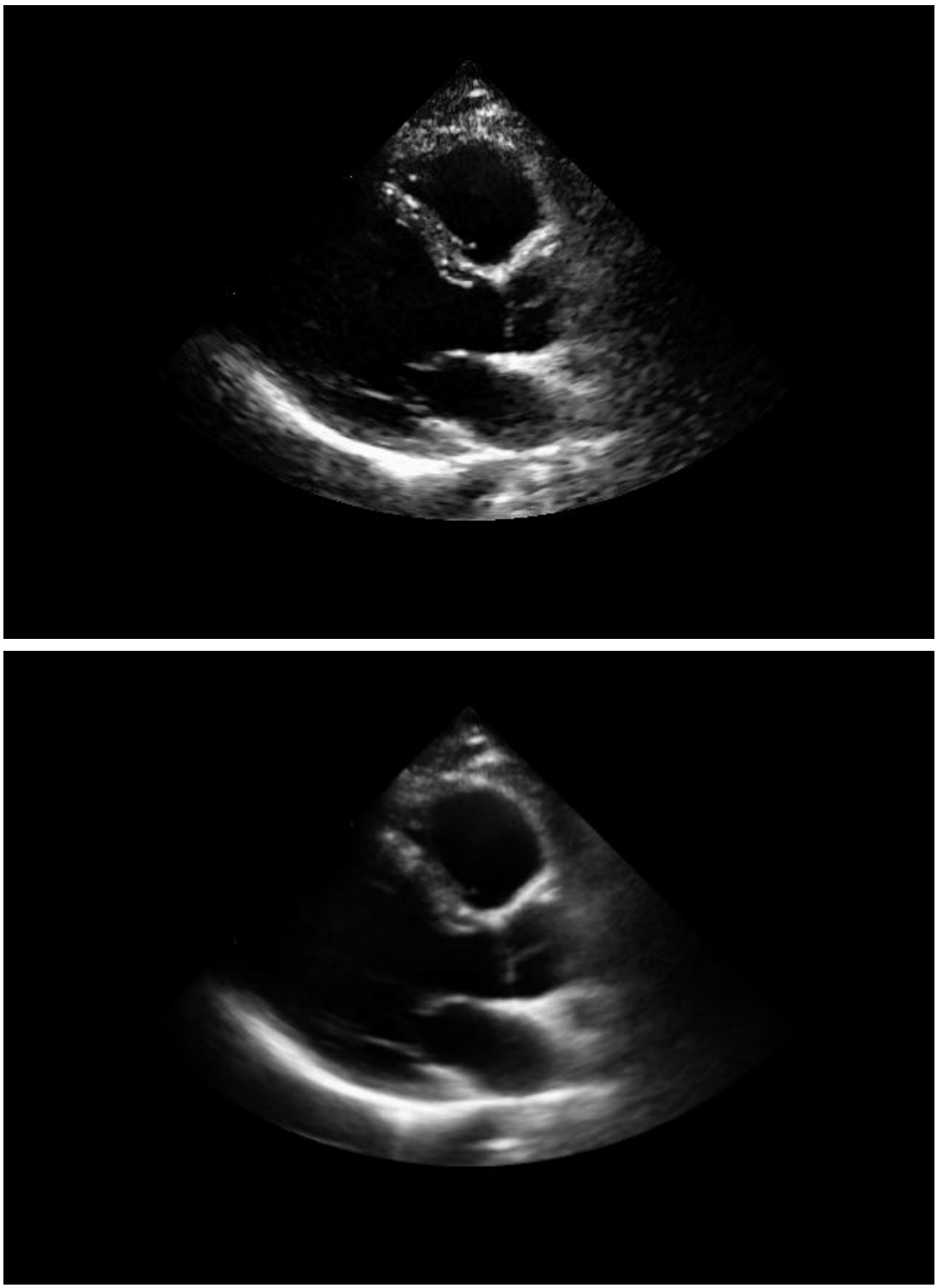

**Figure 6.20.** Contrast enhanced (using DHBIM) (top) and integrated (contrast enhanced followed by temporally compounded) (bottom) ED frames of high diagnostic quality. (Patient 29)

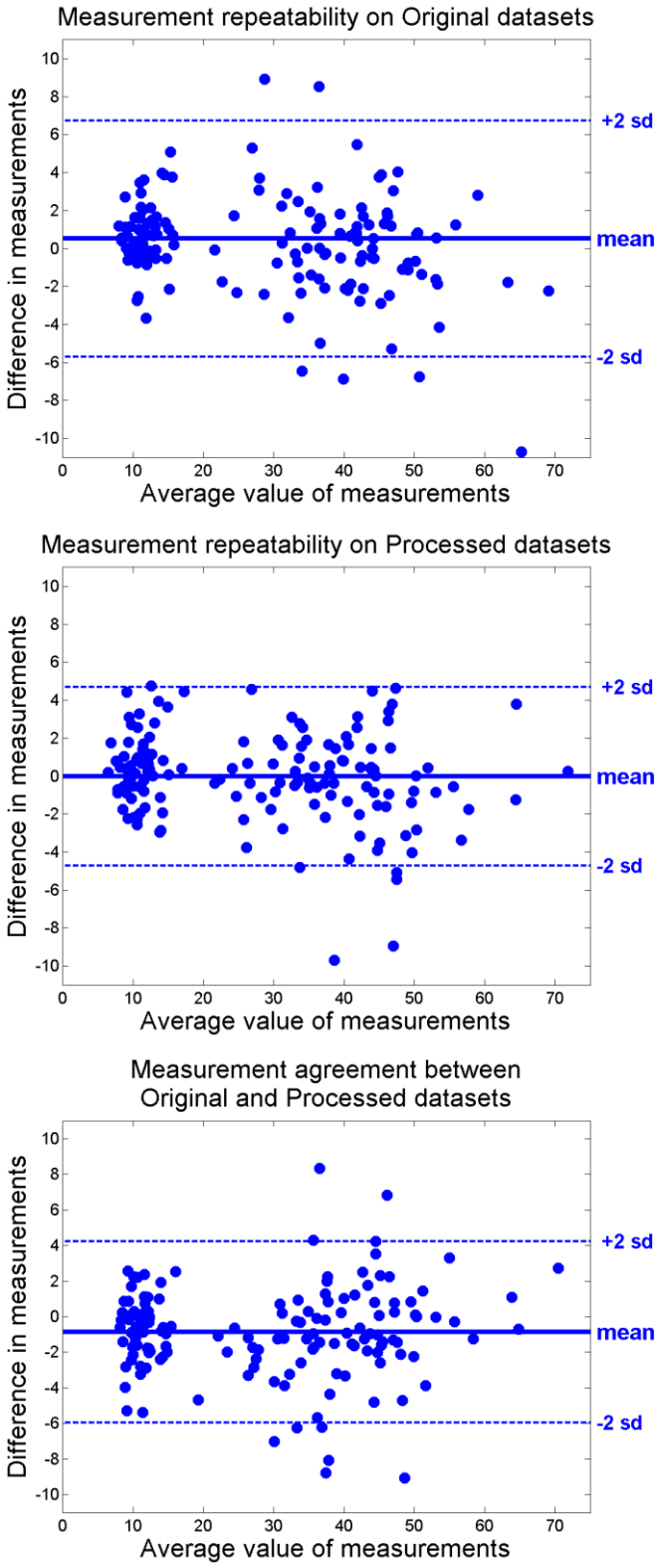


**Figure 6.21.** Bland Altman plots for the repeatability of measurements on original (top) and processed (middle) datasets as well as the agreement between measurements on original and processed datasets (bottom). Measurements performed by Echocardiographer 1. Bias (mean), as well as upper/lower limits of agreement are also included.

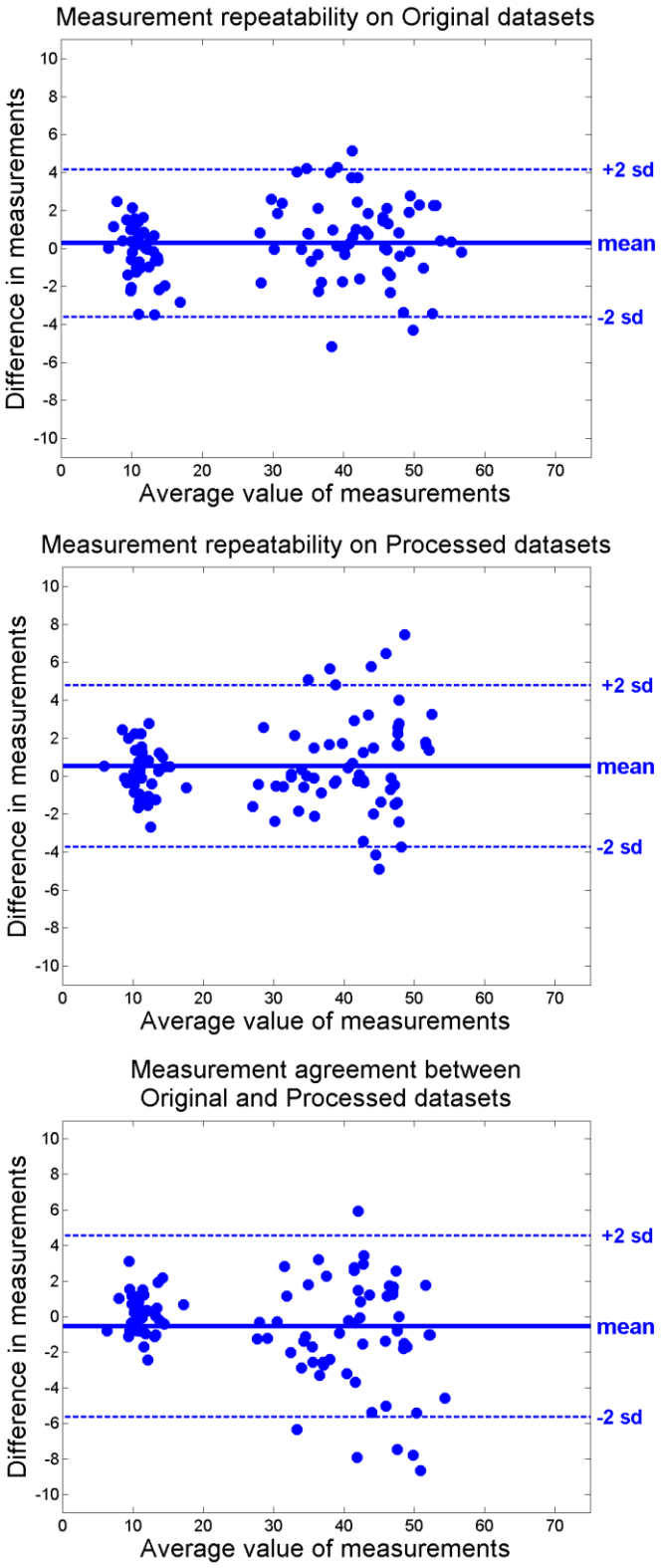


**Figure 6.22.** Bland Altman plots for the repeatability of measurements on original (top) and processed (middle) datasets as well as the agreement between measurements on original and processed datasets (bottom). Measurements performed by Echocardiographer 2. Bias (mean), as well as upper/lower limits of agreement are also included.

**Table 6.6.** Measurement repeatability and agreement coefficient for clinical measurements.

| Measure | Original | | | | Processed | | | | Agreement | | | |
|---|---|---|---|---|---|---|---|---|---|---|---|---|
| (mm) | Mean Diff | +2sd | -2sd | CR | Mean Diff | +2sd | -2sd | CR | Mean Diff | +2sd | - 2sd | CR |
| **Echocardiographer 1** | | | | | | | | | | | | |
| **IVSd** | 1.12 | 4.44 | -2.19 | 3.31 | 0.27 | 3.14 | -2.61 | 2.87 | -1.00 | 2.62 | -4.62 | 3.62 |
| **LVIDd** | -1.06 | 5.99 | -8.12 | 7.06 | -1.38 | 5.10 | -7.87 | -7.87 | -0.02 | 7.22 | -7.26 | 7.24 |
| **LVPWd** | 0.35 | 3.34 | -2.64 | 2.99 | 0.69 | 5.01 | -3.63 | 4.32 | -0.45 | 3.06 | -3.96 | 3.51 |
| **LADs** | -0.31 | 3.86 | -4.48 | 4.17 | -0.06 | 3.88 | -4.00 | 3.94 | -1.18 | 1.54 | -3.91 | 2.72 |
| **LVIDs** | 2.82 | 11.57 | -5.93 | 8.75 | 0.47 | 4.24 | -3.29 | 3.77 | -1.81 | 4.34 | 4.34 | 6.16 |
| **Combined** | **0.52** | **6.74** | **-5.70** | **6.22** | **-0.02** | **4.68** | **-4.73** | **4.71** | **-0.87** | **4.22** | **-5.96** | **5.09** |
| **Echocardiographer 2** | | | | | | | | | | | | |
| **IVSd** | -0.40 | 2.64 | -3.45 | 3.05 | -0.07 | 2.44 | -2.58 | 2.51 | -0.02 | 2.15 | -2.19 | 2.17 |
| **LVIDd** | 0.55 | 4.37 | -3.27 | 3.82 | -0.10 | 4.22 | -4.41 | 4.31 | -0.86 | 5.54 | -7.27 | 6.40 |
| **LVPWd** | 0.01 | 2.71 | -2.69 | 2.70 | 0.65 | 2.66 | -1.36 | 2.01 | 0.36 | 2.49 | -1.76 | 2.13 |
| **LADs** | 0.16 | 4.12 | -3.79 | 3.96 | 1.08 | 6.47 | -4.31 | 5.39 | -1.21 | 4.92 | -7.35 | 6.13 |
| **LVIDs** | 1.59 | 6.52 | -3.33 | 4.93 | 0.85 | 5.99 | -4.28 | 5.14 | -0.90 | 4.91 | -6.71 | 5.81 |
| **Combined** | **0.28** | **4.15** | **-3.60** | **3.88** | **0.52** | **4.77** | **-3.74** | **4.26** | **-0.55** | **4.54** | **-5.64** | **5.09** |

**Table 6.7.** Comparing the effect of individual and integrated methods on measurement repeatability.

| Measure (mm) | Original CR | Compounded CR | Contrast Enh. CR | Integrated CR |
|---|---|---|---|---|
| | | **Echocardiographer 1** | | |
| **IVSd** | 3.31 | 2.93 | 3.49 | 2.87 |
| **LVIDd** | 7.06 | 4.73 | 6.12 | -7.87 |
| **LVPWd** | 2.99 | 2.49 | 4.97 | 4.32 |
| **LADs** | 4.17 | 5.64 | 4.68 | 3.94 |
| **LVIDs** | 8.75 | 6.23 | 5.22 | 3.77 |
| **Combined** | **6.22** | **4.80** | **5.16** | **4.71** |
| | | **Echocardiographer 2** | | |
| **IVSd** | 3.05 | 2.18 | 2.37 | 2.51 |
| **LVIDd** | 3.82 | 2.16 | 4.41 | 4.31 |
| **LVPWd** | 2.70 | 1.40 | 2.02 | 2.01 |
| **LADs** | 3.96 | 4.04 | 6.52 | 5.39 |
| **LVIDs** | 4.93 | 3.15 | 5.75 | 5.14 |
| **Combined** | **3.88** | **3.39** | **4.78** | **4.26** |

**Table 6.8.** List of measurements omitted by Echocardiographer 1 on each individual dataset.

| | **IVSd** | | **LVIDd** | | **LVPWd** | | **LVIDs** | | **LADs** | |
|---|---|---|---|---|---|---|---|---|---|---|
| **Dataset** | **Or** | **Com** | **Or** | **Com** | **Or** | **Com** | **Or** | **Com** | **Or** | **Com** |
| **6** | o | o | o | o | o | o | o | N/A | o | o |
| **7** | o | o | o | o | N/A | o | o | o | o | o |
| **18** | o | o | o | o | o | o | N/A | o | o | o |
| **26** | o | o | o | o | o | o | o | o | N/A | o |
| **28** | o | N/A | o | o | o | o | o | N/A | o | o |
| **Total** | 0 | 1 | 0 | 0 | 1 | 0 | 1 | 2 | 1 | 0 |

**Table 6.9.** List of measurements omitted by Echocardiographer 2 on each individual dataset.

| | IVSd | | LVIDd | | LVPWd | | LVIDs | | LADs | |
|---|---|---|---|---|---|---|---|---|---|---|
| **Dataset** | **Or** | **Com** | **Or** | **Com** | **Or** | **Com** | **Or** | **Com** | **Or** | **Com** |
| **2** | o | o | o | o | o | o | o | N/A | o | o |
| **4** | o | o | o | o | o | o | N/A | N/A | o | o |
| **5** | N/A | o | N/A | o | N/A | o | N/A | N/A | o | o |
| **6** | N/A | N/A | N/A | N/A | N/A | N/A | N/A | N/A | N/A | N/A |
| **7** | o | o | o | o | o | o | o | N/A | o | o |
| **8** | o | o | N/A | o | o | o | o | o | o | o |
| **10** | o | o | o | o | o | o | N/A | N/A | o | o |
| **11** | N/A | N/A | N/A | N/A | N/A | N/A | N/A | o | o | o |
| **16** | o | o | o | o | o | N/A | N/A | o | o | o |
| **17** | o | o | o | o | o | o | o | o | o | o |
| **18** | N/A | o | N/A | o | N/A | o | N/A | o | o | o |
| **19** | N/A | o | N/A | o | N/A | o | N/A | N/A | o | o |
| **20** | N/A | o | N/A | N/A | N/A | o | N/A | N/A | o | o |
| **24** | N/A | N/A | N/A | N/A | N/A | N/A | N/A | N/A | o | o |
| **26** | o | o | o | o | o | o | N/A | o | N/A | N/A |
| **27** | N/A | N/A | N/A | N/A | N/A | N/A | N/A | o | N/A | N/A |
| **28** | N/A | N/A | N/A | N/A | N/A | N/A | N/A | N/A | o | o |
| **30** | N/A | N/A | N/A | N/A | N/A | N/A | o | N/A | o | o |
| **31** | o | o | o | o | o | o | o | o | N/A | o |
| **32** | o | o | o | o | o | o | N/A | o | o | o |
| **Total** | 10 | 6 | 11 | 6 | 10 | 7 | 14 | 11 | 4 | 3 |

## 6.6. Discussion

During the integrated image enhancement method introduced in this chapter, tissue/cavity contrast enhancement using ***DHBIM*** was applied to the original B-mode data prior to the selected spatial compounding approach. Inverting the process, applying spatial compounding prior to contrast enhancement, is expected to generate a very similar effect on cardiac ultrasound data yielding lower noise and higher contrast images. However, preliminary testing demonstrated that utilising ***DHBIM*** to suppress cavity noise and enhance tissue/cavity contrast prior to spatial compounding constitutes a more sensible option. More precisely, as illustrated in Chapters 3 and 4, in some datasets spatial compounding generated minor tissue cavity blurring. In some circumstances, low levels of blurring along with high levels of cavity noise had a limiting effect on the derivation of a representative tissue/cavity threshold. Furthermore, the effectiveness of compounding was heavily based on the accurate

spatio temporal alignment of the multi-cycle data. Image intensity based similarity measures, such as NXC, were used during the spatio temporal data registration. The accuracy of such similarity measures was limited by high noise and low contrast levels in cardiac ultrasound data. Utilising ***DHBIM*** to suppress cavity noise and enhance tissue/cavity contrast prior to spatial compounding can increase the accuracy of the spatio-temporal data registration, resulting in more effective image enhancement.

Chapters 3 and 4 introduced and evaluated two methods that succeeded in suppressing noise in cardiac ultrasound data by spatially compounding spatio-temporally aligned data acquired from a single acoustic window. Both techniques required the acquisition of multiple, partially decorrelated instances of a cardiac cycle. However, both techniques presented an individual data acquisition approach. For ***Temporal Compounding*** the acquisition was materialised over consecutive cardiac cycles. On the other hand, during ***3D-to-2D Compounding*** data could be acquired concurrently as a series of adjacent instances (along the elevation axis) of a cardiac cycle using a 4D matrix transducer. After data acquisition, the processing and analysis steps required, as well as the expected output, were very similar making both compounding approaches interchangeable depending on the available acquisition resources.

Chapter 4 provided a thorough feasibility study on ***3D-to-2D Compounding*** utilising a custom made, mechanically displaced, 2D phased array cardiac probe for the acquisition of adjacent (along the elevation plane) cardiac slices. Due to the nature of the mechanically controlled acquisition system, the method could not be utilised in a clinical setup and could therefore only be evaluated using phantoms as well as healthy volunteers. When compared to the 32 patient datasets utilised in the development and evaluation of ***Temporal Compounding*** and ***DHBIM***, the number and diversity of the available 3D datasets (25 datasets from 5 relatively young and healthy volunteers) can be considered as limited. As a result, employing ***Temporal Compounding*** enabled the utilisation of an ample number of patient datasets with a diverse range of image qualities and diagnostic values for the development and the quantitative assessment of the integrated data enhancement method introduced in this chapter. Furthermore, using a consistent set of images enabled the direct comparison of the results obtained using the integrated approach against the corresponding results obtained using spatial compounding and ***DHBIM*** independently. Given the effectiveness of the integrated image enhancement method and the availability of data acquisition resources, ***Temporal Compounding*** can be easily and effectively replaced by

***3D-to-2D Compounding***, as well as any future compounding method utilising data acquired from a single acoustic window.

### 6.6.1. Effect on tissue SNR, cavity SNR, tissue/cavity contrast and SDNR

Figure 6.4 illustrates the effect of the integrated image enhancement method introduced in this chapter on the tissue and cavity SNR for an increasing number of compounded cardiac cycles. Similar to ***Temporal Compounding***, SNR increased with the increase in number of cardiac cycles utilised during compounding. However, the overall effect varied considerably between different datasets ranging from negligible to very substantial (more than 100%). Variations in the initial SNR amongst the contrast enhanced datasets can be attributed to many reasons, such as different levels of static and dynamic noise, shadowing and non-optimal acquisition set-up. Furthermore, the different level of contrast enhancement obtained using the ***DHBIM*** algorithm prior to spatial compounding can affect the initial SNR value of a dataset. On the other hand, a wide range of artifacts can also appear in a real cardiac ultrasound scan (Chapters 1 and 2). Such artifacts, along with variations on the ROI location and amongst the movement range during data acquisition, attribute to the fluctuation on SNR increase achieved on different datasets. Nevertheless, the mean SNR profile provided a fair representation of the effect of the integrated image enhancement method on cardiac tissue and cavity.

Figure 6.5 enables the direct comparison of the mean tissue and cavity SNR profiles. Comparing the mean tissue and cavity SNR profiles, it is apparent that cavity SNRs demonstrated a higher initial value as well as increase ranges. The higher SNR ranges were due to the absence of speckle in cardiac cavities. Speckle constitutes a major contributor in the lower initial SNR values observed in cardiac tissue. Furthermore, due to the nature of speckle, a higher level of decorrelation between the compounded frames was required for its suppression when compared to the noise present in cardiac cavities. Similar profiles for each of the 32 datasets were derived in order to assess the effect of the integrated image enhancement method on the tissue/cavity detectability index (SDNR) and contrast. In a similar manner to the SNR profiles, the mean SNDR and contrast profiles provided fair representations of the effect of the integrated image enhancement method on the distinction between cardiac tissue and cavity. Figure 6.6 illustrates the corresponding mean SDNR profile. Contrast remained largely unaffected by the number of cardiac cycles used during spatial compounding and the corresponding profile was therefore omitted. By investigating the profile curvatures in Figures 6.4 to 6.6 as well as by comparing them with the corresponding SNR and SDNR profiles obtained by using just ***Temporal Compounding***

(Figures 6.7 and 6.8), it is apparent that all profiles followed very similar patterns. More precisely, all mean SNR and SDNR profiles can be divided into three segments. In the first segment, observed during the compounding of the first 4-5 cardiac cycles, the SNR and SDNR increase introduced was very large. In the second segment, observed during the compounding of up to 12-13 cardiac cycles, the SNR and SDNR increase were more moderate but still considerable. In the final segment, for compounding of more than 13 cardiac cycles, the SNR and SDNR increase was further reduced to very modest levels. Similar to ***Temporal Compounding,*** after a thorough examination on the findings for all 32 datasets, it is believed that 12 cardiac cycles can introduce a sufficient noise suppression and tissue/cavity detectability increase to the processed data while maintaining the acquisition and processing requirements to relatively low levels.

Tables 6.1 to 6.4 demonstrate the quantitative effect of the integrated image enhancement method using 12 cardiac cycles on tissue SNR, cavity SNR, tissue/cavity Contrast and detectability index SDNR. While the effect of the integrated image enhancement method varied amongst the 32 datasets, the overall effect on each quantitative measure followed a similar trend for all datasets with the mean value providing a fair representation of it. Table 6.5 provides a direct comparison on the mean effect of the individual and integrated image enhancement methods on all 4 image quality metrics. From the results illustrated in Tables 6.1 to 6.5 it is apparent that the integrated image enhancement was the only method improving all 4 image quality metrics. Tissue SNR was moderately increased by 14.1%. While considerably lower than the 87.1% increase obtained using ***Temporal Compounding*** it still provided a substantial improvement to the 37.0% SNR decrease as a result of speckle enhancement during ***DHBIM***. Cavity SNR was increased by a respectable mean of 78.2%. Similar to tissue SNR, cavity SNR increase was lower when compared to the corresponding increase obtained using ***Temporal Compounding***. However, the nature of the lower increase should not be confused with higher levels of cavity noise. ***DHBIM*** had already suppressed the cavity noise intensity levels by more than 50%. More precisely, the lower cavity SNR decrease is attributed to sparse cavity pixels with high levels of noise identified as cardiac tissue and therefore not suppressed during ***DHBIM***. Such pixels can considerably increase the SD within a ROI and as a result the corresponding cavity SNR. Tissue/cavity contrast was largely unaffected (marginally decreased) by ***Temporal Compounding***. Therefore, the respectable 72.1% contrast increase introduced by the integrated image enhancement method provided a substantial improvement to the effect introduced by ***Temporal Compounding***. It also lay at almost identical levels to the corresponding value obtained by ***DHBIM***. Finally, the tissue/cavity detectability index SDNR was extensively increased by a mean of 401.4%

ranging from 107.9% to more than 800%. The SDNR increase was impressive when compared to the already considerable increases of 128.6% and 120.9% introduced by ***Temporal Compounding*** and ***DHBIM*** respectively. Since SDNR depends heavily both on tissue/cavity contrast as well as cavity noise, a substantial increase was always anticipated by integrating two methods one of which enhances contrast while the second suppresses cavity noise considerably.

### 6.6.2. Visual effect on cardiac ultrasound data

Figures 6.9 to 6.20 display six examples of original and processed ED frames. Each example illustrates the effect of the individual ***Temporal Compounding*** and ***DHBIM*** methods as well as the proposed integrated image enhancement method on the corresponding multi-cycle dataset. These figures provide characteristic examples of the effects of ***DHBIM*** on clinical data over a range of image qualities and diagnostic values. Datasets are presented in increasing data quality ranging from very low to high (3 low, 2 average and 1 high).

Figures 6.9 and 6.10 display four ED frames corresponding to a dataset with very low image quality and diagnostic value. Figure 6.9 displays the original unprocessed frame as well as the corresponding processed frame obtained using ***Temporal Compounding***. Figure 6.10 displays the contrast enhanced frame using ***DHBIM*** along with the corresponding frame obtained using the integrated image enhancement method introduced in this chapter. The original dataset suffered from very high levels of noise and very limited contrast between cardiac cavities and tissue. The low data quality limited the visual delineation of the majority of cardiac structures. Furthermore, the high noise and low contrast levels limited, and very possibly restricted the suitability of the displayed dataset for most post-processing algorithms such as image segmentation and image registration. ***Temporal Compounding*** substantially suppressed the noise level in cavities as well as the speckle in tissue structures. While the quality of the dataset remained low, mostly due to the low contrast between tissue and cavity, structures such as the RV cavity and the IVS were marginally enhanced making them easier to detect and outline. ***DHBIM*** generated a fairly representative map of tissue structures within the dataset, suppressed cavity noise and enhanced the contrast and detectability between cardiac tissue and cavity considerably. Regardless of the very low quality of the original dataset, ***DHBIM*** substantially enhanced the available information both with respect to image quality (beneficial for data post-processing) and diagnostic value. Cardiac structures such as the RV, LV, IVS, PW and RA were distinguishable in the processed dataset and could be potentially measured accurately and robustly in a clinical setup. However, the speckle enhancement on cardiac tissue could possibly limit the accurate

and robust application of image post-processing methods. The integrated image enhancement method addressed the limitations observed in each individual method while preserving their corresponding advantages. The processed dataset demonstrated considerable improvement in image quality as well as in its diagnostic value. Noise in cardiac cavities was substantially suppressed and all cardiac structures previously masked by high levels of noise and low contrast could be easily outlined, more than in either method independently. Furthermore, speckle and noise in cardiac tissue was suppressed, potentially allowing for a more accurate and robust registration and segmentation of the imaged structure.

Figures 6.11 and 6.12 display four ED frames corresponding to another dataset with low image quality and diagnostic value. Similar to the previous example, the original image suffered from high noise levels making it hard to outline structures such as the IVS, LA and the LVPW. However, the contrast between tissue and cavity was in some cases moderately improved furthering the visual delineation of some structures. As a result, the effect of ***Temporal Compounding*** was more noticeable. More precisely, along with the apparent noise and speckle reduction, cardiac tissue structures, such as the LV cavity, IVS, LV and the LVPW were moderately enhanced making them easier to detect and outline. Nevertheless, the tissue/cavity contrast was still very limited. ***DHBIM*** compensated for low tissue cavity contrast by suppressing cavity noise and enhancing the cardiac tissue dynamic range. As a result, cardiac structures such as the RV, LV, IVS, PW, RA and the Mitral Valve were clearly distinguishable. However, like in the previous example, the speckle enhancement on cardiac tissue could possibly limit the accurate and robust application of image post-processing methods. The integrated image enhancement method not only suppressed cavity noise while enhancing tissue/cavity contrast but it also generated relatively homogeneous and clearly distinguishable cardiac tissue structures. Noise levels were minimal and cardiac structures previously masked by high levels of noise and low contrast could be easily outlined. As a result, by addressing the limitations observed in each individual method while preserving their corresponding advantages, the integrated method enhanced the post-processing and diagnostic value of the dataset from low to a high average.

Figures 6.13 and 6.14 display four ED frames corresponding to the last of the three datasets with low image quality and diagnostic value. The original dataset suffered from high levels of noise which in combination with shadowing masked clinically vital cardiac structures such as segments of the IVS, the PW and the lower end of the LA. As expected, ***Temporal Compounding*** substantially suppressed the noise level in cavities as well as the speckle in tissue structures. However, ***Temporal Compounding*** also compensated for some of the

masked structures, substantially enabling the delineation of the IVS as well as RV, LV and LA cavities. ***DHBIM*** suppressed cavity noise and enhanced the contrast and detectability between cardiac tissue and cavity considerably. However, regardless of the substantial quality improvement, ***DHBIM*** did not compensate for tissue structures masked by high levels of noise and shadowing. Instead, it treated them as cardiac cavity suppressing their corresponding information. The integrated image enhancement method, by benefiting from the advantages of the individual methods, considerably enhanced the post-processing and diagnostic value of the example dataset. The ***DHBIM*** component suppressed the cavity noise and enhanced the tissue/cavity contrast along with the delineation of cardiac structures such as the RV, LA and the Mitral Valve. Furthermore, the contrast enhanced dataset facilitated a more accurate ***Temporal Compounding*** resulting in suppressed blurring along tissue/cavity boundaries in structures such as the IVS, PW and LA. Finally, the ***Temporal Compounding*** component compensated for data masked out by high levels of noise and shadowing and partially filtered out by ***DHBIM***, resulting in relatively homogeneous and clearly distinguishable cardiac tissue structures (IVS and PW and LA).

Figures 6.15 and 6.16 display four ED frames corresponding to the first example with average image quality and diagnostic value. While most cardiac structures were distinguishable, high noise levels masked segments of the IVS and made the delineation of structures such as the LVPW and the LA very challenging. Similar to the previous examples, ***Temporal Compounding*** reduced the speckle/noise level throughout the image and moderately enhanced the structures such as the IVS and the PW. While the enhanced, previously masked out, sections of the IVS were not fully restored, they enabled a moderately improved delineation of the structure. On the other hand, small blurring was introduced around the Mitral Valve and the LA tissue/cavity boundaries. ***DHBIM*** generated a very representative map of the tissue structures imaged within the dataset, suppressed cavity noise and made cardiac structures such as the RV, PW, RA and the Mitral Valve clearly distinguishable. Even masked segments of the IVS were enhanced, and while not fully restored, they enabled a moderately improved delineation of the structure. As expected, the integrated method produced an image where all cardiac structures were clearly distinguishable with very low noise and ample tissue/cavity contrast levels.

Figures 6.17 to 6.20 provide examples of datasets with average and high image quality and diagnostic value respectively. While, the original data in Figure 6.17 demonstrated a moderately higher level of cavity noise and lower level of tissue/cavity contrast with respect to the original data in Figure 6.19, in both datasets cardiac structures were clearly

distinguishable. Nevertheless, ***Temporal Compounding*** considerably suppressed tissue speckle as well as the low levels of cavity noise. The effect was predominantly noticeable around the IVS and RV cavity. Similarly to the previous example modest blurring was introduced around the Mitral Valve. Furthermore, ***DHBIM*** suppressed cavity noise to a minimal level. The noise suppression was more apparent inside the RV cavity, especially at its top half. ***DHBIM*** increased the tissue/cavity contrast as well as the dynamic range within cardiac tissue, enhancing the corresponding speckle information. The integrated image enhancement method generated data of very high image quality and diagnostic value with negligible cavity noise levels, relatively homogeneous tissue structures, as well as high tissue/cavity contrast and detectability levels. As a result, all cardiac structures were clearly distinguishable. Processing was clearly not required in order to enhance the imaged data on both datasets prior to clinical measurements. Nevertheless, the integrated image enhancement method is expected to (i) further improve the accuracy and robustness (repeatability) of clinical measurements performed on the processed datasets, and (ii) increase their post-processing potential, which is limited by the presence of cavity noise and low tissue/cavity contrast.

Overall, after a thorough examination of its effect on all 32 patient datasets, the integrated image enhancement method introduced in this chapter benefited from the advantages while compensated for the limitations of each individual method. In the first instance, the ***DHBIM*** component suppressed cavity noise noticeably while increasing the intensity dynamic range on cardiac tissue. Furthermore, the contrast and delectability between cardiac tissue and cavity were considerably enhanced making cardiac structures clearly distinguishable. The noise suppression was notable in the RV cavity. By applying the algorithm to 4 non-overlapping sectors, mostly representing different cardiac structures, the variations on the mean tissue intensity and cavity noise level with increasing depth were also reduced. On the other hand, the ***Temporal Compounding*** component significantly reduced tissue speckle as well as static and dynamic noise in cardiac tissue and cavities. Furthermore, compensating for ***DHBIM***, averaging a number of partially decorrelated images enhanced cardiac structures whose boundaries were difficult to delineate due to high levels of noise and shadowing. However, it sometimes introduced modest tissue/cavity boundary blurring. Suppressing cavity noise and enhancing tissue/cavity contrast (***DHBIM***) prior to spatio-temporal data alignment resulted in a moderate reduction to the boundary blurring introduced during spatial compounding. Nevertheless, low blurring levels were still observed around fast moving structures, such as valves, with some blurring identified along cavity

walls. It is believed that part of the blurring was due to quantification errors and minor inaccuracies in the spatio-temporal alignment.

### 6.6.3. Effect on clinical measurements performed on patient data

The results presented in Figures 6.21 and 6.22 along with Tables 6.6 to 6.9 enable the evaluation of the effect of the integrated image enhancement method introduced in this chapter on clinical measurements performed during routine cardiac ultrasound examinations. Each point cluster (representing different types of clinical measurements) as well as the corresponding limits of agreement (±2SD) lay in a specific range which appeared to be largely unaffected by whether measurements were performed on the original or the contrast enhanced datasets. Furthermore, the mean measurement difference in each plot lay very close to zero, indicating that no significant or systematic bias was observed within each measurement method or between the two measurement methods. Finally, no major outliers were identified in the repeatability and agreement plots. Consequently, the results indicate a strong potential for the original and processed data to be interchangeable when performing clinical cardiac ultrasound measurements.

Tables 6.6 to 6.9 allow a more thorough investigation on the effect of the integrated method on routine clinical cardiac measurements. The repeatability and agreement coefficients of a clinical measurement depended both on the type of clinical measurement performed as well as the echocardiographer making the measurement. For both echocardiographers the overall level of agreement between clinical measurements performed on original and the contrast enhanced data lay in levels very similar to the corresponding repeatability coefficients with no substantial or systematic bias being observed. Like in all previous experiments, Echocardiographer 1 displayed a confident and sometimes adventurous approach towards making clinical measurements. More precisely, the repeatability coefficient of the measurements on processed data increased by 13%, 8%, 6% and 57% for the IVSd, LVIDd, LADs and LVIDs measurements respectively (Table 6.6). On the other hand, the repeatability coefficient of measurements performed on processed datasets demonstrated a 44% drop for LVPWd (Table 6.6). Nevertheless, when considering all clinical measurements, a substantial overall 24% improvement on the repeatability coefficient was introduced to measurements performed on processed data compared to those performed on the original unprocessed data. This constituted the higher repeatability improvement, building upon the improvement achieved by each of the individual data enhancement methods (Table 6.7). Similar to all previous experiments, Echocardiographer 2 adopted a more thorough and conservative approach towards making clinical measurements and

indicated reluctance on the diagnostic quality of the processed datasets. Such a measurement approach was apparent by the higher repeatability and agreement levels displayed on the clinical measurements when compared with those of Echocardiographer 1. Such higher repeatability and agreement levels in the original data reduced the scope for improvement by using the processed data. Nevertheless, the improved repeatability level for Echocardiographer 1, when using the integrated image enhanced method, lay in comparable levels to the corresponding repeatability for Echocardiographer 2 (Table 6.6). Echocardiographer 2's reluctance towards the processed datasets had an effect on the repeatability level achieved on the clinical measurements demonstrating a modest overall drop in the repeatability coefficient of 10% when compared to those performed on the original unprocessed data (Table 6.6). The observed repeatability level constituted a considerable improvement from the repeatability achieved when using ***DHBIM*** (Table 6.7). This improvement is mostly attributed to compensating for the limitation of ***DHBIM*** in enhancing heavily corrupted cardiac tissue structures by integrating it with ***Temporal Compounding***, a method known to compensate for such masked structures. Furthermore, as discussed in Chapter 5, the modest repeatability drop when compared to the original data is attributed mainly to the high level of familiarity of the echocardiographer with conventional, unprocessed cardiac ultrasound data. Both echocardiographers have been working for many years with challenging cardiac ultrasound data and have developed procedures utilising subtle features that enable them to perform the required clinical measurements. Data processing may modify such features, preventing the echocardiographers from making some challenging clinical measurements on the processed datasets that were presented to them for the first time during this study.

Tables 6.8 and 6.9 indicate whether a clinical measurement was performed or omitted by each echocardiographer on the original and processed datasets. Both echocardiographers chose to abstain from making some clinical measurements. The more conservative approach adopted by Echocardiographer 2 on making clinical measurements when compared to Echocardiographer 2 was again apparent. Echocardiographer 1 chose to attempt the majority of the clinical measurements while Echocardiographer 2 omitted some, taking fewer risks on challenging datasets. Avoiding clinical measurements on challenging datasets reduced the scope for improvement in the repeatability and agreement levels by using the processed data. Nevertheless, a considerable percentage (83%) of the measurements omitted by Echocardiographer 1 was also omitted by Echocardiographer 2. Comparing the omitted measurements with the corresponding ones for compounded and contrast enhanced datasets (Tables 3.12, 3.13 and Tables 5.13, 5.14) it became apparent that there was a high level of

correlation. Similar to ***Temporal Compounding*** and ***DHBIM***, abstaining from making clinical measurements is mostly attributed to high levels of noise and shadowing making the delineation of the IVS and PW structures very challenging in some datasets. Visual inspection of the omitted datasets demonstrated such high levels of corruption on the measured cardiac structures either by high noise or shadowing levels. Overall, utilising the integrated image enhancement method, the number of omitted measurements was lower than the corresponding number encountered utilising ***DHBIM***, and comparable to the levels achieved using ***Temporal Compounding***. Especially for Echocardiographer 2, there was a noticeable drop (approximately 33%) in the number of omitted measurements when utilising processed datasets. This drop is attributed to the substantial overall image quality enhancement introduced by integrating ***Temporal Compounding*** with the ***DHBIM*** algorithm (Sections 6.5.1 and 6.5.2).

The results on the effect of the integrated image enhancement method on routine clinical measurements were very promising. As expected, the integrated method improved on the repeatability level achieved utilising ***DHBIM*** in a way similar to the way ***Temporal Compounding*** improved on measurements performed on the original unprocessed data. For Echocardiographer 1, this improvement translates to achieving the highest level of repeatability when compared to the original data as well as the two individual processing methods. The improved repeatability for Echocardiographer 1 lay on a comparable level to the corresponding repeatability for Echocardiographer 2, substantially reducing the inter-subject variability observed in previous chapters. On the other hand, for Echocardiographer 2, improving on ***DHBIM*** translates to a repeatability level comparable to the one achieved utilising the original data (demonstrating a very modest drop). Such an improvement is a consequence of compensating for the limitation of ***DHBIM*** to enhance heavily corrupted cardiac structures by integrating it with ***Temporal Compounding***. As discussed in Chapter 5, it is expected that by increasing familiarity Echocardiographer 2 may adjust existing procedures employed to make measurements on challenging datasets for use with the contrast enhanced datasets. A higher confidence level in making clinical measurements on processed datasets can potentially increase the repeatability coefficient in a manner similar to Echocardiographer 1. Therefore, the integrated image enhancement approach demonstrates great potential for the further improvement in the repeatability of routine clinical measurements on cardiac ultrasound data. Utilising the benefits introduced by both individual approaches, the integrated method can possibly act as the most beneficial alternative to conventional B-mode imaging for clinical measurements.

## 6.7. Conclusions

In this chapter a method for integrating ***DHBIM*** with spatial compounding was introduced and quantitatively evaluated using a number of patient cardiac ultrasound data. Linear combination of ***DHBIM*** followed by ***Temporal Compounding*** was utilised benefiting from their advantages while compensating for their individual limitations. Optimal acquisition and processing parameters identified in the corresponding chapters were used since each individual method can be applied independently on multi-cycle cardiac ultrasound data. Quantitative assessment verified the choice of optimal parameters such as the number of cardiac cycles and number of non-overlapped sub-sectors utilised during the post-processing of the multi-cycle datasets. The integrated method considerably enhanced the contrast and detectability between tissue and cavity, while suppressing the cavity noise as well as tissue speckle. Furthermore, the integrated method partially compensated for the limitations observed in (i) ***Temporal Compounding*** by enhancing tissue/cavity contrast and therefore reducing tissue/cavity blurring due to averaging and (ii) ***DHDIM*** by averaging a number of decorrelated instances of a masked structure and therefore enhancing its delineation. Therefore, the integrated method is believed to be the most effective in enhancing the image quality of the cardiac ultrasound data when compared to the individual methods described earlier. Due to its simple nature and effectiveness, the integrated image enhancement method can act as a first step to post-processing techniques, such as segmentation and registration.

Having verified the impact of the integrated image enhancement method on cardiac ultrasound image quality, its effect on diagnostic value was investigated by assessing the impact on repeatability levels of routine clinical measurements performed by two experienced echocardiographers. Similar to all previous methods, the effect of the integrated method varied depending on the echocardiographer and the clinical measurement performed. For both echocardiographers, by utilising the integrated image enhancement method the number of omitted measurements due to heavily corrupted datasets was considerably decreased. Furthermore, the repeatability level for Echocardiographer 1 improved substantially to a greater degree than achieved by each individual method. The improved repeatability lay on a very comparable level with the more thorough Echocardiographer 2, indicating the potential to reduce the corresponding Echocardiographer dependability. The performance of Echocardiographer 2 was also improved from the corresponding repeatability level achieved utilising ***DHBIM***. The improved repeatability was of a level comparable to the corresponding one achieved using the original unprocessed datasets. As mentioned in Chapter 5, taking into consideration that both echocardiographers were

presented for first time with the processed data, it is strongly believed that there is further scope for improvement as the familiarity of the echocardiographers with the processed data increases. Consequently, the integrated image enhancement method has a strong potential to provide a valuable alternative to B-mode data for improving image quality prior to data post-processing as well as diagnostic value prior to clinical measurements.

# Chapter 7

# Conclusions

This chapter summarises the principal contributions of the work introduced and evaluated in this thesis. The benefits and general limitations encountered in each individual data enhancement method as well as the integrated method are identified and discussed. Finally, possible directions for future research are presented.

## 7.1. Contributions

Chapters 3 and 4 analyse and evaluate two image enhancement methods that utilise spatial averaging of partially decorrelated data acquired through a single acoustic window. Chapter 3 extends the notion of ***Temporal Compounding***, a method for enhancing cardiac ultrasound data by averaging partially decorrelated instances of the imaged structure acquired over a number of consecutive cardiac cycles. Reliable spatial and temporal alignment of the corresponding frames in consecutive cardiac cycles is vital for effective ***Temporal Compounding***. Insufficient temporal alignment will induce the averaging of frames corresponding to different stages of the cardiac cycle resulting in severe blurring of the imaged structure. Chapter 3 introduces a novel, efficient technique for the accurate and robust temporal alignment of consecutive cardiac cycles with variable temporal characteristics. Utilising a 7 control point interpolating B-Spline, the suggested non-linear temporal alignment approach can compensate for the independent temporal variations within the 7 phases of consecutive cardiac cycles. Similarly, spatial registration is required prior to averaging in order to compensate for respiration motions during the multi-cycle data acquisition. A 2D rigid registration compensates for most spatial misalignments amongst the temporally aligned frames. Chapter 4 introduces ***3D-to-2D compounding***, extending the notion of spatial compounding of cardiac ultrasound data acquired through a single acoustic window presented in Chapter 3. ***3D-to-2D Compounding*** presents a novel image enhancement method by acquiring and compounding spatially adjacent (along the elevation plane), partially decorrelated, 2D slices of the heart. The 2D slices are extracted as a thin

angular sub-sector of a volumetric pyramid scan. Chapter 4 provides a thorough feasibility study on ***3D-to-2D Compounding*** utilising a custom-built human left ventricle phantom along with volunteer data acquired in a controlled laboratory environment. ***3D-to-2D Compounding*** presents an alternative to ***Temporal Compounding*** capable of reducing acquisition and processing requirements.

Both spatial compounding methods analysed in Chapters 3 and 4 enhance cardiac ultrasound data by suppressing cavity noise and tissue speckle (increase SNR). Chapter 5 introduces ***Dynamic Histogram Based Intensity Mapping* (*DHBIM*)**, a novel and fully automated method for suppressing noise in cardiac cavities while enhancing information in cardiac tissue structures. During ***DHBIM*** the temporal variations within the individual frame histograms over consecutive multi-frame cardiac cycles are analysed in order to derive any underutilised intensity values as well as the tissue/cavity intensity threshold. Thereupon, piecewise intensity mapping (contrast stretching) applied on each frame in the B-mode frame sequence (i) increases the cardiac tissue intensity dynamic range and (ii) suppresses cavity noise information. Chapter 6 introduces a data acquisition and analysis protocol for integrating the dynamic intensity mapping along with spatial compounding methods described in earlier chapters. Linear integration of ***DHBIM*** and ***Temporal Compounding*** is implemented and quantitatively assessed. By taking advantage of the benefits and compensating for the limitations of each individual method, the integrated method suppresses cavity noise and tissue speckle while enhancing tissue/cavity contrast as well as the delineation of cardiac tissue boundaries even when heavily corrupted by a range of cardiac ultrasound artifacts. ***3D-to-2D Compounding*** can replace ***Temporal Compounding*** during the integrated method generating similar results on cardiac ultrasound data.

Finally, throughout Chapters 3 to 6 a novel protocol for the quantitative assessment of the effect of each data enhancement method on image quality and diagnostic value is employed. Such a protocol enables the quantitative evaluation of each method as well as the comparison between individual methods using cardiac data from 32 patients. Image quality is assessed using a range of quantitative measures such as tissue Signal-to-Noise Ratio (SNR), cavity SNR, tissue/cavity Contrast and Signal Difference to Noise Ratio (SDNR) also known as detectability index. Diagnostic value is assessed through variations in the repeatability level of routine clinical measurements performed on patient cardiac ultrasound scans by two experienced echocardiographers. Commonly used clinical measures such as IVS and PW wall thickness, as well as LVID and LAD cavity diameter are employed for assessing diagnostic value. Taking into consideration that the processed data are presented for the first

time to both echocardiographers, measurement repeatability is believed to provide a less biased metric on diagnostic value when compared to qualitative assessment methods using data quality criteria.

## 7.2. Conclusions

The concept behind the work presented in this thesis is to enhance cardiac ultrasound data utilising information acquired during a clinical examination, which until now has been predominantly disregarded. The differentiation to past data enhancement studies is that most tend to filter out information based on some static or adaptive selection criteria. All methods introduced in this thesis utilise multiple partially decorrelated instances of a cardiac cycle in order to acquire information required to suppress or enhance certain image features. No filtering out of information is performed at any stage of the processing. More precisely, ***Temporal Compounding*** presented in Chapter 3 enhances cardiac ultrasound data by averaging partially decorrelated instances of the imaged structure over a number of consecutive cardiac cycles. Furthermore, ***3D-to-2D Compounding*** introduced in Chapter 4 extends the notion of spatial compounding of cardiac ultrasound data. ***3D-to-2D Compounding*** presents a novel image enhancement method by acquiring and compounding spatially adjacent (along the elevation plane), partially decorrelated, 2D slices of the heart extracted as a thin angular sub-sector from within a volumetric pyramid scan. Data enhancement for both compounding approaches includes suppressing tissue speckle and cavity noise, substantially increasing their corresponding SNR as well as the tissue/cavity detectability index (SDNR). Furthermore, by averaging decorrelated instances of the same structure, spatial compounding can enhance tissue structures that are masked out by heavy levels of noise and shadowing. Due to their effectiveness and simple nature, both ***Temporal Compounding*** and ***3D-to-2D Compounding*** can act as a first step to post-processing techniques whose effectiveness is limited and sometimes restricted by low image quality (SNR and SDNR) in cardiac ultrasound data.

The ***DHBIM*** introduced in Chapter 5 investigates the temporal variations within image histograms of consecutive frames in order to (i) identify any unutilised/underutilised intensity levels and (ii) derive the tissue/cavity intensity threshold within the processed frame sequence. Piecewise intensity mapping is then used in order to enhance cardiac ultrasound data. Data enhancement includes cavity noise suppression, enhancement of tissue speckle information as well as a considerable increase in tissue/cavity contrast and detectability index. While speckle enhancement may limit the accuracy of data registration,

it can be advantageous for the application of other commonly employed cardiac ultrasound methods such as *Speckle Tracking*. Furthermore, by generating a fairly representative outline of cardiac tissue structures, ***DHBIM*** can act as a pre-processing step to image segmentation whose effectiveness is limited by low contrast in cardiac ultrasound data. Finally, Chapter 6 introduces a method for the integration of ***DHBIM*** with spatial compounding. Linear combination of ***DHBIM*** followed by ***Temporal Compounding*** is utilised benefiting from their advantages while compensating for their individual limitations. Optimal acquisition and processing parameters identified in the corresponding chapters are also utilised since each individual method can be applied independently on multi-cycle cardiac ultrasound data. The integrated method considerably enhances the contrast and detectability between tissue and cavity while suppressing the cavity noise as well as tissue speckle. Furthermore, the integrated method partially compensates for the limitations observed in (i) ***Temporal Compounding***, by enhancing tissue/cavity contrast and therefore reducing tissue/cavity blurring due to averaging and (ii) ***DHBIM***, by averaging a number of decorrelated instances of a masked structure and therefore enhancing its delineation. Thus, the integrated method is believed to be the most effective in enhancing the image quality of the cardiac ultrasound data when compared to the individual methods described earlier in the thesis. Due to its simple nature and effectiveness, the integrated image enhancement method can act as a first step to further image post-processing techniques.

Having verified the impact of each method on cardiac ultrasound image quality, their effect on diagnostic value is investigated by assessing the impact on the repeatability levels for routine clinical measurements performed by two experienced echocardiographers. The effect of each method varies depending on the echocardiographer and the clinical measurement performed. Nevertheless, all methods demonstrate strong potential in replacing unprocessed data during clinical measurements, improving the corresponding repeatability level and reducing the number of omitted measurements due to heavy data corruption.

## 7.3. General limitations

While all methods described in this thesis manage to meet the initial aims of enhancing cardiac ultrasound data, there are still a number of limitations identified throughout the course of this study. ***Temporal Compounding*** along with ***3D-to-2D Compounding*** considerably suppresses cavity noise and tissue speckle, enhancing the delineation of cardiac structure even when heavily corrupted by artifacts. Nevertheless, they are found to have no noteworthy effect on the limited tissue/cavity contrast experienced in cardiac ultrasound

data. Moreover, minor spatio-temporal misalignments combined with high noise levels may result in modest tissue/cavity boundary blurring. On the other hand, ***DHBIM*** suppresses cavity noise while enhancing tissue speckle information along with tissue/cavity contrast. However, when high levels of noise and shadowing completely mask out certain tissue structures, ***DHBIM*** may mis-classify the missing structures as cardiac cavity, suppressing the intensity of their corresponding pixels. Nonetheless, ***DHBIM*** has not been observed to suppress vital clinical information from the original datasets. Furthermore, integrating ***DHBIM*** with ***Temporal Compounding*** compensates in the most part for all limitations identified for each individual method.

Throughout the thesis it has been assumed that multiple, partially decorrelated instances of a cardiac cycle can be acquired in a clinical setup, either consecutively (temporally) or adjacently (spatially). During ***Temporal Compounding***, the acquisition of 10 to 20 cardiac cycles is required for the effective suppression of tissue speckle and cavity noise. During the acquisition process, the operator and patient movements should remain minimal in order to avoid any substantial displacement of the scanning plane. While not very likely, there may be cases where the acquisition of sufficient data is not feasible. In such cases, compounding data acquired over less cardiac cycles may provide decreased yet adequate data enhancement. If available, a 4D matrix probe can also be utilised to acquire all data required for ***3D-to-2D Compounding*** over a single cardiac cycle. However, during ***3D-to-2D Compounding***, the acquisition of adjacent slices over a sector of 6.5° is required for the effective suppression of tissue speckle and cavity noise. Due to the limited acoustic window through the rib cage, there may be cases where the acquisition of sufficient data is not feasible. In such cases, compounding data acquired over a narrower sector may provide decreased yet satisfactory data enhancement. If the width of the acquisition sector is restrictive, acquisition over consecutive cardiac cycles for ***Temporal Compounding*** may provide a worthy alternative.

## 7.4. Future work

Each technique analysed and evaluated in the thesis is considered as stand-alone and can be utilised prior to the clinical analysis or post-processing of cardiac ultrasound data. They are not intended to replace but provide an alternative to conventional B-mode imaging that is capable of enhancing challenging datasets. Each method has been implemented and evaluated to a stage that its feasibility is verified. At the moment, there are three areas where further work can be carried out. Initially, the quantitative assessment protocol can be

extended by (i) including a wider range of clinical data acquired using a number of state of the art cardiac ultrasound scanners, (ii) including qualitative criteria based on structure delineation and motion detection, and (iii) employing a larger number of experienced echocardiographers. Monitoring the variations in the performance of each echocardiographer as become familiar with the processed datasets and develop procedures for making clinical measurements on challenging datasets can also be of great interest. It will enable the verification of the assumption that their clinical measurement repeatability is expected to improve with increased familiarity. Then, each data enhancement method can be implemented as a stand-alone software application. The simple nature of each individual method accommodates their efficient implementation, enabling them to act as both off-line (prior to clinical measurements or further data processing) and on-line (during clinical examinations) add-ons. Finally, the assessment of (i) ***Temporal Compounding***, (ii) ***DHBIM*** and (iii) the integrated image enhancement method on a series of 4D cardiac volumes, acquired using ultrasound as well as other imaging modalities such as MRI, is of great interest. Results comparable to the corresponding 2D cardiac ultrasound are expected, demonstrating considerable noise suppression and contrast enhancement on the 4D cardiac volumes. For data with lower noise levels, such as MRI, ***DHBIM*** is expected to provide a very efficient and effective tissue segmentation method.

# Publications

## Peer reviewed publications

[1] Perperidis, A., Cusack, D., McDicken, W.N., MacGillivray, T., Anderson, T. (2009) 3D-to-2D Compounding and its effect on cardiac ultrasound data. Proceedings of the Medical Imaging Understanding and Analysis Conference. Warwick, UK.

[2] Perperidis, A., Cusack, D., McDicken, W.N., MacGillivray, T., Anderson, T. (2009) Temporal Compounding of cardiac ultrasound data: Improving image quality and clinical measurement repeatability. Proceedings of the IEEE Engineering in Medicine & Biology Society Conference. Minneapolis, USA.

[3] Perperidis, A., White, A., Cusack, D., McDicken, W.N., MacGillivray, T., Anderson, T. (2010) Temporal Compounding and its effect on clinical measurements of cardiac ultrasound data. Proceedings of the Medical Imaging Understanding and Analysis Conference. London, UK.

## Other publications

[4] Perperidis, A., McDicken, W.N., MacGillivray, T., Anderson, T. (2009) 3D-to-2D Compounding: Tissue enhancement and noise suppression. Euroson 2009 (Annual meeting of the European Federation of Societies for Ultrasound in Medicine and Biology). Edinburgh, UK. (Abstract & Poster)

[5] Perperidis, A., Cusack, D., McDicken, W.N., MacGillivray, T., Anderson, T. (2009) Spatial Compounding on 2D cardiac ultrasound data. Two simple, efficient and effective methods for improving image quality. WFUMB 2009 (World Congress of the World Federation for Ultrasound in Medicine and Biology). Sydney, Australia. (E-Poster)

[6] Perperidis, A., White, A., Cusack, D., McDicken, W.N., MacGillivray, T., Anderson, T. (2011) Qualitative and quantitative assessment of 3 novel post-processing methods for enhancing echocardiographic images. EUROECHO and other Imaging Modalities 2011 (Annual meeting of the European Association of Echocardiography), Budapest, Hungary. (Abstract & Poster)

# Bibliography


Abd-Elmoniem, K. Z., Kadah, Y. M. & Youssef, A. B. M. (2000). Real time adaptive ultrasound speckle reduction and coherence enhancement. *Proceedings of the International Conference on Image Processing*, 172-175.

Abd-Elmoniem, K. Z., Youssef, A. B. & Kadah, Y. M. (2002). Real-time speckle reduction and coherence enhancement in ultrasound imaging via nonlinear anisotropic diffusion. *IEEE Transactions on Biomedical Engineering* 49(9), 997-1014.

Abdullah-Al-Wadud, M., Kabir, H., Dewan, M. A. A. & Chae, O. (2007). A dynamic histogram equalization for image contrast enhancement. *IEEE Transactions on Consumer Electronics* 53(2), 593-600.

Abiko, Y., Ito, T. & Nakajima, M. (1997). Improvement on quality of echocardiograms. *Acoustical Imaging* 23, 169-176.

Achim, A., Bezerianos, A. & Tsakalides, P. (2001). Novel Bayesian multiscale method for speckle removal in medical ultrasound images. *IEEE Transactions in Medical Imaging* 20(8), 772-783.

Achmad, B., Mustafa, M. M. & Hussain, A. (2009). Inter-frame enhancement of ultrasound images using Optical flow *Lecture Notes in Computer Science* 5857, 191-201.

Aja-Fernandez, S. & Alberola-Lopez, C. (2006). On the estimation of the coefficient of variation for anisotropic diffusion speckle filtering. *IEEE Transactions on Image Processing* 15(9), 2694-2701.

Allan, P. L., Dubbins, P. A., Pozniak, M. A. & McDicken, W. N. (2006). Clinical Doppler ultrasound, 2nd ed. Philadelphia, Churchill Livingstone Elsevier.

Amorim, J. C., dos Reis, M., de Carvalho, J. L. A., da Rocha, A. F. & Camapum, J. F. (2009). Improved segmentation of echocardiographic images using fusion of images from different cardiac cycles. *Proceedings of the IEEE Engineering in Medicine and Biology Society Conference*, Minneapolis, USA, 511-514.

Arenson, J. W., Cobbold, R. S. C. & Johnston, K. W. (1980). A linear stepped Doppler ultrasound array for real-time two-dimensional blood flow imaging. *Ultrasonics Symposium*, Boston, 775-779.

Averkiou, M. A., Roundhill, D. N. & Powers, J. E. (1997). A new imaging technique based on the nonlinear properties of tissues. *Proceedings of the IEEE Ultrasonics Symposium*, Toronto, Canada, 1561-1566.

Aschkenasy, S. V., Jansen, C., Osterwalder, R., Linka, A., Unser, M., Marsch, S. & Hunziker, P. (2006). Unsupervised image classification of medical ultrasound data by multiresolution elastic registration. *Ultrasound in Medicine and Biology* 32(7), 1047-54.

Baker, K. (2002). The mathematics of computer graphics: Cubic spline curves. Retrieved 01-02-2009 (from http://www.math.ucla.edu/~baker/149.1.02w/handouts/dd_splines.pdf).

Bamber, J. C. & Daft, C. (1986). Adaptive filtering for reduction of speckle in ultrasonic pulse-echo images. *Ultrasonics* 24(1), 41-44.

Barron, J. L., Fleet, D. J., Beauchemin, S. S. & Burkitt, T. A. (1992). Performance of optical flow techniques. *Proceedings of the IEEE Computer Society Conference on Computer Vision and Pattern Recognition*, Champaign, USA, 236-242.

Barsky, B. A. (1982). End conditions and boundary conditions for uniform B-spline curve and surface representations. *Computers in Industry* 3(1-2), 17-29.

Bashford, G. R. & Morse, J. L. (2006). Circular ultrasound compounding by designed matrix weighting. *IEEE Transactions on Medical Imaging* 25(6), 732-741.

Becher, H., Tiemann, K., Schlosser, T., Pohl, C., Nanda, N. C., Averkiou, M. A., Powers, J. E. & Luderitcz, B. (1998). Improvement in endocardial border delineation using tissue harmonic imaging. *Echocardiography* 15(5), 511-517.

Behar, V., Adam, D. & Friedman, Z. (2003). A new method of spatial compounding imaging. *Ultrasonics* 41(5), 377-384.

Belohlavek, M., Tanabe, K., Mulvagh, S. L., Foley, D. A., Greenleaf, J. F. & Seward, J. B. (1998). Image enhancement by noncontrast harmonic echocardiography. Part II. Quantitative assessment with use of contrast-to-speckle ratio. *Mayo Clinic Proceedings* 73(11), 1066-1070.

Bencharit, U., Kaufman, J. L., Bilgutay, N. M. & Saniie, J. A. (1986). Frequency and spatial compounding techniques for improved ultrasonic imaging. *Proceedings of the IEEE Ultrasonics Symposium*, Williamsburg, USA, 1021-1026.

Berne, R. M., Levy, M. N., Koeppen, B. M. & Stanton, B. A. (2004). Physiology, 5th ed. St. Louis, Elsevier.

Berson, M., Roncin, A. & Pourcelot, L. (1981). Compound scanning with an electrically steered beam. *Ultrasonic Imaging* 3(3), 303-308.

Bhat, S., Larina, I. V., Larin, K. V., Dickinson, M. E. & Liebling, M. (2009). Multiple-cardiac-cycle noise reduction in dynamic optical coherence tomography of the embryonic heart and vasculature. *Optics Letters* 34(23), 3704-3706.

Bland, M. J. & Altman, D. G. (1986). Statistical methods for assessing agreement between two methods of clinical measurement. *The Lancet* 327(8476), 307-310.

Blessberger, H. & Binder, T. (2010). Two dimensional speckle tracking echocardiography: clinical applications. *Heart* 96, 2032-2040.

Bonow, R. O., Smaha, L. A., Smith, S. C. J., Mensah, G. A. & Lenfant, C. (2002). World Heart Day 2002: the international burden of cardiovascular disease: responding to the emerging global epidemic. *Circulation* 106(13), 1602-1605.

Boukerroui, D., Noble, J. A. & Brady, M. (2001). Feature enhancement in low quality images with application to echocardiography *Lecture Notes in Computer Science* 2082, 453-460.

Bray, J. J., Cragg, P. A., Macknight, A. D. C. & Mills, R. G. (1999). Lecture notes on human physiology, 4th ed. Oxford, Blackwell Science.

British Heart Foundation (2008). European cardiovascular disease statistics. Retrieved 10/02/2011 (from http://www.heartstats.org/datapage.asp?id=7683).

Brown, L. G. (1992). A survey of image registration techniques. *ACM Computing Surveys* 24(4), 325-376.

Burckhardt, C. B. (1978). Speckle in ultrasound B-Mode scans. *IEEE Transactions on Sonics and Ultrasonics* 25(1), 1-6.

Caglar, H., Caglar, N. & Elfaituri, K. (2006). B-spline interpolation compared with finite difference, finite element and finite volume methods which applied to two-point boundary value problems. *Applied Mathematics and Computation* 175(1), 72-79.

Caidahl, K., Kazzam, E., Lidberg, J., Neumann-Andersen, G., Nordanstig, J., Dahlqvist, S. R., Waldenstrom, A. & Wikh, R. (1998). New concept in echocardiography: harmonic imaging of tissue without use of contrast agent. *The Lancet* 352(9136), 1264-1270.

Carpenter, D. A., Dadd, M. J. & Kossoff, G. (1980). A multimode real time scanner. *Ultrasound in Medicine and Biology* 6(3), 279-284.

Caspi, Y. & Irani, M. (2002). Spatio-temporal alignment of sequences. *IEEE Transactions on Pattern Analysis and Machine Intelligence* 24(11), 1409-1424.

Chen, Y., Yin, R., Flynn, P. & Broschat, S. (2003). Aggressive region growing for speckle reduction in ultrasound images. *Pattern Recognition Letters* 24, 677-691.

Dantas, R. G. & Costa, E. T. (2007). Ultrasound speckle reduction using modified gabor filters. *IEEE Transactions on Ultrasonics, Ferroelectrics and Frequency Control* 54(3), 530-538.

Dekker, D. L., Piziali, R. L. & Dong Jr, E. (1974). A system for ultrasonically imaging the human heart in three dimensions. *Computers and Biomedical Research* 7(6), 544-553.

Delabays, A., Pandian, N. G., Cao, Q. L., Sugeng, L., Marx, G., Ludomirski, A. & Schwartz, S. L. (1995). Transthoracic real-time three-dimensional echocardiography using a fan-like scanning approach for data acquisition: methods, strengths, problems, and initial clinical experience. *Echocardiography* 12(1), 49-59.

D'Hooge, J., Konofagou, E., Jamal, F., Heimdal, A., Barrios, L., Bijnens, B., Thoen, J., Van de Werf, F., Sutherland, G. & Suetens, P. (2002). Two-dimensional ultrasonic strain rate measurement of the human heart in vivo. *IEEE Transactions on Ultrasonics, Ferroelectrics and Frequency Control* 49(2), 281-286.

Donoho, D. L. (1995). De-noising by soft-thresholding. *IEEE Transactions on Information Theory* 41(3), 613-627.

dos Reis, M., da Rocha, A. F., Vasconcelos, D. F., Espinoza, B. L. M., Nascimento, F. A., de Carvalho, J. L. A., Salomoni, S. & Camapum, J. F. (2008). Semi-automatic detection of the left ventricular border. *Proceedings of the IEEE Engineering in Medicine and Biology Society Conference*, Vancouver, Canada, 218-221.

dos Reis, M., Carvalho, J. L. A., Macchiavello, B. L., Vasconcelos, D. F., da Rocha, A. F., Nascimento, F. A. O. & Camapum, J. F. (2009). On the use of motion-based frame rejection in temporal averaging denoising for segmentation of echocardiographic image sequences. *Proceedings of the IEEE Engineering in Medicine and Biology Society Conference*, 507-510.

Entrekin, R., Jackson, P., Jago, J. R. & Porter, B. A. (1999). Real time spatial compound imaging in breast ultrasound: technology and early clinical experience. *Medicamundi* 43(3), 35-43.

Evans, A. N. & Nixon, M. S. (1996). Biased motion-adaptive temporal filtering for speckle reduction in echocardiography. *IEEE Transactions on Medical Imaging* 15(1), 39-50.

Evans, D. H. & McDicken, W. N. (2000). Doppler ultrasound, 2nd ed. New York, Wiley.

Feigenbaum, H. (1976). Echocardiography, 2nd ed. Philadelphia, Lea & Febiger.

Feigenbaum, H. (1994). Echocardiography, 5th ed. Philadelphia, Lea & Febiger.

Felsberg, M. & Sommer, G. (2001). The monogenic signal. *IEEE Transactions on Signal Processing* 49(12), 3136-3144.

Finn, S., Glavin, M. & Jones, E. (2011). Echocardiographic speckle reduction comparison. *IEEE Transactions on Ultrasonics, Ferroelectrics and Frequency Control* 58(1), 82-101.

Fleming, A. D., Xia, X., McDicken, W. N., Sutherland, G. R. & Fenn, L. (1994). Myocardial velocity gradients detected by Doppler imaging. *British Journal of Radiology* 67, 679-688.

Foley, W. D. & Erickson, S. J. (1991). Color Doppler flow imaging. *American Journal of Roentgenology* 156(1), 3-13.

Franke, A., Hoffmann, R., Kühl, H. P., Lepper, W., Breithardt, O. A., Schormann, M. & Hanrath, P. (2000). Non-contrast second harmonic imaging improves interobserver agreement and accuracy of dobutamine stress echocardiography in patients with impaired image quality *Heart* 83(2), 133-140.

Friesen, G. M., Jannett, T. C., Jadallah, M. A., Yates, S. L., Quint, S. R. & Nagle, H. T. (1990). A comparison of the noise sensitivity of nine QRS detection algorithms. *IEEE Transactions on Biomedical Engineering* 37(1), 85-98.

Frost, V. S., Stiles, J. A., Shanmugan, K. S. & Holtzman, J. C. (1982). A Model for Radar Images and Its Application to Adaptive Digital Filtering of Multiplicative Noise. *IEEE Transactions on Pattern Analysis and Machine Intelligence* PAMI-4(2), 157-166.

Fulton, D. R., Marx, G. R., Pandian, N. G., Romero, B. A., Mumm, B., Krauss, M., Wollschlager, H., Ludomirsky, A. & Cao, Q. L. (1994). Dynamic three-dimensional echocardiographic imaging of congenital heart defects in infants and children by computer-controlled tomographic parallel slicing using a single integrated ultrasound instrument. *Echocardiography* 11(2), 155-64.

Fuster, V., O'Rourke, R. A., Walsh, R. A. & Poole-Wilson, P. (2008). Hurst's the heart, 12th ed. New York, McGraw-Hill.

Gao, G., Reddy, K., Yingliang, M. & Rhode, K. S. (2009). Real-time compounding of three-dimensional transesophageal echocardiographic volumes: The phantom study. *Proceedings of the IEEE Engineering in Medicine and Biology Society*, Minneapolis, USA, 499-502.

Geyer, H., Caracciolo, G., Abe, H., Wilansky, S., Carerj, S., Gentile, F., Nesser, H. J., Khandheria, B., Narula, J. & Sengupta, P. P. (2010). Assessment of myocardial mechanics using speckle tracking echocardiography: Fundamentals and clinical applications. *Journal of the American Society of Echocardiography* 23(4), 351-369.

Gonzalez, R. C. & Woods, R. E. (2001). Digital image processing, 2nd ed., Prentice Hall.

Gooding, M. J., Rajpoot, K., Mitchell, S., Chamberlain, P., Kennedy, S. H. & Noble, J. A. (2010). Investigation into the fusion of multiple 4-D fetal echocardiography images to improve image quality. *Ultrasound in Medicine & Biology* 36(6), 957-966.

Goodman, J. W. (1976). Some fundamental properties of speckle. *Journal of the Optical Society of America* 66(11), 1145-1150.

Grau, V. & Noble, J. A. (2005). Adaptive multiscale ultrasound compounding using phase information. *Proceedings of the International Conference on Medical Image Computing and Computer-Assisted Intervention*, Palm Springs, USA, Springer Berlin / Heidelberg, 589-596.

Grau, V., Becher, H. & Noble, J. A. (2006). Phase-based registration of multi-view real-time three-dimensional echocardiographic sequences. *International Conference on Medical Image Computing and Computer-Assisted Intervention – MICCAI 2006*, Copenhagen, Denmark, Springer Berlin / Heidelberg, 612-619.

Grau, V., Becher, H. & Noble, J. A. (2007). Registration of multiview real-time 3-D echocardiographic sequences. *IEEE Transactions on Medical Imaging* 26(9), 1154-1165.

Guo, H., Odegard, J. E., Lang, M., Gopinath, R. A., Selesnick, I. W. & Burrus, C. S. (1994). Wavelet based speckle reduction with application to SAR based ATD/R. *Proceedings of the IEEE International Conference in Image Processing*, 75-79.

Gupta, S., Chauhan, R. C. & Saxena, S. C. (2005). Robust non-homomorphic approach for speckle reduction in medical ultrasound images *Medical and Biological Engineering and Computing* 43(2), 189-195.

Guyton, A. C. (1991). Textbook of medical physiology, 8th ed. Philadelphia, W. B Saunders Company.

Guyton, A. C. & Hall, J. E. (1997). Human physiology and mechanisms of disease, 6th ed. Philadelphia, W.B. Saunders Company.

Hammoude, A. (1998). Endocardial border identification in two-dimensional echocardiographic images: review of methods. *Computerized Medical Imaging and Graphics* 22(3), 181-193.

Hamper, U. M., DeJong, M. R., Caskey, C. I. & Sheth, S. (1997). Power Doppler imaging: clinical experience and correlation with color Doppler US and other imaging modalities. *Radiographics* 17(2), 499-513.

Hao, X., Gao, S. & Gao, X. (1999). A novel multiscale nonlinear thresholding method for ultrasonic speckle suppressing. *IEEE Transactions on Medical Imaging* 18(9), 787-794.

Hashimoto, I., Mori, Y., Rusk, R. A., Davies, C. H., Li, X., Mack, G. K. & Sahn, D. J. (2002). Strain rate imaging: an in vitro "validation" study using a physiologic balloon model mimicking the left ventricle. *Echocardiography* 19(8), 669-677.

Heatlie, G. J. & Pointon, K. (2003). Cardiac magnetic resonance imaging. *Post Graduate Medical Journal* 80(939), 19-20.

Henry, W. L., DeMaria, A., Gramiak, R., King, D. L., Kisslo, J. A., Popp, R. L., Sahn, D. J., Schiller, N. B., Tajik, A., Teichholz, L. E. & Weyman, A. E. (1980). Report of the American Society of Echocardiography committee on nomenclature and standards in two-dimensional echocardiography. *Circulation* 62(2), 212-217.

Herlin, I. L. & Ayache, N. (1992). Features extraction and analysis methods for sequences of ultrasound images. *Lecture Notes in Computer Science* 588, 43-57.

Hernandez, A., Basset, O., Chirossel, P. & Gimenez, G. (1996). Spatial compounding in ultrasonic imaging using an articulated scan arm. *Ultrasound in Medicine & Biology* 22(2), 229-238.

Hill, D. L., Batchelor, P. G., Holden, M. & Hawkes, D. J. (2001). Medical image registration. *Physics in Medicine and Biology* 46(3), 1-45.

Hoskins, P. R. & McDicken, W. N. (1997). Colour ultrasound imaging of blood flow and tissue motion. *British Journal of Radiology* 70(837), 878-890.

Hozumi, T., Yoshida, K., Abe, Y., Kanda, R., Akasaka, T., Takagi, T., Yagi, T., Ogata, Y. & Yoshikawa, J. (1998). Visualization of clear echocardiographic images with near field noise reduction technique: Experimental study and clinical experience. *Journal of the American Society of Echocardiography* 11(6), 660-667.

Huber, S., Wagner, M., Medl, M. & Czembirek, H. (2002). Real-time spatial compound imaging in breast ultrasound. *Ultrasound in Medicine and Biology* 28(2), 155-163.

Hung, J., Lang, R., Flachskampf, F., Shernan, S. K., McCulloch, M. L., Adams, D. B., Thomas, J., Vannan, M. & Ryan, T. (2007). 3D echocardiography: a review of the current status and future directions. *Journal of the American Society of Echocardiography* 20(3), 213-233.

Ibrahim, H. & Kong, N. S. P. (2007). Brightness preserving dynamic histogram equalization for image contrast enhancement. *IEEE Transactions on Consumer Electronics* 53(4), 1752-1758.

Jespersen, S. K., Wilhjelm, J. E. & Sillesen, H. (1998). Multi-angle compound imaging. *Ultrasonic Imaging* 20(2), 81-102.

Jespersen, S. K., Wilhjelm, J. E. & Sillesen, H. (2000). In vitro spatial compound scanning for improved visualization of atherosclerosis. *Ultrasound in Medicine and Biology* 26(8), 1357-1362.

Jin, J. Y., Silva, G. T. & Frery, A. C. (2004). SAR despeckling filters in ultrasound imaging. *Latin American Applied Research* 34(1), 49-53.

Kachelriess, M., Sennst, D. A., Maxlmoser, W. & Kalender, W. A. (2002). Kymogram detection and kymogram-correlated image reconstruction from subsecond spiral computed tomography scans of the heart. *Medical Physics* 29(7), 1489-1503.

Kang, S. C., Lee, S. M. & Hong, S. H. (1998). Noise reduction of echocardiographic images using wavelet filtering. *Proceedings of the International Conference on Signal Processing* Beijing, China, 267-270.

Karaman, M., Kutay, M. A. & Bozdagi, G. (1995). An adaptive speckle suppression filter for medical ultrasonic imaging. *IEEE Transactions on Medical Imaging* 14(2), 283-292.

Kasai, C., Namekawa, K., Koyano, A. & Omoto, R. (1985). Real-time two-dimensional blood flow imaging using an autocorrelation technique. *IEEE Transactions on Sonics and Ultrasonics* 32(3), 458-464.

Kim, K. W., Choi, B. I., Yoo, S. Y., Kim, Y. H., Kim, H. C., Lee, H. J., Lee, K. H., Kim, S. H., Won, H. J. & Han, J. K. (2004). Real-time compound ultrasonography: pictorial review of technology and the preliminary experience in clinical application of the abdomen. *Abdominal Imaging* 29(4), 491-497.

Kim, Y. S. & Ra, J. (2005). Improvement of ultrasound image based on wavelet transform: speckle reduction and edge enhancement *SPIE Proceedings on Medical Imaging* 5747, 1085-1092.

Kofoed, S. C., Gronholdt, M. L., Wilhjelm, J. E., Bismuth, J. & Sillesen, H. (2001). Real-time spatial compound imaging improves reproducibility in the evaluation of atherosclerotic carotid plaques. *Ultrasound in Medicine and Biology* 27(10), 1311-1317.

Koo, J. I. & Park, S. B. (1991). Speckle reduction with edge preservation in medical ultrasonic images using a homogeneous region growing mean filter (HRGMF). *Ultrasonic Imaging* 13(3), 211-237.

Kovesi, P. (1999). Image features from phase congruency. *Videre Journal of Computer Vision Research* 1(3), 1-26.

Krissian, K., Westin, C. F., Kikinis, R. & Vosburgh, K. G. (2007). Oriented speckle reducing anisotropic diffusion. *IEEE Transactions on Image Processing* 16(5), 1412-1424.

Krucker, J. F., Meyer, C. R., LeCarpentier, G. L., Fowlkes, J. B. & Carson, P. L. (2000). 3D spatial compounding of ultrasound images using image-based nonrigid registration. *Ultrasound in Medicine and Biology* 26(9), 1475-1488.

Kruger, R. (2000). Analysis and comparison of the signal difference to noise ratio (SDNR), signal difference (SD), and the signal to noise ratio (SNR): evaluating the suitability of the SD and SDNR as MRI quality control parameters. *Proceedings of the IEEE Engineering in Medicine and Biology Society Conference*, Chicago, USA, 2157-2160.

Kuan, D. T., Sawchuk, A. A., Strand, T. C. & Chavel, P. (1987). Adaptive restoration of images with speckle. *IEEE Transactions on Acoustics, Speech, and Signal Processing* 35(3), 373-383.

Lagarias, J. C., Reeds, J. A., Wright, M. H. & Wright, P. E. (1998). Convergence properties of the Nelder--Mead simplex method in low dimensions. *SIAM Journal on Optimization* 9(1), 112-147.

Laine, A. F., Schuler, S., Jian, F. & Huda, W. (1994). Mammographic feature enhancement by multiscale analysis. *IEEE Transactions on Medical Imaging* 13(4), 725-740.

Langeland, S., D'Hooge, J., Claessens, T., Claus, P., Verdonck, P., Suetens, P., Sutherland, G. R. & Bijnens, B. (2004). RF-based two-dimensional cardiac strain estimation: a validation study in a tissue-mimicking phantom. *IEEE Transactions on Ultrasonics, Ferroelectrics and Frequency Control* 51(11), 1537-1546.

Larson, A. C., White, R. D., Laub, G., McVeigh, E. R., Li, D. & Simonetti, O. P. (2004). Self-gated cardiac cine MRI. *Magnetic Resonance in Medicine* 51(1), 93-102.

Ledesma-Carbayo, M. J., Kybic, J., Desco, M., Santos, A. & Unser, M. (2001). Cardiac motion analysis from ultrasound sequences using non-rigid registration *Lecture Notes in Computer Science* 2208, 889-896.

Ledesma-Carbayo, M. J., Kybic, J., Desco, M., Santos, A., Suhling, M., Hunziker, P. & Unser, M. (2005). Spatio-temporal nonrigid registration for ultrasound cardiac motion estimation. *IEEE Transactions on Medical Imaging* 24(9), 1113-1126.

Lee, J. S. (1980). Digital Image Enhancement and Noise Filtering by Use of Local Statistics. *IEEE Transactions on Pattern Analysis and Machine Intelligence* PAMI-2(2), 165-168.

Leotta, D. F. & Martin, R. W. (2000a). Three-dimensional spatial compounding of ultrasound scans with weighting by incidence angle. *Ultrasonic Imaging* 22(1), 1-19.

Leotta, D. F. & Martin, R. W. (2000b). Three-dimensional ultrasound imaging of the rotator cuff: spatial compounding and tendon thickness measurement. *Ultrasound in Medicine & Biology* 26(4), 509-525.

Lester, H. & Arridge, S. R. (1999). A survey of hierarchical non-linear medical image registration. *Pattern Recognition* 32(1), 129-149.

Lewis, J. P. (1995). Fast normalized cross-correlation. *Vision Interface* 1, 120-123.

Li, W., Gussenhoven, E. J., Zhong, Y., The, S. H. K., Pieterman, H., van Urk, H. & Bom, K. (1994). Temporal averaging for quantification of lumen dimensions in intravascular ultrasound images. *Ultrasound in Medicine & Biology* 20(2), 117-122.

Li, P. C. & O'Donnell, M. (1994). Elevational Spatial Compounding. *Ultrasonic Imaging* 16(3), 176-189.

Lin, C. H., Sun, Y. N. & Lin, C. J. (2010). A motion compounding technique for speckle reduction in ultrasound images. *Journal of Digital Imaging* 23(3), 246-257.

Lin, D. C., Nazarian, L. N., O'Kane, P. L., McShane, J. M., Parker, L. & Merritt, C. R. (2002). Advantages of real-time spatial compound sonography of the musculoskeletal system versus conventional sonography. *American Journal of Roentgenology* 179(6), 1629-1631.

Liu, J., Pagoulatos, N. & Yongmin, K. (2004). Ultrasound spatial compounding via registration of 2D slices into 3D volume. *Proceedings of the IEEE Ultrasonics Symposium*, Davis, USA, 2189-2192.

Loizou, C. P., Pattichis, C. S., Christodoulou, C. I., Istepanian, R. S. H., Pantziaris, M. & Nicolaides, A. (2005). Comparative evaluation of despeckle filtering in ultrasound imaging of the carotid artery. *IEEE Transactions on Ultrasonics, Ferroelectrics and Frequency Control* 52(10), 1653-1669.

Lopes, A., Touzi, R. & Nezry, E. (1990). Adaptive speckle filters and scene heterogeneity. *IEEE Transactions on Geosciences and Remote Sensing* 28(6), 992-1000.

Loupas, T., McDicken, W. N. & Allan, P. L. (1989). An adaptive weighted median filter for speckle suppression in medical ultrasonic images. *IEEE Transactions on Circuits and Systems* 36(1), 129-135.

Ludomirsky, A., Vermilion, R., Nesser, J., Marx, G., Vogel, M., Derman, R. & Pandian, N. (1994). Transthoracic real-time three-dimensional echocardiography using the rotational scanning approach for data acquisition. *Echocardiography* 11, 599-606.

Magnin, P. A. & von Ramm, O. T. (1981). Frequency compounding for improved grey scale imaging,. *Ultrasonic Imaging* 3(2), 213.

Magnin, P. A., von Ramm, O. T. & Thurstone, F. L. (1982). Frequency compounding for speckle contrast reduction in phased array images. *Ultrasonic Imaging* 4(3), 267-281.

Maintz, J. B. A. & Viergever, M. A. (1998). A survey of medical image registration. *Medical Image Analysis* 2(1), 1-36.

Makela, T., Clarysse, P., Sipila, O., Pauna, N., Pham, Q. C., Katila, T. & Magnin, I. E. (2002). A review of cardiac image registration methods. *IEEE Transactions on Medical Imaging* 21(9), 1011-1021.

Martin, R., Blood, E., Sheehan, F., Bashein, G., Otto, C., Derook, F., Filer, E. & Detmer, P. (1993). A miniature position and orientation locator for three dimensional echocardiography. *Proceedings of Computers in Cardiology*, 25-28.

Marwick, T. H., Yu, C. M. & Sun, J. P. (2007). Myocardial imaging, ed. Oxford, Blackwell Publishing.

Massay, R. J., Logan-Sinclair, R. B., Bamber, J. C. & Gibson, D. G. (1989). Quantitative effects of speckle reduction on cross sectional echocardiographic images. *British Heart Journal* 62(4), 298-304.

McDicken, W. N. (1991). Diagnostic ultrasound: Principles and use of instruments, 3rd ed. Edinburgh, Churchill Livingstone.

McDicken, W. N., Sutherland, G. R., Moran, C. M. & Gordon, L. N. (1992). Colour Doppler velocity imaging of the myocardium. *Ultrasound in Medicine and Biology* 18(6-7), 651-654.

Melo, S. A., Macchiavello, B., Andrade, M. M., Carvalho, J. L., Carvalho, H. S., Vasconcelos, D. F., Berger, P. A., da Rocha, A. F. & Nascimento, F. A. (2010). Semi-automatic algorithm for construction of the left ventricular area variation curve over a complete cardiac cycle. *Biomedical Engineering Online* 9(5), 1-17.

Meuwly, J. Y., Thiran, J. P. & Gudinchet, F. (2003). Application of adaptive image processing technique to real-time spatial compound ultrasound imaging improves image quality. *Investigative Radiology* 38(5), 257-262.

Meyer, C. R., Boes, J. L., Kim, B., Bland, P. H., Lecarpentier, G. L., Fowlkes, J. B., Roubidoux, M. A. & Carson, P. L. (1999). Semiautomatic registration of volumetric ultrasound scans. *Ultrasound in Medicine & Biology* 25(3), 339-347.

Michailovich, O. V. & Tannenbaum, A. (2006). Despeckling of medical ultrasound images. *IEEE Transactions on Ultrasonics, Ferroelectrics and Frequency Control* 53(1), 64-78.

Miyatake, K., Yamagishi, M., Tanaka, N., Uematsu, M., Yamazaki, N., Mine, Y., Sano, A. & Hirama, M. (1995). New method for evaluating left ventricular wall motion by color-coded tissue Doppler imaging: in vitro and in vivo studies. *Journal of the American College of Cardiology* 25(3), 717-724.

Mohamed, K. K. & Kadah, Y. M. (2008). Objective analysis of ultrasound images by use of a computational observer. *Proceedings of the IEEE Biomedical Engineering Conference*, Cairo, Egypt, 1-5.

Monaghan, M. J. & Mills, P. (1989). Doppler colour flow mapping: technology in search of an application? *British Heart Journal* 61(2), 133-138.

Moritz, W. E. & Shreve, P. L. (1976). A microprocessor-based spatial-locating system for use with diagnostic ultrasound. *Proceedings of the IEEE* 64(6), 966-974.

Moskalik, A., Carson, P. L., Meyer, C. R., Fowlkes, J. B., Rubin, J. M. & Roubidoux, M. A. (1995). Registration of three-dimensional compound ultrasound scans of the breast for refraction and motion correction. *Ultrasound in Medicine and Biology* 21(6), 769-778.

Muehllehner, G. & Karp, J. S. (2006). Positron emission tomography. *Physics in Medicine and Biology* 51(13), R117-R137.

Mulet-Parada, M. & Noble, J. A. (2000). 2D+T acoustic boundary detection in echocardiography. *Medical Image Analysis* 4(1), 21-30.

Mulvagh, S. L., Foley, D. A., Belohlavek, M. & Seward, J. B. (1998). Image enhancement by noncontrast harmonic echocardiography. Part I. Qualitative assessment of endocardial visualization. *Mayo Clinic Proceedings* 73(11), 1062-1065.

Nandalur, K. R., Dwamena, B. A., Choudhri, A. F., Nandalur, S., R., Reddy, P. & Carlos, R. C. (2008). Diagnostic performance of positron emission tomography in the detection of coronary artery disease: a meta-analysis. *Academic Radiology* 15(4), 444-451.

Nelder, J. A. & Mead, R. (1965). A simplex method for function minimization. *The Computer Journal* 7(4), 308-313.

Nguyen, L. D., Leger, C., Debrun, D., Therain, F., Visser, J. & Busemann Sokole, E. (2003). Validation of a volumic reconstruction in 4-d echocardiography and gated SPECT using a dynamic cardiac phantom. *Ultrasound in Medicine and Biology* 29(8), 1151-1160.

Nikitin, N. P. & Witte, K. K. A. (2004). Application of tissue Doppler imaging in cardiology. *Cardiology* 101(4), 170-184.

Nillesen, M. M., Lopata, R., Gerrits, I. H., Kapusta, L., Huisman, H. J., Thijssen, J. M. & de Korte, C. L. (2007). Segmentation of the heart muscle in 3-D pediatric echocardiographic images. *Ultrasound in Medicine and Biology* 33(9), 1453-1462.

Noble, J. A. & Boukerroui, D. (2006). Ultrasound image segmentation: A survey. *IEEE Transactions on Medical Imaging* 25(8), 987-1010.

Notomi, Y., Lysyansky, P., Setser, R. M., Shiota, T., Popovic, Z. B., Martin-Miklovic, M. G., Weaver, J. A., Oryszak, S. J., Greenberg, N. L., White, R. D. & Thomas, J. D. (2005). Measurement of ventricular torsion by two-dimensional ultrasound speckle tracking imaging. *Journal of the American College of Cardiology* 45(12), 2034-2041.

Nowicki, A., Olszewski, R., Etienne, J., Karlowicz, P. & Adamus, J. (1996). Assessment of wall velocity gradient imaging using a test phantom. *Ultrasound in Medicine & Biology* 22(9), 1255-1260.

O'Dell, W. G. & McCulloch, A. D. (2000). Imaging three-dimensional cardiac function. *Annu Rev Biomed Eng* 2, 431-56.

O'Donnell, M. & Silverstein, S. D. (1988). Optimum displacement for compound image generation in medical ultrasound. *IEEE Transactions on Ultrasonics, Ferroelectrics and Frequency Control* 35(4), 470-476.

Ofili, E. O. & Nanda, N. C. (1998). Color Doppler imaging of the myocardium: current status and potential clinical applications. *Ultrasound in Medicine and Biology* 24(2), 177-185.

Ohyama, W., Wakabayashi, T., Kimura, F., Tsuruoka, S. & Sekioka, K. (2000). Automatic left ventricular endocardium detection in echocardiograms based on ternary thresholding method. *Proceedings of the 15th International Conference on Pattern Recognition*, Barcelona , Spain 320-323.

Oktar, S. O., Yucel, C., Ozdemir, H., Uluturk, A. & Isik, S. (2003). Comparison of conventional sonography, real-time compound sonography, tissue harmonic sonography, and tissue harmonic compound sonography of abdominal and pelvic lesions. *American Journal of Roentgenology* 181(5), 1341-1347.

Ollinger, J. M. F., J.A. (1997). Positron-emission tomography. *IEEE Signal Processing Magazine* 14(1), 43-55.

Olstad, B. (2002). ECG gated ultrasonic image compounding. Patent for *GE Medical Systems Global Technology Company.* 6447450: USA.

Peli, E. (1990). Contrast in complex images. *Journal of the Optical Society of America A* 7(10), 2032-2040.

Perona, P. & Malik, J. (1990). Scale-space and edge detection using anisotropic diffusion. *IEEE Transactions on Pattern Analysis and Machine Intelligence* 12(7), 629-639.

Petrovic, O., Feigenbaum, H., Armstrong, W. F., Ryan, T., West, S. R., Creen-Hess, D., Stewart, J., Friedmeyer, J. L. & Fineberg, N. S. (1986). Digital averaging to facilitate two-dimensional echocardiographic measurements. *Journal of Clinical Ultrasound* 14(5), 367-372.

Pham, D. L., Xu, C. & Prince, J. L. (2000). Current methods in medical image segmentation. *Annual Review of Biomedical Engineering* 2, 315-337.

Pizurica, A., Philips, W., Lemahieu, I. & Acheroy, M. (2003). A versatile wavelet domain noise filtration technique for medical imaging. *IEEE Transactions on Medical Imaging* 22(3), 323-331.

Playford, D. A., Levine, R. A., Picard, M. H. & Handschumacher, M. D. (2003). Illusion of contraction from Out-of-Plane translation: can Doppler tissue velocities resolve it? *Journal of the American Society of Echocardiography* 16(8), 832-840.

Pratt, W. K. (1977). Digital Signal Processing, New York, Wiley.

Press, W. K., Teukolsky, S. A., Vetterling, W. T. & Flannery, B. P. (1992). Numerical recipes in C - The art of scientific computing, 2nd ed. Cambridge, Cambridge University Press.

Raab, F. H., Blood, E. B., Steiner, T. O. & Jones, H. R. (1979). Magnetic position and orientation tracking system. *IEEE Transactions on Aerospace and Electronic Systems* AES-15(5), 709-718.

Rabbani, H., Vafadust, M., Abolmaesumi, P. & Gazor, S. (2008). Speckle noise reduction of medical ultrasound images in complex wavelet domain using mixture priors. *IEEE Transactions on Biomedical Engineering* 55(9), 2152-2160.

Rajpoot, K., Noble, J. A., Grau, V., Szmigielski, C. & Becher, H. (2009). Multiview RT3D echocardiography image fusion *Lecture Notes in Computer Science* 5528, 134-143.

Richards, F. J. (1959). A flexible growth function for empirical use. *Journal of Experimental Botany* 10(2), 290-301.

Roelandt, J. R., Sutherland, G. R., Iliceto, S. & Linker, D. T. (1993). Cardiac ultrasound, 1st ed. Edinburhg, Churchill Livingstone.

Rohling, R., Gee, A. & Berman, L. (1997). Three-dimensional spatial compounding of ultrasound images. *Medical Image Analysis* 1(3), 177-193.

Rohling, R. N., Gee, A. H. & Berman, L. (1998). Automatic registration of 3-D ultrasound images. *Ultrasound in Medicine & Biology* 24(6), 841-854.

Rubin, J. M., Bude, R. O., Carson, P. L., Bree, R. L. & Adler, R. S. (1994). Power Doppler US: a potentially useful alternative to mean frequency-based color Doppler US. *Radiology* 190(3), 853-856.

Rusk, R. A., Mori, Y., Davies, C. H., Irvine, T., Kenny, A. & Sahn, D. J. (2000). Comparison of ventricular volume and mass measurements from B- and C-scan images with the use of real-time 3-dimensional echocardiography: studies in an in vitro model. *Journal of the American Society of Echocardiography* 13(10), 910-917.

Sahoo, P. K., Soltani, S. & Wong, A. K. C. (1988). A survey of thresholding techniques. *Computer Vision, Graphics, and Image Processing* 41(2), 233-260.

Salustri, A. & Roelandt, J. R. (1995). Ultrasonic three-dimensional reconstruction of the heart. *Ultrasound in Medicine and Biology* 21(3), 281-293.

Satomura, S. (1957). Ultrasonic Doppler method for the inspection of cardiac functions. *Journal of the Acoustical Society of America* 29(11), 1181-1185.

Schoenhagen, P., Stillman, A. E., Halliburton, S. S. & White, R. D. (2005). CT of the heart: Principles, advances, clinical uses. *Cleveland Clinic Journal of Medicine* 72(2), 127-138.

Seeley, R. R., Stephens, T. D. & Tate, P. (1996). Essentials of anatomy & physiology, 2nd ed. St. Louis, Mosby.

Seo, B. K., Oh, Y. W., Kim, H. R., Kim, H. W., Kang, C. H., Lee, N. J., Kim, J. H., Park, B. J., Cho, K. R., Lee, J. Y., Lee, K. Y. & Bae, J. W. (2002). Sonographic evaluation of breast nodules: comparison of conventional, real-time compound, and pulse-inversion harmonic images. *Korean Journal of Radiology* 3(1), 38-44.

Sezgin, M. & Sankur, B. (2004). Survey over image thresholding techniques and quantitative performance evaluation *Journal of Electronic Imaging* 13(1), 146-165.

Shankar, P. M. (1986). Speckle reduction in ultrasound B-scans using weighted averaging in spatial compounding. *IEEE Transactions on Ultrasonics, Ferroelectrics and Frequency Control* 33(6), 754-758.

Shapiro, R. S., Simpson, W. L., Rausch, D. L. & Yeh, H. C. (2001). Compound spatial sonography of the thyroid gland: evaluation of freedom from artifacts and of nodule conspicuity. *American Journal of Roentgenology* 177(5), 1195-1198.

Shapiro, R. S., Wagreich, J., Parsons, R. B., Stancato-Pasik, A., Yeh, H. C. & Lao , R. (1998). Tissue harmonic imaging sonography: evaluation of image quality compared with conventional sonography. *American Journal of Roentgenology* 171, 1203-1206.

Shattuck, D. P. & von Ramm, O. T. (1982). Compound scanning with a phased array. *Ultrasonic Imaging* 4(2), 93-107.

Sheikh, K., Smith, S. W., von Ramm, O. T. & Kisslo, J. (1991). Real-time, three-dimensional echocardiography: feasibility and initial use. *Echocardiography* 8(1), 119-125.

Shekhar, R. & Zagrodsky, V. (2002). Mutual information-based rigid and nonrigid registration of ultrasound volumes. *IEEE Transactions on Medical Imaging* 21(1), 9-22.

Shekhar, R., Zagrodsky, V., Garcia, M. J. & Thomas, J. D. (2004). Registration of real-time 3-D ultrasound images of the heart for novel 3-D stress echocardiography. *IEEE Transactions on Medical Imaging* 23(9), 1141-1149.

Shrimali, V., Anand, R. S. & Kumar, V. (2009). Current Trends in Segmentation of Medical Ultrasound B-mode Images: A Review. *IETE Technical Review* 26(1), 8-17.

Sinclair, R. B. L., Oldershaw, P. J. & Gibson, D. G. (1983). Computing in echocardiography. *Progress in Cardiovascular Diseases* 25(6), 465-486.

Skolnick, D. G., Sawada, S. G., Feigenbaum, H. & Segar, D. S. (1999). Enhanced endocardial visualization with noncontrast harmonic imaging during stress echocardiography. *Journal of the American Society of Echocardiography* 12(7), 559-563.

Smith, S. W. & Rinaldi, J. E. (1989). Anthropomorphic cardiac ultrasound phantom. *Proceedings of the IEEE Ultrasonics Symposium*, 931-934.

Smith, S. W., Combs, M. P., Adams, D. B. & Kisslo, J. A. (1993). Improved cardiac anthropomorphic phantom. *Journal of Ultrasound in Medicine* 13(8), 601-605.

Smith, S. W., Lopath, P. D., Adams, D. B. & Walcott, G. P. (1995). Cardiac ultrasound phantom using a porcine heart model. *Ultrasound in Medicine & Biology* 21(5), 693-697.

Soler, P., Gerard, O., Allain, P., Saloux, E., Angelini, E. & Bloch, I. (2005). Comparison of fusion techniques for 3D+T echocardiography acquisitions from different acoustic windows. *Proceedings of the IEEE Computers in Cardiology Conference*, Lyon, France, 141-144.

Spicer, D. & Marwick, T. H. (2000). Three-dimensional echocardiography: Research toy or clinical tool? *Heart Lung and Circulation* 9(3), 98-107.

Studholme, C., Hill, D. L. G. & Hawkes, D. J. (1999). An overlap invariant entropy measure of 3D medical image alignment. *Pattern Recognition* 32(1), 71-86.

Sudha, S., Suresh, G. & Sukanesh, R. (2009). Speckle noise reduction in ultrasound images using context-based adaptive wavelet thresholding. *International Journal of Computer Theory and Engineering* 55(3), 135-143.

Suetens, P. (2006). Fundamentals of medical imaging, 4th ed. New York, Cambridge University Press.

Sun, Q., Hossack, J. A., Tang, J. & Acton, S. T. (2004). Speckle reducing anisotropic diffusion for 3D ultrasound images. *Computerized Medical Imaging and Graphics* 28(8), 461-470.

Sutton, M. G. S. J. & Rutherford, J. D. (2004). Clinical cardiovascular imaging, ed. Philadelphia, Elsevier Saunders.

Szmigielski, C., Rajpoot, K., Grau, V., Myerson, S. G., Holloway, C., Noble, J. A., Kerber, R. & Becher, H. (2010). Real-Time 3D Fusion Echocardiography. *Journal of the American College of Cardiology: Cardiovascular Imaging* 3(7), 682-690.

Tay, P. C., Garson, C. D., Acton, S. T. & Hossack, J. A. (2010). Ultrasound despeckling for contrast enhancement. *IEEE Transactions on Image Processing* 19(7), 1847-1860.

Teirlinck, C. J. P. M., Bezemer, R. A., Kollmann, C., Lubbers, J., Hoskins, P. R., Fish, P., Fredfeldt, K. & Schaarschmidt, U. G. (1998). Development of an example flow test object and comparison of five of these test objects, constructed in various laboratories. *Ultrasonics* 36(1-5), 653-660.

Thomas, G. (2004). Tissue Doppler echocardiography - a case of right tool, wrong use. *Cardiovascular Ultrasound* 2(12), 1-6.

Trahey, G. E., Allison, J. W., Smith, S. W. & von Ramm, O. T. (1986a). Simultaneous frequency and spatial compounding for increased speckle reduction. *Ultrasonic Imaging* 8(1), 68.

Trahey, G. E., Smith, S. W. & von Ramm, O. T. (1986b). Speckle pattern correlation with lateral aperture translation: experimental results and implications for spatial compounding. *IEEE Transactions on Ultrasonics, Ferroelectrics and Frequency Control* 33(3), 257-264.

Trahey, G. E., Allison, J. W., Smith, S. W. & von Ramm, O. T. (1986c). A quantitative approach to speckle reduction via frequency compounding. *Ultrasonic Imaging* 8(3), 151-164.

Unser, M. A., Dong, L., Pelle, G., Brun, P. & Eden, M. (1989). Restoration of echocardiograms using time warping and periodic averaging on a normalized time scale. *SPIE Proceedings on Medical Imaging*, 84-93.

van Ocken, E., Glaes, V. A. & Brutsaert, D. L. (1981). Image enhancement by digital averaging of 2-dimensional echopictures. *Proceedings of the Fourth European Congress on Ultrasound in Medicine*, Amsterdam, Netherlands, 69.

Vitale, D. F., Lauria, G., Pelaggi, N., Gerundo, G., Bordini, C., Leosco, D., Rengo, C. & Rengo, F. (1993). Optimal number of averaged frames for noise reduction of ultrasound images. *Proceedings of the IEEE Computers in Cardiology Conference*, London, UK, 639-641.

von Ramm, O. T. & Smith, S. W. (1990). Real time volumetric ultrasound imaging system *Journal of Digital Imaging* 3(4), 261-266.

von Ramm, O. T., Smith, S. W. & Pavy, H. G., Jr. (1991). High-speed ultrasound volumetric imaging system. II. Parallel processing and image display. *IEEE Transactions on Ultrasonics, Ferroelectrics and Frequency Control* 38(2), 109-115.

Wagner, R. F., Smith, S. W., Sandrik, J. M. & Lopez, H. (1983). Statistics of speckle in ultrasound B-Scans. *IEEE Transactions on Sonics and Ultrasonics* 30(3), 156-163.

Walimbe, V., Zagrodsky, V., Raja, S., Jaber, W. A., DiFilippo, F. P., Garcia, M. J., Brunken, R. C., Thomas, J. D. & Shekhar, R. (2003). Mutual information-based multimodality registration of cardiac ultrasound and SPECT images: a preliminary investigation. *The International Journal of Cardiovascular Imaging* 19(6), 483-494.

Wang, X. F., Deng, Y. B., C., N. N., Deng, J., P., M. A. & Xie, M. X. (2003). Live three-dimensional echocardiography: imaging principles and clinical application. *Echocardiography* 20(7), 593-604.

Wang, Z., Bovik, A. C., Sheikh, H. R. & Simoncelli, E. P. (2004). Image quality assessment: from error visibility to structural similarity. *IEEE Transactions on Image Processing* 13(4), 600-612.

Ward, B., Baker, A. C. & Humphrey, V. F. (1995). Non-linear propagation applied to the improvement of lateral resolution in medical ultrasound scanners. *Proceedings of the World Congress on Ultrasonics Conference*, Berlin, Germany, 965-968.

Ward, B., Baker, A. C. & Humphrey, V. F. (1997). Nonlinear propagation applied to the improvement of resolution in diagnostic medical ultrasound. *Journal of Acoustical Society of America* 101(1), 143-154.

Weickert, J. (1998). Anisotropic diffusion in image processing, ed. Stuttgart, Teubner-Verlag.

World Health Organization (2008). World Health Statistics 2008. Retrieved 10/02/2011 (from http://www.who.int/whosis/whostat/EN_WHS08_Full.pdf).

World Health Organization (2009). World health statistics 2009. Retrieved 10/02/2011 (from http://www.who.int/whosis/whostat/EN_WHS09_Full.pdf).

Xiao, G., Brady, M., Noble, J. A. & Zhang, Y. (2002). Segmentation of ultrasound B-mode images with intensity inhomogeneity correction. *IEEE Transactions on Medical Imaging* 21(1), 48-57.

Xie, M. X., Wang, X. F., Cheng, T. O., Lu, Q., Yuan, L. & Liu, X. (2005). Real-time 3-dimensional echocardiography: a review of the development of the technology and its clinical application. *Progress in Cardiovascular Diseases* 48(3), 209-225.

Yang, H. S., Bansal, R. C., Mookadam, F., Khandheria, B. K., Tajik, A. J. & Chandrasekaran, K. (2008). Practical guide for three-dimensional transthoracic echocardiography using a fully sampled matrix array transducer. *Journal of the American Society of Echocardiography* 21(9), 979-989.

Yao, C. & Penney, G. P. (2008). Spatial compounding of 3D echocardiography: novel methodologies for large sets of images. *Proceedings of the Medical Image Understanding and Analysis Conference*, Dundee, UK.

Yao, C., Simpson, J. M., Schaeffter, T. & Penney, G. P. (2010). Spatial compounding of large numbers of multi-view 3D echocardiography images using feature consistency. *Proceedings of the IEEE International Symposium in Biomedical Imaging: From Nano to Macro*, London, UK, 968-971.

Yin, X., Goudriaan, J., Lantinga, E. A., Vos, J. & Spiertz, H. J. (2003). A flexible sigmoid function of determinate growth. *Annals of Botany* 91(3), 361-371.

Yu, Y. & Acton, S. T. (2002). Speckle reducing anisotropic diffusion. *IEEE Transactions on Image Processing* 11(11), 1260-1270.

Yue, Y., Croitoru, M. M., A., B., Zwischenberger, J. B. & Clark, J. W. (2005). Ultrasound speckle suppression and edge enhancement using multiscale nonlinear wavelet diffusion. *Proceedings of the IEEE Engineering in Medicine and Biology Conference*, Shanghai, China,

Zagrodsky, V., Shekhar, R. & Cornhill, J. F. (2000). Mutual information-based registration of cardiac ultrasound volumes *Proceedings of the SPIE Image Processing Conference*, San Diego, USA, 1605-1614.

Zagrodsky, V., Shekhar, R. & Cornhill, J. F. (2001). Multi-function extension of simplex optimization method for mutual information-based registration of ultrasound volumes. *Proceedings of the SPIE Image Processing Conference*, San Diego, USA, 508-515.

Zagrodsky, V., Walimbe, V., Castro-Pareja, C. R., Qin, J. X., Song, J. M. & Shekhar, R. (2005). Registration-assisted segmentation of real-time 3-D echocardiographic data using deformable models. *IEEE Transactions on Medical Imaging* 24(9), 1089-1099.

Zhong, H., Kanade, T. & Schwartzman, D. (2006). "Virtual Touch": An efficient registration method for catheter navigation in left atrium *Lecture Notes in Computer Science* 4190, 437-444.

Zitova, B. & Flusser, J. (2003). Image registration methods: a survey. *Image and Vision Computing* 21(11), 977-1000.

Zong, X., Laine, A. F. & Geiser, E. A. (1998). Speckle reduction and contrast enhancement of echocardiograms via multiscale nonlinear processing. *IEEE Transactions on Medical Imaging* 17(4), 532-540.

Zwirn, G. & Akselrod, S. (2004). A histogram-based technique for echocardiographic image enhancement. *Proceedings of the Computers in Cardiology Conference*, 81-84.

Zwirn, G. & Akselrod, S. (2005). Adaptive brightness transfer functions in echocardiography. *Ultrasound in Medicine & Biology* 31(5), 649-661.

Zwirn, G. & Akselrod, S. (2006). Stationary clutter rejection in echocardiography. *Ultrasound in Medicine & Biology* 32(1), 43-52.

# Appendix A: Example peer reviewed papers

# Temporal compounding of cardiac ultrasound data: Improving image quality and clinical measurement repeatability.

Antonios Perperidis, David Cusack, Norman McDicken, Tom MacGillivray, Tom Anderson

***Abstract*—Echocardiography provides a powerful and versatile tool for assessing cardiac morphology and function. However, cardiac ultrasound suffers from speckle as well as static and dynamic noise. Over the last three decades, a number of studies have attempted to address the challenging problem of speckle/noise suppression in cardiac ultrasound data. No single method has managed to provide a widely accepted solution. *Temporal Compounding* is a noise suppression method that utilises spatial averaging of temporally aligned cardiac B-Mode data. Reliable temporal alignment is vital for effective *Temporal Compounding*. In this study we introduce a novel, accurate and robust technique for the temporal alignment of cardiac cycles with variable temporal characteristics and examine the effect of *Temporal Compounding* in four clinical measurements performed on routine echocardiographic examinations. Results from 32 patients demonstrate speckle/noise suppression, shadowing reduction, anatomical structure enhancement and improvement in measurement repeatability with no significant or systematic bias introduced. Temporally compound data may be able to provide a good alternative to B-Mode data in clinical measurements as well as a first step to further post-processing of cardiac ultrasound data.**

## I. Introduction

Cardiovascular diseases (CVD) constitute the single most important cause of death in the developed world [1]. The early diagnosis and treatment of CVDs is crucial in order to reduce mortality and to improve patients' quality of life. Echocardiography, a widely used tool for assessing cardiac morphology and function, offers a number of advantages when compared to other available imaging modalities. However, cardiac ultrasound suffers from speckle as well as static and dynamic noise which tend to: (i) obscure fine structure, (ii) mask out low contrast regions, (iii) reduce the ability of the human observer to resolve fine detail during a diagnostic examination and (iv) decrease the effectiveness of further image processing such as edge detection, image registration and object classification. As a result, techniques are required for removing or reducing noise aiming to improve image quality (by increasing Signal to Noise Ratio – SNR) and the diagnostic potential of medical ultrasound.

Speckle/noise suppression on medical ultrasound data has been an ongoing research theme for the last three decades. Ultrasound scans represent a challenging application for noise reduction algorithms because, although they are heavily corrupted by noise, they contain spatial features that should be preserved. Spatial compounding, a widely used technique, suppresses noise by combining independent or partially uncorrelated images of an anatomic structure whose speckle patterns have been modified by imaging the target region of interest from varying angles. Intensity averaging is the most commonly used compounding strategy yielding satisfactory results on speckle/noise suppression.

Spatial compounding of cardiac ultrasound data is challenging due to the constant, rapid movement of the heart and the limited acoustic windows through the patient rib-cage and lungs. Two studies have utilised the almost periodic cardiac motion that enables the acquisition of multiple 2D images of the same heart structure from the same acoustic window [2]-[3]. Frames of consecutive cardiac cycles within a multi-cycle B-Mode sequence are temporally aligned and spatially compounded (Fig. 2). These frames may not be independent but are partially uncorrelated due to dynamic noise changes, patient respiration and probe motion during data acquisition. The method has been referred as *Temporal Compounding* and is an extension of the Synchronised Summing Method used to improve SNR of noisy periodic signals in signal processing. Reliable temporal alignment is a key step for effective *Temporal Compounding*. Both studies identified the potential of *Temporal Compounding* and demonstrated (in small numbers of datasets) the SNR improvement that can be achieved. However, neither made any mention on the effect of *Temporal Compounding* on clinical measures performed on a typical cardiac ultrasound examination. In this study we introduce a novel, efficient and robust non-linear temporal alignment method and examine the effect of *Temporal Compounding* on routine clinical measurements on cardiac ultrasound examinations.

## II. Data acquisition and manual analysis

### A. Data acquisition process

Data from 32 patients (18 male, 14 female, ages ranging

Manuscript received April 7, 2009. This work has been funded by the ESPSRC (EP/C523776/1).

A. Perperidis is with the Medical Physics and Medical Engineering, Edinburgh, EH16 4SA, Scotland (corresponding author - phone: +44 131 242 6311; fax: +44 131 242 6314; e-mail: A.Perperidis@sms.ed.ac.uk).

D. Cusack is with the Echocardiography Department, Western General Hospital, Edinburgh, EH4 2XU, Scotland (e-mail: cusackdavid@aol.com).

N. McDicken is with the Medical Physics and Medical Engineering, Edinburgh, EH16 4SA, Scotland (e-mail: N.McDicken@ed.ac.uk).

T. MacGillivray is with the Wellcome Trust Clinical Research Facility, Western General Hospital, Edinburgh, EH4 2XU, Scotland (e-mail: T.J.MacGillivray@ed.ac.uk).

T. Anderson is with the Medical Physics and Medical Engineering, Edinburgh, EH16 4SA, Scotland (e-mail: Tom.Anderson@ed.ac.uk).

from 21 to 88 with an average age of 60) were acquired by an experienced echocardiographer in the Echocardiography department of the Western General Hospital, Edinburgh, during January 2009. For the data acquisition a GE Vivid 7 Dimension ultrasound scanner was used along with a 3MHz phased array probe. B-Mode data of 25 cardiac cycles of the Parasternal Long-Axis view were acquired according to the standards set by the British (BSE) and American Society of Echocardiography (ASE) [4]. 25 cardiac cycles were found to provide a good trade-off between noise suppression and increase in the cardiac examination duration. Images were captured at 25 frames per second (FPS). B-Mode image sequences of 434 x 636 pixels were exported as DICOM files with no compression applied to them.

Following data acquisition, the echocardiographer manually identified a left ventricular End-Diastolic (ED) and an End-Systolic (ES) frame within the captured cine-loop. Manual caliper measurements of the Interventricular Septal Thickness (IVSd), Left Ventricular Internal Dimension (LVIDd) and Left Ventricular Posterior Wall (LVPWd) were performed on each ED frame. Similarly, measurements of the Left Ventricular Internal Dimension (LVIDs) were performed on each ES frame. The above measurements are typical, widely used clinical measurements performed during a routine cardiac examination. All measurements were taken according to the BSE standards.

### B. Data analysis

Prior to any processing each dataset was manually labeled as *good* (12), *average* (12) or *bad* (8) according to the visually observed quality as well as the diagnostic value of its images. Then, all ED and ES frames in each B-Mode dataset were manually identified. Four cues were employed in the ED and ES identification process: (i) the opening and closing of the Mitral Valve, (ii) the periodic motion of the Left Ventricle (LV) cavity, (iii) the periodic motion of the Right Ventricle (RV) cavity and (iv) the QRS complex on the available ECG signal. Due to noise and shadowing, no single cue was robust enough to identify the ED and ES on all datasets. In order to assess intra-operator variability, the ED and ES detection was repeated 3 times for each dataset.

## III. DATA PROCESSING

There are 3 steps to *Temporal Compounding*: (i) identification of ED and ES frames within a sequence, (ii) non-linear alignment of frames of consecutive cardiac cycles and (iii) spatial compounding of temporally aligned data.

### A. Identification of ED and ES frames

We propose a semi-automatic approach that identifies ED and ES frames utilising intensity information from the B-Mode image sequence. The method is based on the left ventricular deformation during the cardiac cycle and requires the manual identification of one ED (ED1) and one ES (ES1) frame. The similarity between each subsequent frame of the sequence and the ED1 and ES1 frames is estimated using the normalised cross correlation coefficient (CC) [5]:

$$CC = \frac{\sum_x \sum_y (S_0(x,y) - \overline{S_0}) \bullet (S_i(x,y) - \overline{S_i})}{\sqrt{\sum_x \sum_y (S_0(x,y) - \overline{S_0})^2} \bullet \sqrt{\sum_x \sum_y (S_i(x,y) - \overline{S_i})^2}} \quad (1)$$

where $S_0$ corresponds to ED1 or ES1, $S_i$ is the *i-th* frame in the sequence and $\overline{S}_i$ its mean intensity.

During systole, due to left ventricular contraction, each consecutive frame will appear less similar to ED1 and more similar to ES1. Likewise, during diastole, due to left ventricular relaxation, each consecutive frame will seem more similar to ED1 and less similar to ES1. As a result, each end-diastolic frame demonstrates maximum similarity with ED1 and minimum similarity to ES1. On the other hand, each end-systolic frame demonstrates maximum similarity with ES1 and minimum similarity to ED1. In theory, a single similarity test between each frame and the manually identified ED would be sufficient for the identification of ED and ES frames. The corresponding *CC* would demonstrate local maxima on end-diastole and local minima in end-systole. However, the high noise levels contained in cardiac ultrasound data necessitate for a more robust approach. Therefore, a coefficient that combines information on the similarity of each frame with respect to both ED1 and ED2 is defined as:

$$CCC = CCED - CCES \quad (2)$$

where *CCED* is the correlation coefficient of a frame with respect to ED1 and *CCES* is the correlation coefficient of a frame with respect to ES1. *CCC* stands for *Combined Correlation Coefficient* and is a simple linear combination of the two coefficients that is expected to demonstrate a stronger local maxima relationship between ED1 and ED frames as well as a stronger local minima relationship between ED1 and ES frames.

### B. Non-linear temporal alignment

The temporal behaviour of the heart may vary during a cardiac ultrasound examination. Variations in the temporal dynamics range from small, for healthy hearts, to large for hearts suffering from arrhythmia or other cardiac diseases. These variations tend to be non-linear with greater effect in the relaxation phase of the cardiac cycle. In order to address this, a novel transformation $T_{temp}$ is introduced, which enables the temporal alignment of the corresponding frames between two cardiac cycles. $T_{temp}$ is modeled by a free form deformation using a *1D relaxed uniform interpolating cubic B-Spline* curve [6]:

$$T_{temp}(t) = \sum_{l=0}^{3} B_l(t) P_i \quad (3)$$

where $P_i$ represents the *i-th* control point, $B_l$ represents the *l-th* basis function of the B-Spline while *t* is a global parameter that corresponds to internal knot values. Each cardiac cycle is defined by an ED-ES-ED frames sequence. $T_{temp}$

temporally aligns two cardiac cycles by fitting a smooth curve through the temporal position of the corresponding ED and ES frame pairs (Fig. 1). The non-linear temporal alignment is applied between every pair of cardiac cycles within a B-Mode sequence.

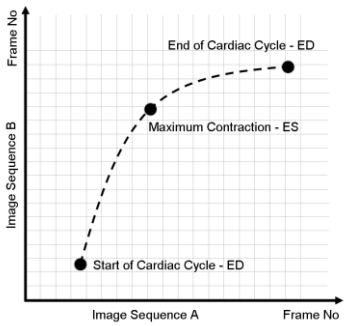


Fig. 1. Example of non-linear temporal mapping between 2 frame sequences using $T_{temp}$, which aligns the 3 states that define a cardiac cycle.

### C. Spatial compounding

Each frame within the B-mode sequence is replaced by a compound frame generated from the temporally aligned images, one from each cardiac cycle (Fig. 2). Intensity averaging is utilised as the spatial compounding method since it is a well established and effective method for noise suppression in ultrasound datasets. The intensity of each pixel within the resulting frame is therefore set as the average intensity value of the corresponding pixels from all the temporally aligned data (Fig. 2).

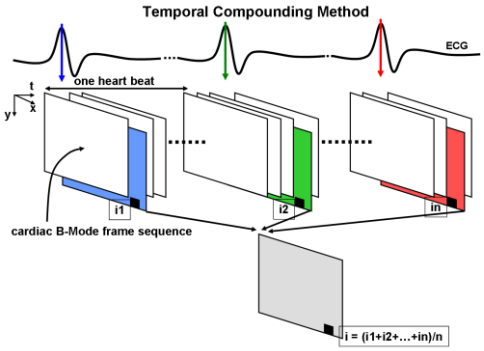


Fig. 2. *Temporal Compounding*: Intensity averaging of temporally aligned frames from consecutive cardiac cycles.

## IV. Clinical Measurements

An experienced echocardiographer was asked to perform routine clinical measurements on ED and ES frames from both the original B-Mode as well as the temporally compound data. A sequence of ED frames was presented and the IVSd, LVIDd and LVPWd measurements were performed on each frame. Similarly, a sequence of ES frames was presented and the LVIDs measurement was performed on each frame. Each frame sequence contained one original and one averaged frame for each of the datasets (64 frames in total). The order of the frames was randomised to ensure no bias in the results. Clinical measures were performed twice to enable the examination of measurement agreement and repeatability.

## V. Results and Discussion

Fig. 3 and Fig. 4 illustrate the effect of *Temporal Compounding* on cardiac ultrasound data. In both figures the original frames suffer from speckle/noise. Furthermore, the low quality frame (Fig. 3 *left*) is heavily corrupted by noise making it hard to identify cardiac anatomic structures. *Temporal Compounding* suppresses speckle/noise and improves the appearance of anatomic structures. We derived the SNR increase introduced by *Temporal Compounding* using a 40 x 40 pixel region around the IVSd. The SNR increase for all 32 datasets ranges between 4% and 79% with mean SNR increase of 39% and Standard Deviation of 20%.

Accurate temporal alignment prior to spatial compounding is a key process for effective *Temporal Compounding*. Insufficient temporal alignment would result in compounding frames corresponding to different cardiac phases leading to severe blurring of anatomic structures making clinical measurements inaccurate and unrepeatable.

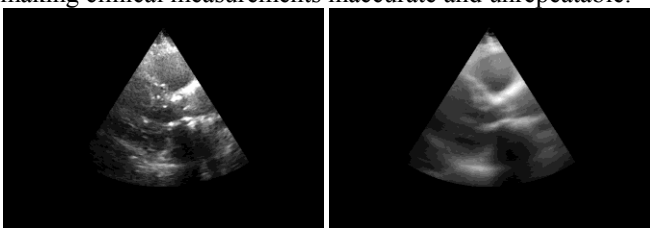

Fig. 3. Original (*left*) and compound (*right*) ED frames of low image and diagnostic quality.

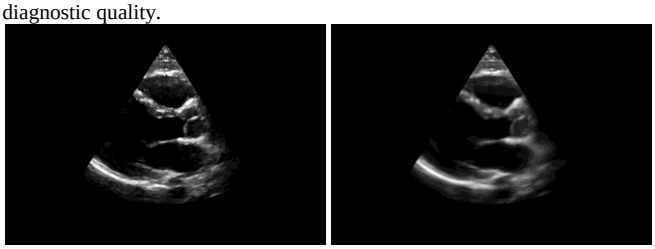

Fig. 4. Original (*left*) and compound (*right*) ED frames of high image and diagnostic quality.

Bland Altman plots [7] were used for the quantitative assessment of the effect of *Temporal Compounding* on clinical measurements. The first plot examines the repeatability of measurements performed on the original ultrasound data (Fig. 5 – *top row*). The second plot examines the repeatability of measurements performed on the compound ultrasound data (Fig. 5 – *middle row*). Finally, the third plot examines the agreement between the measurements performed on the original and the compound data (Fig. 5 – *bottom row*). Table I summarises the bias, similarity and agreement measures and coefficients derived from the Bland Altman plots for all four clinical measurements performed. The Coefficients of Repeatability [8] (CR - Table I) indicate that measurements on the compound data demonstrate improvement in repeatability level of up to 14.3% when compared to measurements on the original unprocessed images. Moreover, measurements on original and compound data demonstrate good measuring agreement with no systematic bias observed. Our results suggest that measurements on temporally compound data may provide a method to improve current cardiac measurements.

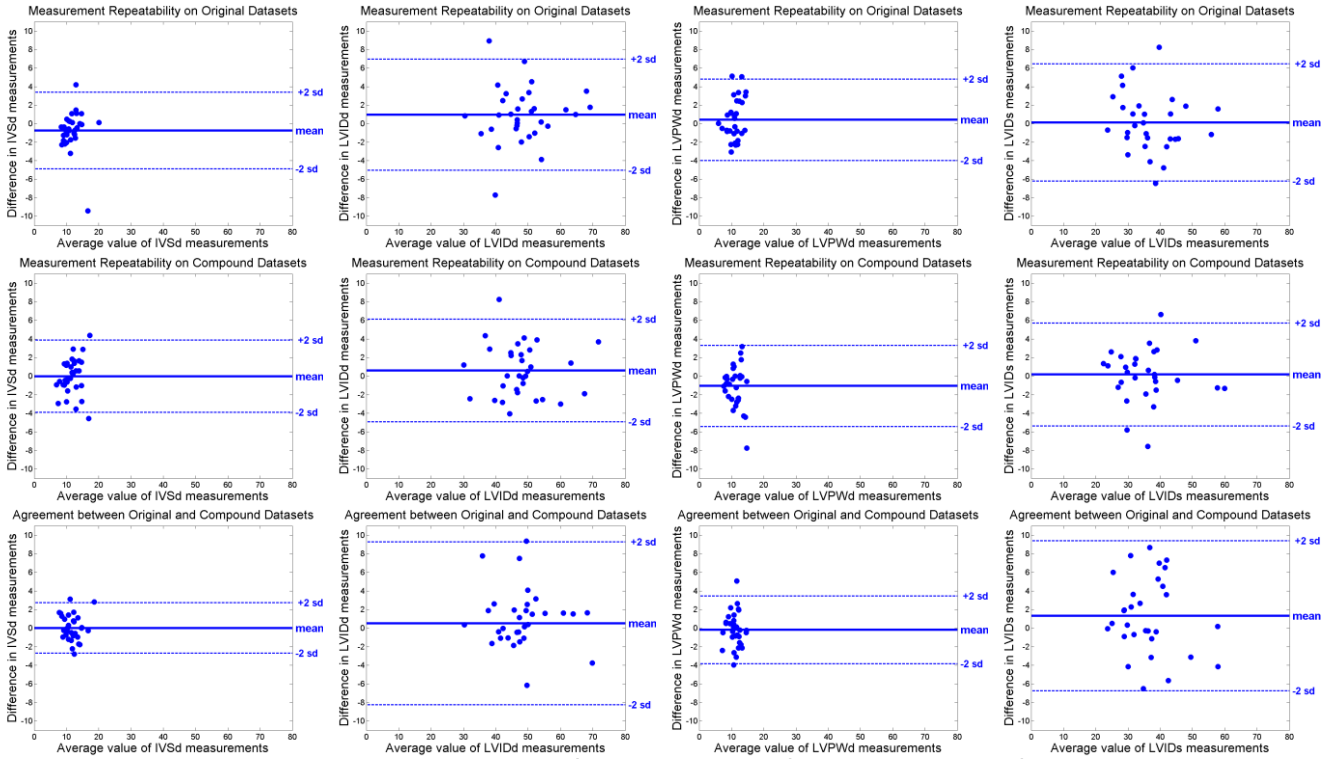


Fig. 5. Bland Altman plots for IVSd (1st Column), LVIDd (2nd Column), LVPWd (3rd Column) and LVIDs (4th Column) measurements showing repeatability on the original data (*top*), the compound data (*middle*) as well as the measuring agreement between original and compound data (*bottom*). The bias as well as the upper and lower limits of agreement is included.

TABLE I

MEASUREMENT REPEATABILITY AND AGREEMENT COEFFICIENT FOR CLINICAL MEASUREMENTS.

| **Measurement** | **Original** | | | | **Compound** | | | | **Agreement** | | | |
|---|---|---|---|---|---|---|---|---|---|---|---|---|
| (mm) | **Mean diff** | **+ 2sd** | **- 2sd** | **CR** | **Mean diff** | **+ 2sd** | **- 2sd** | **CR** | **Mean diff** | **+ 2sd** | **- 2sd** | **CR** |
| IVSd | -0.74 | 3.40 | -4.88 | 4.14 | -0.02 | 3.88 | -3.91 | 3.90 | 0.01 | 2.73 | -2.71 | 2.72 |
| LVIDd | 0.96 | 6.95 | -5.03 | 5.99 | 0.60 | 6.12 | -4.92 | 5.52 | 0.51 | 9.28 | -8.26 | 8.77 |
| LVPWd | 0.41 | 4.81 | -3.99 | 4.40 | -1.06 | 3.32 | -5.44 | 4.38 | -0.19 | 3.46 | -3.85 | 3.66 |
| LVIDs | 0.12 | 6.45 | -6.21 | 6.33 | 0.18 | 5.72 | -5.36 | 5.54 | 1.32 | 9.41 | -6.76 | 8.08 |

## VI. CONCLUSIONS

*Temporal Compounding* provides a simple and effective technique for suppressing speckle/noise and enhancing anatomic structures within cardiac ultrasound data. *Temporal Compounding*, unlike other methods, appears to improve the repeatability of routine clinical measurements on cardiac ultrasound data. Due to its simple nature, *Temporal Compounding* can act as a first step to other post-processing techniques, such as segmentation and registration, whose effectiveness is limited and sometimes restricted by the low image quality (SNR). Our future work includes examining (i) the effect of *Temporal Compounding* on more clinical measures such as the End-Systolic Left Atrium Diameter (LADs), (ii) the intra-operator variability in clinical measurements performed by additional echocardiographers and (iii) the performance of *Temporal Compounding* against other available spatial and frequency compounding methods.

## ACKNOWLEDGMENT

The authors would like to thank Audrey White from the Echocardiography department of the Western General hospital, Edinburgh, for her valuable input in this study.

## REFERENCES

[1] World Health Organization (December 2003), "The world health repor – 2003. Shaping the future" [online report]. Available: http://www.who.int/whr/2003/en/whr03_en.pdf. 2003.

[2] M. Unser, L. Dong, G. Pelle, P. Brun & M. Eden, "Restoration of echocardiograms using time warping and periodic averaging on a normalised time scale". In *SPIE Proc. Medical Imaging III: Image Processing*, vol. 1092, Newport Beach - California, 1989, pp. 84-93.

[3] Y. Abiko, T. Ito, M. Nakajima, "Improvement on quality of echocardiograms". *Acoustical Imaging*, vol. 23, pp. 169-176. 1997.

[4] L.H. Henry, A. DeMaria, R.Gramiak, D.L. King, J.A. Kisslo, R.L. Popp, D.J. Sahn, N.B. Schiller, A. Tajik, L.E. Teichholz, A.E. Weyman, "Report of the American Society of Echocardiography. Committee on Nomenclature and standards in two-dimensional echocardiography". *Circulation*, vol. 62 (2), pp. 212-217. 1980.

[5] J.P. Lewis, "Fast Template Matching". Vision Interface, pp. 163-165. 1995.

[6] M. Unser, "Splines. A perfect fit for signal and image processing". *IEEE Signal Processing Magazine*, vol. 16 (6), pp. 22-38. November 1999.

[7] J.M. Bland & D.G. Altman, "Statistical methods for assessing agreement between two methods of clinical measurement". *The Lancet*. pp. 307-310. 1986.

[8] British Standards Institution, "Precision of test methods I. Guide for the determination and reproducibility for a standard test method". BS 5497 - Part 1. London: BSI. 1979.

# 3D-to-2D Compounding and its effect on cardiac ultrasound data.

Antonios Perperidis[1*]
A.Perperidis@sms.ed.ac.uk
Audrey White[2]
David Cusack[2]
Norman McDicken[1]
Tom MacGillivray[3]
Tom Anderson[1]

[1] Medical Physics & Medical Engineering, University Of Edinburgh, Edinburgh.
[2] Echocardiography Department, Western General Hospital, Edinburgh.
[3] Wellcome Trust Clinical Research Facility, Western General Hospital, Edinburgh.

**Abstract**

Echocardiography, though an established tool for assessing cardiac morphology and function, suffers from speckle as well as static and dynamic noise. In this study, we introduce *3D-to-2D Compounding*, which suppresses speckle/noise by averaging adjacent (along the elevation plane), partially uncorrelated, 2D slices of the heart extracted as a sector of a volumetric pyramid scan. We then examine the effect of *3D-to-2D Compounding* on clinical measurements performed on routine echocardiographic examinations. Results from 20 volunteers demonstrate speckle/noise suppression (mean SNR increase of 36%), anatomical structure enhancement and improvement in clinical measurement repeatability (CR increase of up to 49%) with no significant or systematic bias introduced. Due to recent advances in real-time 4D acquisition technology, *3D-to-2D Compounding* can be implemented for use in clinical examinations as an alternative to B-Mode data and act as a first step to further post-processing of cardiac ultrasound data.

## 1 Introduction

Cardiovascular diseases (CVD) constitute the single most important cause of death in the UK [1]. The early diagnosis and treatment of CVDs is crucial in order to reduce mortality and improve patients' quality of life. Echocardiography, a widely used tool for assessing cardiac morphology and function, offers a number of advantages when compared to other available imaging modalities. However, cardiac ultrasound suffers from speckle as well as static and dynamic noise which tend to reduce: (i) the ability of the human observer to resolve fine detail during a diagnostic examination and (ii) the effectiveness of further image processing methods such as image segmentation and registration. As a result, there is wide scope for improving image quality (increase Signal-to-Noise Ratio, SNR) and therefore the diagnostic potential of cardiac ultrasound.

Spatial compounding suppresses noise by combining partially uncorrelated images of an anatomic structure by imaging the target region-of-interest from various angles. Spatial compounding on cardiac ultrasound data is challenging due to the constant, rapid heart motion and the limited acoustic windows through the patient rib cage and lungs. Recent advances in data acquisition technologies, such as matrix transducers, enable the acquisition of real-time, non-gated, 4D cardiac ultrasound data through a single acoustic window [2]. In this study we introduce *3D-to-2D Compounding*, a novel and effective noise/speckle suppression and tissue enhancement method. *3D-to-2D Compounding* utilises 4D ultrasound technology for the acquisition of adjacent, partially uncorrelated cardiac slices compounding them to an improved 2D B-Mode frame sequence. We then examine the effect of *3D-to-2D Compounding* on routine clinical measurements performed during cardiac ultrasound examinations.

# 2 Data acquisition

## 2.1 Scanning setup

B-Mode frame sequences over adjacent slices (along the elevation plane) were acquired using a mechanically displaced 2D phased array cardiac probe (Figure 1). The 2D probe was attached to a unipolar geared stepper motor which was driven by an arbitrary function generator. Each slice was offset slightly from the previous with a small angular displacement $\boldsymbol{\theta}$. The collection of adjacent slices formed a thin angular 3D sector of a volumetric pyramid scan (Figure 1). The combined B-Mode frame sequences acquired over each adjacent slice formed a 4D sector of the scanned cardiac structure. In a clinical setup, a 4D matrix transducer can be used for the real-time, simultaneous acquisition of the adjacent slices. However, a manually controlled displacement of a 2D probe enabled us to investigate for optimal acquisition parameters such as inter-slice angular displacement and 3D sector angular width. Such parameters have direct effect on SNR as well as the tissue boundary blurring introduced by compounding. Using a left ventricle (LV) phantom we found that sectors with angular range of 5° and angular inter-slice distance of 0.36° provide a good trade-off between SNR increase and tissue boundary blurring.

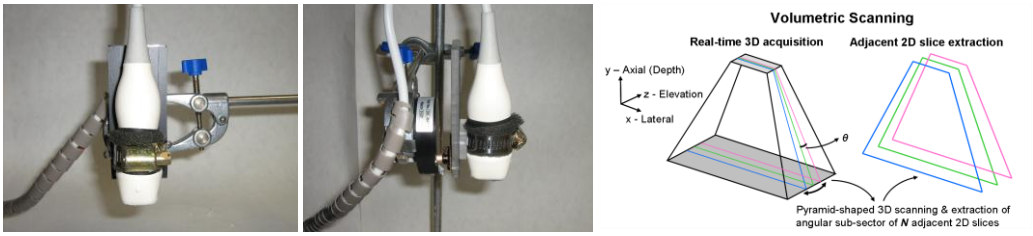


Figure 1: Close up of the motor-arm attached to the 2D phased array probe (left and middle) that accommodates acquisition of adjacent slices by angular displacement of the probe (right).

## 2.2 Data acquisition process

Twenty-five multi-cycle cardiac datasets from five healthy volunteers (all male, mean age: 36) were acquired by an experienced echocardiographer during November of 2009. B-Mode data of the Parasternal Long-Axis view were acquired according to the standards set by the British and American Society of Echocardiography (BSE and ASE) [3]. Each cardiac cycle was acquired with an angular displacement relative to the previous acquisition resulting in a 4D sector as described in Section 2.1. During the multi-cycle acquisition the volunteers were requested to breathe as smoothly as possible to avoid large displacements along the scan plane.

For the data acquisition we used an Ultrasonix Sonix-RP ultrasound scanner and a 2-4 MHz phased array probe at 32 frames-per-second (FPS). Acquisition parameters such as scanning frequency, depth, beam focus, sector width and gain were optimally set by the operator for each volunteer. The captured B-Mode data were exported as DICOM image sequences of 640 x 480 pixels with no compression applied to them. Following data acquisition, each dataset was manually labeled as *good* (14), *average* (6) or *bad* (5) according to the visually observed quality and diagnostic value of the B-Mode data. Five datasets were discarded due to repeated loss of contact between the probe and the patient possibly as a result of heavy breathing.

# 3 Data processing

There are three steps to *3D-to-2D Compounding* (see Figure 2)*:* (i) the identification of all End Diastolic (ED) and End Systolic (ES) frames, (ii) the non-linear alignment amongst frames of consecutive cardiac cycles, and (iii) the spatial compounding of temporally aligned data.

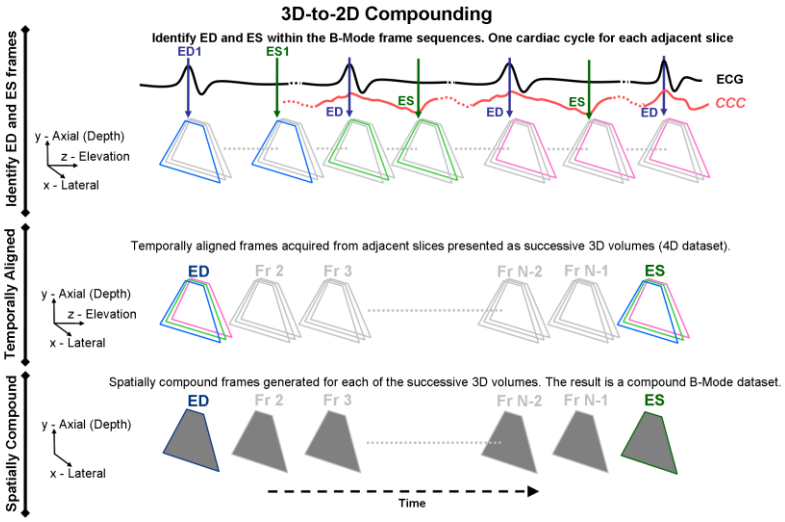


Figure 2: Three steps for *3D-to-2D Compounding*.

### 3.1 Identification of ED and ES frames and non-linear temporal alignment

The temporal behaviour of a heart may vary over consecutive cardiac cycles. When the adjacent 2D slices are acquired in succession their B-Mode frame sequences need to be temporally aligned prior to any spatial compounding. This step is not required if the adjacent slices are acquired using a 4D matrix transducer. However, with our acquisition setup, insufficient temporal alignment would result in the compounding of frames from two different cardiac phases and lead to severe blurring of anatomic structures. We utilised the non-linear method introduced by Perperidis *et al.* [4] for the temporal alignment of our datasets. Initially, an inter-frame similarity coefficient was used to semi-automatically identify all ED and ES frames within a B-Mode frame sequence. Then a *1D relaxed uniform interpolating cubic B-Spline* was used to temporally align all corresponding frames within the cardiac cycle acquired for each adjacent slice.

### 3.2 Spatial compounding

Temporally aligned frames from adjacent slices were spatially compounded to a single B-Mode frame sequence. Intensity averaging was utilised as the spatial compounding method since it is a well established and effective method for noise suppression in ultrasound data. The intensity of each pixel within the resulting frame was therefore set as the average intensity value of the corresponding pixels from all the temporally aligned frames.

## 4 Clinical measurements

Two experienced echocardiographers performed routine clinical measurements on both the original and compound data. We presented each echocardiographer a set of ED frames on which they measured the Inter-ventricular Septal Thickness (IVSd), Left Ventricular Internal Dimension (LVIDd) and Left Ventricular Posterior Wall (LVPWd). Similarly, they measured the Left Atrium Dimension (LADs) and Left Ventricular Internal Dimension (LVIDs) on a sequence of ES frames. Each image set contained one original and one averaged frame for each of the datasets (40 frames in total). The order of the frames was randomised to ensure no bias in the results. All clinical measurements were taken according to the BSE standards and performed twice to enable the examination of measurement agreement and repeatability.

# 5 Results and discussion

Figure 3 illustrates the effect of *3D-to-2D Compounding* on cardiac ultrasound data. *3D-to-2D Compounding* suppresses speckle/noise and can improve the appearance of anatomic structures such as the IVS. The mean SNR increase introduced over tissue around the IVS is 36%.

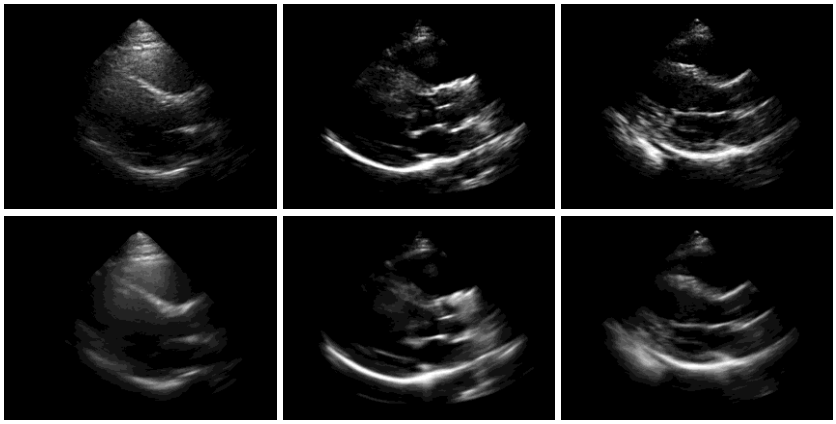

Figure 3: Original (top) and compound (bottom) ED frames of low (left), average (middle) and high (right) data quality.

Bland Altman plots [5] were used for the quantitative assessment of the effect of *3D-to-2D Compounding* on clinical measurements (Figure 4). The plots indicate the repeatability of measurements performed on the original data and the compounded data as well as the agreement between the measurements on the original and the compounded data. Table 1 summarises the bias, similarity and agreement measures and coefficients derived from the plots.

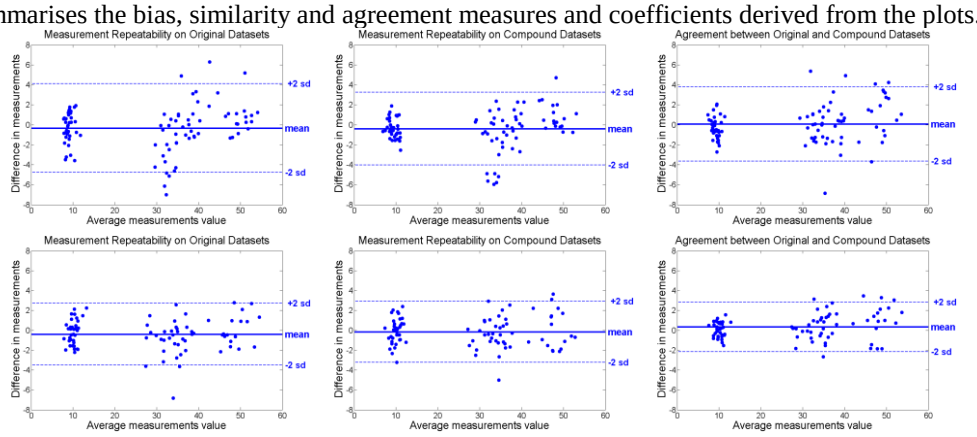


Figure 4: Bland Altman plots for measurements performed by Echocardiographer 1 (Top) and Echocardiographer 2 (Bottom). Bias as well as upper/lower limits of agreement included.

The Coefficients of Repeatability [6] (CR) in Table 1 indicate that measurements on compound data demonstrate improvement in repeatability level of up to 49% when compared to measurements on original unprocessed images. The effect of *3D-to-2D Compounding* varies depending on the echocardiographer and the clinical measurement performed. Nevertheless, *3D-to-2D Compounding* predominantly induces improvement in the repeatability of clinical measurements. In addition, measurements on original and compound data demonstrate good agreement with no systematic bias observed. Compounding 4D datasets acquired in real-time using a matrix transducer will remove some of the tissue boundary blurring introduced due to movements during the multi-cycle acquisition of our 3D datasets. Moreover, measurement

repeatability on the compounded data is expected to increase as the familiarity of the echocardiographers with them increases. Therefore, we believe that *3D-to-2D Compounding* can provide a good alternative to B-Mode for improving cardiac measurements.

| **Measure** | **Original** | | | | **Compound** | | | | **Agreement** | | | |
|---|---|---|---|---|---|---|---|---|---|---|---|---|
| **(mm)** | **Mean Diff** | **+2sd** | **-2sd** | **CR** | **Mean Diff** | **+2sd** | **-2sd** | **CR** | **Mean Diff** | **+2sd** | **- 2sd** | **CR** |
| **Echocardiographer 1** | | | | | | | | | | | | |
| **IVSd** | 0.21 | 2.27 | -1.85 | 2.06 | -0.47 | 1.64 | -2.57 | 2.10 | -0.47 | 1.48 | -2.43 | 1.96 |
| **LVIDd** | 0.81 | 3.84 | -2.22 | 3.03 | 0.86 | 3.60 | -1.88 | 2.74 | 1.16 | 5.60 | -3.28 | 4.44 |
| **LVPWd** | -0.76 | 2.60 | -4.13 | 3.37 | -0.31 | 1.40 | -2.03 | 1.71 | -0.16 | 2.09 | -2.41 | 2.25 |
| **LADs** | 1.06 | 5.01 | -2.89 | 3.95 | -0.03 | 3.67 | -3.72 | 3.70 | 0.08 | 3.69 | -3.54 | 3.62 |
| **LVIDs** | -2.98 | 0.90 | -6.86 | 3.88 | -1.97 | 2.60 | -6.55 | 4.58 | -0.15 | 4.50 | -4.80 | 4.65 |
| **Combined** | **-0.33** | **4.12** | **-4.77** | **4.45** | **-0.39** | **3.25** | **-4.04** | **3.64** | **0.08** | **3.80** | **-3.64** | **3.72** |
| **Echocardiographer 2** | | | | | | | | | | | | |
| **IVSd** | 0.08 | 2.92 | -2.77 | 2.85 | 0.42 | 2.79 | -1.94 | 2.37 | -0.09 | 1.54 | -1.71 | 1.62 |
| **LVIDd** | 0.09 | 3.11 | -2.93 | 3.02 | 0.12 | 3.85 | -3.62 | 3.74 | 0.93 | 4.28 | -2.43 | 3.36 |
| **LVPWd** | -0.43 | 1.47 | -2.32 | 1.89 | -0.54 | 1.79 | -2.88 | 2.34 | 0.21 | 1.50 | -1.09 | 1.29 |
| **LADs** | -1.01 | 2.86 | -4.88 | 3.87 | -0.92 | 1.81 | -3.65 | 2.73 | 0.47 | 2.76 | -1.82 | 2.29 |
| **LVIDs** | -0.70 | 2.13 | -3.53 | 2.83 | 0.48 | 3.48 | -2.52 | 3.00 | 0.14 | 3.16 | -2.88 | 3.02 |
| **Combined** | **-0.40** | **2.71** | **-3.50** | **3.11** | **-0.15** | **2.93** | **-3.23** | **3.08** | **0.35** | **2.85** | **-2.15** | **2.50** |

Table 1. Measurement repeatability and agreement coefficients for clinical measurements.

# 6 Conclusions

*3D-to-2D Compounding* provides a simple and effective technique for suppressing speckle/noise, enhancing anatomic structures within cardiac ultrasound data as well as improving clinical measurements. Due to its simple nature, *3D-to-2D Compounding* can act as a first step to post-processing techniques such as segmentation and registration, whose effectiveness is limited and sometimes restricted by low image quality (SNR). Our future work includes (i) acquiring and compounding real time 4D datasets using a matrix transducer and (ii) examining the effect of *3D-to 2D Compounding* on a wider range of clinical datasets.

# References

[1] British Heart Foundation. 2006 - Coronary heart Disease Statistics. Available from: http://www.bhf.org.uk, 2006.

[2] J. Hung, R. Lang, F. Flachskampf, S.K. Shernan, M.L. McCulloch, D.B. Adams, J. Thomas, M. Vannan, T. Ryan. 3D echocardiography: A review of the current status and future directions. *Journal of the American Society of Echocardiography*, 20 (3): 213-233, 2007.

[3] L.H. Henry, A. DeMaria, R.Gramiak, D.L. King, J.A. Kisslo, R.L. Popp, D.J. Sahn, N.B. Schiller, A. Tajik, L.E. Teichholz, A.E. Weyman. Report of the American Society of Echocardiography. Committee on Nomenclature and standards in two-dimensional echocardiography. *Circulation*, 62 (2): 212-217, 1980.

[4] A. Perperidis, D. Cusack, W.N. McDicken, T. MacGillivray, T. Anderson. Temporal Compounding of cardiac ultrasound data: Improving image quality and clinical measurement repeatability. In *Proceedings of Annual International Conference of the IEEE Engineering in Medicine and Biology Society*: 3661-3664, 2009.

[5] J.M. Bland & D.G. Altman. Statistical methods for assessing agreement between two methods of clinical measurement. *The Lancet*: 307-310, 1986

[6] British Standards Institution. Precision of test methods I. Guide for the determination and reproducibility for a standard test method. *BS 5497 - Part 1*. London: BSI, 1979.